Publishing House ASV

begell house, inc. publishers

Scientific coordination is carried out by the Russian Academy of Architecture and Construction Sciences (RAACS)

Volume 22 • Issue 1 • 2026

ISSN 2588-0195 (Online)
ISSN 2587-9618 (Print) Continues ISSN 1524-5845

International Journal for

Computational Civil and Structural Engineering

Международный журнал по расчету гражданских и строительных конструкций

https://ijccse.iasv.ru/

DOI: 10.22337/2587-9618
GICID: 71.0000.1500.2830

EXECUTIVE EDITOR

Vladimir I. Travush,
Full Member of RAACS, Professor, Dr.Sc.,
Vice-President of the Russian Academy
of Architecture and Construction Sciences;
Urban Planning Institute
of Residential and Public Buildings;
24, Ulitsa Bolshaya Dmitrovka, 107031, Moscow, Russia

EDITOR-IN-CHIEF

Vladimir N. Sidorov,
Full Member of RAACS, Professor, Dr.Sc., National Research Moscow State University of Civil Engineering; Russian University of Transport (RUT – MIIT); Moscow Institute of Architecture (State Academy); Perm National Research Polytechnic University; 26, Yaroslavskoe Shosse, 129337, Moscow, Russia

EDITORIAL DIRECTOR

Valery I. Telichenko,
Full Member of RAACS, Professor, Dr.Sc.,
The First Vice-President of the Russian Academy
of Architecture and Construction Sciences;
Honorary President of National Research
Moscow State University of Civil Engineering;
24, Ulitsa Bolshaya Dmitrovka, 107031, Moscow, Russia

MANAGING EDITOR

Nadezhda S. Nikitina,
Professor, Ph.D.,
Director of ASV Publishing House;
National Research Moscow State University
of Civil Engineering;
26, Yaroslavskoe Shosse, 129337, Moscow, Russia

ASSOCIATE EDITORS

Pavel A. Akimov,
Full Member of RAACS, Professor, Dr.Sc.,
Acting Rector of National Research
Moscow State University of Civil Engineering;
Vice-President of the Russian Academy
of Architecture and Construction Sciences;
Tomsk State University of Architecture and Building;
Russian University of Friendship of Peoples;
26, Yaroslavskoe Shosse, 129337, Moscow, Russia

Alexander M. Belostotsky,
Full Member of RAACS, Professor, Dr.Sc.,
Research & Development Center "STADYO";
National Research Moscow State University of Civil Engineering; Russian University of Transport (RUT – MIIT); Russian University of Friendship of Peoples;
Perm National Research Polytechnic University;
Tomsk State University of Architecture and Building;
Irkutsk National Research Technical University;
8th Floor, 18, ul. Tretya Yamskogo Polya,
125040, Moscow, Russia

Mikhail Belyi, Professor, Dr.Sc.,
Dassault Systèmes Simulia;
1301 Atwood Ave Suite 101W
02919 Johnston, RI, United States

Vitaly Bulgakov, Professor, Dr.Sc.,
Micro Focus;
Newbury, United Kingdom

Nikolai P. Osmolovskii, Professor, Dr.Sc.,
Systems Research Institute, Polish Academy of Sciences;
Kazimierz Pulaski University
of Technology and Humanities in Radom;
29, ul. Malczewskiego, 26-600, Radom, Poland

Gregory P. Panasenko, Professor, Dr.Sc.,
Equipe d'Analise Numerique; NMR CNRS 5585
University Gean Mehnet;
23 rue. P.Michelon 42023, St.Etienne, France

Scientific coordination is carried out by the Russian Academy of Architecture and Construction Sciences (RAACS)

PUBLISHER

ASV Publishing House
(ООО «Издательство АСВ»)
19/1,12, Yaroslavskoe Shosse, 120338, Moscow, Russia
Tel. +7(925)084-74-24; E-mail: iasv@iasv.ru; Интернет-сайт: http://iasv.ru/

ADVISORY EDITORIAL BOARD

Mojtaba Aslami, Ph.D,
Fasa University; Daneshjou blvd,
Fasa, Fars Province, Iran

Klaus-Jurgen Bathe, Professor
Massachusetts Institute
of Technology;
Cambridge, MA 02139, USA

Alexander T. Bekker,
Academician of RAACS,
Professor, Dr.Sc.,
Far Eastern Federal University;
Russian Academy of Architecture
and Construction Sciences;
8, Sukhanova Street, Vladivostok,
690950, Russia

Tomas Bock, Professor, Dr.-Ing.,
Technical University of Munich,
Arcisstrasse 21, D-80333
Munich, Germany

Jan Buynak, Professor, Ph.D.,
University of Žilina;
1, Univerzitná, Žilina, 010 26,
Slovakia

Vladimir T. Erofeev,
Full Member of RAACS,
Professor, Dr.Sc.,
Ogarev Mordovia State University;
68, Bolshevistskaya Str., Saransk
430005, Republic of Mordovia,
Russia

Victor S. Fedorov,
Full Member of RAACS,
Professor, Dr.Sc.,
Russian University of Transport
(RUT – MIIT);
9b9 Obrazcova Street, Moscow,
127994, Russia

Sergey V. Fedosov,
Full Member of RAACS,
Professor, Dr.Sc.,
Russian Academy of Architecture
and Construction Sciences;
24, Ul. Bolshaya Dmitrovka, 107031,
Moscow, Russia

Sergiy Yu. Fialko,
Professor, Dr.Sc.,
Cracow University of Technology;
24, Warszawska Street, Kraków,
31-155, Poland

Vladimir G. Gagarin,
Corresponding Member
of RAACS, Professor, Dr.Sc.,
Research Institute of Building
Physics of Russian Academy
of Architecture and Construction
Sciences;
21, Lokomotivny Proezd,
Moscow, 127238, Russia

Vyatcheslav A. Ilyichev,
Full Member of RAACS,
Professor, Dr.Sc.,
Russian Academy of Architecture
and Construction Sciences;
Podzemproekt Ltd.;
24, Ulitsa Bolshaya Dmitrovka,
Moscow, 107031, Russia

Marek Iwański,
Professor, Dr.Sc.,
Kielce University of Technology;
7, al. Tysiąclecia Państwa Polskiego
Kielce, 25 – 314, Poland

Sergey Yu. Kalashnikov,
Corresponding Member of RAACS,
Professor, Dr.Sc.,
Volgograd State Technical
University; 28, Lenin avenue,
Volgograd, 400005, Russia

Semen S. Kaprielov,
Academician of RAACS,
Professor, Dr.Sc.,
Research Center of Construction;
6, 2nd Institutskaya St., Moscow,
109428, Russia

Nikolay I. Karpenko,
Full Member of RAACS,
Professor, Dr.Sc.,
Research Institute of Building
Physics of Russian Academy
of Architecture and Construction
Sciences; Russian Academy of
Architecture and Construction
Sciences; 21, Lokomotivny Proezd,
Moscow, 127238, Russia

Vladimir V. Karpov,
Professor, Dr.Sc., Saint Petersburg
State University of Architecture and
Civil Engineering;
4, 2-nd Krasnoarmeiskaya Steet,
Saint Petersburg, 190005, Russia

Galina G. Kashevarova,
Corresponding Member
of RAACS, Professor, Dr.Sc.,
Perm National Research
Polytechnic University;
29 Komsomolsky pros., Perm,
Perm Krai, 614990, Russia

John T. Katsikadelis,
Professor, Dr.Eng, PhD, Dr.h.c.,
National Technical University of
Athens; Zografou Campus
9, Iroon Polytechniou str
15780 Zografou, Greece

Vitaly I. Kolchunov,
Full Member of RAACS,
Professor, Dr.Sc., Southwest State
University; Russian Academy of
Architecture and Construction
Sciences; 94, 50 let Oktyabrya,
Kursk, 305040, Russia

Dmitry V. Kozlov, Corresponding
Member of RAACS
Dr. Sc. Engineering, Professor, Head
of the Department of Hydraulics and
Hydrotechnical Construction, NRU
MGSU, 26, Yaroslavskoe Shosse.,
129337, Moscow, Russia

Markus König, Professor
Ruhr-Universität Bochum;
150, Universitätsstraße, Bochum,
44801, Germany

Sergey B. Kositsin,
Advisor of RAACS,
Professor, Dr.Sc.,
Russian University of Transport
(RUT – MIIT); 9b9 Obrazcova
Street, Moscow, 127994, Russia

Sergey B. Krylov,
Full Member of RAACS,
Professor, Dr.Sc.,
Research Center of Construction;
6, 2nd Institutskaya St., Moscow,
109428, Russia

Sergey A. Kudryavtsev,
Corresponding Member of of
RAACS, Professor, Dr.Sc., Far
Eastern State Transport University;
47, Serysheva St., 680021,
Khabarovsk, Russia

Sergey V. Kuznetsov,
Professor, Dr.Sc.,
Ishlinsky Institute for Problems in Mechanics of the Russian Academy of Sciences;
101-1, Prosp. Vernadskogo,
Moscow, 119526, Russia

Vladimir V. Lalin,
Professor, Dr.Sc.,
Peter the Great Saint-Petersburg Polytechnic University;
29, Ul. Politechnicheskaya,
Saint-Petersburg, 195251, Russia

Leonid S. Lyakhovich,
Full Member of RAACS,
Professor, Dr.Sc., Tomsk State University of Architecture and Building; 2, Solyanaya Sq., Tomsk, 634003, Russia

Rashid A. Mangushev,
Corresponding Member of RAACS, Professor, Dr.Sc.,
Saint Petersburg State University of Architecture and Civil Engineering;
4, 2-nd Krasnoarmeiskaya Steet,
Saint Petersburg, 190005, Russia

Ilizar T. Mirsayapov,
Corresponding Member of RAACS, Professor, Dr.Sc., Kazan State University of Architecture and Engineering; 1, Zelenaya Street, Kazan, 420043, Republic of Tatarstan, Russia

Vladimir L. Mondrus,
Corresponding Member of RAACS, Professor, Dr.Sc.,
National Research Moscow State University of Civil Engineering;
Yaroslavskoe Shosse 26,
Moscow, 129337, Russia

Valery I. Morozov,
Corresponding Member of RAACS, Professor, Dr.Sc.,
Saint Petersburg State University of Architecture and Civil Engineering;
4, 2-nd Krasnoarmeiskaya Steet,
Saint Petersburg, 190005, Russia

Igor G. Ovchinnikov, Professor, Dr.Sc., Tyumen Industrial University; 38, Volodarsky St., 625000, Tyumen, Russia

Anatoly V. Perelmuter,
Foreign Member of RAACS,
Professor, Dr.Sc., SCAD Soft;
Office 1,2, 3a Osvity street,
Kiev, 03037, Ukraine

Alexey N. Petrov,
Advisor of RAACS, Professor, Dr.Sc., Petrozavodsk State University; 33, Lenina Prospect, Petrozavodsk, 185910, Republic of Karelia, Russia

Vladilen V. Petrov,
Full Member of RAACS,
Professor, Dr.Sc.,
Yuri Gagarin State Technical University of Saratov;
77 Politechnicheskaya Street,
Saratov, 410054, Russia

Jerzy Z. Piotrowski,
Professor, Dr.Sc.,
Kielce University of Technology;
al. Tysiąclecia Państwa Polskiego 7,
Kielce, 25 – 314, Poland

Chengzhi Qi, Professor, Dr.Sc.,
Beijing University of Civil Engineering and Architecture;
1, Zhanlanlu, Xicheng District,
Beijing, China

Vladimir P. Selyaev,
Full Member of RAACS,
Professor, Dr.Sc., Ogarev Mordovia State University;
68, Bolshevistskaya Str., Saransk 430005, Republic of Mordovia, Russia

Eun Chul Shin,
Professor, Ph.D.,
Incheon National University;
(Songdo-dong)119 Academy-ro,
Yeonsu-gu, Incheon, Korea

D.V. Singh,
Professor, Ph.D,
University of Roorkee;
Roorkee, India, 247667

Wacław Szcześniak,
Foreign Member of RAACS,
Professor, Dr.Sc.,
Lublin University of Technology;
Ul. Nadbystrzycka 40,
20-618 Lublin, Poland

Tadatsugu Tanaka,
Professor, Dr.Sc.,
Tokyo University; 7-3-1 Hongo,
Bunkyo, Tokyo, 113-8654, Japan

Josef Vican,
Professor, Ph.D,
University of Žilina;
1, Univerzitná, Žilina, 010 26,
Slovakia

Zbigniew Wojcicki,
Professor, Dr.Sc.,
Wroclaw University of Technology;
11 Grunwaldzki Sq., 50-377,
Wrocław, Poland

Artur Zbiciak, Professor, Dr.Sc.,
Warsaw University of Technology;
Pl. Politechniki 1, 00-661 Warsaw,
Poland

Segrey I. Zhavoronok, Ph.D.,
Institute of Applied Mechanics of Russian Academy of Sciences;
Moscow Aviation Institute (National Research University);
7, Leningradsky Prt.,
Moscow, 125040, Russia

Askar Zhussupbekov,
Professor, Dr.Sc.,
Eurasian National University;
5, Munaitpassov street, Astana,
010000, Kazakhstan

TECHNICAL EDITOR

Taymuraz B. Kaytukov,
Advisor of RAACS,
Associate Professor, Ph.D.,
Vice-Rector of National Research Moscow State University of Civil Engineering;
Yaroslavskoe Shosse 26,
Moscow, 129337, Russia

EDITORIAL TEAM

Vadim K. Akhmetov, Professor, Dr.Sc., National Research Moscow State University of Civil Engineering; 26, Yaroslavskoe Shosse, 129337 Moscow, Russia

Pavel A. Akimov, Full Member of RAACS, Professor, Dr.Sc., Acting Rector of National Research Moscow State University of Civil Engineering; Vice-President of the Russian Academy of Architecture and Construction Sciences; Tomsk State University of Architecture and Building; Russian University of Friendship of Peoples; 26, Yaroslavskoe Shosse, 129337, Moscow, Russia

Alexander M. Belostotsky, Full Member of RAACS, Professor, Dr.Sc., Research & Development Center "STADYO"; National Research Moscow State University of Civil Engineering; Russian University of Transport (RUT – MIIT); Russian University of Friendship of Peoples; Perm National Research Polytechnic University; Tomsk State University of Architecture and Building; Irkutsk National Research Technical University; 8th Floor, 18, ul. Tretya Yamskogo Polya, 125040, Moscow, Russia

Mikhail Belyi, Professor, Dr.Sc., Dassault Systèmes Simulia; 1301 Atwood Ave Suite 101W 02919 Johnston, RI, United States

Vitaly Bulgakov, Professor, Dr.Sc., Micro Focus; Newbury, United Kingdom

Charles El Nouty, Professor, Dr.Sc., LAGA Paris-13 Sorbonne Paris Cite; 99 avenue J.B. Clément, 93430 Villetaneuse, France

Natalya N. Fedorova, Professor, Dr.Sc., Novosibirsk State University of Architecture and Civil Engineering (SIBSTRIN); 113 Leningradskaya Street, Novosibirsk, 630008, Russia

Darya Filatova, Professor, Dr.Sc., Probability, Assessment, Reasoning and Inference Studies Research Group, EPHE Laboratoire CHART (PARIS) 4-14, rue Ferrus, 75014 Paris

Vladimir Ya. Gecha, Professor, Dr.Sc., Research and Production Enterprise All-Russia Scientific-Research Institute of Electromechanics with Plant Named after A.G. Iosiphyan; 30, Volnaya Street, Moscow, 105187, Russia

Taymuraz B. Kaytukov, Advisor of RAACS, Associate Professor, Ph.D, Vice-Rector of National Research Moscow State University of Civil Engineering; 26, Yaroslavskoe Shosse, 129337, Moscow, Russia

Marina L. Mozgaleva, Professor, Dr.Sc., National Research Moscow State University of Civil Engineering; 26, Yaroslavskoe Shosse, 129337 Moscow, Russia

Nadezhda S. Nikitina, Professor, Ph.D., Director of ASV Publishing House; National Research Moscow State University of Civil Engineering; 26, Yaroslavskoe Shosse, 129337 Moscow, Russia

Nikolai P. Osmolovskii, Professor, Dr.Sc., Systems Research Institute Polish Academy of Sciences; Kazimierz Pulaski University of Technology and Humanities in Radom; 29, ul. Malczewskiego, 26-600, Radom, Poland

Gregory P. Panasenko, Professor, Dr.Sc., Equipe d'Analise Numerique NMR CNRS 5585 University Gean Mehnet; 23 rue. P.Michelon 42023, St.Etienne, France

Andreas Rauh, Prof. Dr.-Ing. habil. Carl von Ossietzky Universität Oldenburg, Germany School II - Department of Computing Science Group Distributed Control in Interconnected Systems D-26111 Oldenburg, Germany

Zhan Shi, Professor LPSM, Université Paris VI 4 place Jussieu, F-75252 Paris Cedex 05, France

Marina V. Shitikova, National Research Moscow State University of Civil Engineering, Advisor of RAACS, Professor, Dr.Sc., Voronezh State Technical University; 14, Moscow Avenue, Voronezh, 394026, Russia

Igor L. Shubin, Corresponding Member of RAACS, Professor, Dr.Sc., Research Institute of Building Physics of Russian Academy of Architecture and Construction Sciences; 21, Lokomotivny Proezd, Moscow, 127238, Russia

Vladimir N. Sidorov, Full Member of RAACS, Professor, Dr.Sc., National Research Moscow State University of Civil Engineering; Russian University of Transport (RUT – MIIT); Moscow Institute of Architecture (State Academy); Perm National Research Polytechnic University; 26, Yaroslavskoe Shosse, 129337, Moscow, Russia

Valery I. Telichenko, Full Member of RAACS, Professor, Dr.Sc., The First Vice-President of the Russian Academy of Architecture and Construction Sciences; National Research Moscow State University of Civil Engineering; 24, Ulitsa Bolshaya Dmitrovka, 107031, Moscow, Russia

Vladimir I. Travush, Full Member of RAACS, Professor, Dr.Sc., Vice-President of the Russian Academy of Architecture and Construction Sciences; Urban Planning Institute of Residential and Public Buildings; 24, Ulitsa Bolshaya Dmitrovka, 107031, Moscow, Russia

INVITED REVIEWERS

Akimbek A. Abdikalikov, Professor, Dr.Sc.,
Kyrgyz State University of Construction, Transport and Architecture n.a. N. Isanov;
34 Maldybayeva Str., Bishkek, 720020, Biskek, Kyrgyzstan

Vladimir N. Alekhin, Advisor of RAACS, Professor, Dr.Sc.,
Ural Federal University named after the first President of Russia B.N. Yeltsin;
19 Mira Street, Ekaterinburg, 620002, Russia

Irina N. Afanasyeva, Ph.D., University of Florida; Gainesville, FL 32611, USA

Ján Čelko, Professor, PhD, Ing., University of Žilina; Univerzitná 1, 010 26, Žilina, Slovakia

Tatyana L. Dmitrieva, Professor, Dr.Sc.,
Irkutsk National Research Technical University; 83, Lermontov street, Irkutsk, 664074, Russia

Petr P. Gaidzhurov, Advisor of RAACS, Professor, Dr.Sc.,
Don State Technical University; 1, Gagarina Square, Rostov-on-Don, 344000, Russia

Jacek Grosel, Associate Professor, Dr inz.
Wroclaw University of Technology; 11 Grunwaldzki Sq., 50-377, Wrocław, Poland

Stanislaw Jemioło, Professor, Dr.Sc.,
Warsaw University of Technology; 1, Pl. Politechniki, 00-661, Warsaw, Poland

Konstantin I. Khenokh, M.Ing., M.Sc.,
General Dynamics C4 Systems; 8201 E McDowell Rd, Scottsdale, AZ 85257, USA

Christian Koch, Dr.-Ing., Ruhr-Universität Bochum;
Lehrstuhl für Informatik im Bauwesen, Gebäude IA, 44780, Bochum, Germany

Gaik A. Manuylov, Professor, Ph.D.,
Moscow State University of Railway Engineering; 9, Obraztsova Street, Moscow, 127994, Russia

Alexander S. Noskov, Professor, Dr.Sc.,
Ural Federal University named after the first President of Russia B.N. Yeltsin;
19 Mira Street, Ekaterinburg, 620002, Russia

Ilya I. Ovchinnikov, Professor, Dr.Sc., Tyumen Industrial University; 38, Volodarsky St., 625000, Tyumen, Russia

Grzegorz Świt, Professor, Dr.hab. Inż.,
Kielce University of Technology; 7, al. Tysiąclecia Państwa Polskiego, Kielce, 25 – 314, Poland

AIMS AND SCOPE

The aim of the Journal is to advance the research and practice in structural engineering through the application of computational methods. The Journal will publish original papers and educational articles of general value to the field that will bridge the gap between high-performance construction materials, large-scale engineering systems and advanced methods of analysis.

The scope of the Journal includes papers on computer methods in the areas of structural engineering, civil engineering materials and problems concerned with multiple physical processes interacting at multiple spatial and temporal scales. The Journal is intended to be of interest and use to researches and practitioners in academic, governmental and industrial communities.

ОБЩАЯ ИНФОРМАЦИЯ О ЖУРНАЛЕ

International Journal for Computational Civil and Structural Engineering

(Международный журнал по расчету гражданских и строительных конструкций)

Международный научный журнал "International Journal for Computational Civil and Structural Engineering (Международный журнал по расчету гражданских и строительных конструкций)" (IJCCSE) является ведущим научным периодическим изданием по направлению «Инженерные и технические науки», издаваемым, начиная с 1999 года (ISSN 2588-0195 (Online); ISSN 2587-9618 (Print) Continues ISSN 1524-5845). В журнале на высоком научно-техническом уровне рассматриваются проблемы численного и компьютерного моделирования в строительстве, актуальные вопросы разработки, исследования, развития, верификации, апробации и приложений численных, численно-аналитических методов, программно-алгоритмического обеспечения и выполнения автоматизированного проектирования, мониторинга и комплексного наукоемкого расчетно-теоретического и экспериментального обоснования напряженно-деформированного (и иного) состояния, прочности, устойчивости, надежности и безопасности ответственных объектов гражданского и промышленного строительства, энергетики, машиностроения, транспорта, биотехнологий и других высокотехнологичных отраслей.

В редакционный совет журнала входят известные российские и зарубежные деятели науки и техники (в том числе академики, члены-корреспонденты, иностранные члены, почетные члены и советники Российской академии архитектуры и строительных наук). Основной критерий отбора статей для публикации в журнале − их высокий научный уровень, соответствие которому определяется в ходе высококвалифицированного рецензирования и объективной экспертизы, поступающих в редакцию материалов.

Журнал входит в Перечень ВАК РФ ведущих рецензируемых научных изданий, в которых должны быть опубликованы основные научные результаты диссертаций на соискание ученой степени кандидата наук, на соискание ученой степени доктора наук по научным специальностям и соответствующим им отраслям науки:

- 1.1.8 – Механика деформируемого твердого тела (технические науки),
- 1.2.2 – Математическое моделирование численные методы и комплексы программ (технические науки),
- 2.1.1 – Строительные конструкции, здания и сооружения (технические науки),
- 2.1.2 – Основания и фундаменты, подземные сооружения (технические науки),
- 2.1.5 – Строительные материалы и изделия (технические науки),
- 05.23.07 – Гидротехническое строительство (технические науки),
- 2.1.9 – Строительная механика (технические науки)

В Российской Федерации журнал индексируется Российским индексом научного цитирования (РИНЦ).

Журнал входит в базу данных Russian Science Citation Index (RSCI), полностью интегрированную с платформой Web of Science. Журнал имеет международный статус и высылается в ведущие библиотеки и научные организации мира.

Издатели журнала – *Издательство Ассоциации строительных высших учебных заведений /АСВ/* (Россия, г. Москва) и до 2017 года *Издательский дом Begell House Inc*. (США, г. Нью-Йорк). Официальными партнерами издания является *Российская академия архитектуры и строительных наук* (РААСН), осуществляющая научное курирование издания, и *Научно-исследовательский центр СтаДиО* (ЗАО НИЦ СтаДиО).

Цели журнала – демонстрировать в публикациях российскому и международному профессиональному сообществу новейшие достижения науки в области вычислительных методов решения фундаментальных и прикладных технических задач, прежде всего в области строительства.

Задачи журнала:

• предоставление российским и зарубежным ученым и специалистам возможности публиковать результаты своих исследований;

• привлечение внимания к наиболее актуальным, перспективным, прорывным и интересным направлениям развития и приложений численных и численно-аналитических методов решения фундаментальных и прикладных технических задач, совершенствования технологий математического, компьютерного моделирования, разработки и верификации реализующего программно-алгоритмического обеспечения;

• обеспечение обмена мнениями между исследователями из разных регионов и государств.

Тематика журнала. К рассмотрению и публикации в журнале принимаются аналитические материалы, научные статьи, обзоры, рецензии и отзывы на научные публикации по фундаментальным и прикладным вопросам технических наук, прежде всего в области строительства. В журнале также публикуются информационные материалы, освещающие научные мероприятия и передовые достижения Российской академии архитектуры и строительных наук, научно-образовательных и проектно-конструкторских организаций.

Тематика статей, принимаемых к публикации в журнале, соответствует его названию и охватывает направления научных исследований в области разработки, исследования и приложений численных и численно-аналитических методов, программного обеспечения, технологий компьютерного моделирования в решении прикладных задач в области строительства, а также соответствующие профильные специальности, представленные в диссертационных советах профильных образовательных организациях высшего образования.

Редакционная политика. Политика редакционной коллегии журнала базируется на современных юридических требованиях в отношении авторского права, законности, плагиата и клеветы, изложенных в законодательстве Российской Федерации, и этических принципах, поддерживаемых сообществом ведущих издателей научной периодики.

За публикацию статей плата с авторов не взымается. Публикация статей в журнале бесплатная. На платной основе в журнале могут быть опубликованы материалы рекламного характера, имеющие прямое отношение к тематике журнала.

Журнал предоставляет непосредственный открытый доступ к своему контенту, исходя из следующего принципа: свободный открытый доступ к результатам исследований способствует увеличению глобального обмена знаниями.

Индексирование. Публикации в журнале входят в системы расчетов индексов цитирования авторов и журналов. «Индекс цитирования» – числовой показатель, характеризующий значимость данной статьи и вычисляющийся на основе последующих публикаций, ссылающихся на данную работу.

Авторам. Прежде чем направить статью в редакцию журнала, авторам следует ознакомиться со всеми материалами, размещенными в разделах сайта журнала (интернет-сайт Российской академии архитектуры и строительных наук (http://raasn.ru); подраздел «Издания РААСН» или интернет-сайт Издательства АСВ (http://iasv.ru); подраздел «Журнал IJCCSE»): с основной информацией о журнале, его целями и задачами, составом редакционной коллегии и редакционного совета, редакционной политикой, порядком рецензирования направляемых в журнал статей, сведениями о соблюдении редакционной этики, о политике авторского права и лицензирования, о представлении журнала в информационных системах (индексировании), информацией о подписке на журнал, контактными данными и пр. Журнал работает по лицензии Creative Commons типа cc by-nc-sa (Attribution Non-Commercial Share Alike) – Лицензия «С указанием авторства – Некоммерческая – Копилефт».

Рецензирование. Все научные статьи, поступившие в редакцию журнала, проходят обязательное двойное слепое рецензирование (рецензент не знает авторов рукописи, авторы рукописи не знают рецензентов).

Заимствования и плагиат. Редакционная коллегия журнала при рассмотрении статьи проводит проверку материала с помощью системы «Антиплагиат». В случае обнаружения многочисленных заимствований редакция действует в соответствии с правилами COPE.

Подписка. Журнал зарегистрирован в Федеральном агентстве по средствам массовой информации и охраны культурного наследия Российской Федерации. Индекс в общероссийском каталоге РОСПЕЧАТЬ − 18076.

По вопросам подписки на международный научный журнал “International Journal for Computational Civil and Structural Engineering (Международный журнал по расчету гражданских и строительных конструкций)” обращайтесь в Агентство «Роспечать» (Официальный сайт в сети Интернет: http://www.rosp.ru/) или в издательство Ассоциации строительных вузов (АСВ) в соответствии со следующими контактными данными:

ООО «Издательство АСВ»

Юридический адрес: 129337, Россия, г. Москва, Ярославское ш., д. 26, офис 705;

Фактический адрес: 129337, Россия, г. Москва, Ярославское ш., д. 19, корп. 1, 5 этаж, офис 12 (ТЦ Соле Молл);

Телефоны: +7 (925) 084-74-24;

Интернет-сайт: www.iasv.ru. Адрес электронной почты: iasv@iasv.ru.

Контактная информация. По всем вопросам работы редакции, рецензирования, согласования правки текстов и публикации статей следует обращаться к главному редактору журнала академику РААСН *Сидорову Владимиру Николаевичу* (адреса электронной почты: sidorov.vladimir@gmail.com, sidorov@iasv.ru, iasv@iasv.ru, sidorov@raasn.ru) или к техническому редактору журнала советнику РААСН *Кайтукову Таймуразу Батразовичу* (адреса электронной почты: tkaytukov@gmail.com; kaytukov@raasn.ru). Кроме того, по указанным вопросам, а также по вопросам размещения в журнале рекламных материалов можно обращаться к генеральному директору ООО «Издательство АСВ» *Никитиной Надежде Сергеевне* (адреса электронной почты: iasv@iasv.ru, nsnikitina@mail.ru, ijccse@iasv.ru).

Журнал становится технологичнее. Издательство АСВ с сентября 2016 года является членом Международной ассоциации издателей научной литературы (Publishers International Linking Association (PILA)), осуществляющей свою деятельность на платформе CrossRef. Оригинальным статьям, публикуемым в журнале, будут присваиваться уникальные номера (индексы DOI – Digital Object Identifier), что значительно облегчит поиск метаданных и местонахождение полнотекстового произведения. DOI – это система определения научного контента в сети Интернет.

С октября 2016 года стал возможен прием статей на рассмотрение и рецензирование через онлайн систему приема статей Open Journal Systems на сайте журнала (электронная редакция): https://ijccse.iasv.ru.

Автор имеет возможность следить за продвижением статьи в редакции журнала в личном кабинете Open Journal Systems и получать соответствующие уведомления по электронной почте.

В феврале 2018 года журнал был зарегистрирован в Directory of open access journals (DOAJ) (это один из самых известных поисковых сервисов в мире, который предоставляет открытый доступ к материалам и индексирует не только заголовки журналов, но и научные статьи), в сентябре 2018 года включен в продукты EBSCO Publishing.

В ноябре 2020 года журнал начал индексироваться в международной базе Scopus.

Журнал International Journal for Computational Civil and Structural Engineering входит в первый уровень Единого государственного перечня научных изданий – «Белого списка» – Министерства Науки и высшего образования Российской Федерации (ЕГПНИ)

International Journal for
Computational Civil and Structural Engineering
(Международный журнал по расчету гражданских и строительных конструкций)
Volume 22, Issue 1 ***2026***

Scientific coordination is carried out by the Russian Academy of Architecture and Construction Sciences (RAACS)

CONTENTS

Numerical Modeling of Concrete Creep Under Various Stress States **14**
Petr D. Arleninov

About Multiscale Modeling with The Use of Haar Discrete Wavelets for Targeted Data Extraction in Problems of Structural Mechanics **28**
Mojtaba Aslami, Pavel A. Akimov

Assessment of the Robustness for Frame Structures Based on a Probability Index **35**
Anatoliy V. Alekseytsev, Natalya S. Kurchenko

Reliability of Enclosing Structures According to a Given Criterion of Thermal Protection **56**
Natalya L. Galaeva

Numerical Simulation of Swirling Flows with Separation Zones **65**
Vadim K. Akhmetov

Application of Computer Vision to Detect Defects in Welds **74**
Marina E. Dement'eva

Simulation of the Operation of a Pressure Pipeline with an Internal Lining of a Protective Coating **86**
Vladimir A. Orlov, Sergey P. Zotkin, Maria A. Bolshakova

Mathematical Model of Optimization of the Transparent Partition Thickness in the Trombe Wall Heat Exchange System **92**
Ivan K. Andrianov, Elena K. Chepurnova, Sergey A. Kostikov

Nonlinear Dynamic Analysis of the Steel-Rubber Vibration Isola-tors with Perforation **104**
Vladimir L. Mondrus, Dmitry K. Sizov, Timofei M. Kvasnikov

Higher-Mode Effects in Glass Pane Response to Close-Range Blast: a Finite Element and SDOF Model Comparison **118**
Ilham Nurhuda, Nelson T.K. Lam

Determination of the Soil Resistance Value for the Foundation Design of Reconstructed Buildings **133**
Anatolii I. Polishchuk, Shuhong Wang, Nadezhda S. Nikitina, Maxim B. Marinichev

Analysis of the Physical and Mechanical Properties of a Fibreglass Composite Pipe with Binder Modified by Plasticizers **144**
Sergey V. Shashkin, Tatyana A. Matseevich

Numerical Simulation of Dynamic Structural Response to Vibrations Induced by Railway Transport **157**
Alexander M. Belostotsky, Alexander I. Nagibovich, Dmitry S. Dmitriev, Andrey A. Aul, Tatiana N. Vasileva

Construction Properties of Subsidible Soils in Mongolia Under Climate Change: Problem and Solution **169**
Nyamdorj Setev, Uranchimeg Davaasuren, Sukh-Erdene Khureltsooj, Erdenetsetseg Enkhbaatar

Assessment of the Influence of Adjacent Excavation Step Length on Shield Tunnel Deflection **179**
Nguyen Van Hung, Nguyen Trong Tam

International Journal for
Computational Civil and Structural Engineering
(Международный журнал по расчету гражданских и строительных конструкций)
Volume 22, Issue 1 ***2026***

Scientific coordination is carried out by the Russian Academy of Architecture and Construction Sciences (RAACS)

СОДЕРЖАНИЕ

Численное моделирование ползучести бетона при разных видах НДС **14**
П.Д. Арленинов

О многоуровневом моделировании с использованием дискретных вейвлетов Хаара для целевого извлечения данных в задачах строительной механики **28**
М. Аслами, П.А. Акимов

Метод оценки живучести рамных конструкций на основе вероятностного индекса **35**
А.В. Алексейцев, Н.С. Курченко

Надежность ограждающих конструкций по заданному критерию тепловой защиты **56**
Н.Л. Галаева

Численное моделирование закрученных течений с отрывными зонами **65**
В.К. Ахметов

Применение компьютерного зрения для обнаружения дефектов в сварных швах **74**
М.Е. Дементьева

Моделирование работы напорного трубопровода с внутренней облицовкой защитным покрытием **86**
В.А. Орлов, С.П. Зоткин, М.А. Большакова

Математическая модель оптимизации толщины стенки прозрачной перегородки в системе теплообмена стены тромба **92**
И.К. Андрианов, С.А. Костиков, Е.К. Чепурнова

Нелинейный динамический анализ перфорированных резинометаллических виброизоляторов **104**
В.Л. Мондрус, Д.К. Сизов, Т.М. Квасников

Влияние высших форм колебаний на отклик стеклянных панелей при ближних взрывах: сравнение моделей МКЭ и SDOF **118**
Ильхам Нурхуда, Нельсон Т.К. Лам

Определение расчетного сопротивления грунта основания при проектировании фундаментов реконструируемых зданий **133**
А.И. Полищук, Ш. Ванг, Н.С. Никитина, М.Б. Мариничев

Исследование физико-механических свойств трубы из модифицированного пластификаторами стеклокомпозита **144**
С.В. Шашкин, Т.А. Мацеевич

Численное моделирование динамического отклика несущих конструкций здания от вибрационного воздействия рельсового транспорта **157**
А.М. Белостоцкий, А.И. Нагибович, Д.С. Дмитриев, А.А. Аул, Т.Н. Васильева

Конструктивные свойства неустойчивых грунтов монголии в условиях изменения климата: проблеммы и решения **169**
Сэтэв Ньямдорж, Даваасурэн Уранчимэг, Хурэлцооож Сух-Эрдэнэ, Энхбаатар Эрдэнэцэцэг

Оценка влияния длины шага смежной выемки на прогиб щитового тоннеля
Нгуен Ван Хунг, Нгуен Чонг Там **179**

DOI:10.22337/2587-9618-2026-22-1-14-27

NUMERICAL MODELING OF CONCRETE CREEP UNDER VARIOUS STRESS STATES

Petr D. Arleninov

Research, Design and Technological Institute of Concrete and Reinforced Concrete of the National Research Center "Construction", National Research Moscow State University of Civil Engineering, Moscow, RUSSIA

Abstract: The article addresses the problem of numerically modeling creep deformations in modern high-strength modified self-compacting concretes. The relevance of the research is driven by the imperfections in the regulatory framework, specifically SP 63.13330.2018, which offers an overly simplified and conservative approach to accounting for creep. This approach fails to consider the specific characteristics of modern concretes and does not enable reliable forecasting. Conversely, the existing, more detailed domestic recommendations from 1984 are technically obsolete and inapplicable to high-strength concretes.

The aim of the study is to assess the applicability of modern and outdated computational creep models for predicting deformations in high-strength concrete across different humidity conditions. The research was conducted using numerical modeling in the ATENA software complex, with verification of the results against experimental data.

The results demonstrated that the direct application of even the most modern models (B3, MC 2010) leads to significant errors (ranging from 13% to 130%), which vary depending on humidity. Models from the 1970s-80s (exemplified by ACI-78) proved entirely inapplicable, showing discrepancies of up to 600% compared to experimental data. The necessity of modifying models not only for the specific concrete composition but also for its curing conditions and humidity levels is demonstrated.

The study concludes that the verification and calibration of computational models based on experimental data are critically important before modeling complex stress-strain states. An action algorithm is proposed to enhance the accuracy of creep prediction under multiaxial loads, which includes mandatory experimental verification of boundary conditions.

Keywords: concrete creep, numerical modeling, high-strength concrete, ATENA, B3 creep model, fib Model Code, finite element method, stress-strain state

ЧИСЛЕННОЕ МОДЕЛИРОВАНИЕ ПОЛЗУЧЕСТИ БЕТОНА ПРИ РАЗНЫХ ВИДАХ НДС

П.Д. Арленинов

НИИЖБ им. А.А. Гвоздева АО «НИЦ «Строительство», Москва, Россия; НИУ МГСУ, Москва, РОССИЯ

Аннотация: В статье рассматривается проблема численного моделирования деформаций ползучести современных высокопрочных модифицированных самоуплотняющихся бетонов. Актуальность исследования обусловлена несовершенством нормативной базы, в частности, СП 63.13330.2018, который предлагает чрезмерно упрощенный и консервативный подход к учету ползучести, не учитывающий особенности современных бетонов и не позволяющий выполнять прогнозирование. Существующие более детальные отечественные рекомендации 1984 года, напротив, морально устарели и не применимы к высокопрочным бетонам.

Целью работы является оценка применимости современных и устаревших расчетных моделей ползучести для прогнозирования деформаций высокопрочного бетона класса в различных условиях влажности. Исследование проводилось методом численного моделирования в программном комплексе ATENA с верификацией результатов на экспериментальных данных.

Результаты показали, что прямое применение даже самых современных моделей (B3, MC 2010) приводит к значительным погрешностям (от 13% до 130%), варьирующимся в зависимости от влажности. Модели 1970-80-х годов (на примере ACI-78) оказались полностью неприменимы, демонстрируя расхождения с экспериментом до 600%. Показана необходимость модификации моделей не только под конкретный состав бетона, но и под условия его твердения и влажности.

Сделан вывод о критической важности верификации и калибровки вычислительных моделей на основе экспериментов перед моделированием сложного напряженно-деформированного состояния. Предложен алгоритм действий для повышения точности прогнозирования ползучести при многоосных нагрузках, включающий обязательную экспериментальную проверку граничных условий.

Ключевые слова: ползучесть бетона, численное моделирование, высокопрочный бетон, ATENA, модели ползучести B3, Model Code

INTRODUCTION

The main regulatory document that governs the calculation and design of reinforced concrete structures in our country is SP 63.13330.2018. It serves as the primary source for related documents such as SP 266.1325800.2016, which covers the design and calculation of steel-reinforced concrete structures; SP 430.1325800.2018, which regulates the design of cast-in-place structures; and the design code currently under development for reinforced concrete structures with external sheet reinforcement. Some formulas, tables, and provisions in these design codes are identical to those in SP 63.13330.2018. In particular, this applies to the description of the concrete creep process. However, the section on concrete creep accounting is very short. SP 63.13330.2018 does not provide any information on shrinkage accounting.

SP 63.13330.2018 does not offer a method for predicting creep. It only includes one formula, (1), for reducing the elastic modulus under prolonged loading while accounting for creep. Formula (1) includes only the initial modulus and the creep coefficient. Formula (2) accounts for inelastic deformations and rapid creep when specifying the elastic modulus under short-term loading. For shear, the code recommends taking the modulus of elasticity as 0.4 of the initial value, but does not specify whether this applies to long-term or short-term effects. This code does not provide any other recommendations for accounting for concrete creep. The creep coefficient, $\varphi_{b,cr}$, included in formula (1), is a tabulated value that depends only on the concrete class and ambient humidity. Furthermore, for high-strength concrete (with a compressive strength of 60 MPa and above, as per class designations), this coefficient is applied as a single, unified value. This approach is conservative and has been criticized by many researchers [1, 2]. Its inclusion was not based on experimental or theoretical substantiation but rather on a review of foreign literature (American and European documents) conducted in the early 2000s during the development of the then-new Russian concrete design code, SP 52-101-2003. This was a practical solution, as the technology and industry were ready for the use of high-strength concrete, but its characteristics - particularly its deformation properties - were largely unstudied; nearly all scientific research in this area within the country had ceased.

Eurocode 2 (1992), which was thoroughly examined during the preparation of the 2001 Russian code, proposed the use of distinct creep coefficients for concrete grades up to class C100, with differentiation at five-class intervals. Currently, international research in this field has advanced considerably [3-5]. Studies now investigate the effects of creep not only under compression but also under other stress-strain state conditions, and there are ongoing efforts to utilize modern software for developing creep models, among other advancements [6-8]. In contrast, due to the fact that creep testing can only be conducted in a few organizations within our country, such research remains sporadic [9,10].

$$E_{b,\tau} = \frac{E_b}{1+\varphi_{b,cr}} \quad (1)$$

$$E_{b,1} = 0.85 \cdot E_b \quad (2)$$

Before the publication of the design code SP 52-101-2003, which was used alongside the existing SNiP 2.03.01-84*, the Recommendations of the NIIZhB for Considering Shrinkage and Creep (1984) were also in effect. Interestingly, this document has never been officially revoked and, paradoxically, remains valid to this day. This was a fundamental body of work. A large number of

specialists participated in its development, and all its dependencies and tabulated values were based on an extensive array of experimental research conducted in the Soviet Union.

These recommendations allow predicting the creep and shrinkage deformations of concrete up to class B60, accounting for a wide range of input variables (such as concrete mix composition, loading age, and structure type). At the time of their release, these recommendations were not only highly relevant within the country but were also competitive on a global scale. The creep model they proposed was on par with leading European and American models of that era [11, 12]. Following the publication of these recommendations, some specialists continued in-depth research on creep [13-15], and there were attempts to introduce improved models [16, 17]. However, these subsequent studies were never incorporated into the regulatory documents. When attempts were made to apply both the models from the 1984 recommendations and those from other leading Russian and Soviet scientists to modern concretes, certain contradictions and inconsistencies were revealed [18]. Furthermore, direct attempts to predict the creep deformations of high-strength concrete using these models resulted in significant inaccuracies, to the point of complete inapplicability. This also applies to the accelerated method for determining creep deformations (which was present in GOST 24544-84) that was removed during the latest update of that standard. Later, this article will demonstrate the inadequacy of the 1978 American concrete creep model when applied to modern concretes.

Over the past 15 years, the author has conducted extensive experimental and theoretical research on the deformation characteristics of high-strength concretes. Some of these findings are presented in this article. The study examines an approach that combines the classical experimental evaluation of creep deformations according to GOST 24544-2020 with the use of modern computational tools based on advanced software complexes that have various built-in concrete creep models. This work is critically important because manually calculating the creep effects in a complex structural element or joint is practically infeasible when such an analysis is required.

METHODS

To assess the applicability of existing creep theories, enable three-dimensional computer modeling of long-term experiments in analysis software, and evaluate the feasibility of computer modeling of complex stress-strain states under sustained loading, a numerical simulation was performed. This simulation imitated the deformation of prism specimens under three different humidity conditions using the most advanced creep models: B3, B3 improved, MC 2010, and the American ACI-78 model. The ATENA software package was used as the computational tool.

This particular software package was selected because its built-in model, which accounts for the physical nonlinearity of concrete properties—the Fracture–Plastic Constitutive Model CC3DCementitious2 developed by Červenka Consulting—has proven highly effective in modeling reinforced concrete elements under various stress-strain states. These include concentric and eccentric compression [19, 20], bending [21], biaxial compression, shear, punching shear [22], steel-concrete composite structures of varying complexity [23], and structures with external sheet reinforcement [24, 25], including those made of high-strength concrete. The model is based on a combination of a tensile fracture model (Rankine-Fracturing Model) and a compressive failure model for the material (Menétrey-Willam). A review of the literature indicates that calculation results obtained with the built-in CC3DCementitious2 concrete model generally show good agreement with experimental data—the discrepancy in results from various researchers, both Russian and international, typically remains within 10%.

For the computer simulation, a specific high-strength modified self-compacting concrete mix of class B75 (determined according to GOST 18105 and GOST 31914) was selected. Detailed

studies of modified high-strength concretes with similar characteristics, for which the authors of the report conducted concurrent tests to determine creep and shrinkage deformations under three different humidity conditions, are presented in [26]. The specimens were loaded at the age of 88 days. (For some modified concretes, achieving the design strength class at an age of 60 days or more is considered normal; the design age for this concrete was 90 days). Based on the test results for density and slump flow, conducted in accordance with the requirements of GOST 26633 and GOST R 59715, the mix can be classified as self-compacting. This particular composition was chosen for the computer study to evaluate the applicability of existing concrete creep models to modern high-strength modified self-compacting concretes. Given that practically all concretes with a strength class above B60 fall into this category, this research task is highly relevant.

Predicting creep deformations under different humidity conditions for a single concrete mix is an important task. This is because the same concrete, even within a single structure, can cure under various conditions (e.g., an enclosed steel section restricts moisture migration from the concrete, while exposed surfaces imply standard temperature and humidity conditions). Furthermore, when using creep coefficients in calculations, it is essential to know their potential maximum values for the concrete class in question, enabling a probabilistic forecast of worst-case scenarios. (Conversely, the worst-case design scenario may sometimes involve maximum stiffness of structural elements, which corresponds to minimum creep coefficients—see Formula 1). Figure 2 presents the experimental deformation curves for the concrete under sustained load at different humidity levels. This figure also shows the testing setups located in rooms with normal humidity; the tests at elevated and reduced humidity were conducted in separate climate-controlled chambers.

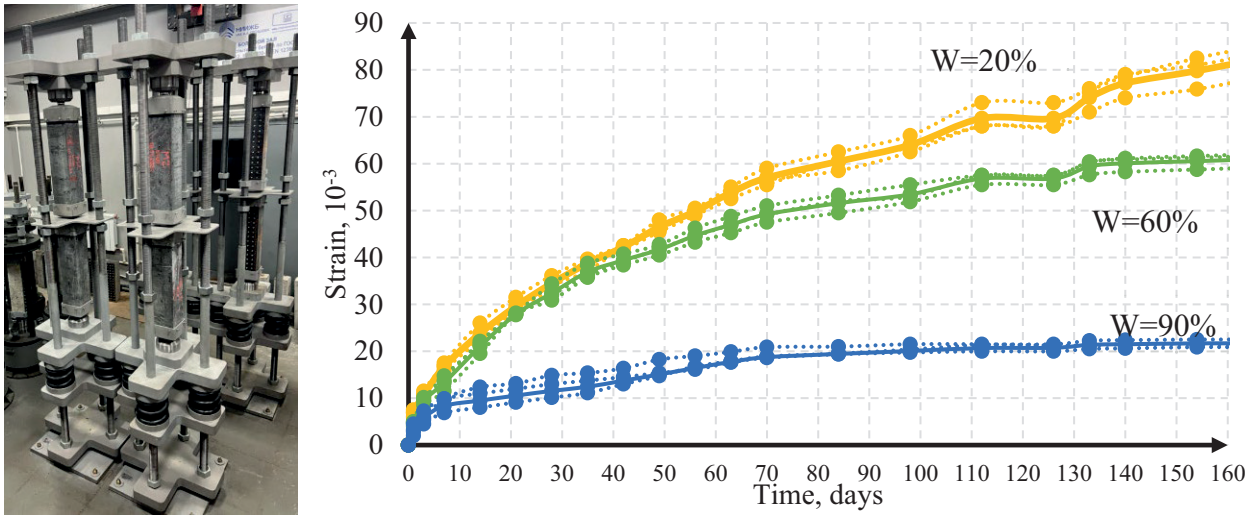


Figure 1. Experimental creep and shrinkage strains for various humidity conditions

The ATENA software package includes a built-in module for considering concrete creep. Within this module, it is possible to select virtually any modern creep model, and the proposed models can also be modified. The program allows for the full exploitation of the simulation capabilities inherent in the calculation models. For example, it enables loading the specimen at any age, modeling various curing conditions prior to load application, and applying additional load during the test.

Figure 2 (left) presents a diagram illustrating the algorithm for defining sustained load, alongside

the results of verification calculations performed using the B3, ACI, and CEB models (right), based on data from studies [26-30].
As can be seen from this table, the average error when using the ACI model reaches 58%. Furthermore, when evaluating individual experiments, the error can reach 100% or more. This assessment was conducted for each model using data from 17 known experiments performed by various researchers on different concrete mixes.
Figure 3 shows the calculation model of the specimen with different configurations of the finite element mesh, which was used for a sensitivity test. Based on the results of this test, a mesh with an element size of 30×30×30 mm was selected for modeling the prism specimen.

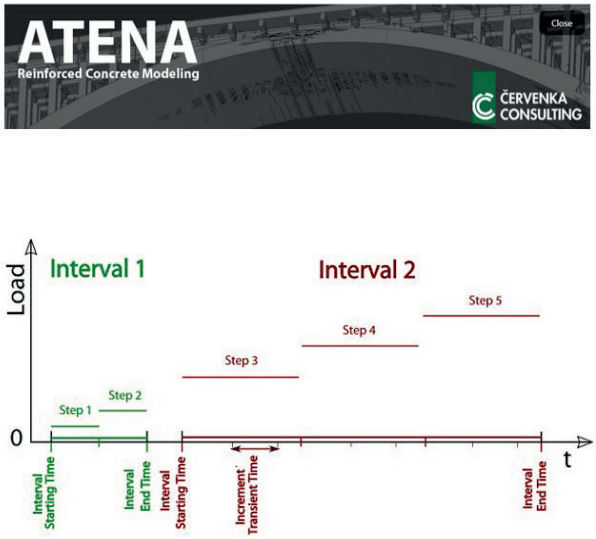


Table 2.1: Coefficients of variation of errors (expressed as percentage) of basic creep predictions for various models.

Model	B3	ACI	CEB
Test data	$\bar{\omega}$	$\bar{\omega}$	$\bar{\omega}$
1. Keeton	19.0	37.5	42.8
2. Kommendant et al	15.3	31.8	8.1
3. L'Hermite et al.	49.4	133.4	66.2
4. Rostasy et al.	15.2	47.6	5.0
5. Troxell et al.	4.6	13.9	6.2
6. York et al.	5.6	37.7	12.8
7. McDonald	6.9	48.4	22.2
8. Maity and Meyers	33.8	30.0	15.7
9. Mossiossian and Gamble	18.6	51.5	47.3
10. Hansen and Harboe et al. (Ross Dam)	14.1	51.2	31.1
11. Browne et al. (Wylfa vessel)	44.7	47.3	53.3
12. Hansen and Harboe et al. (Shasta Dam)	22.7	107.8	43.1
13. Brooks and Wainwright	12.6	14.9	15.4
14. Pirtz (Dworshak Dam)	12.5	58.2	32.5
15. Hansen and Harboe et al. (Canyon ferry Dam)	33.3	70.2	56.9
16. Russell and Burg (Water Tower Place)	15.7	19.3	31.5
17. Hanson	14.1	63.3	12.1
$\bar{\omega}_{all}$	23.6	58.1	35.0

Figure 2. Algorithm for modelling loading regime in creep analysis using ATENA software (left), comparison of various creep models with respect to experimental data (right)

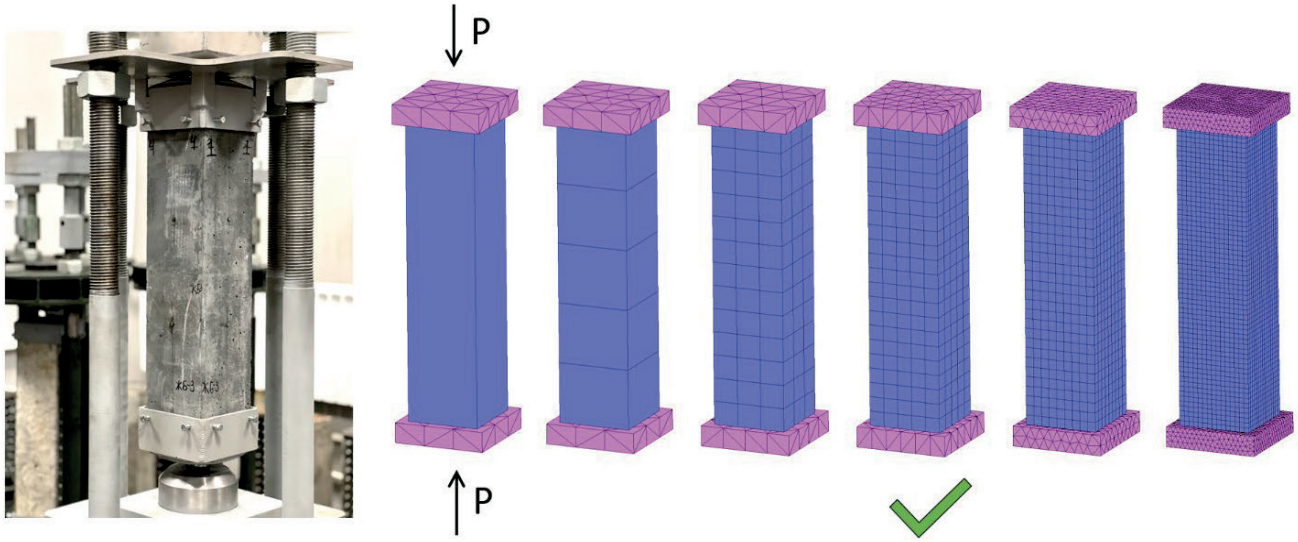


Figure 3. Finite element model of the tested specimen

RESULTS

Following the preparation of the computational model for a concrete prism specimen with dimensions of 150×150×600 mm as a standard specimen for creep tests according to GOST 24544-2020, restrained between two support plates with axial load transfer (simulating load application via a steel ball in a spring-loaded setup), a series of numerical analyses was performed. These analyses predicted creep deformations using four distinct models: MC 2010 (the current Model Code model), B3 (the most widely used creep model globally at present, proposed by Bažant in 1994), B3 improved (the latest enhanced B3 model, which allows for a greater number of input parameters, particularly for better accounting of early-age shrinkage), and ACI-78 (the now-outdated model from the American Concrete Institute). The 1978 ACI model was included in the comparison to provide a general assessment of the applicability of models from the 1970s and 1980s to modern modified self-compacting high-strength concretes. In this context, the calculation results obtained with this model indirectly reflect the applicability of the domestic model from the 1984 Recommendations for Considering Shrinkage and Creep of Concrete. A direct verification of this latter model in any computer software is impossible because all advanced software packages capable of three-dimensional modeling of long-term concrete tests are foreign (e.g., Ansys, ATENA, Abaqus) and lack integration with Soviet and Russian scientific developments and regulatory documents.

Figures 4-6 present the results of the computer-predicted creep deformations according to the considered models for humidity levels of 20%, 60%, and 90%. For ease of comparing the experimental and calculated curves, the deformation values are given in absolute terms. Next to the model's name, the percentage deviation from the experimental results is indicated. Data for the modified model based on B3 are labeled "modify" on the graphs; the modifications to the B3 model were implemented by adding a set of coefficients to achieve the best possible fit between the modified model and the experimental results obtained under normal humidity conditions.

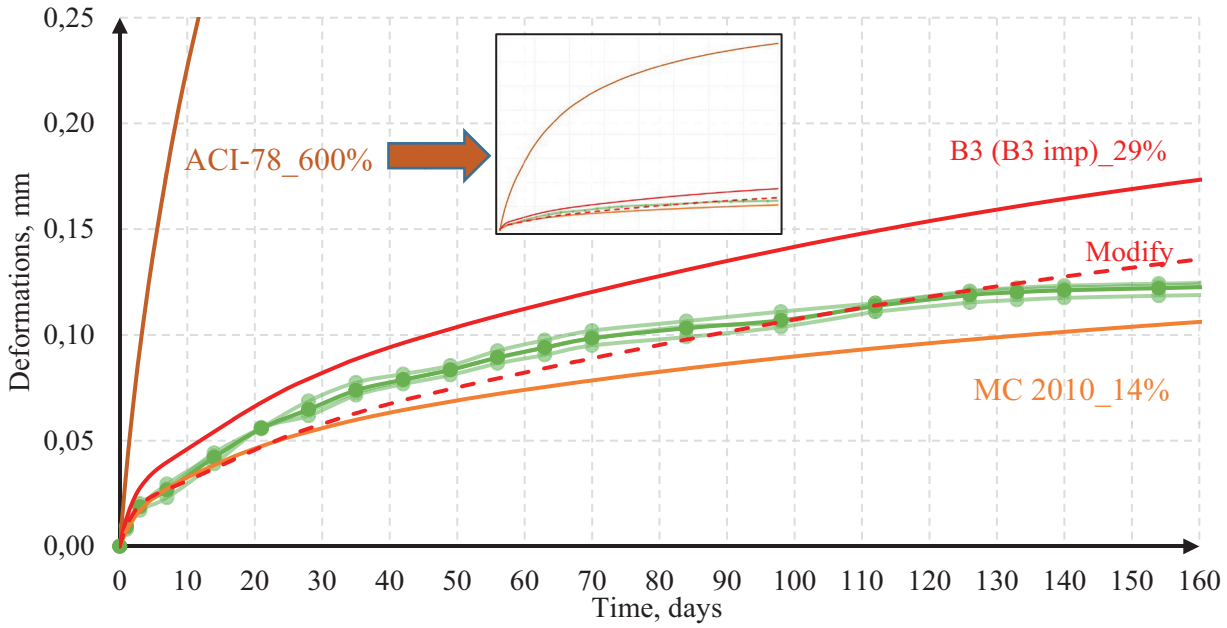


Figure 4. Calculated and experimental creep deformations at normal humidity conditions

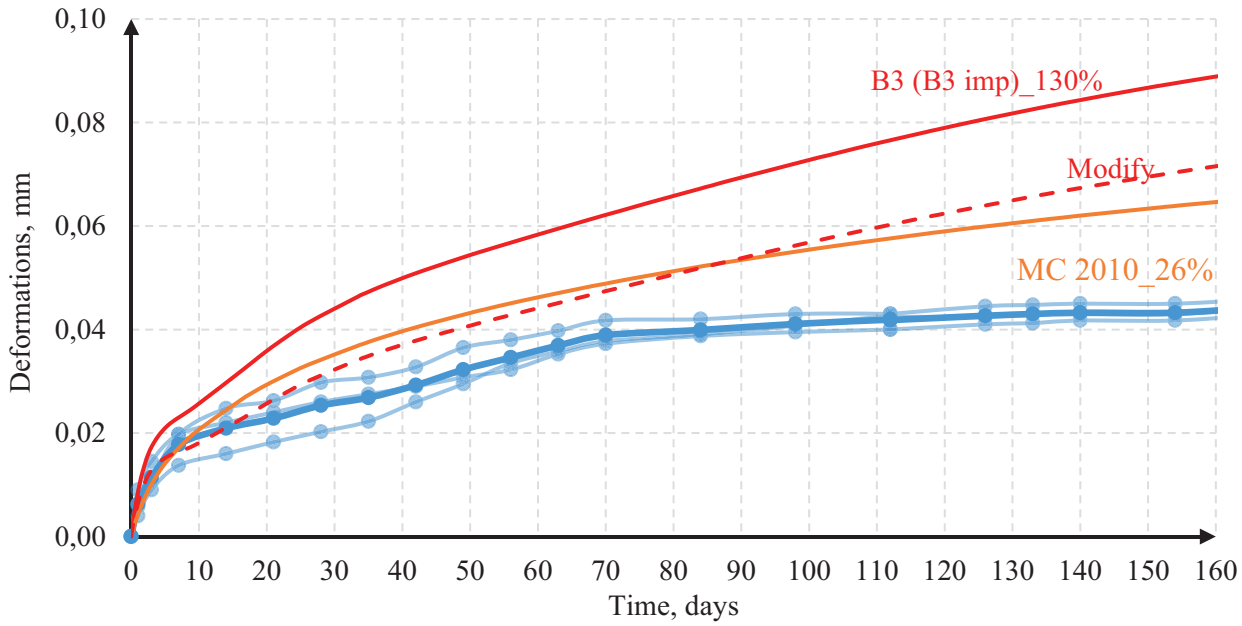


Figure 5. Calculated and experimental creep deformations at high humidity conditions

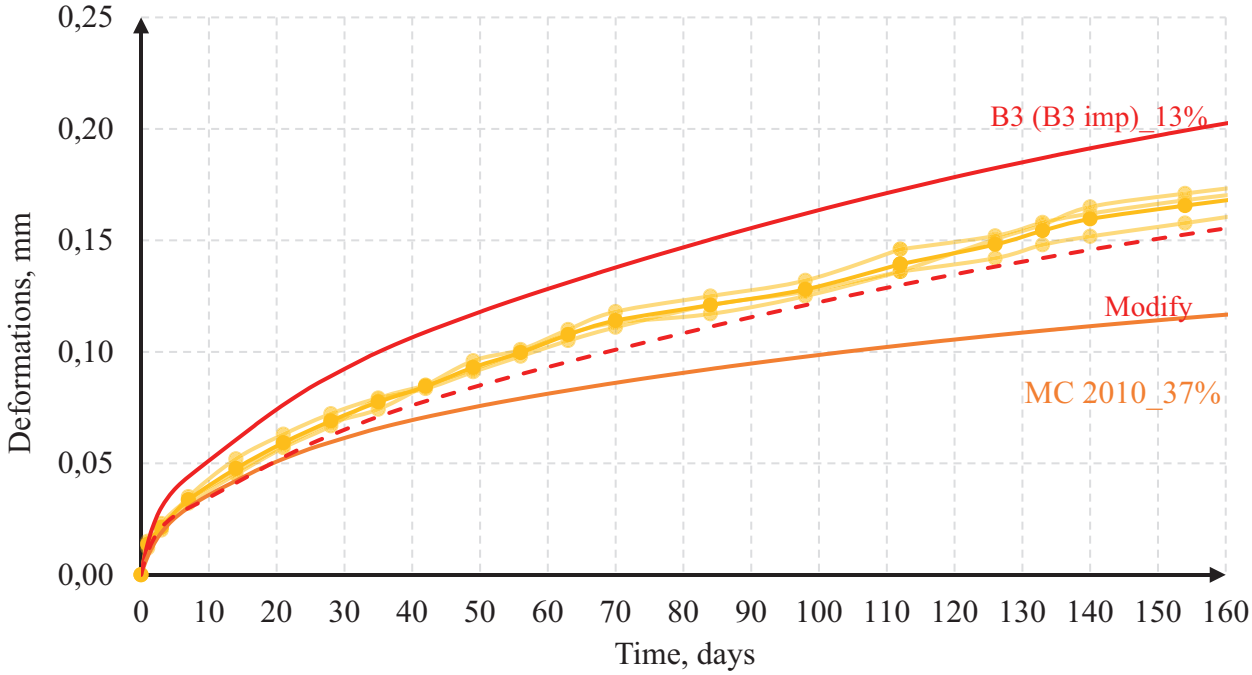


Figure 6. Calculated and experimental creep deformations at low humidity conditions

As can be seen from the calculation results, the direct application of any of the considered models for predicting the creep of modern concretes can lead to significant errors. Models from the 1970s and 1980s, exemplified by the ACI-78 model, are entirely inapplicable.

Another noteworthy observation is that when simulating the experiment in a high-humidity environment, all models showed a decreased level of agreement with the experimental data. It should also be noted that the results from the B3 model and the B3 improved model were virtually

identical. This is because the main enhancements in the more recent model are designed to more accurately capture concrete deformation during the first few months after loading. However, in the experiment under consideration, the specimens were loaded at the age of 88 days, which completely nullified the new algorithms of the B3 improved model. Furthermore, the experimental data recorded in normal and high-humidity conditions indicate an earlier stabilization (attenuation) of creep deformations—a phenomenon frequently observed in high-strength modified concretes—which none of the considered models account for.

The most significant outcome of this modeling effort, however, is the fact that the same model exhibits varying degrees of error under different humidity conditions. The creep curves that were closest to the experimental results were not consistently from a single model; this was also true for the modified model based on B3. Although this modified version was calibrated using data from normal humidity conditions, it showed considerable deviations from the experimental results in a high-humidity environment.

After performing these calculations with different models and ultimately selecting the one that most closely (perhaps after specific modifications) describes the experimental curve under the required temperature and humidity conditions, the software complex can be used to model long-term experiments of any complexity under various stress-strain states. However, the verification of any additional parameters is absolutely essential.

For example, if it is necessary to simulate a creep test under tension on a computer, but specialized lever-type testing machines are unavailable (such setups are currently very rare; according to the author's information, such tests within the Russian Federation can only be conducted at the Donbas National Academy of Civil Engineering and Architecture, where they have been preserved), it is possible to conduct a long-term verification test on concrete beam specimens under bending. Since the beams operate without cracking—part of the beam is compressed while another part is tensioned—this can be done in accordance with Appendix E of GOST 24544-2020. The chosen creep model could then be further modified if necessary.

Consider another example: modeling triaxial long-term compression. This type of stress-strain state is relatively rare, but the construction projects for which experimental studies of concrete creep are typically undertaken are unique and extremely complex. In such structures, accounting for the actual stress-strain state under sustained loads in their structural elements can be critically important. Currently, there are no facilities in Russia for determining creep under triaxial compression (only a single such setup existed in the entire USSR). However, it is possible, for instance, to conduct long-term tests under biaxial compression. The capability for such testing exists at the Gvozdev Research Institute of Concrete and Reinforced Concrete (NIIZHB), and tests on high-strength concrete are currently underway there, with results to be published soon.

The importance of such additional verification can be demonstrated through computer modeling of biaxial compression in the ATENA software complex. Two additional distribution steel plates were added to the sides of the previously used model of a 150×150×600 mm concrete prism, which already had top and bottom distribution plates. These side plates were used to apply lateral pressure. Depending on the magnitude of friction at the interface between the side steel plates and the concrete prism, the results will vary significantly. Figure 7 shows the creep curve for biaxial compression in the limiting case where the steel plate is rigidly connected to the concrete. In such a scenario, the plate can absorb a portion of the compressive stresses from the longitudinal load, potentially leading to underestimated total creep deformations. The true interface condition that must be incorporated into the computational model for such an experimental setup can only be determined through physical testing.

A simplified approach could involve conducting a short-term biaxial compression test, simulating

it on a computer, calibrating the interface parameters based on that short-term test, and then using the calibrated model to simulate long-term tests. The result obtained this way would certainly be more accurate than one with no additional verification, but it could still differ somewhat from a real long-term biaxial compression test. The flowchart presented in Figure 8 illustrates the recommended procedure for computer modeling of concrete creep under complex stress-strain states. Actions performed on the computer are shown in dark blue, while the experimental part of the work is shown in light blue. The more comprehensive this experimental part, the more accurate the final result will be.

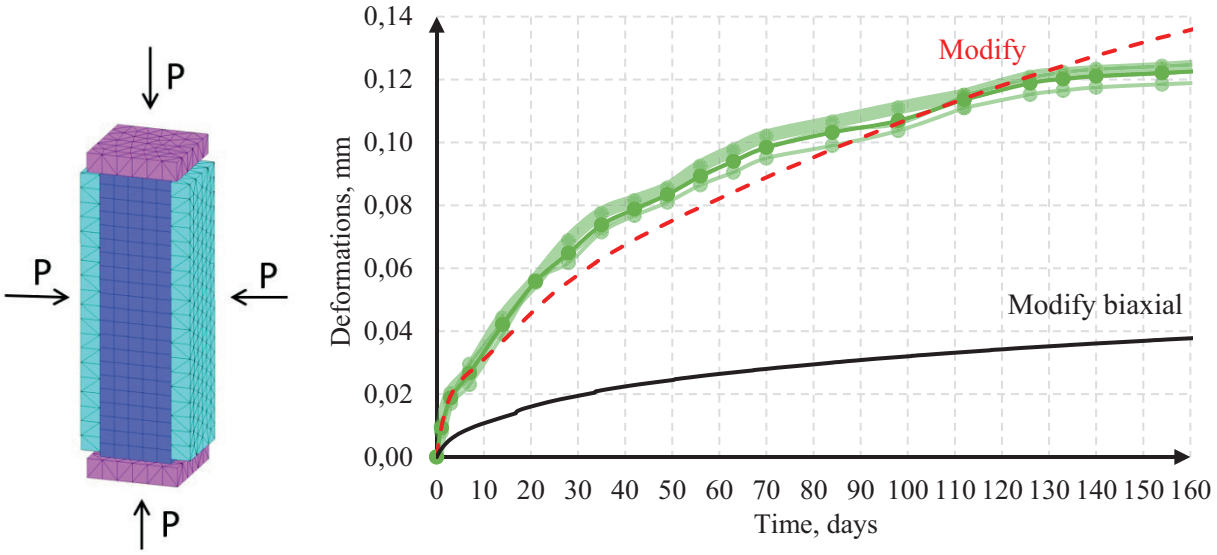


Figure 7. Calculated and experimental creep deformations at low humidity conditions

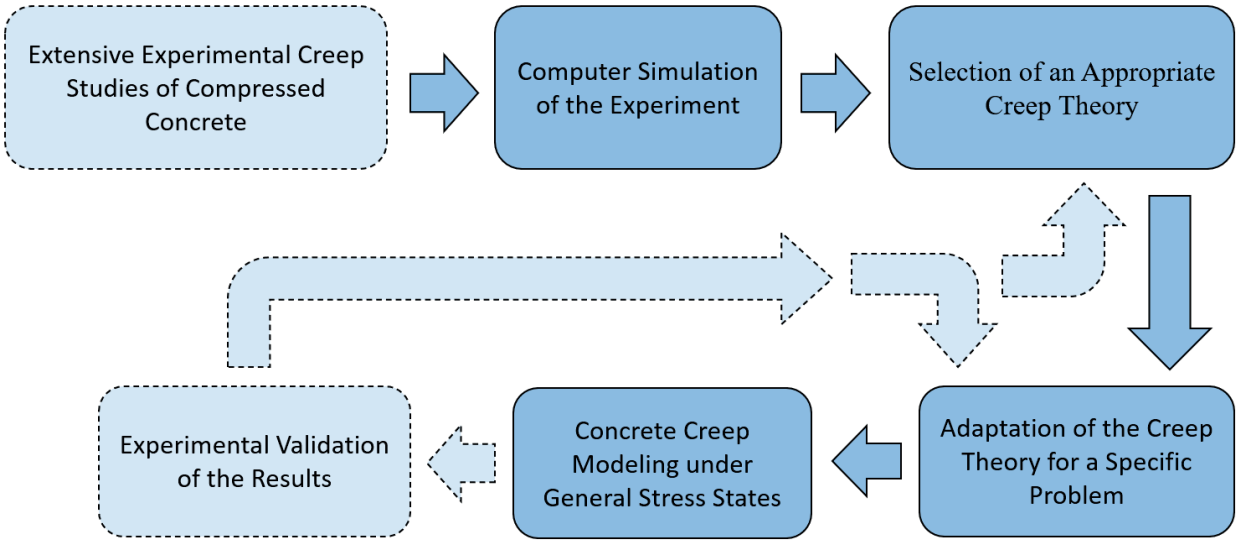


Figure 8. Flow-chart of the algorithm for concrete creep modelling at complex stress-strain state

CONCLUSIONS

Based on the results of the conducted work, the following conclusions can be drawn:

Using modern software, it is possible to predict concrete creep deformations based on advanced calculation models. When employing the B3 and Model Code 2010 models, the deviations from

experimental results obtained under normal humidity conditions (tests according to GOST 24544-2020 and corresponding international standards) were within 30% – which is considered an acceptable result for predicting long-term deformation.

Models from the 1980s, when applied to modern high-strength modified self-compacting concretes, can produce significant errors. For instance, using the ACI-78 model in calculations resulted in a deviation of 600% compared to experimental data. This indicates that predicting concrete creep processes using classical theories, which form the basis of current Russian codes and, to some extent, some foreign standards, can lead to critical inaccuracies. This pertains specifically to the Recommendations for Considering Shrinkage and Creep of Concrete from 1984, which currently remain the only regulatory document allowing for the prediction of creep deformations, as these recommendations have neither been reissued nor officially revoked.

Even the most up-to-date creep models, without modification for a specific experiment, can yield considerable errors. When using the three aforementioned theories (B3, MC 2010, ACI-78), the range of deviations varied from 13% (under reduced humidity) to 130% (under increased humidity). This is corroborated by the verification experiments conducted by the developers of these models, shown in Figure 2, where deviations ranging from 23% to 58% were considered acceptable outcomes.

The modification of creep models should be performed not only for a specific concrete mix composition but also for the specific temperature and humidity conditions of the test. A model modified based on normal humidity data can produce substantial errors when applied to conditions of reduced or increased humidity. This also applies to various loading scenarios that differ from standard tests according to GOST or international standards.

Prior to computer modeling of complex stress-strain states in any structural elements, besides verifying the creep models on simple prism specimens under the relevant temperature and humidity conditions, the boundary conditions must also be verified. An example is the friction from lateral confinement plates when simulating biaxial or triaxial long-term experiments. In the case of lateral confinement, the distribution plates generating this pressure can act as an additional restraining factor against the vertical compressive forces, which can significantly influence the final result.

REFERENCES

1. **Domarova E.V**. (2022) Vliyanie polzuchesti na napryazhenno-deformirovannoe sostoyanie zhelezobetonnykh mnogoetazhnykh zdanii [Influence of creep on the stress-strain state of reinforced concrete multi-story buildings]. Construction and Reconstruction, №9, pp. 14–22. DOI: 10.33979/2073-7416-2022-101-3-14-22.
2. **Bezgodov I.M., Kapustin D.E., Efishov L.I.** (2024) Physical-mechanical and rheological characteristics of high-strength concrete and granite. Industrial and Civil Construction, no. 8, pp. 48–56. DOI: 10.33622/0869-7019.2024.08.48-56.
3. **Garas V.Y., Kurtis K.E., Kahn L.F**. (2012) Creep of UHPC in tension and compression: Effect of thermal treatment. Cement and Concrete Composites, vol. 34, no. 4, pp. 493–502. DOI: 10.1016/j.cemconcomp.2011.12.002.
4. **Huang Y., Wang J., Wei Q., Shang H., Liu X.** (2023) Creep behaviour of ultra-high-performance concrete (UHPC): A review. Journal of Building Engineering, vol. 69, p. 106187. DOI: 10.1016/j.jobe.2023.106187.
5. **Xu Y., Liu J., Liu J., Zhang P., Zhang Q., Jiang L.** (2018) Experimental studies and modeling of creep of UHPC. Construction and Building Materials, vol. 175, pp. 643–652. DOI: 10.1016/j.conbuildmat.2018.04.157.
6. **Switek-Rey A., Denarié E., Brühwiler E.** (2016) Early age creep and relaxation of

UHPFRC under low to high tensile stresses. Cement and Concrete Research, vol. 83, pp. 57–69. DOI: 10.1016/j.cemconres.2016.01.005.
7. **Zeng Y., Zhang W., Yu H., Li W.** (2025) Study on two-dimensional creep effects of RC slab structures. Applied Mathematical Modelling, vol. 138, Part B. DOI: 10.1016/j.apm.2024.115824.
8. **Aghani K., Afshin H., Abedi K., Farahmand-Tabar S.** (2025) Advanced creep modeling for pre-stressed CFRP-strengthened RC beams: An AAEM-based automated ABAQUS subroutine. Advances in Engineering Software, vol. 211, p. 104041. DOI: 10.1016/j.advengsoft.2025.104041.
9. **Krylov S.B., Arleninov P.D.** (2024) Mathematical Modeling of Relaxation Process in Concrete. International Journal for Computational Civil and Structural Engineering, vol. 20, no. 2, pp. 25–33. DOI: 10.22337/2587-9618-2024-20-2-25-33.
10. **Bezgodov I.M., Kaprielov S.S., Sheynfeld A.V.** (2022) Relationship between Strength and Deformation Characteristics of High-Strength Self-Compacting Concrete. International Journal for Computational Civil and Structural Engineering, vol. 18, no. 2, pp. 175–183. DOI: 10.22337/2587-9618-2022-18-2-175-183.
11. **Branson D.E., Christiason M.L.** (1971) Time Dependent Concrete Properties Related To Design-Strength and Elastic Properties, Creep, and Shrinkage. ACI Special Publication, vol. 27, pp. 257–278. DOI: 10.14359/17187.
12. **Bazant Z.P.** (1982) Mathematical models for creep and shrinkage of concrete. In: Bazant Z.P., Wittmann F.H. (eds.) Creep and Shrinkage in Concrete Structures. London: J. Wiley & Sons, pp. 163–256.
13. **Galustov K.Z.** (2006) Nelineinaya teoriya polzuchesti i raschet zhelezobetonnykh konstruktsii [Nonlinear Theory of Creep and Design of Reinforced Concrete Structures]. Moscow: Fizmatlit, 248 p.
14. **Tamrazyan A.G., Esayan S.G.** (2012) Mekhanika polzuchesti betona [Mechanics of Concrete Creep]. Moscow: MGSU, 490 p.
15. **Sanzharovsky R.S.** (2014) Nelineinaya nasledstvennaya teoriya polzuchesti [Nonlinear hereditary theory of creep]. Stroitel'naya mekhanika inzhenernykh konstruktsii i sooruzhenii, no. 1, pp. 63–68.
16. **Krylov S.B., Arleninov P.D.** (2009) Proverka sovmestimosti uravnenii lineinoi teorii polzuchesti i predlozheniya ryada bolee tochnykh zavisimostei [Compatibility check of the equations of the linear theory of creep and proposals for a number of more accurate dependencies]. In: Aktual'nye problemy issledovanii po teorii sooruzhenii: Sbornik nauchnykh statei [Current Problems of Research in the Theory of Structures: Collection of Scientific Articles]. Moscow: OAO «TsPP», vol. Part 2, pp. 245–252.
17. **Mkrtchan A.M., Aksenov V.M.** (2013) Analiticheskoe opisanie diagrammy deformirovaniya vysokoprochnykh betonov [Analytical description of the deformation diagram of high-strength concretes]. Inzhenernyi vestnik Dona, no. 3.
18. **Arleninov P.D.** (2016) Deformirovanie i ustoichivost' szhatykh i vnetsentrennoszhatykh sterzhnevykh zhelezobetonnykh elementov s uchetom polzuchesti i treshchinoobrazovaniya [Deformation and stability of compressed and eccentrically compressed reinforced concrete bar elements taking into account creep and cracking]. PhD Thesis. Moscow, 143 p.
19. **Krylov S.B., Kornyushina M.P., Kozlov G.M., Kalmakova P.S.** (2024) Effektivnost' sochetaniya komp'yuternykh metodov modelirovaniya stroitel'nykh konstruktsii i printsipov klassicheskogo analiza [The effectiveness of combining computer modeling methods for building structures and the principles of classical analysis]. Academia. Arkhitektura i stroitel'stvo, no. 1, pp. 166–170. DOI: 10.22337/2077-9038-2024-1-166-170.

20. **Konin D.V., Krylov A.S., Gavrilov D.N.** (2023) O rabote stalezhelezobetonnykh konstruktsii pri vnetsentrennom szhatii [On the behavior of steel-concrete structures under eccentric compression]. Promyshlennoe i grazhdanskoe stroitel'stvo, no. 12, pp. 31–37. DOI: 10.33622/0869-7019.2023.12.31-37.
21. **Cervenka V., Cervenka J., Kadlec L.** (2018) Model uncertainties in numerical simulations of reinforced concrete structures. Structural Concrete, vol. 19, no. 3, pp. 779–789. DOI: 10.1002/suco.201700287.
22. **Kabantsev O.V., Krylov S.B., Trofimov S.V**. (2021) Numerical Investigation on the Punching Shear Mechanism for Reinforced Concrete Thin and Thick Slabs. International Journal for Computational Civil and Structural Engineering, vol. 17, no. 4, pp. 91–105. DOI: 10.22337/2587-9618-2021-17-4-91-105.
23. **Krylov A.S.** (2019) Chislennye raschety stalezhelezobetonnykh balok s uchetom kontaktnogo vzaimodeistviya stalnogo serdechnika s betonom [Numerical analysis of steel-concrete beams with regard to contact interaction between the steel core and concrete]. Vestnik Tomskogo gosudarstvennogo arkhitekturno-stroitel'nogo universiteta, vol. 21, no. 2, pp. 175–184. DOI: 10.31675/1607-1859-2019-21-2-175-184.
24. **Travush V., Arleninov P., Desyatkin M.** (2023) Nesuschaya sposobnost' stalezhelezobetonnykh sten s listovym armirovaniem na staticheskie nagruzki [Bearing capacity of steel-concrete walls with sheet reinforcement under static loads]. International Journal for Computational Civil and Structural Engineering, vol. 19, no. 4, pp. 166–181. DOI: 10.22337/2587-9618-2023-19-4-166-181.
25. **Travush V.I., Konin D.V., Krylov A.S.** (2024) The stiffness of steel-plate composite structures for short-term loads. International Journal for Computational Civil and Structural Engineering, vol. 20, no. 4, pp. 105–118. DOI: 10.22337/2587-9618-2024-20-4-105-118.
26. **Kaprielov S.S., Arleninov P.D., Sheynfeld A.V., Kalmakova P.S.** (2025) Vliyanie otnositel'noi vladhnosti vozdukha na koeffitsient polzuchesti vysokoprochnykh samouplotnyayushchikhsya betonov [Influence of relative air humidity on the creep coefficient of high-strength self-compacting concretes]. Stroitel'nye materialy, no. 10 (840), pp. 25–35.
27. **Bazant Z.P., Baweja S.** (1994) Creep and shrinkage prediction model for analysis and design of concrete structures—Model B3. Structural Engineering Report 94-10/603c. Northwestern University.
28. **Bazant Z.P., Baweja S.** (2000) Creep and shrinkage prediction model for analysis and design of concrete structures: Model B3. In: Al-Manaseer A. (ed.) Adam Neville Symposium: Creep and Shrinkage—Structural Design Effects. ACI Special Publication SP-194. Farmington Hills: American Concrete Institute, pp. 1–83.
29. **Chiorino M.A.** (1984) CEB Design Manual: Structural effects of time dependent behaviour of concrete. Saint-Saphorin: Georgi Publishing Company, 391 p.
30. **Chiorino M.A.** (1993) Revision of the design aids of the CEB Design Manual Structural effects of time dependent behaviour of concrete, in accordance with the CEB-FIP Model Code 1990. Bulletin d'Information, no. 215. Lausanne: Comité Euro-International du Béton, 297 p.

СПИСОК ЛИТЕРАТУРЫ

1. **Domarova E.V.** Influence of creep on the stress-strain state of reinforced concrete multi-story buildings. // Building and Reconstruction №.9, 2022, P. 14–22. DOI: 10.33979/2073-7416-2022-101-3-14-22.
2. **Bezgodov, I. M, Kapustin, D.E., Efishov L.I.** Physical-mechanical and rheological characteristics of high-strength concrete and

granite. // Industrial and Civil Construction. – №. 8, 2024, P. 48-56. DOI: 10.33622/0869-7019.2024.08.48-56.

3. **Garas V.Y., Kurtis K.E., Kahn L.F.** Creep of UHPC in tension and compression: Effect of thermal treatment // Cement and Concrete Composites. Volume 34, 2012, Issue 4, Pages 493-502. DOI: 10.1016/j.cemconcomp.2011.12.002.
4. **Huang Y., Wang J., Wei Q., [et al.].** Creep behaviour of ultra-high-performance concrete (UHPC): A review. // Journal of Building Engineering, Volume 69, 2023, 106187. DOI: 10.1016/j.jobe.2023.106187.
5. **Xu Y., Liu Jiaping, Liu Jianzhong, [et al.].** Experimental studies and modeling of creep of UHPC. // Construction and Building Materials, Volume 175, 2018, Pages 643-652. DOI: 10.1016/j.conbuildmat.2018.04.157.
6. **Switek-Rey A., Denarié E., Brühwiler E.** Early age creep and relaxation of UHPFRC under low to high tensile stresses. // Cement and Concrete Research. Volume 83, 2016, Pages 57-69. DOI: 10.1016/j.cemconres.2016.01.005.
7. **Zeng Y., Zhang W., Yu H., [et al.].** On two-dimensional creep effects of RC slab structures. // Applied Mathematical Modelling. Volume 138, 2025, Part B, DOI: 10.1016/j.apm.2024.115824.
8. **Aghani K., Afshin H., Abedi K., [et al.].** Advanced creep modeling for pre-stressed CFRP-strengthened RC beams: An AAEM-based automated ABAQUS subroutine. // Advances in Engineering Software. Volume 211, 2025, DOI: 10.1016/j.advengsoft.2025.104041.
9. **Krylov S.B., Arleninov P.D.** Mathematical Modeling of Relaxation Process in Concrete. // International Journal for Computational Civil and Structural Engineering. – Vol. 20, No. 2, 2024, P. 25-33. – DOI 10.22337/2587-9618-2024-20-2-25-33.
10. **Bezgodov I.M. Kaprielov S.S., Sheynfeld A.V.** Relationship between Strength and Deformation Characteristics of High-Strength Self-Compacting Concrete. // International Journal for Computational Civil and Structural Engineering, 2022, Vol. 18, No. 2. – P. 175-183. – DOI 10.22337/2587-9618-2022-18-2-175-183.
11. **Branson D.E., Christiason M.L.** Time Dependent Concrete Properties Related To Design-Strength and Elastic Properties, Creep, and Shrinkage. // ACI Special Publication. Vol. 27, 1971, No – P. 257-278. – DOI 10.14359/17187.
12. **Bazant, Z.P., Wittmann F.H.** Mathematical models for creep and shrinkage of concrete, Chapter 7 in Creep and Shrinkage in Concrete Structures. // J. Wiley & Sons, London, 1982, P. 163–256.
13. **Галустов К.З**. Нелинейная теория ползучести и расчет железобетонных конструкций, 2006, М.: Физматлит, 248 с.
14. **Тамразян А.Г., Есаян С.Г.** (2012) Механика ползучести бетона. –М: МГСУ, 490 с.
15. **Санжаровский Р.С.** Нелинейная наследственная теория ползучести. // Строительная механика инженерных конструкций и сооружений. № 1. 2014, С. 63–68.
16. **Крылов С.Б., Арленинов П.Д.** Проверка совместимости уравнений линейной теории ползучести и предложения ряда более точных зависимостей. // Актуальные проблемы исследований по теории сооружений: Сборник научных статей, Москва/ ЦНИИСК им. В.А. Кучеренко. Том Часть 2. – Москва: ОАО «ЦПП», 2009, – С. 245-252.
17. **Мкртчан А.М., Аксенов В.М.** Аналитическое описание диаграммы деформирования высокопрочных бетонов. // Инженерный вестник Дона.2013 - №3.
18. **Арленинов П.Д.** Деформирование и устойчивость сжатых и внецентренно-сжатых стержневых железобетонных элементов с учетом ползучести и трещинообразования: специальность 05.23.01 "Строительные конструкции, здания и сооружения": диссертация на соискание ученой степени кандидата технических наук Арленинов Петр Дмитриевич. – Москва, 2016 – 1,43 с.

19. **Крылов С.Б., Корнюшина М.П., Козлов Г.М., Калмакова П.С.** Эффективность сочетания компьютерных методов моделирования строительных конструкций и принципов классического анализа. // Academia. Архитектура и строительство – № 1.2024 – С. 166-170. – DOI 10.22337/2077-9038-2024-1-166-170.
20. **Конин Д.В., Крылов А.С., Гаврилов Д.Н.** О работе сталежелезобетонных конструкций при внецентренном сжатии. // Промышленное и гражданское строительство. – № 12.2023 – С. 31-37. – DOI 10.33622/0869-7019.2023.12.31-37. – EDN SSHTRX.
21. **Cervenka V, Cervenka J, Kadlec L.** Model uncertainties in numerical simulations of reinforced concrete structures // Structural Concrete, 2018, – P. 1-13. DOI: 10.1002/suco. 201700287.
22. **Kabantsev O.V., Krylov S.B., Trofimov S.V.** Numerical Investigation on the Punching Shear Mechanism for Reinforced Concrete Thin and Thick Slabs. // International Journal for Computational Civil and Structural Engineering, 2021 – Vol. 17, No. 4. – P. 91-105. – DOI 10.22337/2587-9618-2021-17-4-91-105.
23. **Крылов А.С.** Численные расчеты сталежелезобетонных балок с учетом контактного взаимодействия стального сердечника с бетоном. // Вестник Томского государственного архитектурно-строительного университета. – Т. 21, № 2. 2019 – С. 175-184. – DOI 10.31675/1607-1859-2019-21-2-175-184. – EDN SCLBGF.
24. **Travush, V.I., Arleninov, P.D. Desyatkin M.A.** [et al.] Несущая способность сталежелезобетонных стен с листовым армированием на статические нагрузки. // International Journal for Computational Civil and Structural Engineering. – Vol. 19, 2023, No. 4. – P. 166-181. – DOI 10.22337/2587-9618-2023-19-4-166-181.
25. **Travush V.I., Konin D.V., Krylov A.S.** The stiffness of steel-plate composite structures for short-term loads. // International Journal for Computational Civil and Structural Engineering, 2024 – Vol. 20, No. 4. – P. 105-118. – DOI 10.22337/2587-9618-2024-20-4-105-118.
26. **Каприелов С.С., Арленинов П.Д., Шейнфельд А.В., Калмакова П.С.** Влияние относительной влажности воздуха на коэффициент ползучести высокопрочных самоуплотняющихся бетонов. // Строительные материалы, 2025, № 10 (840). С.25-35.
27. **Bažant, Z.P. and Baweja, S.** Creep and shrinkage prediction model for analysis and design of concrete structures – Model B3. // Structural Engineering Report, 1994, 94-10/603 c (Northwestern University)
28. **Neville A.** Creep and Shrinkage – Structural Design Effects. // ACI SP– 194, A.Al-Manaseer ,ed., Am. Concrete Institute, Farmington Hills, Michigan, 2000, – P. 1–83.
29. **Chiorino M.A.** (Chairman of editorial team), "CEB Design Manual: Structural effects of time dependent behaviour of concrete," Georgi Publ. Co. Saint Saphorin (Switzerland), 1984, 391 pp. 18. CEB.
30. **Chiorino M.A.** Revision of the design aids of the CEB Design Manual Structural effects of time dependent behaviour of concrete, in accordance with the CEB-FIP Model Code 1990. // Bulletin d'Information, 1993, N.215 297pp

Petr Dmitrievich Arleninov – Ph.D. in Technical Sciences, Deputy Head of Laboratory No. 8 "Reinforced Concrete Mechanics", Joint Stock Company "Research Center "Construction" (JSC "Research Center "Construction"), 6, 2-ya Institutskaya St., Moscow, 109428, Russia, docent Department of Reinforced Concrete and Masonry Structures of the National Research Moscow State University of Civil Engineering, 26, Yaroslavskoye Shosse, Moscow, Russia, 129337, niizhb_lab8@mail.ru, +7 (916) 198-78-41

Петр Дмитриевич Арленинов – к.т.н., зам. зав. лабораторией №8 «Механики железобетона», Акционерное Общество «Научно-исследовательский центр «Строительство» (АО «НИЦ «Строительство»), 6, 2-я Институтская, Москва, 109428, Доцент кафедры «Железобетонных и каменных конструкций» Национально-исследовательского Московского Государственного Строительного Университета, niizhb_lab8@mail.ru, +7(916)198-78-41

DOI:10.22337/2587-9618-2026-22-1-28-34

ABOUT MULTISCALE MODELING WITH THE USE OF HAAR DISCRETE WAVELETS FOR TARGETED DATA EXTRACTION IN PROBLEMS OF STRUCTURAL MECHANICS

Mojtaba Aslami [1,2]***, Pavel A. Akimov*** [1]
[1] National Research Moscow State University of Civil Engineering, Moscow, RUSSIA
[2] Fasa University, Fasa, IRAN

Abstract: The distinctive paper is devoted to multiscale modelling of functions with the use of Haar discrete wavelets. Numerical implementation is realized with the use of "Fortran" programming language ("Intel Visual Fortran" software). Particularly several sample functions are under consideration. Three basic parts of corresponding algorithm include full wave reconstruction (implementing the entire Hilbert space of the wave); extraction of wave components constructed solely by wavelet functions; isolation and visualization of the final wavelet layer. Modeling wave behavior from multiple perspectives enables the extraction of highly valuable information, which can reveal defects in mechanical or structural systems. The Haar discrete wavelet, due to its basis and step-like wavelet functions, is particularly suitable for numerical implementation (programming, computation), featuring straightforward algorithms.

Keywords: Haar wavelet, fault detection, modeling, structural analysis

О МНОГОУРОВНЕВОМ МОДЕЛИРОВАНИИ С ИСПОЛЬЗОВАНИЕМ ДИСКРЕТНЫХ ВЕЙВЛЕТОВ ХААРА ДЛЯ ЦЕЛЕВОГО ИЗВЛЕЧЕНИЯ ДАННЫХ В ЗАДАЧАХ СТРОИТЕЛЬНОЙ МЕХАНИКИ

М. Аслами [1,2]***, П.А. Акимов*** [1]
[1] Национальный исследовательский Московский государственный строительный университет, г. Москва, РОССИЯ
[2] Университет Фаса, г. Фаса, ИРАН

Аннотация: В настоящей статье рассматривается многоуровневое моделирование функций с использованием дискретных вейвлетов Хаара. Численная реализация выполнена на основе применения языка программирования "Fortran" (соответствующее программное обеспечение "Intel Visual Fortran"). В частности, рассматриваются несколько примеров функций. Три основные части соответствующего алгоритма включают полную реконструкцию соответствующей волны (реализация всего гильбертова пространства волны); извлечение волновых компонент, построенных исключительно на основе вейвлет-функций; выделение и визуализацию конечного вейвлет-слоя. Моделирование поведения волны с разных точек зрения позволяет извлекать ценную информацию, которая может выявлять дефекты в механических или конструктивных системах. Дискретный вейвлет Хаара исключительно удобен для численной реализации (программирования, вычислений), характеризуется соответствующими простыми алгоритмами.

Ключевые слова: вейвлет Хаара, выявление дефектов, моделирование, расчеты строительных конструкций

INTRODUCTION

Wavelet analysis is a relatively recent mathematical tool that emerged in the late 1980s and is now widely applied to fundamental and practical problems, including engineering. Notable applications include image processing [1-3]. This analysis offers flexible signal processing techniques as an alternative to classical Fourier analysis [4-5].

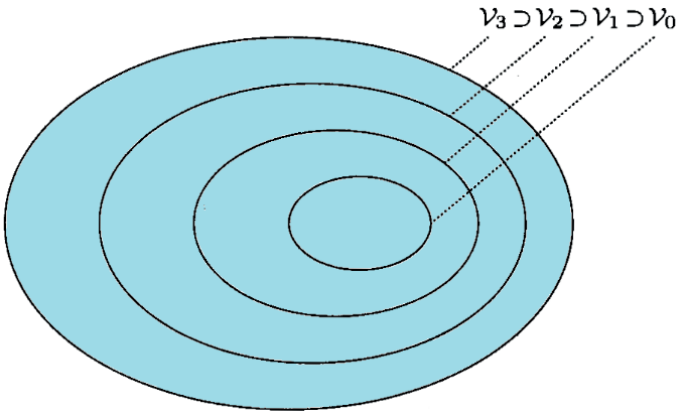


Figure 1. Decomposition of a function's Hilbert space into subspaces V

Thus, it enables solutions to problems where traditional Fourier methods are ineffective. A key advantage of wavelet analysis is its ability to detect highly localized variations in signals (waves), including jumps and irregularities. In contrast, Fourier analysis lacks the resolution to track rapid, minute changes, as its coefficients reflect wave behavior over an infinite range, making it inefficient for analyzing fast-varying signals or noise.

Wavelet analysis is a powerful tool for hierarchical mathematical decomposition, representing a wave's overall space as a combination of low- and high-frequency components. In this study, we employ Visual Fortran [6] to examine sample functions using Haar wavelet analysis [7-11], presenting their mathematical space in three distinct models. The presented modeling of the mathematical space of a wave makes it possible to examine the behavior of that wave from different perspectives and monitor its changes, whereas conventional wave observation often fails to capture expected data.

1. WAVE SPACE DECOMPOSITION WITH THE USE OF WAVELET THEORY

If a wave resides in a Hilbert space ($L_2(R)$), it can be constructed using simpler subspaces (Figure1):

$$L_2(R) = \bigoplus_{j \in Z} V_j . \quad (1)$$

The accuracy of the reconstructed wave model depends on the completeness of the selected subspace V_j. This modeling requires subspaces V_j to satisfy the following conditions:

$$V_0 \subset V_1 \subset V_2 \subset ... \subset L_2(R) . \quad (2)$$

In wavelet analysis, the target space is partitioned into nested subspaces, transitioning to a base space and complementary orthogonal subspaces (Figure 2). Here, subspaces V_j and W_j must meet the following criteria:

$$L_2(R) = V_0 \oplus W_0 \oplus W_1 \oplus ... ; \quad (3)$$

$$V_{j+1} = V_j \oplus W_j, \quad j \in Z ; \quad (4)$$

$$\bigcap_{j \in Z} W_j = \{0\} , \quad (5)$$

where Z is the set of integers.

In wavelet-based wave reconstruction, subspaces are mutually orthogonal and non-overlapping. This unique property enables the extraction of critical information not available in other modeling techniques. Such information can reveal mechanical or structural defects [12-16], as healthy systems exhibit predictable harmonic waves, while defective ones introduce uncontrolled noise and anomalous frequencies.

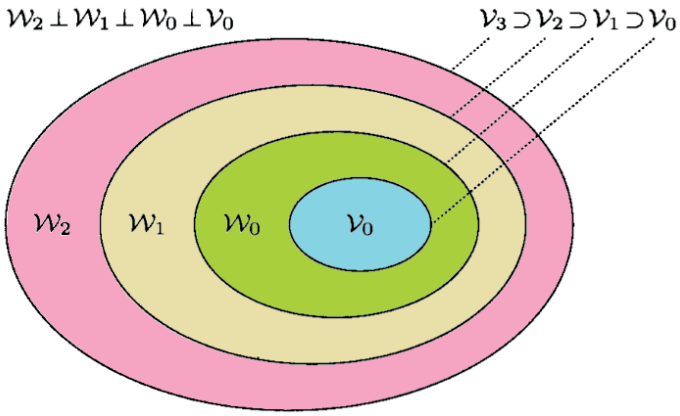


Figure 2. Decomposition of a function's Hilbert space into subspaces V_j and W_j

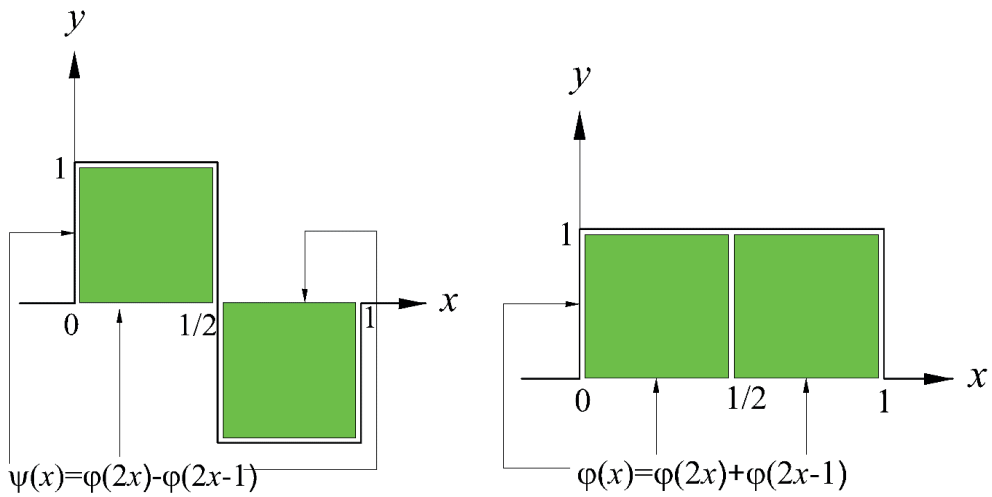


Figure 3. First two stages of the scaling function (φ) and wavelet function (ψ) in the Haar wavelet.

2. HAAR WAVELET

Mathematically, wavelet analysis permits diverse V_j and W_j subspaces for wave reconstruction, a distinctive feature of this method. The discrete Haar wavelet [17] is one of the simplest yet most effective wavelet tools, fully compatible with computational implementation and applicable to mechanical and structural problems [18-21] (Figure 3):

$$\phi(x) = \sqrt{2} \sum_{k=-\infty}^{\infty} h_k \phi(2x-k); \qquad (6)$$

$$\psi(x) = \sqrt{2} \sum_{k=-\infty}^{\infty} \tilde{h}_k \phi(2x-k); \qquad (7)$$

$$\tilde{h}_k = -(-1)^k h_{1-k}, \quad k \in Z. \qquad (8)$$

3. NUMERICAL MODELING WAVES DECOMPOSITION AND DATA EXTRACTION

Using "Intel Visual Fortran", we modeled and analyzed several sample functions via the Haar discrete wavelet algorithm. The modeling was implemented in three categories, each providing distinct wave insights:

- full wave reconstruction (implementing the entire Hilbert space);
- extraction of wavelet-only components;
- isolation of the final wavelet layer.

One application of this analysis is crack and defect detection in structures.

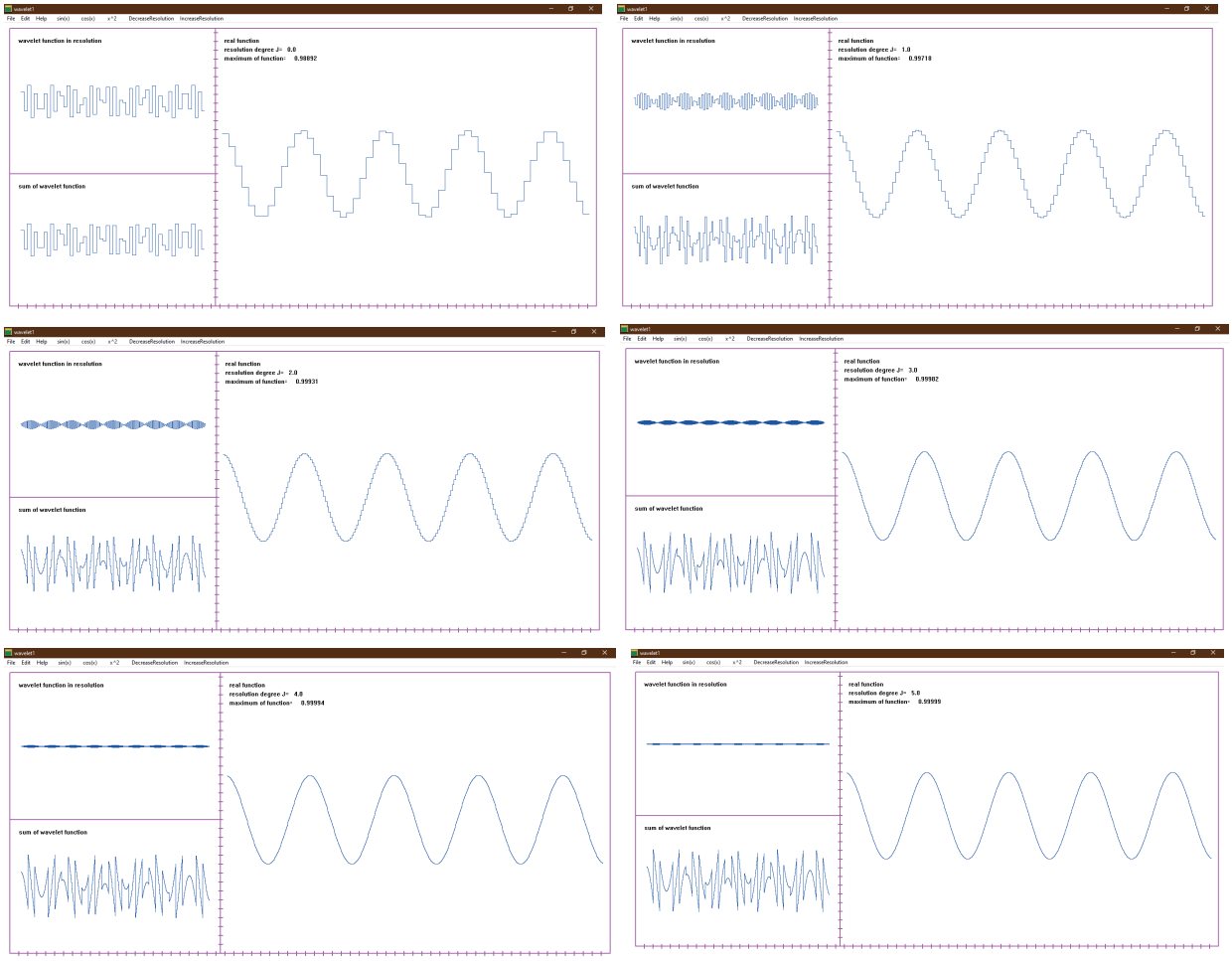


Figure 4. Implementation of sin(x)

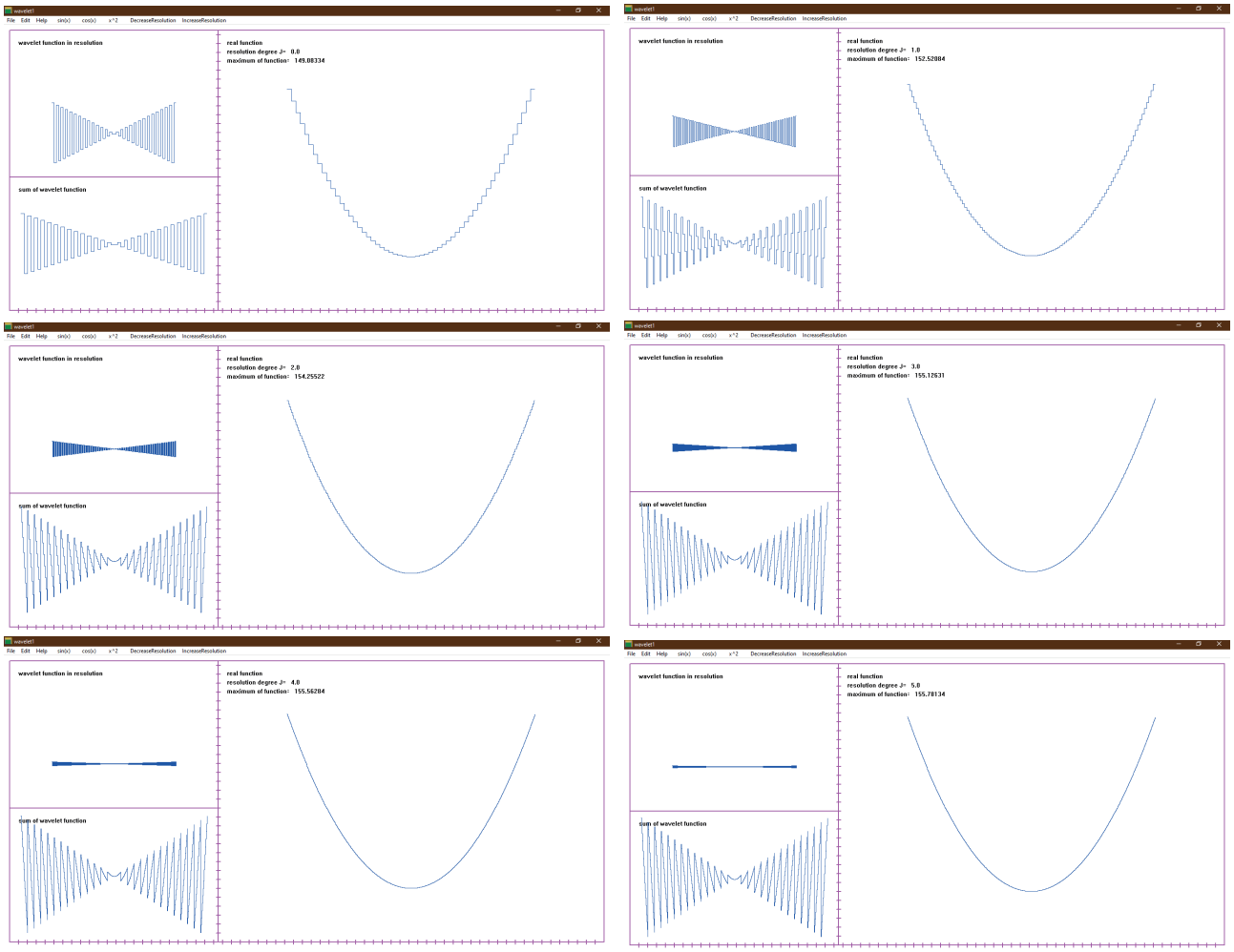
By deploying seismic wave controllers at various points, load-induced waves can be monitored and decomposed via wavelets to detect frequency deviations. The study tested the algorithm on sin(x) (Figure 4), cos(x), and x^2 (Figure 5). Results show rapid convergence with increasing wavelet resolution, a key advantage over Fourier analysis. The method accommodates both regular and irregular waves. Subspace-based models yielded data fundamentally different from the original wave, offering precise behavioral details. For random or harmonic waves, temporal variations were accurately captured.

CONCLUSION

This paper employed Visual Fortran to analyze functions using Haar wavelets in three distinct models. Multi-perspective wave modeling extracts unique, actionable insights, enabling defect detection in mechanical/structural systems. Healthy systems exhibit controlled harmonics, whereas defective ones introduce uncontrolled noise. The Haar wavelet's simplicity and numerical efficiency make it ideal for engineering applications.

Key Features of the Translation:

- formal academic tone with precise technical terminology;
- logical flow mirroring the original structure;
- figures and equations referenced per academic conventions;
- concise yet comprehensive rendering of complex concepts.



REFERENCES

1. **Olivier R., Vetterli M.** Wavelets and signal processing. // IEEE signal processing magazine, 1991, Volume 8, No. 4, pp. 14-38.
2. **Coifman R.R., Meyer Y., Wickerhauser V.M.** Wavelet analysis and signal processing. // In Wavelets and their applications, 1992.
3. **Mallat S.** A wavelet tour of signal processing. Elsevier, 1999, 620 pages.
4. **Körner T.W.** Fourier analysis. Cambridge university press, 2022, 606 pages.
5. **Grafakos L.** Classical fourier analysis. Volume 2. New York, Springer, 2008, 492 pages.
6. **Norman L.** Compaq Visual Fortran: A guide to creating windows applications. Elsevier, 2002, 462 pages.
7. **Chen C.F., Hsiao C.H.** Haar wavelet method for solving lumped and distributed-parameter systems. // IEE Proceedings-Control Theory and Applications, Volume 144, No. 1, 1997, pp. 87-94.
8. **Burrus C.S.** Introduction to wavelets and wavelet transforms: a primer. Pearson, 1997, 288 pages.
9. **Mohamed A.R., Baleanu D.** Haar wavelets scheme for solving the unsteady gas-flow in 4-D. // Thermal Science, Volume 24, No. 2, Part B, 2020, pp. 1357-1367.
10. **Jin-Sheng G., Jiang W.-S.** The Haar wavelets operational matrix of integration. // International Journal of Systems Science, Volume 27, No. 7, 1996, pp. 623-628.
11. **Lepik Ü.** Numerical solution of differential equations using Haar wavelets. // Mathe-

matics and computers in simulation, Volume 68, No. 2, 2005, pp. 127-143.
12. **Xinhua X., Xiao F., Wang S.** Enhanced chiller sensor fault detection, diagnosis and estimation using wavelet analysis and principal component analysis methods. // Applied Thermal Engineering, Volume 28, No. 2-3, 2008, pp, 226-237.
13. **Abubakar U. et al.** Induction motor fault detection based on multi-sensory control and wavelet analysis. // IET Electric Power Applications, Volume 14, No. 11, 2020, pp. 2051-2061.
14. **Shen Y.-L., Wai R.-J.** Wavelet-Analysis-Based Singular-Value-Decomposition Algorithm for Weak Arc Fault Detection via Current Amplitude Normalization. // IEEE Access, Volume 9, 2021, pp. 71535-71552.
15. **Hani M., Kim H.** Damage detection in concrete by Fourier and wavelet analyses. // Journal of Engineering Mechanics, Volume 129, No. 5, 2003, pp. 571-577.
16. **Kim H., Hani M.** Damage detection of structures by wavelet analysis. // Engineering structures, Volume 26, No. 3, 2004, pp. 347-362.
17. **Lepik Ü., Helle H.** Haar wavelets. Springer Science & Business Media, 2014, 207 pages.
18. **Aslami M., Akimov P.A.** Wavelet-based finite element method for multilevel local plate analysis. // Thin-Walled Structures, Volume 98, 2016, pp. 392-402.
19. **Mohammed O.A., Abed N.Y., Ganu S.** Modeling and characterization of induction motor internal faults using finite-element and discrete wavelet transforms. // IEEE Transactions on Magnetics, Volume 42, No. 10, 2006, pp. 3434-3436.
20. **Oruç Ö., Fatih B., Alaattin E.** Numerical solutions of regularized long wave equation by Haar wavelet method. // Mediterranean Journal of Mathematics, Volume 13, No. 5, 2016, pp. 3235-3253.
21. **Kim K. et al.** Application of Haar wavelet discretization method for free vibration analysis of inversely coupled composite laminated shells. // International Journal of Mechanical Sciences, Volume 204, 2021, pp. 106549.

СПИСОК ЛИТЕРАТУРЫ

1. **Olivier R., Vetterli M.** Wavelets and signal processing. // IEEE signal processing magazine, 1991, Volume 8, No. 4, pp. 14-38.
2. **Coifman R.R., Meyer Y., Wickerhauser V.M.** Wavelet analysis and signal processing. // In Wavelets and their applications, 1992.
3. **Mallat S.** A wavelet tour of signal processing. Elsevier, 1999, 620 pages.
4. **Körner T.W.** Fourier analysis. Cambridge university press, 2022, 606 pages.
5. **Grafakos L.** Classical fourier analysis. Volume 2. New York, Springer, 2008, 492 pages.
6. **Norman L.** Compaq Visual Fortran: A guide to creating windows applications. Elsevier, 2002, 462 pages.
7. **Chen C.F., Hsiao C.H.** Haar wavelet method for solving lumped and distributed-parameter systems. // IEE Proceedings-Control Theory and Applications, Volume 144, No. 1, 1997, pp. 87-94.
8. **Burrus C.S.** Introduction to wavelets and wavelet transforms: a primer. Pearson, 1997, 288 pages.
9. **Mohamed A.R., Baleanu D.** Haar wavelets scheme for solving the unsteady gas-flow in 4-D. // Thermal Science, Volume 24, No. 2, Part B, 2020, pp. 1357-1367.
10. **Jin-Sheng G., Jiang W.-S.** The Haar wavelets operational matrix of integration. // International Journal of Systems Science, Volume 27, No. 7, 1996, pp. 623-628.
11. **Lepik Ü.** Numerical solution of differential equations using Haar wavelets. // Mathematics and computers in simulation, Volume 68, No. 2, 2005, pp. 127-143.
12. **Xinhua X., Xiao F., Wang S.** Enhanced chiller sensor fault detection, diagnosis and estimation using wavelet analysis and prin-

cipal component analysis methods. // Applied Thermal Engineering, Volume 28, No. 2-3, 2008, pp, 226-237.
13. **Abubakar U. et al.** Induction motor fault detection based on multi-sensory control and wavelet analysis. // IET Electric Power Applications, Volume 14, No. 11, 2020, pp. 2051-2061.
14. **Shen Y.-L., Wai R.-J.** Wavelet-Analysis-Based Singular-Value-Decomposition Algorithm for Weak Arc Fault Detection via Current Amplitude Normalization. // IEEE Access, Volume 9, 2021, pp. 71535-71552.
15. **Hani M., Kim H.** Damage detection in concrete by Fourier and wavelet analyses. // Journal of Engineering Mechanics, Volume 129, No. 5, 2003, pp. 571-577.
16. **Kim H., Hani M.** Damage detection of structures by wavelet analysis. // Engineering structures, Volume 26, No. 3, 2004, pp. 347-362.
17. **Lepik Ü., Helle H.** Haar wavelets. Springer Science & Business Media, 2014, 207 pages.
18. **Aslami M., Akimov P.A.** Wavelet-based finite element method for multilevel local plate analysis. // Thin-Walled Structures, Volume 98, 2016, pp. 392-402.
19. **Mohammed O.A., Abed N.Y., Ganu S.** Modeling and characterization of induction motor internal faults using finite-element and discrete wavelet transforms. // IEEE Transactions on Magnetics, Volume 42, No. 10, 2006, pp. 3434-3436.
20. **Oruç Ö., Fatih B., Alaattin E.** Numerical solutions of regularized long wave equation by Haar wavelet method. // Mediterranean Journal of Mathematics, Volume 13, No. 5, 2016, pp. 3235-3253.
21. **Kim K. et al.** Application of Haar wavelet discretization method for free vibration analysis of inversely coupled composite laminated shells. // International Journal of Mechanical Sciences, Volume 204, 2021, pp. 106549.

Aslami Mojtaba, Candidate of Technical Sciences, Associate Professor of Department of Applied Mathematics, National Research Moscow State University of Civil Engineering; 26, Yaroslavskoe Shosse, Moscow, 129337, Russia; Fasa University, Daneshjou blvd, Fasa, Fars Province, Iran; Email: aslami.mojtaba@gmail.com.

Pavel A. Akimov, Full Member of the Russian Academy of Architecture and Construction Sciences, Professor, Dr.Sc.; Rector of National Research Moscow State University of Civil Engineering; 26, Yaroslavskoe Shosse, Moscow, 129337, Russia; E-mail: AkimovPA@mgsu.ru, rector@mgsu.ru, pavel.akimov@gmail.com.

Аслами Моджтаба, кандидат технических наук; доцент кафедры прикладной математики Национального исследовательского Московского государственного строительного университета; 129337, Россия, г. Москва, Ярославское шоссе, дом 26; Университет г. Фаса, Daneshjou blvd, Fasa, Fars Province, Iran; Email: aslami.mojtaba@gmail.com.

Акимов Павел Алексеевич, академик РААСН, профессор, доктор технических наук; ректор Национального исследовательского Московского государственного строительного университета; 129337, Россия, г. Москва, Ярославское шоссе, дом 26; Email: AkimovPA@mgsu.ru, rector@mgsu.ru, pavel.akimov@gmail.com.

DOI:10.22337/2587-9618-2026-22-1-35-55

ASSESSMENT OF THE ROBUSTNESS FOR FRAME STRUCTURES BASED ON A PROBABILITY INDEX

Anatoliy V. Alekseytsev, Natalya S. Kurchenko

National Research Moscow State University of Civil Engineering, Moscow, RUSSIA

Abstract: In the process of designing buildings and structures, the issue arises of ensuring their mechanical safety under accidental loads. Furthermore, existing buildings and structures are often subjected to technogenic impacts that may lead to complete or partial failure of the structural system. To provide a quantitative characterization of the resistance of load-bearing structures to such factors, the concept of survivability has been introduced in the modern scientific literature. However, the formalization of survivability in the form of specific quantitative indicators remains a pressing and insufficiently explored problem for both steel and reinforced concrete structures. This study proposes a methodology for computing the probabilistic survivability index for frame structural systems. The calculation is based on a modified model of classical reliability theory, which assumes that the failure of the frame system occurs through the formation of a mechanism with a minimum number of plastic hinges. The assessment of structural failure or component degradation is performed on an energy basis using the J-integral. To analyze the scatter of random parameters, statistical modeling based on empirical data is employed. The article provides examples of survivability index calculations. Practical implementation of the proposed method has demonstrated its effectiveness, allowing it to be recommended for evaluating the mechanical safety of steel and reinforced concrete frame structures, including cases with increased responsibility requirements and specific robustness criteria against progressive collapse.

Keywords: robustness, mechanical safety, deformations, steel structures, reinforced concrete structures, emergency situation, progressive collapse, reliability, probability of failure

МЕТОД ОЦЕНКИ ЖИВУЧЕСТИ РАМНЫХ КОНСТРУКЦИЙ НА ОСНОВЕ ВЕРОЯТНОСТНОГО ИНДЕКСА

А.В. Алексейцев, Н.С. Курченко

Национальный исследовательский Московский государственный строительный университет, г. Москва, РОССИЯ

Аннотация: В процессе проектирования зданий и сооружений возникает задача обеспечения их механической безопасности при воздействии аварийных нагрузок. Кроме того, существующие здания и сооружения нередко подвергаются техногенным воздействиям, приводящим к полному или частичному разрушению конструктивной системы. Для количественной характеристики сопротивляемости несущих конструкций данным факторам в современной научной литературе введено понятие живучести. Однако формализация живучести в виде конкретных количественных показателей, является актуальной и недостаточно проработанной как для стальных, так и для железобетонных конструкций. В настоящем исследовании предлагается методика вычисления вероятностного индекса живучести для рамных конструктивных систем. В основе расчёта лежит модифицированная модель классической теории надёжности, предполагающая, что разрушение рамной системы происходит посредством формирования механизма с минимальным числом пластических шарниров. Оценка разрушаемости конструкций или компонентов, их составляющих, выполняется на энергетической основе с использованием J-интеграла. Для анализа разброса случайных параметров используется метод статистического моделирования на базе эмпирических данных. В статье приведены примеры расчёта индекса живучести. Практическая реализация предложенного метода показала его эффективность, что позволяет рекомендовать его применение для оценки механической безопасности объектов с каркасами из стали или железобетона, в том числе при наличии повышенных требований по ответственности и особых критериев устойчивости к прогрессирующему разрушению.

Ключевые слова: живучесть, механическая безопасность, деформации, стальные конструкции, железобетонные конструкции, аварийная ситуация, прогрессирующее разрушение, надежность, вероятность отказа

1. INTRODUCTION

Current issues of ensuring the robustness of frame structural systems in buildings and structures represent one of the priority areas in modern construction science. The analysis of recent scientific research has made it possible to systematize the key directions of this subject area:

- assessment of the robustness of structural systems based on the analysis of nodal connections of elements;
- development and improvement of sets of deterministic and probabilistic robustness characteristics, as well as the integration of intelligent predictive models influencing the progression of progressive collapse;
- investigation of progressive collapse processes in structural systems using limit analysis methods and numerical simulation;
- analysis of types of accidental impacts and loads;
- development of structural solutions aimed at effectively preventing the development of progressive collapse;
- development and enhancement of methodologies for robustness assessment and management using search optimization algorithms combined with machine learning and artificial neural networks.

A systematic review of scientific studies covering the above-mentioned directions is presented below, which confirms the necessity of developing a probabilistic methodology for robustness assessment, as proposed in this research.

Progressive collapse and robustness criteria. In [1], the influence of initial localized defects on the ability of steel profiles to maintain their functionality under accidental scenarios is investigated. Numerical simulations and experimental observations have shown that damage concentrated in limited zones leads to accelerated formation of plastic hinges, which in turn reduces the overall robustness of the structure. It was established that an increase in the number of stories in a building, as well as the removal of edge or end columns, significantly increases the system's susceptibility to progressive collapse. An alternative interpretation of the concept of structural robustness based on plastic limit analysis is proposed in [2], which is considered more accurate compared to traditional quasi-static and dynamic evaluation methods. This approach makes it possible to account for the actual reserves of the structure's load-bearing capacity without the need for labor-intensive dynamic calculations.

Methods of load and damage identification as a basis for quantitative evaluation of the real robustness index of structures are also reflected in a number of studies. For example, [3] emphasizes the importance of accurate diagnostics of the actual condition of a structure for subsequent robustness assessment. In [4], an algorithm based on decision-tree methods is proposed, which employs vibration response data in combination with a calibrated finite element model. This approach allows determining the hazard level of damages, evaluating the residual service life, and providing a quantitative measure of robustness under potential accidental scenarios.

The evaluation of the load-bearing capacity of steel elements under localized thermal loads is addressed in [5], where the behavior of structures in fire conditions is studied. Despite the considerable number of studies devoted to the deformational properties and patterns of progressive collapse in frame systems, the evaluation of structural strength as a factor limiting the spread of failures still requires further systematization both within deterministic and probabilistic models.

Accidental Loads and Impacts. Research in the field of robustness assessment of structural systems under accidental loads is focused on developing parameters that quantitatively characterize the intensity of extreme actions, including seismic ones [6]. Such parameters include spectral accelerations and displacements, which make it possible to indirectly assess the stability of the system

against progressive collapse. These data demonstrate the multifactorial nature of conditions influencing robustness. The distinctive feature of this approach lies in comparing the parameters of the impact not only by their amplitude characteristics but also according to criteria of efficiency, feasibility, and distance to the epicenter of the accidental action.

In [7], emphasis is placed on the behavior of steel frames under thermal effects caused by fire. A methodology is proposed that involves local evaluation of thermal impact on individual elements of the structure, followed by a generalized verification of the strength of the entire system. Fire scenarios consider both the removal of central (internal) and edge columns, thereby allowing different failure configurations to be analyzed.

The methodology of local–global analysis is applied in [8], where the robustness of frame structures under thermal heating is assessed. In this approach, a single column is subjected to dynamic loading, while the remaining part of the frame is analyzed under static loading. It is shown that such a method can be universally applied to structures made of various materials and improves the accuracy of evaluating system behavior under accidental conditions.

Influence of Joint Connections on Structural Robustness. The study [9] focuses on analyzing the stability of steel frame buildings with bolted connections depending on their height. Buildings with 5, 10, and 15 stories were considered, and the results showed that taller buildings demonstrated better robustness characteristics. Particular attention was paid to probabilistic approaches, in particular, the construction of fragility curves for various progressive collapse scenarios. In [10], [11], it is emphasized that the robustness of a structure is a determining parameter of its safety, especially in steel frame systems where the key elements are beam-to-column joints. The Monte Carlo method was applied to account for stochastic variations in mechanical parameters, which was used to analyze system vulnerability under accidental impacts. Tornado diagrams were employed to evaluate the sensitivity of the system to variations in parameters such as span length, modulus of elasticity, and yield strength of elements, considering statistical variability of material properties. Studies [12], [13] are dedicated to the behavior of frame joints subjected to bending moments. The authors highlight the importance of forming a ductile failure mechanism of connections to increase the overall robustness and reliability of the system. Parameters promoting joint ductility are proposed, enabling the effect of sequential localization of failures. Publications [14], [15] investigate the behavior of steel frames under sudden column removal and in the presence of flange end-plates. It was found that including end-plates contributes to effective localization of damage, thereby improving robustness. Accident scenario analyses in [16], [17], [18] demonstrated that the strength and design characteristics of joints have a decisive influence on the system's ability to withstand both instantaneous and progressive failures of columns. Experimental data indicate that flange geometry significantly affects damage localization and thus determines the level of robustness. In [19], a solution is proposed to enhance the ductility of beam-to-column joints by using special slots, which enable a chain-reaction mechanism and thereby increase the overall robustness of the frame.

Deterministic and Probabilistic Indicators of Robustness. Integration of Artificial Intelligence Technologies. In several studies [20], [21], the problem of robustness of structural systems is addressed using a combined approach that integrates traditional engineering calculation methods with modern artificial intelligence tools. Data obtained from the analysis of deformation characteristics of structures under different accidental scenarios are processed using machine learning algorithms. This makes it possible to develop predictive models that assess the influence of structural parameters on overall robustness. Results demonstrate that optimizing geometric

configuration has a stronger impact on improving robustness than the use of materials with higher mechanical properties. In [22], [23], the introduction of a structural safety index is proposed, which incorporates uncertainties inherent in design conditions. Such an index allows for informed decisions regarding the need to adjust design parameters, taking into account the probability of progressive collapse development. It was found that the inclusion of uncertainties in calculations can reduce the estimated robustness by up to 30% compared to deterministic assessments. At the same time, the strength of steel is particularly emphasized as a key parameter influencing the final evaluation. Modern approaches to structural health monitoring also include damage detection technologies employing neural network models. For instance, [24] proposes a method of visual image analysis that uses artificial neural networks to determine the degree of corrosion damage in steel elements, enabling more accurate quantitative evaluation of the robustness index. A comprehensive robustness assessment of seismic-resistant structures is presented in [25], where the robustness index is defined as the difference between unity and the sum of both material and non-material losses. These losses are calculated based on failure scenarios obtained through direct dynamic simulation, fragility curve construction [26], and probabilistic failure evaluation. Depending on the obtained robustness index values, a classification of seismic resistance levels of multi-story steel-framed buildings is proposed. In [27], robustness is considered through the lens of strength loss in elements resulting from structural vulnerability. Accidental scenarios in this approach are modeled either as completed events or with assigned probabilities. It is concluded that systems with high ductility demonstrate higher robustness indices. In [28], a multi-criteria methodology for robustness evaluation is proposed, which considers energy, loading, and stiffness parameters, as well as specific failure mechanisms. A system of indices is introduced that comprehensively characterizes the mechanical safety of steel-framed buildings and structures. Here, robustness is defined as the ability of the system to maintain stability in the presence of local damages that could trigger cascading collapse. Publication [29] provides a comparative analysis of approaches to evaluating the robustness of steel structures against progressive collapse. Both a deterministic method, applied in seismic design of buildings [30], and a probabilistic method, based on event-tree construction, are used. Simulation results led to the formulation of a new robustness index that accounts for both the potential of chain failure and the deformational properties of frame joints.

Engineering Solutions Aimed at Preventing Progressive Collapse. In [31], a structural solution is proposed to enhance the robustness of steel frame systems by incorporating an additional roof truss. This truss redistributes internal forces in cases of partial or complete removal of beam or column elements under different accidental scenarios. Results of numerical modeling showed that under accidental loading the system transitions into a plastic state, with deformations forming due to the development of plastic hinges. Optimal stiffness values of truss elements were determined, which provide the highest efficiency under emergency conditions. The influence of diagonal bracing on the robustness of steel frames against progressive collapse is examined in [32]. Two system configurations were considered—with and without bracing. It was found that including diagonal members significantly increased the ultimate load-bearing capacity of the structure—by 129.7% and 45.1% in different cases. These results demonstrate the substantial effect of bracing schemes on robustness. It should be noted, however, that robustness in this work was evaluated solely within a deterministic framework. In [33], high-rise buildings (50 stories) designed according to ASCE 7 and AISC standards were analyzed. Alongside assessing frame robustness, the effect of building plan configuration on resistance to progressive collapse was also studied. It was

established that when the central column is removed, the overall plan shape of the building has a decisive influence on system behavior. Conversely, when edge columns are removed, local factors dominate and the plan geometry plays a smaller role. Thus, plan geometry may be considered an additional parameter affecting robustness in certain collapse scenarios. Publication [34] is also devoted to the robustness of tall buildings, while [35] considers a combined scenario in which the initial accidental action is an earthquake, followed by fire. The research focused on four- and eight-story steel frame structures with V-shaped or diagonal bracing. The obtained results highlight the importance of considering combined impact scenarios when evaluating robustness parameters.

Based on the literature review, the scientific relevance of the task addressed in this study—probabilistic robustness assessment of frame structural systems—has been substantiated.

2. METHODS

The following assumptions are used as the main prerequisites for checking the robustness of a frame structure:

- the condition that the structure remains in a final deformed state without transition into a collapse mechanism after accidental loading;
- the condition of non-fracture of sections after stabilization of the dynamic effect of the accidental action;
- the condition of section strength under peak dynamic loads.

2.1 Geometric Stability After Accidental Loading. Such a state can be mathematically expressed as follows:

$$\left([K]\cdot\{\delta\} = \frac{1}{\alpha}\{P_0\} + \{P_M\} \right) \wedge \wedge \left(\left(cond_{\infty}[K] \right)^{-1} \le \lambda \right) \qquad (1)$$

where $[K]$ is the global stiffness matrix of the frame finite elements; $\{\delta\}$ is the displacement vector; $\{P_M\}$ is the nodal load vector simulating the application of moments at plastic hinge formation points; $\{P_0\}$ is the external nodal load vector; $\alpha = P_0/P_{\lim}$, $P_{\lim}$ is the limiting load factor at which equilibrium conditions are still satisfied. The parameter λ is presented in Table 1.

Table 1. Determination of parameter λ

Characteristic of the system		
Geometrically stable	Instantly unstable	Geometrically unstable
$\lambda > 10^{3}$	$10^{-10} < \lambda < 10^{-2}$	$\lambda < 10^{-16}$

Geometric instability of the system under accidental action may arise not only due to the applied loads but also because of member failure. The coefficient λ may be computed through selection or by solving an extremal combinatorial problem. The conditioning number of the stiffness matrix is calculated using the infinity norm:

$$cond_{\infty}[K] = \left\| [K] \right\|_{\infty} \times \left\| [K]^{-1} \right\|_{\infty}, \qquad (2)$$

where $\|\bullet\|_{\infty}$ is the symbol for the infinite norm.

2.2 Condition of Non-Fracture After Dynamic Effect of Accidental Loading. As a rule, building structures use materials that initiate elastoplastic fracture. For most structures, this type of failure begins with the formation of a crack. If the crack propagates, the structure first undergoes local damage and then complete failure. The condition of local crack growth in fracture mechanics is approximately described by the Rice–Cherepanov contour J-integral [36]:

$$J = \int_{C} \left(W dy - \sigma_{iy} n_y \frac{\partial U_i}{\partial x} \right) dc \ge J_{cr}, \qquad (3)$$

where W is the strain energy density at the crack tip; σ_{iy}, U_i are the equivalent stresses and displacements at contour point C in direction y perpendicular to crack propagation; J_{cr} is the critical value of the integral defining the energy required for crack growth.

2.3 Strength Condition of Structural Members. Practical experience in analysis and design of load-bearing structures has shown that the strength of members under peak dynamic loads can be assessed in quasi-static form. The static equivalent is obtained by multiplying the static load by a dynamic coefficient, which usually does not exceed 2.0. Material strain-rate strengthening should also be considered. In this case, standardized design methods can be applied. For reinforced concrete and steel structures, the main formulas are summarized in Table 2.

Table 2. Strength assessment conditions for members under accidental action

Beams	Columns	Joints
Steel structures [37]		
1. Strength in the span under compression and bending according to formula (106). 2.Overall stability of the element according to formula (69) 3.Shear strength in support sections according to formula (42) for structural design class 1, according to formulas (54)-(55) for classes 2 and 3.	1. Overall stability of the element in accordance with formula (109) 2. Strength check using formula (106) for short columns	1. Welded joints, formulas (175)-(181) 2. Bolted joints, formulas (186)-(188), (190)
Reinforced concrete structures [38]		
$M < M_{ult}$, M is the bending moment resulting from an emergency impact. M_{ult} is the maximum moment absorbed by the cross-section with control deformations in tensioned rebars.	$Ne < M_{ult}$; $N < N_{ult}$, $M_{ult} = R_b b x(h_0 - 0,5x) +$ $+R_{sc} A'_s (h_0 - a')$ e is the eccentricity of the longitudinal force, N, N_{ult} are the forces acting and perceived by the cross-section, respectively.	Condition $l_{an}^{ef} \geq l_{an}$ of actual anchoring reinforcement. Condition $\sigma_s \leq R_s$ of tensile strength of reinforcement σ_s, R_s are the stress and design resistance of reinforcement.

2.3 Reliability Indices for Robustness Assessment

2.3.1 Steel Structures. Two criteria are introduced for reliability indices: the probability of failure due to normal stress exceeding limits (Eq. 4), and due to shear stress (Eq. 5). These failure types are typical for sections of steel frame elements:

$$\beta_\sigma = \frac{\left|R_y\right| - \left|\sigma_{MN}\right|}{\sqrt{S(\sigma_{MN})^2 + S(R_y)^2}},$$
$$\sigma_{MN} = N / A \pm M_x y / I_x,\ N = f_1(Q),\quad (4)$$
$$M_x = f_2(Q)$$

$$\beta_\tau = \frac{|R_s| - |\tau_x|}{\sqrt{S(\tau_x)^2 + S(R_s)^2}},$$
$$\tau_x = \begin{cases} Q_x S / I_x t_w : \text{1 class of SSS} \\ Q_x / A_w : \text{2, 3 classes of SSS} \end{cases}, \quad (5)$$
$$Q_x = f(Q)$$

where β_σ, β_τ are reliability indices; σ_{MN}, τ_x are mean values of normal and shear stresses in critical sections; R_y, R_s are design strengths in bending and shear; $S(g)$ are standard deviation of values, $N, M_x, Q_x, \sigma_{MN}, \tau_x$ are values of variants in samples of internal forces and stresses obtained by statistical modeling or based on data monitoring of the technical condition of structures; A, S, I_x, t_w, A_w, y values are the geometric characteristics of the section under consideration, in particular for an I-beam, this is the area, static moment, central moment of inertia, wall thickness, web area, and the coordinate of the point where the stress is calculated; Q is the value of the random variable of the applied load; f, f_1, f_2 are analytical laws that determine the dependence of internal forces on the load. The standard deviation of the random variable σ_{MN} (1) in the presence of longitudinal forces and bending moments in the section is calculated as:

$$S(\sigma_{MN}) = \sqrt{D(N/A) + D(M_x y / I_x) + 2\operatorname{cov}\left((N/A),(M_x y / I_x)\right)}, \quad (6)$$

$$\operatorname{cov}\left((N/A),(M_x y / I_x)\right) = \frac{1}{n}\sum_{i=1}^{n}\left((NM_x y)/(I_x A)\right)_i - (N/A)(M_x y / I_x), \quad (7)$$

where $D(g)$ is the variance from the argument; $\operatorname{cov}((g),(g))$ is the covariance, $(\bar{g})$ is the mean value for the sample population under consideration, n is the sample size.

When beam elements of the structural system fail due to stability conditions, the reliability index takes the form:

$$\beta_s = \frac{|R_y| - |\sigma_{Mx}|}{\sqrt{S(\sigma_M)^2 + S(R_y)^2}}, \sigma_{Mx} = \frac{M_x}{\varphi_b W_{cx}}, \quad (8)$$

where σ_M is conditional normal stress in the beam, taking into account the longitudinal force; W_{cx}, φ_b are values determined by regulatory documents during stability analysis, in particular according to [37].

For columns loaded as a result of emergency impact by longitudinal force and bending moment, the stability reliability index is:

$$\beta_{st} = \frac{|R_y| - |\sigma_N|}{\sqrt{S(\sigma_N)^2 + S(R_y)^2}}, \sigma_N = \frac{N}{\varphi_e A}, \quad (9)$$

where σ_N is conditional normal stress in the column, taking into account the longitudinal force; φ_e is stability coefficient under compression with bending, determined depending on the values of relative eccentricity η and conditional flexibility $\bar{\lambda}$ and relative eccentricity, reduced to the cross-section shape by a coefficient.

2.3.2 Reinforced Concrete Structures

The specific features of reinforced concrete failure imply two principal failure mechanisms. The first corresponds to section failure due to the formation of a plastic hinge. The second occurs when concrete is excluded from load-bearing, resulting in a chain-type mechanism.

For the first failure mechanism, the reliability index β_R of beams is calculated as follows:

$$\beta_R = \frac{|M_{ult}| - |M_{\max}|}{\sqrt{S(M_{ult})^2 + S(M_{\max})^2}}, \quad (10)$$

where M_{ult} is the bending moment in the section that can be resisted by concrete and reinforcement; $M_{\max}$ is the maximum moment in this section under accidental loading; $S(M_{ult})$, $S(M_{\max})$ are the standard deviations of the random variables M_{ult}, $M_{\max}$.

For reinforced concrete columns, the reliability index β_C under accidental action is determined as:

$$\beta_C = \frac{\left(|N_{ult}| - |N_{\max}|\right) \cdot e}{\sqrt{S(eN_{ult})^2 + S(eN_{\max})^2}} \quad (11)$$

where N_{ult}, $N_{\max}$ are the maximum axial forces carried by concrete and reinforcement in the section and the axial force under accidental loading; respectively; e is the eccentricity of axial force; $S(eN_{ult})$, $S(eN_{\max})$ are the standard deviations.

In the absence of experimental data, the standard deviations can be generated under the assumption of a normal distribution of the random variables. In the case of the chain-type failure mechanism, columns subjected to additional accidental loads generally do not fail. Therefore, the reliability indices may only be calculated for beams. In this case, rupture of reinforcement and its slip in the intact part (loss of anchorage) may occur. For reinforcement rupture, the reliability index can be expressed as (12), and for anchorage loss as (13):

$$\beta_{RV1} = \frac{|\varepsilon_u| - |\varepsilon_{\max}|}{\sqrt{S(\varepsilon_u)^2 + S(\varepsilon_{\max})^2}}, \quad (12)$$

$$\beta_{RV2} = \frac{l_{an} - l_{an}^{ef}}{\sqrt{S(l_{an})^2 + S(l_{an}^{ef})^2}}, \quad (13)$$

where ε_u is the rupture strain of reinforcement; $\varepsilon_{\max}$ is the tensile strain of reinforcement under accidental load; l_{an} is the design anchorage length determined according to standards; l_{an}^{ef} is the anchorage length of reinforcement after formation of the kinematic chain under accidental loading; $S(\varepsilon_u)$, $S(\varepsilon_{\max})$ $S(l_{an})$, $S(l_{an}^{ef})$ denotes the standard deviations of these random variables.

2.4 Quantitative Assessment of Robustness

Robustness of structural systems in the works of both domestic and international researchers has most often been evaluated using deterministic indicators. These were associated with the analysis of transition into a geometrically unstable system under accidental actions. For frame structural systems, robustness can be assessed using a probabilistic indicator. Its physical meaning lies in the fact that the system does not fail either under normal service conditions or under accidental scenarios, that is:

$$W_R = P_{no} P_{dam}^E, \quad (14)$$

where P_{no} is the probability of no-failure of the system under normal operation, and P_{dam}^E is the probability of no-failure of the system under an accident or different accidental scenarios. In conventional design, this probability is typically within $P_{no} = 0.95 \div 1$; in optimal design aimed at minimizing costs without consideration of robustness, it is $0.98 \div 1$. For a fully safe system in the idealized case, $W_R = 1$, but in such a case the cost of the structure may become unacceptably high.

For a frame structural system with *m* beams, *n* columns, and *k* joints, the probabilistic indicator of robustness can be computed as:

$$W_R = \prod_{i=1}^{m_R}\left(P_{no,i}\left(1-P_{dam,i}\right)\right)\times$$
$$\times\prod_{j=1}^{m_c}\left(P_{no,j}\left(1-P_{dam,j}\right)\right)\times \quad . \qquad (15)$$
$$\times\prod_{k=1}^{m_U}\left(P_{no,k}\left(1-P_{dam,k}\right)\right)$$

Here $P_{no,i}$, $P_{no,j}$, $P_{no,k}$ are the probabilities of no-failure of beams, columns, and joints of the frame in the absence of accidents under normal service; $P_{dam,i}$ is the probability of accidental failure of column i; $P_{dam,j}$ is the probability of accidental failure of beam j; is the same for joint k. These probabilities are determined as:

$$P_{dam} = 1-(0,5+\Phi(\beta)) \qquad (16)$$

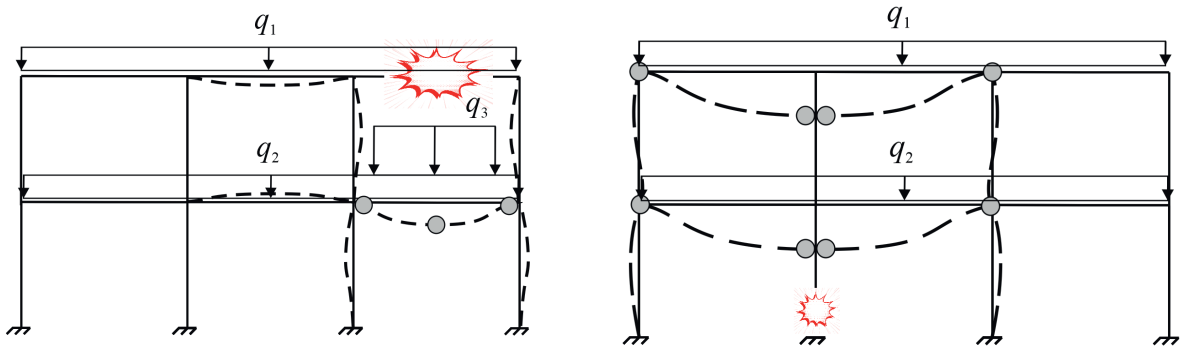
where $\Phi(\beta)$ is the Laplace function, β is the reliability index (Eqs. (4), (5), (8)–(13)) calculated for each structural element or joint. If the condition of no-failure for one or more groups of elements or joints is not satisfied, robustness of the system is considered not ensured. In this case, it can be written as:

$$\left.\begin{array}{l}\left(\prod_{i=1}^{m_R}(w_i)\right)\vee \\ \vee\left(\prod_{j=1}^{m_c}(w_j)\right)\vee \\ \vee\left(\prod_{k=1}^{m_U}(w_k)\right)\end{array}\right| \begin{array}{l} P_{dam}^{\max}=0,5; \\ \Phi(\beta)=0; \ =[0\div 0,6] \\ \beta=0.\end{array} \qquad (17)$$

In particular, if all beams and joints of the frame remain functional but columns fail, the system is not considered robust

$$W_R = 0,95\cdot 0,6\cdot 0,95 \approx 0,55 < 0,6\,.$$

Under different accidental scenarios, element failures may be multiple and realized according to a sequential scheme (Fig. 1a) or a parallel scheme (Fig. 1b).



a) b)

Figure 1. Possible failure schemes: (a) failure of a beam; (b) failure of a central column; shaded circles – zones of possible plastic hinge formation

For example, the probability of failure for a system of two beams failing one after another in sequence 1–2 can be determined on Fig. 1a as:

$P_{dam} = P_{dam1} + P_{dam1}\cdot P_{dam2}$. If condition (1) is not satisfied, or according to (2) the system is geometrically unstable, then robustness is not ensured $W_R = 0$.

3. RESULTS AND DISCUSSION

A steel frame made of structural steel with a yield strength of $R_{yn} = 375$ MPa is considered. The scheme is shown in Figure 2. Each element is assigned a number: beams and columns are designated by digits. The cross-sections of members were selected with a safety margin of load-bearing capacity. It is assumed that this reserve of strength may be mobilized under accidental conditions. Potential accidental scenarios are indicated with crosses. These situations may be accompanied by the formation of a system of plastic hinges. It is assumed that such a mechanism ensures localization of failure and prevents further progression.

The design of the structure was carried out with account of standard service loads. The calculation included the following factors:

- self-weight (dead load) of reinforced concrete slab and steel elements $q = 40$ kN/m;
- wind load including mean and pulsating components, applied from both directions;
- snow load for Region III (Moscow) $s = 13,2$ kN/m;
- additional snow accumulation $ds = 39,6$ kN/m;
- live load on floor slabs $v = 9$ kN/m;
- live load on the roof $v_0 = 3$ kN/m.

Standard deviations of random load values, corresponding stresses, and strength of S375 structural steel were determined using statistical modeling. To obtain the required standard deviations, a base random sample of values uniformly distributed between 0 and 1 was generated. Sample values are given in Table 3.

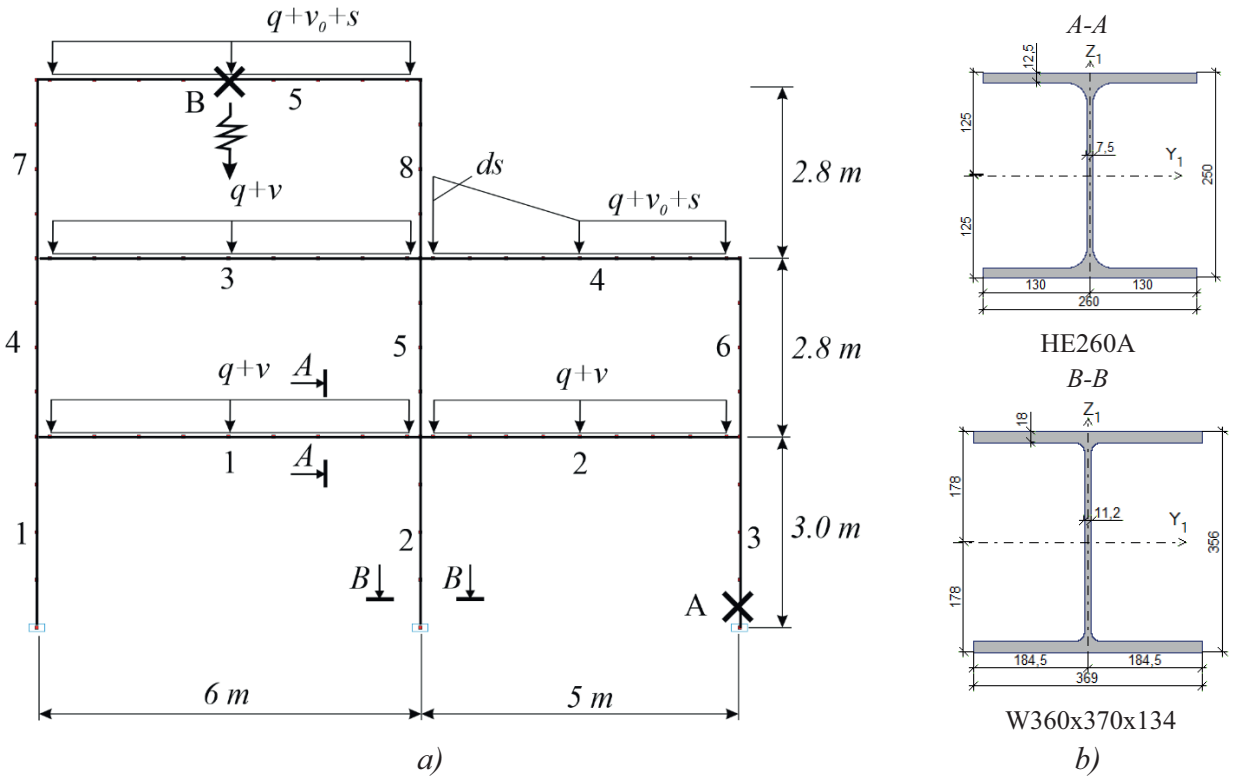


Figure 2. Calculation scheme of the frame (a): 1–8 – column numbers, 1–5 – beam numbers; cross-sections of columns and beams (b)

Table 3. Sample data for determining standard deviations under the normal distribution law

ω_{1-10}	ω_{11-20}	ω_{21-30}	ω_{31-40}	ω_{41-50}	ω_{51-60}	ω_{61-70}	ω_{71-80}	ω_{81-90}	ω_{91-100}
0,980	0,112	0,733	0,266	0,212	0,140	0,740	0,847	0,233	0,368
0,070	0,370	0,017	0,540	0,028	0,757	0,336	0,611	0,812	0,355
0,115	0,209	0,591	0,708	0,896	0,438	0,885	0,981	0,961	0,189
0,069	0,896	0,250	0,715	0,926	0,567	0,458	0,187	0,917	0,904
0,938	0,463	0,396	0,623	0,753	0,674	0,010	0,701	0,093	0,989
0,329	0,969	0,398	0,627	0,914	0,486	0,471	0,836	0,759	0,500
0,079	0,127	0,843	0,105	0,245	0,025	0,742	0,050	0,565	0,629
0,810	0,441	0,831	0,752	0,327	0,022	0,293	0,574	0,419	0,003
0,196	0,935	0,960	0,149	0,981	0,667	0,525	0,066	0,297	0,016
0,958	0,166	0,248	0,937	0,705	0,453	0,368	0,052	0,431	0,761

Experimental data on the coefficient of variation of steel strength under uniaxial tension were used as initial input. Statistical variants of stress σ_{MN} and strength R_y values were calculated as: $\sigma_{MN,i} = \omega_i \overline{\sigma}_{MN}$, $R_{y,i} = \omega_i \overline{R}_y$, $\overline{\sigma}_{MN}, \overline{R}_y$ are the sample means for the normal stress and the design strength. Thus, using the data of synthetic statistics based on the normal distribution (or processing experimental data when available), the reliability indices can be calculated according to formulas (4) and (5).

3.1 Normal Service Conditions. For normal service conditions of structural elements, which from the perspective of structural mechanics are considered long members, normal stresses act as the determining factor in strength evaluation. However, in critical sections of beams, the influence of shear forces additionally manifests itself. Therefore, using only normal stresses for assessing load-bearing capacity may lead to an incomplete characterization of the stress state. To improve the accuracy of analysis, it is advisable to apply equivalent stresses according to the von Mises criterion. This approach makes it possible to account for the combined action of normal and shear stresses. The distribution of equivalent stresses is shown in Figure 3a. For comparison, Figure 3b presents a frame optimized according to the criterion of minimum material consumption. These data were taken as the initial input for calculating the reliability indices, the values of which are given in Table 4.

Analysis of the data presented in Table 4 shows that optimization of the structure according to the criterion of minimum material consumption leads to an economically efficient design solution. However, this significantly reduces the level of structural reliability. The reduction reaches several orders of magnitude. Under such conditions, the probability of failure of load-bearing elements increases, and even factors arising from the statistical nature of the mechanical properties of steel or variability of applied loads may trigger failure. For quantitative evaluation, calculations of the probabilities of no-failure of columns and beams were performed. The results of these calculations are presented in Table 5.

Table 4. For calculating the probability of element failure under normal service conditions

№ of element	Original structure, $\frac{\sigma_e / \varphi}{R_y}$, MPa	Optimal structure, $\frac{\sigma_{e,opt} / \varphi_{opt}}{R_y}$, MPa	$\frac{\beta_R}{\beta_{Ropt}}$	$\frac{\Phi(\beta_R)}{\Phi(\beta_{Ropt})}$	$\frac{P_{dam,i}}{P_{dam,i,opt}}$
Columns					
1	56/337,5	119/300	$\frac{\beta_R > 5}{4,76}$ [3]	$\frac{0,5}{0,499997}$	$\frac{0}{3 \cdot 10^{-6}}$
2	57/337,5	130/320	$\frac{\beta_R > 5}{\beta_{Ropt} > 5}$	$\frac{0,5}{0,5}$	$\frac{0}{0}$
3	28/337,5	83/280	Same	Same	Same
4	61/345,0	128/321	-//-	-//-	Same
5	53/345,0	94/342	-//-	-//-	Same
6	67/345,0	205/299	$\frac{\beta_R > 5}{2,47}$	$\frac{0,5}{0,4933}$	$\frac{0}{6,7 \cdot 10^{-3}}$
7	84/345,0	193/321	$\frac{\beta_R > 5}{3,36}$	$\frac{0,5}{0,49955}$	$\frac{0}{4,5 \cdot 10^{-4}}$
8	86/345,0	196/342	$\frac{\beta_R > 5}{3,84}$	$\frac{0,5}{0,499922}$	$\frac{0}{8,8 \cdot 10^{-5}}$
Beams					
1	192/375	289/375	$\frac{4,81}{2,26}$	$\frac{0,499997}{0,4881}$	$\frac{3 \cdot 10^{-6}}{1,19 \cdot 10^{-2}}$
2	163/375	260/375	$\frac{\beta_R > 5}{3,02}$	$\frac{0,5}{0,49863}$	$\frac{0}{1,37 \cdot 10^{-3}}$
3	204/375	313/375	$\frac{4,5}{1,63}$	$\frac{0,499997}{0,4484}$	$\frac{3 \cdot 10^{-6}}{5,16 \cdot 10^{-2}}$
4	225/375	368/375	$\frac{3,9}{0,18}$	$\frac{0,499948}{0,0714}$	$\frac{5,2 \cdot 10^{-5}}{0,4286}$
5	224/375	313/375	$\frac{4,0}{1,63}$	$\frac{0,499968}{0,4484}$	$\frac{3,2 \cdot 10^{-5}}{5,16 \cdot 10^{-2}}$

Table 5. For calculating the probability P_{no}

Original structure		Optimal structure		Probability of the frame nonfailure	Risk at a loss of 1 million rubles
Columns $\prod_{i=1}^{8} P_{no,i}$	Beams $\prod_{i=1}^{5} P_{no,i}$	Columns $P_{no,c} = \prod_{i=1}^{8} P_{no,i}$	Beams $P_{no,b} = \prod_{i=1}^{5} P_{no,i}$		
1	$0,999997 \times \times 0,999997 \times \times \cdot 0,999948 \times \times 0,999968 = 0,99991$	$0,999997 \cdot 0,9933 \times \times 0,99955 \times 0,999912 = 0,99276$	$0,9881 \cdot 0,99863 \cdot 0,9484 \times \times 0,5714 \cdot 0,9484 = 0,50714$	$\frac{0,99991}{0,5034}$	$\frac{90}{496600}$

Table 5 shows that the design optimized solely according to the criterion of minimizing material consumption is characterized by a significantly higher level of risk. In this case, the probability of material losses exceeds the corresponding indicator of the initial design by several orders of magnitude. At the same time, failure of the load-bearing system does not necessarily lead to its complete collapse. The most probable scenario is damage to the support joint of the roof beam in the area of increased snow accumulation. Based on the analysis of the data in Tables 4 and 5, it is evident that designs optimized only in terms of material efficiency do not possess robustness.

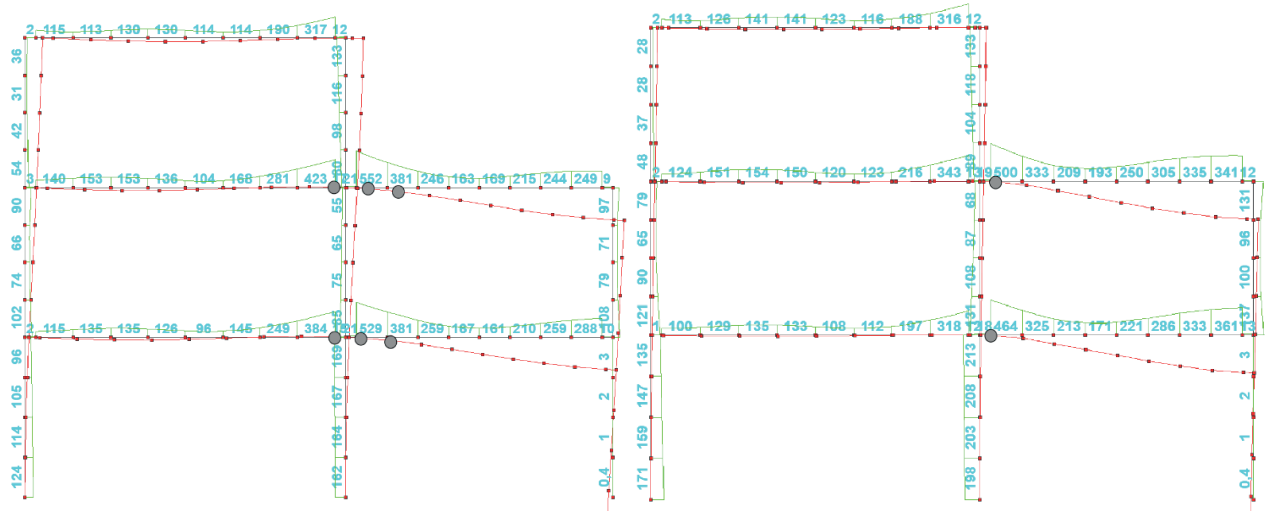
3.3 Accidental Scenarios. Dynamic effects arising from support removal are modeled in a quasi-static formulation, using the well-known formula of G.A. Geniev. In this study, only the initial design is analyzed, without optimization. It is assumed that in all variants of the frame system, joints function without failure. The probabilistic assessment of the robustness of the frame is carried out step by step:

a) The probability of no-failure of the system under normal operation is determined. It is computed as the product of the probabilities of no-failure of individual elements. In conventional design, this probability is close to unity (see Table 5).

b) The probability of no-failure of beams and columns is calculated under the condition of removing one column. In this case, the frame elements follow a parallel failure scheme.

c) The probability of no-failure of beams is determined under the condition of removing one beam while all columns remain intact. In this case, the beams of the frame follow a sequential failure scheme.

3.3.1 Accidental Scenario A. The results of the linear quasi-static analysis are presented in Figure 4a. Analysis of the stiffness matrix of the system showed that it is geometrically stable. Verification of equilibrium conditions made it possible to construct a calculation scheme with a minimum number of plastic hinges. The obtained data are used to form the initial parameters presented in Table 6.



a) *b)*

Figure 4. Diagrams of equivalent stresses (MPa) of the frame: (a) linear analysis with plastic hinges; (b) analysis considering physical and geometric nonlinearity

Table 6. Calculation of failure probability for structural elements

№ of element	$\frac{\sigma_e / \varphi}{R_y}$, MPa	β_R	$\Phi(\beta_b)$	$P_{dam,i}$
Columns				
1	124/337,5	$\beta > 5$	0,5	0
2	169/337,5	4,43	0,499997	$3,0 \cdot 10^{-6}$
3	-	-	-	-
4	102/345,0	$\beta > 5$	0,5	0
5	85/345,0	То же	То же	То же
6	108/345,0	-//-	-//-	-//-
7	54/345,0	-//-	-//-	-//-
8	133/345,0	-//-	-//-	-//-
Beams				
1	249/375	3,31	0,49945	0,00055
2	288/375	2,28	0,4887	0,0113
3	281/375	2,47	0,4933	0,0067
4	246/375	3,39	0,4996	0,0004
5	317/375	1,52	0,4357	0,0643

Based on the data in Tables 5 and 6, it is determined:

$$W_R \approx 0,999997 \cdot (1-0,00055) \cdot 1 \cdot (1-0,0113) \cdot 0,999997 \cdot (1-0,0067) \cdot 0,999948 \cdot (1-0,0004) \times$$
$$\times 0,999968 \cdot (1-0,0643) \cdot 1 \cdot \left(1-3 \cdot 10^{6}\right) \approx 0,9179.$$

The robustness condition is satisfied: $W_R \approx 0,9179 > 0,6$. Nonlinear analysis also confirmed that the system retains robustness. During deformation, two plastic hinges are formed in the beams. The maximum deflection reaches about 49 cm. With a story height of 280 cm, such a deflection does not hinder evacuation of people and/or removal of equipment. It should be emphasized that in this case robustness is ensured by a structural solution providing a partial cantilever suspension effect realized by the beams. However, with an increase in applied loading this solution may prove insufficient. In such situations, the installation of diagonal elements is required to redistribute forces and enhance the system's resistance to progressive collapse.

3.3.2 Accidental Scenario B. The condition of physical fracture of the beam is examined. First, condition (3) is verified. If it is false, then at a certain maximum value of kinetic energy and under the actual stress–strain state, the beam is capable of sustaining the accidental impact with the formation of plastic hinges. In this case, a kinematic chain is formed, and the element continues to function as part of the frame according to the principle of a cable system. If condition (3) is true, a crack is initiated in the beam. Its propagation leads to rupture of the structural element. For definiteness, in this practical calculation the presence of a micro-defect in the support joint of the roof beam is assumed. An approximate evaluation of the Rice integral in this particular case, considering the I-

section profile and the condition of lateral bending, is carried out using the formula obtained by transforming expression (3).

$$J = 2\sum \int_{i=0}^{\Delta_i} \left(\frac{\Delta P_i}{2hb_i} + \frac{\Delta \sigma_{s0i} R_u h}{b_i R_s} \right) d_{\Delta_i}, \quad (17)$$

$$\sigma_{s0} = \sqrt{\left(\frac{\sigma_z + \sigma_y}{2} \right)^2 + 3\left(\frac{\sigma_z - \sigma_y}{2} \right)^2 + 3\tau_{zy}^2}. \quad (18)$$

where $\Delta\sigma_{s0i}$ is the increment of equivalent stresses at each integration step, ΔP_i is the increment of accidental load, h, b_i are the section width and the height from the crack mouth to the opposite edge of the section, respectively; R_u, R_s are the temporary and design strengths of steel; Δ_i is the increment of structural deflection corresponding to the value ΔP_i. It was established that under vertical dynamic loading applied to the roof beam (Fig. 2), the magnitude of which after conversion to a static equivalent with a coefficient of 2 amounts to $P_D \approx 120$ kN, an uncontrollable crack growth occurs, leading to rupture of the section. In this case, part of the load is transferred to the beam of the lower story. To describe such a failure scenario, the computational model may be modified by introducing contact elements. However, since these modeling aspects are beyond the scope of the present study, they are not considered here. For simplification, it is assumed that approximately 5/6 of the static equivalent of the accidental load, i.e., about 100 kN, is transferred to the underlying beam through the support node. The modified scheme for analyzing the probabilistic robustness indicator is shown in Figure 7. The corresponding values of the reliability index are presented in Table 7. Even the linear quasi-static calculation (Fig. 7a) demonstrates that rupture of the beam causes a significant additional bending moment in the left column of the two adjacent stories. Nonlinear analysis confirms that redistribution of bending forces also occurs in the first-story beam, where a plastic hinge forms in the support section (Fig. 7b). Taking into account the sequential failure of beam 3 and beam 1, we obtain:

$$W_R = \prod_{i=1}^{8} \left(P_{no,i} \left(1 - P_{dam,i} \right) \right) \left[P_{no,1} \left(1 - P_{dam,1} P_{dam,3} \right) \right] \times$$

$$\times \prod_{j=2}^{5} \left(P_{no,j} \left(1 - P_{dam,j} \right) \right) = 0,6318 > 0,55.$$

In this accidental scenario, the system possesses robustness, which is confirmed by the results of nonlinear analysis.

The right-hand side of the robustness criterion ($W_R > 0,6$) for the load-bearing system can be refined depending on the type of structural scheme and the adopted serviceability criteria. However, the performed calculations showed that for reinforced concrete and steel frame systems of buildings and structures subjected to service loads, this condition is fulfilled.

The question of applicability of preliminary quasi-static assessment for predicting robustness remains debatable. Nevertheless, comparison of results from geometric instability evaluation with plastic hinges and multiple analyses considering physical, geometric, and structural nonlinearities revealed no discrepancies between the forecast and subsequent calculations.

Future research perspectives are associated with extending the developed provisions to other types of frame systems, including high-rise and unique structures. At the same time, it is reasonable to consider not only the design stage aimed at preventing accidental states but also the service period, during which damage accumulation is possible. Such damages may include defects caused by overloading, changes in planning solutions, as well as environmental impacts such as corrosion processes.

As potential accidental scenarios, alongside column removal, standard fire exposures and various degradation patterns of elements due to corrosion may also be considered.

CONCLUSION

1. A methodology for probabilistic robustness assessment of frame systems in buildings and structures has been developed. The approach is based on an indicator that accounts for the probability of maintaining the functionality of part of the structural elements while allowing for failure of individual members in the zone of accidental action localization. Through calculations on steel and reinforced concrete frames, an integral threshold value of the proposed robustness criterion $W_R > 0,6$ was obtained, at which the robustness of frame systems is ensured under typical accidental scenarios.
2. The applicability of the methodology has been demonstrated using different schemes of accidental action localization in a steel frame with I-shaped profiles. This confirms its suitability for analyzing both newly designed and retrofitted steel systems.
3. The method allows evaluation of the effectiveness of various strengthening measures for the load-bearing system and for increasing its resistance to progressive collapse. High effectiveness of diagonal bracing in frames has been established, which is consistent with other research findings. At the same time, the limited efficiency of merely increasing cross-sectional sizes for localizing progressive collapse without forming a kinematic chain has been demonstrated.

ACKNOWLEDGEMENTS

The authors would like to thank the organizers of the XIII International Scientific Conference, "Tasks and Methods of Computer Modeling of Structures and Buildings" (Zolotovsky Readings), which was part of the program of the III International Scientific and Practical Symposium, "The Future of the Construction Industry: Challenges and Development Prospects," for the opportunity to present their work for scientific discussion and publication.

REFERENCES

1. **Mozafari, N.; Hashemi, S.S.; Jahangiri, M.; Vaghefi, M.; Javidi, S**. Assessment of Progressive Collapse Mechanisms in Cold-Formed Steel-Framed Structures Facing Multi-Element Initial Damage Conditions. Structures 2025, 78, 109343, doi:10.1016/J.ISTRUC.2025.109343.
2. **Naji, A.** Robustness of Steel Moment Frames against Progressive Collapse by Means of Plastic Limit Analysis. International Journal of Structural Integrity 2020, 11, doi:10.1108/IJSI-06-2019-0051.
3. **Xie, D.; Xu, Y.; Nadarajan, S.; Viswanathan, V.; Gupta, A.K.** Robust Stability-Constrained Optimization for Load Restoration with Uncertain Dynamic Loads. Appl Energy 2025, 395, 126070, doi:10.1016/J.APENERGY.2025.126070.
4. **Barros, B.; Conde, B.; Cabaleiro, M.; Riveiro, B.** Design and Testing of a Decision Tree Algorithm for Early Failure Detection in Steel Truss Bridges. Eng Struct 2023, 289, doi:10.1016/j.engstruct.2023.116243.
5. **Suwondo, R.; Cunningham, L.; Gillie, M.; Suangga, M.; Hidayat, I.** Improving the Robustness of Steel Frame Structures under Localised Fire Conditions. Journal of Structural Fire Engineering 2022, 13, doi:10.1108/JSFE-07-2021-0046.
6. **Kalapodis, N.A.; Muho, E. V.; Beskos, D.E.** Structure-Specific, Multi-Modal and Multi-Level Scalar Intensity Measures for Steel Plane Frames. Soil Dynamics and Earthquake Engineering 2025, 190, 109185, doi:10.1016/J.SOILDYN.2024.109185.
7. **Jiang, B.; Wang, M.; Shen, Y.; Li, Y.** Robustness Assessment of Planar Steel Frames Caused by Failure of a Side Column under Localized Fire. Structural Design of Tall and Special Buildings 2020, 29, doi:10.1002/tal.1711.
8. **Jiang, B.; Li, G.Q.; Yam, M.C.H.** Simplified Robustness Assessment of Steel Framed Structures under Fire-Induced

Column Failure. Steel and Composite Structures 2020, 35, doi:10.12989/scs.2020.35.2.199.
9. **Emamikoupaei, A.; Tsavdaridis, K.D.; Bigdeli, A.; Saffarzadeh, K.** Fragility-Based Robustness Assessment of Steel Modular Building Systems: Connection and Building Height. J Constr Steel Res 2025, 226, 109199, doi:10.1016/J.JCSR.2024.109199.
10. **Rodríguez, D.; Brunesi, E.; Nascimbene, R.** Fragility and Sensitivity Analysis of Steel Frames with Bolted-Angle Connections under Progressive Collapse. Eng Struct 2021, 228, doi:10.1016/j.engstruct.2020.111508.
11. **Li, L.L.; Li, G.Q.; Jiang, B.; Lu, Y.** Analysis of Robustness of Steel Frames against Progressive Collapse. J Constr Steel Res 2018, 143, 264–278, doi:10.1016/J.JCSR.2018.01.010.
12. **Xie, Z.; Chen, Y.** Numerical Study of the Robustness of Steel Moment Connections under Catenary Effect. Eng Struct 2022, 252, doi:10.1016/j.engstruct.2021.113658.
13. **Wang, Y.; Li, J. ze; Bai, C.; Shen, H. xia; Tian, L. min** Novel Beam–Column Joint with the Folded Plates for Improving Progressive Collapse Resistance of Steel-Frame Structures. Structures 2024, 61, 106047, doi:10.1016/J.ISTRUC.2024.106047.
14. **Kozlowski, A.; Kukla, D.** Numerical Investigation of Steel Frame Robustness under External Sudden Column Remova. Archives of Civil Engineering 2023, 69, doi:10.24425/ace.2023.145262.
15. **Wang, X.; Wang, P.; Chen, W.** Test on Progressive Collapse of Steel Moment-Resisting Frame with Upper-and-Lower Flange Angle Steel Connection. Structures 2024, 68, 107171, doi:10.1016/J.ISTRUC.2024.107171.
16. **Kukla, D.; Kozlowski, A.** Numerical Study of the Robustness of Steel Frames with Bolted End-Plate Joints Subjected to Sudden and Gradual Internal Column Loss. International Journal of Steel Structures 2023, 23, doi:10.1007/s13296-023-00761-z.
17. **Possidente, L.; Freddi, F.; Tondini, N.** Dynamic Increase Factors for Progressive Collapse Analysis of Steel Structures Considering Column Buckling. Eng Fail Anal 2024, 160, 108209, doi:10.1016/J.ENGFAILANAL.2024.108209.
18. **Lan, X.; Li, Z.; Fu, F.; Qian, K.** Robustness of Steel Braced Frame to Resist Disproportionate Collapse Caused by Corner Column Removal. Journal of Building Engineering 2023, 69, 106226, doi:10.1016/J.JOBE.2023.106226.
19. **Ma, Y.X.; Chen, S.; Tan, K.H.** Experimental Study of Steel Beam-Column Joints with Novel Slot-Bolted Connections under a Central-Column-Removal Scenario. J Constr Steel Res 2024, 214, doi:10.1016/j.jcsr.2024.108481.
20. **Guo, Y.; Yang, B.; Alqawzai, S.; Chen, K.; Kong, D.** Machine Learning-Based and Interpretable Models for Predicting the Resistance and Probability of Progressive Collapse of Steel Frame-Composite Floor Structures. Eng Struct 2025, 332, 120089, doi:10.1016/J.ENGSTRUCT.2025.120089.
21. **Miao, X.; Wang, Y.; Peng, L.; Zhao, Y.** Feature Extraction and Quantitative Analysis of Steel Corrosion in Reinforced Concrete Components Based on XCT Scanning and Deep Learning Model. Journal of Building Engineering 2025, 106, 112652, doi:10.1016/J.JOBE.2025.112652.
22. **Lin, K.; Chen, Z.; Li, Y.; Lu, X.** Uncertainty Analysis on Progressive Collapse of RC Frame Structures under Dynamic Column Removal Scenarios. Journal of Building Engineering 2022, 46, doi:10.1016/j.jobe.2021.103811.
23. **Zhu, X.; Ou, G.** Wind Fragility Modeling of Transmission Tower-Line System Based on Threat-Dependent Structural Robustness Index. Structural Safety 2025, 114, 102571, doi:10.1016/J.STRUSAFE.2024.102571.
24. **Khayatazad, M.; Honhon, M.; De Waele, W.** Detection of Corrosion on Steel Structures Using an Artificial Neural Network. Structure and Infrastructure

Engineering 2023, 19, doi:10.1080/15732479.2022.2069272.
25. **Roshani, M.** Quantification of Structural and Non-Structural Robustness of Tall Steel Buildings Using a Straightforward Methodology. Structures 2024, 62, doi:10.1016/j.istruc.2024.106220.
26. **Noruzvand, M.; Mohebbi, M.; Shakeri, K.** Performance-Based Seismic Design of Low-Rise Steel Moment-Resisting Frames Targeting Collapse Fragility Curve. Structures 2024, 70, 107630, doi:10.1016/J.ISTRUC.2024.107630.
27. **Jiang, L.; Ye, J.** Risk-Based Overall Seismic Robustness Assessment of Cold-Formed Steel Structures Considering Vulnerability and Fragility. Bulletin of Earthquake Engineering 2022, 20, doi:10.1007/s10518-022-01435-7.
28. **Tavakoli, H.R.; Afrapoli, M.M.** Robustness Analysis of Steel Structures with Various Lateral Load Resisting Systems under the Seismic Progressive Collapse. Eng Fail Anal 2018, 83, doi:10.1016/j.engfailanal.2017.10.003.
29. **Formisano, A.; Landolfo, R.; Mazzolani, F.M.** Robustness Assessment Approaches for Steel Framed Structures under Catastrophic Events. Comput Struct 2015, 147, doi:10.1016/j.compstruc.2014.09.010.
30. **Solgi, M.; Rajabi, E.; Amiri, G.G.; Raissi Dehkordi, M.** Seismic Resilience Evaluation of a 3D Steel Moment Frame Building with Triple Friction Pendulum Isolators. Structures 2025, 72, 108075, doi:10.1016/J.ISTRUC.2024.108075.
31. **Freddi, F.; Ciman, L.; Tondini, N.** Retrofit of Existing Steel Structures against Progressive Collapse through Roof-Truss. J Constr Steel Res 2022, 188, doi:10.1016/j.jcsr.2021.107037.
32. **Li, Z.; Xue, T.; Li, G.; Lan, X.; Qian, K.** Influence of Steel Braces on Robustness of Multilayer Steel Frames against Progressive Collapse. Jianzhu Jiegou Xuebao/Journal of Building Structures 2023, 44, doi:10.14006/j.jzjgxb.2021.0824.
33. **Shokoohimatin, M.; Hosseini, M.; Firoozi Nezamabadi, M.** The Effect of Plan Geometry on Progressive Collapse of Tall Buildings with Diagrid Structure Based on Nonlinear Static and Dynamic Analyses. International Journal of Steel Structures 2024, 24, doi:10.1007/s13296-023-00801-8.
34. **Yang, X.; Ma, R.; Bi, K.; Li, H.; Du, X.** Effectiveness and Robustness of Using Nonlinear Pendulum Tuned Mass Damper Inerters for Wind-Induced Vibration Mitigation of High-Rise Buildings. Structures 2025, 73, 108356, doi:10.1016/J.ISTRUC.2025.108356.
35. **Jakab, D.; Marginean, I.; Dubina, D.** ROBUSTNESS CAPACITY OF MULTISTOREY STEEL STRUCTURES IN CASE OF FIRE AFTER EARTHQUAKE EVENTS. Proceedings of the Romanian Academy Series A - Mathematics Physics Technical Sciences Information Science 2023, 24, doi:10.59277/pra-ser.a.24.1.09.
36. **Rice, J.R.** A Path Independent Integral and the Approximate Analysis of Strain Concentration by Notches and Cracks. Journal of Applied Mechanics, Transactions ASME 1968, 35, doi:10.1115/1.3601206.
37. SP 16.13330.2017 "Steel structures" // Ministry of Construction of Russia.
38. SP 63.13330.2018 "Concrete and reinforced concrete structures. Basic provisions" // Ministry of Construction of Russia.

СПИСОК ЛИТЕРАТУРЫ

1. **Mozafari, N.; Hashemi, S.S.; Jahangiri, M.; Vaghefi, M.; Javidi, S**. Assessment of Progressive Collapse Mechanisms in Cold-Formed Steel-Framed Structures Facing Multi-Element Initial Damage Conditions. Structures 2025, 78, 109343, doi:10.1016/J.ISTRUC.2025.109343.
2. **Naji, A.** Robustness of Steel Moment Frames against Progressive Collapse by Means of Plastic Limit Analysis.

International Journal of Structural Integrity 2020, 11, doi:10.1108/IJSI-06-2019-0051.
3. **Xie, D.; Xu, Y.; Nadarajan, S.; Viswanathan, V.; Gupta, A.K.** Robust Stability-Constrained Optimization for Load Restoration with Uncertain Dynamic Loads. Appl Energy 2025, 395, 126070, doi:10.1016/J.APENERGY.2025.126070.
4. **Barros, B.; Conde, B.; Cabaleiro, M.; Riveiro, B.** Design and Testing of a Decision Tree Algorithm for Early Failure Detection in Steel Truss Bridges. Eng Struct 2023, 289, doi:10.1016/j.engstruct.2023.116243.
5. **Suwondo, R.; Cunningham, L.; Gillie, M.; Suangga, M.; Hidayat, I.** Improving the Robustness of Steel Frame Structures under Localised Fire Conditions. Journal of Structural Fire Engineering 2022, 13, doi:10.1108/JSFE-07-2021-0046.
6. **Kalapodis, N.A.; Muho, E. V.; Beskos, D.E.** Structure-Specific, Multi-Modal and Multi-Level Scalar Intensity Measures for Steel Plane Frames. Soil Dynamics and Earthquake Engineering 2025, 190, 109185, doi:10.1016/J.SOILDYN.2024.109185.
7. **Jiang, B.; Wang, M.; Shen, Y.; Li, Y.** Robustness Assessment of Planar Steel Frames Caused by Failure of a Side Column under Localized Fire. Structural Design of Tall and Special Buildings 2020, 29, doi:10.1002/tal.1711.
8. **Jiang, B.; Li, G.Q.; Yam, M.C.H.** Simplified Robustness Assessment of Steel Framed Structures under Fire-Induced Column Failure. Steel and Composite Structures 2020, 35, doi:10.12989/scs.2020.35.2.199.
9. **Emamikoupaei, A.; Tsavdaridis, K.D.; Bigdeli, A.; Saffarzadeh, K.** Fragility-Based Robustness Assessment of Steel Modular Building Systems: Connection and Building Height. J Constr Steel Res 2025, 226, 109199, doi:10.1016/J.JCSR.2024.109199.
10. **Rodríguez, D.; Brunesi, E.; Nascimbene, R.** Fragility and Sensitivity Analysis of Steel Frames with Bolted-Angle Connections under Progressive Collapse. Eng Struct 2021, 228, doi:10.1016/j.engstruct.2020.111508.
11. **Li, L.L.; Li, G.Q.; Jiang, B.; Lu, Y.** Analysis of Robustness of Steel Frames against Progressive Collapse. J Constr Steel Res 2018, 143, 264–278, doi:10.1016/J.JCSR.2018.01.010.
12. **Xie, Z.; Chen, Y.** Numerical Study of the Robustness of Steel Moment Connections under Catenary Effect. Eng Struct 2022, 252, doi:10.1016/j.engstruct.2021.113658.
13. **Wang, Y.; Li, J. ze; Bai, C.; Shen, H. xia; Tian, L. min** Novel Beam–Column Joint with the Folded Plates for Improving Progressive Collapse Resistance of Steel-Frame Structures. Structures 2024, 61, 106047, doi:10.1016/J.ISTRUC.2024.106047.
14. **Kozlowski, A.; Kukla, D.** Numerical Investigation of Steel Frame Robustness under External Sudden Column Remova. Archives of Civil Engineering 2023, 69, doi:10.24425/ace.2023.145262.
15. **Wang, X.; Wang, P.; Chen, W.** Test on Progressive Collapse of Steel Moment-Resisting Frame with Upper-and-Lower Flange Angle Steel Connection. Structures 2024, 68, 107171, doi:10.1016/J.ISTRUC.2024.107171.
16. **Kukla, D.; Kozlowski, A.** Numerical Study of the Robustness of Steel Frames with Bolted End-Plate Joints Subjected to Sudden and Gradual Internal Column Loss. International Journal of Steel Structures 2023, 23, doi:10.1007/s13296-023-00761-z.
17. **Possidente, L.; Freddi, F.; Tondini, N.** Dynamic Increase Factors for Progressive Collapse Analysis of Steel Structures Considering Column Buckling. Eng Fail Anal 2024, 160, 108209, doi:10.1016/J.ENGFAILANAL.2024.108209.
18. **Lan, X.; Li, Z.; Fu, F.; Qian, K.** Robustness of Steel Braced Frame to Resist Disproportionate Collapse Caused by Corner Column Removal. Journal of

Building Engineering 2023, 69, 106226, doi:10.1016/J.JOBE.2023.106226.
19. **Ma, Y.X.; Chen, S.; Tan, K.H.** Experimental Study of Steel Beam-Column Joints with Novel Slot-Bolted Connections under a Central-Column-Removal Scenario. J Constr Steel Res 2024, 214, doi:10.1016/j.jcsr.2024.108481.
20. **Guo, Y.; Yang, B.; Alqawzai, S.; Chen, K.; Kong, D.** Machine Learning-Based and Interpretable Models for Predicting the Resistance and Probability of Progressive Collapse of Steel Frame-Composite Floor Structures. Eng Struct 2025, 332, 120089, doi:10.1016/J.ENGSTRUCT.2025.120089.
21. **Miao, X.; Wang, Y.; Peng, L.; Zhao, Y.** Feature Extraction and Quantitative Analysis of Steel Corrosion in Reinforced Concrete Components Based on XCT Scanning and Deep Learning Model. Journal of Building Engineering 2025, 106, 112652, doi:10.1016/J.JOBE.2025.112652.
22. **Lin, K.; Chen, Z.; Li, Y.; Lu, X.** Uncertainty Analysis on Progressive Collapse of RC Frame Structures under Dynamic Column Removal Scenarios. Journal of Building Engineering 2022, 46, doi:10.1016/j.jobe.2021.103811.
23. **Zhu, X.; Ou, G.** Wind Fragility Modeling of Transmission Tower-Line System Based on Threat-Dependent Structural Robustness Index. Structural Safety 2025, 114, 102571, doi:10.1016/J.STRUSAFE.2024.102571.
24. **Khayatazad, M.; Honhon, M.; De Waele, W.** Detection of Corrosion on Steel Structures Using an Artificial Neural Network. Structure and Infrastructure Engineering 2023, 19, doi:10.1080/15732479.2022.2069272.
25. **Roshani, M.** Quantification of Structural and Non-Structural Robustness of Tall Steel Buildings Using a Straightforward Methodology. Structures 2024, 62, doi:10.1016/j.istruc.2024.106220.
26. **Noruzvand, M.; Mohebbi, M.; Shakeri, K.** Performance-Based Seismic Design of Low-Rise Steel Moment-Resisting Frames Targeting Collapse Fragility Curve. Structures 2024, 70, 107630, doi:10.1016/J.ISTRUC.2024.107630.
27. **Jiang, L.; Ye, J.** Risk-Based Overall Seismic Robustness Assessment of Cold-Formed Steel Structures Considering Vulnerability and Fragility. Bulletin of Earthquake Engineering 2022, 20, doi:10.1007/s10518-022-01435-7.
28. **Tavakoli, H.R.; Afrapoli, M.M.** Robustness Analysis of Steel Structures with Various Lateral Load Resisting Systems under the Seismic Progressive Collapse. Eng Fail Anal 2018, 83, doi:10.1016/j.engfailanal.2017.10.003.
29. **Formisano, A.; Landolfo, R.; Mazzolani, F.M.** Robustness Assessment Approaches for Steel Framed Structures under Catastrophic Events. Comput Struct 2015, 147, doi:10.1016/j.compstruc.2014.09.010.
30. **Solgi, M.; Rajabi, E.; Amiri, G.G.; Raissi Dehkordi, M.** Seismic Resilience Evaluation of a 3D Steel Moment Frame Building with Triple Friction Pendulum Isolators. Structures 2025, 72, 108075, doi:10.1016/J.ISTRUC.2024.108075.
31. **Freddi, F.; Ciman, L.; Tondini, N.** Retrofit of Existing Steel Structures against Progressive Collapse through Roof-Truss. J Constr Steel Res 2022, 188, doi:10.1016/j.jcsr.2021.107037.
32. **Li, Z.; Xue, T.; Li, G.; Lan, X.; Qian, K.** Influence of Steel Braces on Robustness of Multilayer Steel Frames against Progressive Collapse. Jianzhu Jiegou Xuebao/Journal of Building Structures 2023, 44, doi:10.14006/j.jzjgxb.2021.0824.
33. **Shokoohimatin, M.; Hosseini, M.; Firoozi Nezamabadi, M.** The Effect of Plan Geometry on Progressive Collapse of Tall Buildings with Diagrid Structure Based on Nonlinear Static and Dynamic Analyses. International Journal of Steel Structures 2024, 24, doi:10.1007/s13296-023-00801-8.
34. **Yang, X.; Ma, R.; Bi, K.; Li, H.; Du, X.** Effectiveness and Robustness of Using Nonlinear Pendulum Tuned Mass Damper

Inerters for Wind-Induced Vibration Mitigation of High-Rise Buildings. Structures 2025, 73, 108356, doi:10.1016/J.ISTRUC.2025.108356.
35. **Jakab, D.; Marginean, I.; Dubina, D.** ROBUSTNESS CAPACITY OF MULTISTOREY STEEL STRUCTURES IN CASE OF FIRE AFTER EARTHQUAKE EVENTS. Proceedings of the Romanian Academy Series A - Mathematics Physics Technical Sciences Information Science 2023, 24, doi:10.59277/pra-ser.a.24.1.09.
36. **Rice, J.R.** A Path Independent Integral and the Approximate Analysis of Strain Concentration by Notches and Cracks. Journal of Applied Mechanics, Transactions ASME 1968, 35, doi:10.1115/1.3601206.
37. SP 16.13330.2017 "Steel structures" // Ministry of Construction of Russia.
38. SP 63.13330.2018 "Concrete and reinforced concrete structures. Basic provisions" // Ministry of Construction of Russia.

Alekseytsev Anatoly Viktorovich, doctor of technical sciences, associated professor, professor of the department "Reinforced concrete and stone structures"; National Research Moscow State Technical University (NRU MGSU), Russia, Moscow, Yaroslavskoe sh., 26, Scopus ID: 57191530761, Researcher ID: I-3663-2017, ORCID: 0000-0002-4765-5819, e-mail: alekseytsevav@mail.ru.

Kurchenko Natalya Sergeevna, candidate of technical sciences, associated professor of the department "Reinforced concrete and stone structures"; National Research Moscow State Technical University (NRU MGSU), Russia, Moscow, Yaroslavskoe sh., 26, Scopus ID: 57196073119, ORCID: 0000-0002-5434-4277, e-mail: ms.kurchenko@mail.ru.

Алексейцев Анатолий Викторович, доктор технических наук, доцент, профессор кафедры «Железобетонные и каменные конструкции»; Национальный исследовательский московский государственный технический университет (НИУ МГСУ), Россия, г. Москва, Ярославское ш., 26, Scopus ID: 57191530761, Researcher ID: I-3663-2017, ORCID: 0000-0002-4765-5819, e-mail: alekseytsevav@mgsu.ru.

Курченко Наталья Сергеевна, кандидат технических наук, доцент кафедры «Железобетонные и каменные конструкции»; Национальный исследовательский московский государственный технический университет (НИУ МГСУ), Россия, г. Москва, Ярославское ш., 26, Scopus ID: 57196073119, ORCID: 0000-0002-5434-4277, e-mail: ms.kurchenko@mail.ru.

DOI:10.22337/2587-9618-2026-22-1-56-64

RELIABILITY OF ENCLOSING STRUCTURES ACCORDING TO A GIVEN CRITERION OF THERMAL PROTECTION

Natalya L. Galaeva

National Research Moscow State University of Civil Engineering, Moscow, RUSSIA

Abstract: The requirements of thermal protection, along with the requirements of mechanical strength and stability imposed on enclosing structures, are among the key requirements that must be taken into account, taken into account and monitored not only when developing building projects, but also after their construction, since it is these indicators that will determine the energy efficiency and cost-effectiveness of the construction projects being implemented. These requirements are presented in the current regulatory documentation of the Russian Federation and are described by certain mathematical models consisting of a set of parameters. When using these models, the expert (or the designer) can conclude whether the enclosing structure meets a certain requirement, for example, the requirement for reduced heat transfer resistance, or does not meet this requirement, however, he (the expert) cannot say and assess how reliable this structure is by one or another criterion of thermal protection or by a set of criteria. This article presents specific methods for determining the quantitative indicator of the reliability of thermal protection of enclosing structures and proposes to reduce the reliability assessment to a value or range of values that will range from 0 to 1. This approach will allow for a multifactorial assessment of the energy efficiency of enclosing structures and allows experts, based on the results obtained, to draw conclusions about reliability. enclosing structures according to various criteria of thermal protection.

Keywords: reliability, enclosing structures thermal protection, climatic parameters, resistance to heat transfer, possibility, probability, probability of uptime, the need for trouble-free operation

НАДЕЖНОСТЬ ОГРАЖДАЮЩИХ КОНСТРУКЦИЙ ПО ЗАДАННОМУ КРИТЕРИЮ ТЕПЛОВОЙ ЗАЩИТЫ

Н.Л. Галаева

Национальный исследовательский Московский государственный строительный университет, г. Москва, РОССИЯ

Аннотация: Требования тепловой защиты на ряду с требованиями механической прочности и устойчивости, предъявляемые к ограждающим конструкциям являются одними из ключевых требований, которые необходимо принимать во внимание, учитывать и контролировать не только при разработке проектов зданий, но и после их возведения, т.к. именно от этих показателей будет зависеть энергоэффективность и экономичность эксплуатации реализуемых строительных объектов. Данные требования представлены в действующей нормативной документации Российской Федерации и описаны определенными математическими моделями, состоящими из набора параметров. При использовании этих моделей эксперт (или проектировщик) может сделать вывод соответствует ли ограждающая конструкция определенному требованию, например, требованию к приведенному сопротивлению теплопередачи, или не соответствует этому требованию, однако, он (эксперт) не может сказать и оценить насколько данная конструкция надежна по тому или иному критерию тепловой защиты или по совокупности критериев. В настоящей статье представлены частные методики для определения количественного показателя надежности тепловой защиты ограждающих конструкций и предлагается привести оценку надежности к значению или интервалу значений, которые будут находиться в диапазоне от 0 до 1. Такой подход позволит проводить многофакторную оценку энергетической эффективности ограждающих конструкций и дает возможность экспертам, на основе полученных результатов, делать выводы о надежности ограждающих конструкций по различным критериям тепловой защиты.

Ключевые слова: надежность, ограждающие конструкции, тепловая защита, климатические параметры, сопротивление теплопередаче, возможность, вероятность, вероятность безотказной работы, необходимость безотказной работы

INTRODUCTION

The current regulatory documents of the Russian Federation, the requirements of which must be taken into account when designing enclosing structures forming the heat-protective shell of buildings to provide thermal protection, establish a certain set of requirements, including a requirement for the value of the reduced resistance to heat transfer [1]. At the design stage of the building, design engineers, based on the initial data obtained in the terms of reference, develop design solutions for enclosing structures, which are confirmed not only by appropriate engineering and technical calculations, but also by the results of modeling temperature fields in various specialized software packages, in particular, it can be the Elcut software package, which allows to accurately simulate the distribution of temperatures along the thickness of various types of enclosing structures [2-4, etc.]. After the implementation of the building project under development, its construction, or after a certain period of time, after the facility is put into operation, it is possible that the entire enclosing structure or its individual fragments do not meet the thermal engineering indicators stated in the developed building project (i.e., the values may be lower than those set by the project), as well as the requirements stated in current regulatory documents, which In the future, the operation of the building will lead to increased energy consumption. Such discrepancies can be caused by various factors: a. deviation from the accepted design decisions, for example, the use of analog materials during the construction of a building (in particular, external enclosing structures), the thermal properties of which may not correspond to the design values; b. violation of production technologies during the installation of facade systems; c. deterioration of thermal engineering properties of external enclosing structures as a result of exposure to an aggressive environment, including atmospheric influences, duration of operation of the enclosing structure, etc. If the first two (a, b) of the above-mentioned causes of deterioration of the thermal engineering properties of the enclosing structure may arise as a result of the "human factor" and can be eliminated by introducing stricter control over the materials and structures used, as well as the process of building construction, then the third (c) possible cause may be the result of natural deterioration of thermal engineering properties resulting from: 1. wear and aging of materials and components of the facade system; 2. various possible adverse effects on the exterior enclosing structure, i.e. natural processes occur that occur during the entire period of operation of the enclosing structure, leading to irreversible changes in the properties of materials, in other words, natural wear of the enclosing structure occurs, which is not always possible to stop. At the design stage of the enclosing structure, a certain level of its thermal reliability is laid, the value of which will change over time as a result of changes in the properties of materials. It is known that reliability is the property or ability of an object, building element, or building structure to maintain its functions that ensure its normal operation over time. The existing regulatory documents do not contain information on how to quantify the reliability of thermal protection of the enclosing structure. The issues of evaluation and development of reliability calculation methods are presented in a fairly large number of scientific papers [5-12, etc.]. However, in most cases they are aimed specifically at finding methods for determining reliability and evaluating it according to criteria such as strength, stability, etc. From the point of view of decision-making, a building or a certain structure can be considered as a system that consists of a certain set of elements, each of which will have its own impact on the overall reliability of the entire system. when assessing the overall reliability, for example, of a building as a whole or its individual external enclosing structure, it is necessary to identify a list of criteria, including not only criteria for mechanical strength and stability of system elements, but also criteria describing the requirements for their thermal protection. In the proposed article: 1. the methods of determining the quantitative indicator of the

reliability of a fragment of an external enclosing structure according to one of the criteria of its thermal protection are shown (an element-by-element requirement is considered), using the provisions of mathematical statistics, probability theories and fuzzy set theory; 2. it is proposed to reduce the assessment of the thermal reliability of enclosing structures to a value or range of values that will range from 0 to 1.

METHODS

In the framework of this work, particular methods for calculating the reliability of the enclosing structure are considered according to the criterion of meeting the element-by-element requirement for thermal protection established by the regulatory document SP 50.13330.2024, respectively, for two variants of the initial data set for controlled parameters. The mathematical model describing the condition of the element-by-element requirement in relation to the thermal protection of a fragment of the enclosing structure can be written as follows:

$$R_o^r \geq R_o^{reg}, \qquad (1)$$

where R_o^r and R_o^{reg} are the values of the reduced and normalized heat transfer resistance, respectively, $m^2 \cdot °C/W$. For a thermally homogeneous fragment, condition (1) can be written as $R_0 \geq R_o^{reg}$. To calculate a quantitative indicator that will characterize the thermal reliability of a fragment of the enclosing structure, it is necessary to conduct a preliminary examination, during which the following must be performed: 1. identification of the enclosing structure according to the available design documentation (installed: the type of enclosing structure, the number of layers, their compositions, components, for example, which were used to attach thermal insulation boards to a load-bearing base, etc.); 2. preliminary thermal imaging examination in order to identify thermal inhomogeneities; 3. assessment of the multiplicity of room air exchange. Based on the results of the survey, the expediency and possibility of conducting field tests of the selected fragment of the enclosing structure is established in order to collect the necessary information on the controlled parameters. One of the options in which a fragment of the enclosing structure cannot be used for conducting field studies is the case in which there are defects caused, for example, by infiltration of the enclosing structures, etc. A preliminary examination of the building's enclosing structures in order to select the fragments under study is an important step in assessing their reliability, which helps to obtain the most reliable calculation results. Since the parameters included in equation (1) may be variable, equation (1) can be written as:

$$\tilde{R}_o^r \geq \tilde{R}_o^{reg} \text{ (or } \tilde{R}_0 \geq \tilde{R}_o^{reg}), \qquad (2)$$

where $R_o^{reg}=(a\cdot((t_{int}-t_{ht})z_{ht})+b)\cdot m_r$ (a, b are coefficients taken depending on the building group; $m_r=1$ is a coefficient that takes into account the specifics of the construction region) in the problem considered in the article can be considered as a deterministic value, because all the parameters included in the formula for its determination can be taken strictly in accordance with the requirements of the current regulatory documentation, but it is likely that it may be necessary to determine the value of the parameter R_o^{reg} for a certain location of the construction site for which official statistics on the required climatic parameters are not available, in particular in this case, the parameter $\tilde{R}_o^{reg}$ can be considered as a random variable or a fuzzy variable, for example, the parameters: a, b and t_{int} can be taken as deterministic quantities, and t_{ht} or z_{ht} can be taken as a random variable or a fuzzy variable, depending on the completeness and quality of the initial set of information, according to controlled parameters that can be used in calculations. For example, in [8-11and et al.], the issues of probabilistic and statistical modeling of climate data arrays, including using artificial intelligence, are raised and a conclusion is given on the applicability and expediency of such an approach. In other words, the parameter $\tilde{R}_o^{reg}$ in some cases can be represented as a certain set of values: $\{R_{0,1}^{reg}; R_{0,2}^{reg}, \ldots, R_{0,n}^{reg}\}$ $m^2 \cdot °C/W$. Let's assume

that there are no official climate data for the geographical location on which the construction object is located, while the specified object is located at approximately the same but sufficiently large distance from the nearest settlements for which official climate statistics are available and these data have a significant (for a certain situation) difference in temperature values and may further affect influence on the decisions made based on the results of calculations, it is necessary to analyze the available information, Mathematical data modeling can be used. In some cases, fuzzy set theory can be used to enable data description. To determine the set of statistical information for the parameter $\tilde{R}_o^r$ (or $\tilde{R}_0$), it is necessary to conduct field studies, as a result of which a certain set of values will be determined: for a thermally homogeneous fragment – $\{R_{0,1}^r;\ R_{0,2}^r,\ \dots\ ,\ R_{0,n}^r\}$ m^2·°C/W or for thermally homogeneous – $\{R_{0,1};\ R_{0,2},\ \dots\ ,\ R_{0,n}\}$ m^2·°C/W. For this purpose, depending on the task, enclosing structures oriented to N, N-W or N-E are selected in accordance with the requirements of the national standard GOST R 59939-2021. As a result of the research, sets of statistical data are obtained on the following parameters: temperatures (1. internal (t_{int}) and external (t_{ext}) air; 2. internal (τ_{int}) and external (τ_{ext}) surfaces of the surveyed enclosing structure); actual heat flux density (q). For a thermally homogeneous fragment of the enclosing structure, the parameter $\tilde{R}_0$ can be determined for each set of the above parameters according to the equation: $\tilde{R}_0=\frac{(\tilde{t}_{int}-\tilde{\tau}_{int})}{\tilde{q}}+\frac{(\tilde{\tau}_{int}-\tilde{\tau}_{ext})}{\tilde{q}}+\frac{(\tilde{\tau}_{ext}-\tilde{t}_{int})}{\tilde{q}}=\frac{(\tilde{t}_{int}-\tilde{t}_{ext})}{\tilde{q}}$, m^2·°C/W (written $\tilde{R}_0$, because the thermally homogeneous fragment); for a thermally inhomogeneous fragment of the enclosing structure – $\tilde{R}_o^r = A/(\sum A_i/\tilde{R}_{0i})$, m^2·°C/W, where A is the area of the enclosing structure under examination, m^2; A_i is the area of the characteristic isothermal zone, which is determined by the results of thermal imaging of a fragment of the structure under examination, m^2; $\tilde{R}_{0i}$ is the heat transfer resistance of the characteristic zone, m^2 °C/W. $\tilde{R}_o^r$ (or $\tilde{R}_0$), depending on the completeness obtained as a result of field tests, statistical information about the parameters $\tilde{t}_{int}$, $\tilde{t}_{ext}$, $\tilde{\tau}_{int}$, $\tilde{\tau}_{ext}$ and q can be represented as random variables or fuzzy variables. Next, it is necessary to analyze the data on the parameters $\tilde{R}_o^{reg}$ and $\tilde{R}_o^r$ and, depending on the completeness of the information received, methods of probability theory can be applied to determine the reliability of the enclosing structure (or its fragment) according to the criterion of fulfilling the piecemeal requirement for thermal protection. or fuzzy set theory. Let's consider two options for calculating reliability using the mathematical model (2):

1. Let the parameters $\tilde{R}_o^r$ and $\tilde{R}_o^{reg}$ be used to obtain complete statistical information, according to which the law of their distribution (the normal distribution law) and its parameters were established: $m_{R_o^r}$, $m_{R_o^{reg}}$, $S_{R_o^r}$, $S_{R_o^{reg}}$ – i.e. $\tilde{R}_o^r$ and $\tilde{R}_o^{reg}$ are random variables. In this case, the reliability of the fragment under study will be characterized by an indicator of uptime according to a given criterion and a safety characteristic can be used: $\gamma=\frac{m_{R_o^r}-m_{R_o^{reg}}}{\sqrt{S_{R_o^r}^2+S_{R_o^{reg}}^2}}$, according to which the value of the probability of uptime according to criterion (2) can be determined using tables of normal distribution functions:

$$P(R_o^r \geq R_o^{reg})=\Phi(\gamma), \qquad (3)$$

2. Let's assume that there are limited statistical data available for the parameters $\tilde{R}_o^r$ and $\tilde{R}_o^{reg}$, i.e. the statistical information turned out to be incomplete. In this case, $\tilde{R}_o^r$ and $\tilde{R}_o^{reg}$ are considered as fuzzy variables that will be characterized by the same opportunity distribution function (ODF) of the form:

$$\pi_R(R)=e^{-[(R-a_R)/b_R]^2}, \qquad (4)$$

where $a_R=(R_{max}+R_{min})/2$, $b_R=(R_{max}-R_{min})/(2\sqrt{-\ln\alpha})$, $\alpha\in[0;1]$, α – the risk level. The use of this function (ODF) to describe uncertainty and determine reliability indicators (the possibility method) was shown in the works of Doctor of Technical Sciences, Professor V.S. Utkin, as well as in the works of his students [13-15 et al.] applied to building structure elements.For the case considered in the article, for fuzzy variables $\tilde{R}_o^r$ and $\tilde{R}_o^{reg}$ we will have:

$$\begin{cases} \pi_{\widetilde{R}_o^{reg}}(R_o^{reg}) = e^{-\left[\left(R_o^{reg} - a_{R_o^{reg}}\right)/b_{R_o^{reg}}\right]^2} \\ \pi_{\widetilde{R}_o^{r}}(R_o^{r}) = e^{-\left[\left(R_o^{r} - a_{R_o^{r}}\right)/b_{R_o^{r}}\right]^2} \end{cases}, \quad (5)$$

Graphically, the functions $\pi_{\widetilde{R}_o^{reg}}(R_o^{reg})$ and $\pi_{\widetilde{R}_o^{r}}(R_o^{r})$ can be represented as shown in Fig. 1.

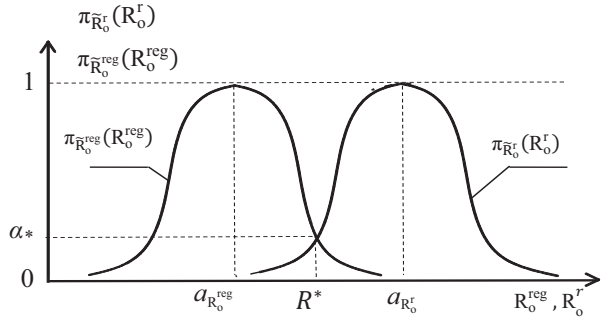


Figure 1. Graphical representation of functions: $\pi_{\widetilde{R}_o^{reg}}(R_o^{reg})$ *and* $\pi_{\widetilde{R}_o^{r}}(R_o^{r})$

According to Fig. 1, if $a_{R_o^{r}} > a_{R_o^{reg}}$, then the possibility of trouble-free operation will be equal to R=1 (not to be confused with the designation of heat transfer resistance). The value of the possibility of failure can be found by finding the abscissa of the intersection point R^* ODF: $\pi_{\widetilde{R}_o^{reg}}(R_o^{reg})$ and $\pi_{\widetilde{R}_o^{r}}(R_o^{r})$ and substituting this value into any of the values specified in equations (4), for example, $Q=\pi_{\widetilde{R}_o^{r}}(R^*)=e^{-\left[\left(R^* - a_{R_o^{r}}\right)/b_{R_o^{r}}\right]^2}$. The need for uptime: $N=1-Q$ and, therefore, the reliability interval will have the form: $[R;N]$.

RESULTS AND DISCUSSION

As an object of research, we will take a fragment of the enclosing structure, which is a fragment of a blank exterior wall of a building with a hinged facade system (type FTCS, facade thermal insulation composite system). Let it be that, as a result of a preliminary thermal imaging examination of the fragment, the possibility and feasibility of field tests were established, no temperature anomalies were detected. The geographical location of the construction site is Moscow, Moscow region. We will take the initial climatic parameters based on the data from the weather archive of the meteorological station No. 27612 (Exhibition of Achievements of National Economy, Moscow) for the period from 2014 to 2023. The results of the analysis of the arrays of climatic data obtained from the weather sensor for the specified period are summarized in Table 1.

Table 1. Climatic parameters

№	Year	the average temperature of the period at $t_{ext} \leq 8$ °C	Duration of the period, day
1	2014	-1.5	195
2	2015	0.17	198
3	2016	-1.9	195
4	2017	-0.32	210
5	2018	-3.28	183
6	2019	0.035	186
7	2020	1.11	192
8	2021	-1.93	203
9	2022	-0.9	194
10	2023	-1.33	181

In table 2, the values of the parameters are determined based on the climatic data and the data in table 1.: 1. degree-day of the heating period (D_d); 2. the normalized value of the heat transfer resistance $\widetilde{R}_o^{reg}$ for a given location of the studied enclosing structure (Moscow).

Table 2. Parameter values: D_d *and* R_o^{reg}

№	Year	D_d, °C·day	R_o^{reg}, m^2·°C/W
1	2014	4197.32	2.87
2	2015	3926.05	2.77
3	2016	4278.02	2.90
4	2017	4266.66	2.89
5	2018	4260.68	2.89
6	2019	3713.51	2.70
7	2020	3626.33	2.67
8	2021	4451.58	2.96
9	2022	4047.24	2.82
10	2023	3861.35	2.75

Thus, the parameter R_o^{reg} is represented as a certain set of values.: {2.87; 2.77; 2.90; 2.89; 2.89; 2.70; 2.67; 2.96; 2.82; 2.75} m²·°C/W. Let's consider it as a random variable distributed according to the normal distribution law, with distribution parameters: $m_{R_o^{reg}}$ = 2.82 m²×°C/W; $S_{R_o^{reg}}$ = 0.091 m²·°C/W. Let's assume that in order to collect statistical information on the parameter $\tilde{R}_o^r$ (or $\tilde{R}_0$), field studies were conducted, during which arrays of data on the parameters were obtained: 1. the temperatures of the outer (t_{ext}) and inner surfaces (t_{int}) of the fragment under study; 2. the density of the heat flux passing through the fragment (q) under natural conditions. Let's assume that the period during which the changes were carried out is 10 days. After the formation and processing of the obtained arrays of statistical data on the controlled parameters, the sets of values of the parameter $\tilde{R}_o^r$ are determined. For a more visual representation of the problem being solved, we will generate a data array consisting of 100 values of the parameter $\tilde{R}_o^r$. For the resulting set of values $\{R_{0,1}^r; R_{0,2}^r, \dots, R_{0,100}^r\}$, we carry out statistical processing and analysis of data, after which we accept the parameter $\tilde{R}_0^r$ as a random variable distributed according to the normal distribution law, with distribution parameters: $m_{R_o^r}$ = 3.06 m²·°C/W; $S_{R_o^r}$ = 0.07 m²·°C/W. A fragment of the array will look like this: {3.15; 2.97; 3.13; ... ; 3.07; 3.12} m²·°C/W; maximum value: $R_{o,\,max}^r$ =3.23 m²·°C/W; minimum value: $R_{o,\,min}^r$ = 2.89 m²·°C/W. Then, the probability of trouble-free operation under the condition of equation (2) using equation (3) will be equal to $P(R_o^r \geq R_o^{reg}) = \Phi(\gamma) = \Phi\left(\frac{3.06-2.82}{\sqrt{0.07^2+0.091^2}}\right) = 0.9817$. Let's consider the same example, but let's take both parameters $\tilde{R}_o^r$ and $\tilde{R}_o^{reg}$ as fuzzy variables that will be characterized by a set of the form (4). The parameters of the set are: 1. $\pi_{\tilde{R}_o^r}(R_o^r) - a_{R_o^r}$=3.06 m²·°C/W; $b_{R_o^r}$=0.10 m²·°C/W; 2. $\pi_{\tilde{R}_o^{reg}}(R_o^{reg}) - a_{R_o^{reg}}$=2.82 m²·°C/W; $b_{R_o^{reg}}$=0.11 m²·°C/W. The possibility of trouble-free operation will be equal to R=1, because $a_{R_o^r}$=3.06 m²·°C/W > $a_{R_o^{reg}}$=2.82. The value of the abscissa of the intersection point R^* ODF: $\pi_{\tilde{R}_o^{reg}}(R_o^{reg})$ and $\pi_{\tilde{R}_o^r}(R_o^r)$ will be equal to 2.95 m²·°C/W, then the value of the possibility of failure is substituted by R^* in any of equations (5), and will be equal to Q = 0.27, and the need for trouble-free operation will be equal to N=1-0.27=0.73. The reliability of the studied fragment of the enclosing structure under the condition of fulfilling the piecemeal requirement for thermal protection will be characterized by the interval [0.73;1]. The value of the reliability indicator P=0.9817, obtained using methods of probability theory, is more convincing for experts from the point of view of decision-making, since it is unambiguous, compared with the value of the reliability indicator in the form of an interval estimate [N=0.73; R=1], obtained using fuzzy set theory. In this case, the value of P=0.9817 falls within the range [0.73; 1], i.e. the true reliability value was inside the obtained range. The example considered in the article shows that when calculating reliability according to the criterion described by equation (2) for a fragment of an enclosing structure, some useful statistical information was lost when using the probability method. At the same time, one rather important point should be noted: the use of this method may be advisable in the absence of complete statistical information on controlled parameters from experts.

CONCLUSION

The proposed work presents methods for determining the quantitative indicator of the reliability of the enclosing structure according to the criterion of fulfilling a piecemeal requirement (requirements for reduced resistance to heat transfer), using the provisions of classical mathematical apparatus, namely the provisions of mathematical statistics, probability theory and theory of fuzzy sets. Depending on the amount of information available to experts about the controlled parameters obtained as a result of technical inspections and monitoring studies, a methodology is selected for calculating the reliability indicator. The presented approaches to calculating the quantitative indicator of thermal

reliability make it possible to bring the reliability estimate to a value that will be in the range [0; 1], which facilitates a multifactorial assessment of the energy efficiency of various types of enclosing structures.

REFERENCES

1. **Frolova A., Petrov G., Frolov D., Lebediuk A.** The required level of thermal protection of enclosing structures of administrative buildings in the transport infrastructure in Russia and European countries // E3S Web of Conferences : International Scientific Conference "Fundamental and Applied Scientific Research in the Development of Agriculture in the Far East" (AFE-2022), Tashkent, Uzbekistan, 25–28.01.2023. Vol. 371. – Tashkent, Uzbekistan: EDP Sciences, 2023. – P. 04017. – DOI 10.1051/e3sconf/202337104017.
2. **Barysheva O, Barysheva A.** Thermophysical Properties of Aerated Concrete Enclosing Structures // Proceedings of STCCE : International Scientific Conference on Socio-Technical Construction and Civil Engineering 2022 : Lecture Notes in Civil Engineering, Kazan, 21–29.04.2022. Vol. 291. – Switzerland: Springer Nature, 2022. – P. 227-243. – DOI 10.1007/978-3-031-14623-7_20.
3. **Galaeva N.** The influence of the dowel mounting scheme in facade systems on the thermal protection properties of the enclosing structure // E3S Web of Conferences. – 2024. – Vol. 583. – P. 06002. – DOI 10.1051/e3sconf/202458306002.
4. **Dement'eva M.** Evaluation of exploitation suitability of enclosing structures of filling stations // MATEC Web of Conferences, Warsaw, 19–21.08.2017. Vol. 117. – Warsaw: EDP Sciences, 2017. – P. 00037. – DOI 10.1051/matecconf/201711700037.
5. **Belentsov Yu. A**. Method of calculating building structures by reliability level // Building Materials. – 2020. – No. 11. – pp. 54-60. – DOI 10.31659/0585-430X-2020-786-11-54-59.
6. **Semko V., Leshchenko M., Cherednikova O.** Standardization of required level probability of no-failure operation of the building envelopes by the criterion of total thermal resistance // International Journal of Engineering and Technology(UAE). – 2018. – Vol. 7, No. 3. – P. 382-387. – DOI 10.14419/ijet.v7i3.2.14557.
7. **Kuligin D., Shkoliar F.** Influence of the probabilistic method to summarize loads on the reliability and material consumption of building structures // Architecture and Engineering. – 2023. – Vol. 8, No. 2. – P. 49-57. – DOI 10.23968/2500-0055-2023-8-2-49-57.
8. **Samarin O. D.** The probabilistic-statistical modeling of the external climate in the cooling period // Magazine of Civil Engineering. – 2017. – No. 5(73). – P. 62-69. – DOI 10.18720/MCE.73.6.
9. **Kayusi F., Chavula P., Lungu G., Mambwe H**. AI-Driven Climate Modeling: Validation and Uncertainty Mapping – Methodologies and Challenges//*LatIA*, vol. 3, p. 332, Mar. 2025. – DOI 10.62486/latia2025332
10. **Ahmadi M., Kamangar M.** Statistical analysis and forecasting monthly temperature of Sanandaj synoptic station with application of SARIMA model // Water and Soil Management and Modeling, 3(1), 2023. – P. 1-13. DOI: 10.22098/MMWS.2022.11080.1099
11. **Wu Y, Xue W.** Data-Driven Weather Forecasting and Climate Modeling from the Perspective of Development/ Y. Wu, W. Xue// *Atmosphere*. – 2024,15(6):689. https://doi.org/10.3390/atmos15060689
12. **Utkin V. S.** Calculation of the reliability of reinforced concrete piles in the foundations // Construction: science and education. – 2018. – Vol. 8, No. 3. – p. 2. – DOI 10.22227/2305-5502.2018.3.2.

13. **Utkin V. S.** Calculation of the reliability of pile racks taking into account the forces of friction and adhesion on the surface of the pile // Construction: science and education. – 2020. – Vol. 10, No. 1. – p. 2. – DOI 10.22227/2305-5502.2020.1.2.
14. **Utkin V. S., Sushev L. A.** The Reliability Analysis of Existing Reinforced Concrete Piles in Permafrost Regions // International Journal for Computational Civil and Structural Engineering. – 2017. – Vol. 13, No. 2. – P. 64-72.
15. **Galaeva, N.L.** (2023). Calculation of Reliability of Beam with Corrugated Wall with Limited Information About the Controlled Parameters at the Stage of Operation. In: Klyuev, S.V., Klyuev, A.V., Vatin, N.I., Sabitov, L.S. (eds) Innovations and Technologies in Construction. BUILDINTECH BIT 2022. Lecture Notes in Civil Engineering, vol 307. Springer, Cham. DOI 10.1007/978-3-031-20459-3_41

СПИСОК ЛИТЕРАТУРЫ

1. **Frolova A., Petrov G., Frolov D., Lebediuk A.** The required level of thermal protection of enclosing structures of administrative buildings in the transport infrastructure in Russia and European countries // E3S Web of Conferences : International Scientific Conference “Fundamental and Applied Scientific Research in the Development of Agriculture in the Far East” (AFE-2022), Tashkent, Uzbekistan, 25–28.01.2023. Vol. 371. – Tashkent, Uzbekistan: EDP Sciences, 2023. – P. 04017. – DOI 10.1051/e3sconf/202337104017.
2. **Barysheva O, Barysheva A.** Thermophysical Properties of Aerated Concrete Enclosing Structures // Proceedings of STCCE : International Scientific Conference on Socio-Technical Construction and Civil Engineering 2022 : Lecture Notes in Civil Engineering, Kazan, 21–29.04.2022. Vol. 291. – Switzerland: Springer Nature, 2022. – P. 227-243. – DOI 10.1007/978-3-031-14623-7_20.
3. **Galaeva N.** The influence of the dowel mounting scheme in facade systems on the thermal protection properties of the enclosing structure // E3S Web of Conferences. – 2024. – Vol. 583. – P. 06002. – DOI 10.1051/e3sconf/202458306002.
4. **Dement'eva M.** Evaluation of exploitation suitability of enclosing structures of filling stations // MATEC Web of Conferences, Warsaw, 19–21.08.2017. Vol. 117. – Warsaw: EDP Sciences, 2017. – P. 00037. – DOI 10.1051/matecconf/201711700037.
5. **Беленцов, Ю.А.** Метод расчета строительных конструкций по уровню надежности // Строительные материалы. – 2020. – № 11. – С. 54-60. – DOI 10.31659/0585-430X-2020-786-11-54-59.
6. **Semko V., Leshchenko M., Cherednikova O.** Standardization of required level probability of no-failure operation of the building envelopes by the criterion of total thermal resistance // International Journal of Engineering and Technology(UAE). – 2018. – Vol. 7, No. 3. – P. 382-387. – DOI 10.14419/ijet.v7i3.2.14557.
7. **Kuligin D., Shkoliar F.** Influence of the probabilistic method to summarize loads on the reliability and material consumption of building structures // Architecture and Engineering. – 2023. – Vol. 8, No. 2. – P. 49-57. – DOI 10.23968/2500-0055-2023-8-2-49-57.
8. **Samarin O. D.** The probabilistic-statistical modeling of the external climate in the cooling period // Magazine of Civil Engineering. – 2017. – No. 5(73). – P. 62-69. – DOI 10.18720/MCE.73.6.
9. **Kayusi F., Chavula P., Lungu G., Mambwe H**. AI-Driven Climate Modeling: Validation and Uncertainty Mapping – Methodologies and Challenges//*LatIA*, vol. 3, p. 332, Mar. 2025. – DOI 10.62486/latia2025332

10. **Ahmadi M., Kamangar M.** Statistical analysis and forecasting monthly temperature of Sanandaj synoptic station with application of SARIMA model // Water and Soil Management and Modeling, 3(1), 2023. – P. 1-13. DOI: 10.22098/MMWS.2022.11080.1099
11. **Wu Y, Xue W.** Data-Driven Weather Forecasting and Climate Modeling from the Perspective of Development/ Y. Wu, W. Xue// *Atmosphere*. – 2024,15(6):689. https://doi.org/10.3390/atmos15060689
12. **Уткин, В.С.** Расчет надежности железобетонных свай-стоек в основаниях фундаментов // Строительство: наука и образование. – 2018. – Т. 8, № 3. – С. 2. – DOI 10.22227/2305-5502.2018.3.2. – EDN YLUYJN.
13. **Уткин, В.С.** Расчет надежности свай-стоек с учетом сил трения-сцепления на поверхности сваи // Строительство: наука и образование. – 2020. – Т. 10, № 1. – С. 2. – DOI 10.22227/2305-5502.2020.1.2.
14. **Utkin V.S., Sushev L.A.** The Reliability Analysis of Existing Reinforced Concrete Piles in Permafrost Regions // International Journal for Computational Civil and Structural Engineering. – 2017. – Vol. 13, No. 2. – P. 64-72.
15. **Galaeva, N.L.** (2023). Calculation of Reliability of Beam with Corrugated Wall with Limited Information About the Controlled Parameters at the Stage of Operation. In: Klyuev, S.V., Klyuev, A.V., Vatin, N.I., Sabitov, L.S. (eds) Innovations and Technologies in Construction. BUILDINTECH BIT 2022. Lecture Notes in Civil Engineering, vol 307. Springer, Cham. DOI 10.1007/978-3-031-20459-3_41

Galaeva Natalya Leonidovna – Candidate of Technical Sciences, Associate Professor of the Department of Architectural and Construction Design and Environmental Physics at the National Research Moscow State University of Civil Engineering; 129337, Russia, Moscow, Yaroslavskoe Shosse, 26. e-mail: Natalia-fdf@rambler.ru

Галаева Наталья Леонидовна – к.т.н., доцент кафедры «Архитектурно-строительного проектирования и физики среды» Национального исследовательского Московского государственного строительного университета; 129337, Россия, г. Москва, Ярославское шоссе, д. 26. e-mail: Natalia-fdf@rambler.ru

International Journal for Computational Civil and Structural Engineering, 22(1) 65–73 (2026)

DOI:10.22337/2587-9618-2026-22-1-65-73

NUMERICAL SIMULATION OF SWIRLING FLOWS WITH SEPARATION ZONES

Vadim K. Akhmetov

Moscow State University of Civil Engineering, Moscow, RUSSIA

Abstact. A numerical study of axisymmetric viscous swirling flows of fluid was carried out at moderate Reynolds numbers. The mathematical model is based on the use of the complete Navier-Stokes system equations, written in terms of the stream function, vorticity and azimuthal velocity variables. Boundary value problems for flows with different configurations are formulated. The numerical solution is carried out by the finite-difference relaxation method using the Leonard scheme of the third order of accuracy for approximating the convective terms in the transport equations and the method of incomplete reduction for solving the Poisson equation. The flow streamlines and velocity distribution patterns were obtained. The results are compared with available experimental data. The possibility of using the obtained results for the analysis of turbulent flows by introducing effective parameters is considered.

Keywords: swirling flows, coaxial flows, finite difference method, recirculation zones, vortex breakdown, effective parameters

ЧИСЛЕННОЕ МОДЕЛИРОВАНИЕ ЗАКРУЧЕННЫХ ТЕЧЕНИЙ С ОТРЫВНЫМИ ЗОНАМИ

В.К. Ахметов

Национальный исследовательский Московский государственный строительный университет, Москва, РОССИЯ

Аннотация. Проведено численное исследование осесимметричных закрученных течений вязкой жидкости при умеренных числах Рейнольдса. Математическая модель основана на использовании полной системы уравнений Навье-Стокса, записанной в переменных функции тока, завихренности и азимутальной скорости. Сформулированы краевые задачи для течений с различной конфигурацией. Численное решение проводится конечно-разностным методом установления с применением схемы Леонарда третьего порядка точности для аппроксимации конвективных членов в уравнениях переноса и метода неполной редукции при решении уравнения Пуассона. Получены картины линий тока и распределения скоростей в потоке. Результаты сравниваются с имеющимися экспериментальными данными. Рассмотрена возможность использования полученных результатов для анализа турбулентных течений за счет введения эффективных параметров.

Ключевые слова: закрученные течения, коаксиальные потоки, метод конечных разностей, рециркуляционные зоны, распад вихря, эффективные параметры

1. INTRODUCTION

Swirling flows are widely used in various technical devices [1, 2] and hydraulic engineering structures [3-5]. The properties of swirling flows are utilized for combustion stabilization, intensification of mixing processes, gas cleaning from dust, particle separation, thermal separation of flows, energy dissipation in vortex drop shafts, in counter-vortex devices for reservoir aeration, as well as in many other fields, particularly in the petrochemical, microbiological, and food industries. A distinctive feature of swirling flows is the formation of separated recirculation zones upon reaching a certain critical value of the initial flow swirl. These zones can be beneficial or may cause undesirable effects. The aim of this work is to perform numerical simulation of swirling flows with separation

zones in relation to various technical applications and problems in hydraulic engineering construction.

2. PROBLEM STATEMENT AND RESEARCH METHODS

Studies of the hydrodynamics of swirling flows of a viscous incompressible fluid at moderate Reynolds numbers are based on the complete system of Navier-Stokes equations. Assuming axisymmetry of the flow in a cylindrical coordinate system r, φ, z. Here, z-axis is directed along the axis of the flow under study, in terms of the stream function ψ, vorticity Ω, and azimuthal velocity V_φ, these equations can be represented as follows:

$$\frac{1}{r}\frac{\partial^2\psi}{\partial z^2}+\frac{\partial}{\partial r}\left(\frac{1}{r}\frac{\partial\psi}{\partial r}\right)=-\Omega, \qquad (1)$$

$$\frac{\partial\Omega}{\partial t}+\frac{\partial}{\partial z}\left(V_z\Omega\right)+\frac{\partial}{\partial r}\left(V_r\Omega\right)=$$
$$=\frac{1}{\mathrm{Re}}\left[\frac{\partial^2\Omega}{\partial z^2}+\frac{\partial^2\Omega}{\partial r^2}+\frac{\partial}{\partial r}\left(\frac{\Omega}{r}\right)\right]+G^2\frac{1}{r}\frac{\partial\left(V_\varphi\right)^2}{\partial z}, \qquad (2)$$

$$\frac{\partial V_\varphi}{\partial t}+\frac{\partial}{\partial z}\left(V_zV_\varphi\right)+\frac{1}{r}\frac{\partial}{\partial r}\left(rV_rV_\varphi\right)+\frac{V_rV_\varphi}{r}=$$
$$=\frac{1}{\mathrm{Re}}\left[\frac{\partial^2V_\varphi}{\partial z^2}+\frac{1}{r}\frac{\partial}{\partial r}\left(r\frac{\partial V_\varphi}{\partial r}\right)-\frac{V_\varphi}{r^2}\right], \qquad (3)$$

$$V_r=-\frac{1}{r}\frac{\partial\psi}{\partial z},\quad V_z=\frac{1}{r}\frac{\partial\psi}{\partial r},\quad \Omega=\frac{\partial V_r}{\partial z}-\frac{\partial V_z}{\partial r}. \qquad (4)$$

The system of equations (1)-(4) is written in a conservative dimensionless form. The axial V_z and radial V_r velocities are referred to the characteristic value U_0. The azimuthal velocity V_φ refers to the characteristic value W_0. The coordinates refer to the characteristic size R, time refers to the value R/U_0. The parameters of the system are the Reynolds number $\mathrm{Re}=U_0R/\nu$, where ν is the kinematic viscosity, and the swirl parameter $G=W_0/U_0$. These equations are essentially nonlinear. Analytical solutions for specific problems can only be obtained in a number of special cases.

The boundary value problem is formulated by setting boundary conditions, which include a given velocity distribution of the flow at the inlet to the considered flow region, no-slip conditions on solid surfaces, symmetry conditions on the flow axis, and soft boundary conditions at the outlet.

For an axisymmetric channel with solid walls, at the inlet of which a swirling flow arrives with a velocity distribution:

$$\begin{aligned}
&V_{z0}(r)=D_0+D_1\exp(-B_1r^2),\ 0\le r\le r_0,\\
&V_{z0}(r)=a_0+a_1r+a_2r^2,\qquad r_0\le r\le 1,\\
&V_{\varphi0}(r)=\frac{A}{r}(1-\exp(-B_2r^2)),\ 0\le r\le r_0,\\
&V_{\varphi0}(r)=b_0+b_1r+b_2r^2,\qquad r_0\le r\le 1
\end{aligned} \qquad (5)$$

the set of boundary conditions is written as follows:

$$\psi=\psi_0(r),\quad V_\varphi=V_{\varphi0}(r),$$
$$\frac{\partial\psi}{\partial z}=0,\quad 0\le r\le 1,\quad z=0, \qquad (6)$$

$$\psi=\psi_0(1)=\psi_1,\quad V_\varphi=0,$$
$$\frac{\partial\psi}{\partial r}=0,\quad 0\le z\le z_k,\quad r=1, \qquad (7)$$

$$\psi=0,\ V_\varphi=0,\ \Omega=0,\ 0\le z\le z_k,\ r=0, \qquad (8)$$

$$\frac{\partial\psi}{\partial z}=\frac{\partial\Omega}{\partial z}=\frac{\partial V_\varphi}{\partial z}=0,\ 0\le r\le 1,\ z=z_k. \qquad (9)$$

To solve the boundary value problem (1)-(4), (6)-(9) with the initial distribution (5), the finite difference method was used, employing the incomplete reduction method [6] for equation (1) and approximation of the convective terms in equations (2)-(3) using Leonard's scheme [7]. The calculations assumed the following values: $D_0=1$, $D_1=0$, $B_1=0$, $B_2=14$, $A=0.419$, $r_0=0.75$, $z_k=10$. The characteristic flow pattern with two separation zones is presented in Fig. 1.

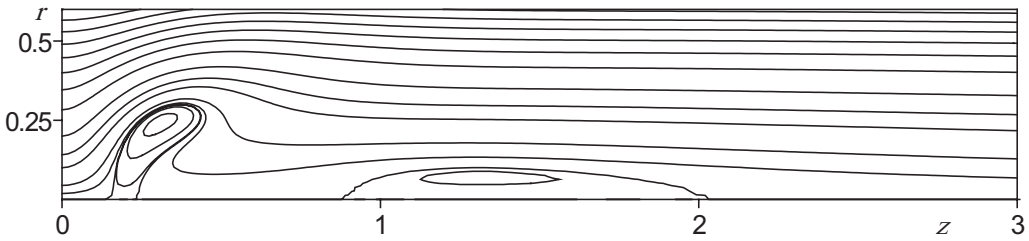


Figure 1. Streamlines for Re=150, G=2.6

If the flow is in a channel with permeable walls, one can assume that additional inflow occurs at a constant velocity $-V_0$ on a part of the lateral surface $0 \le z \le z_0$, $r = 1$. Then the boundary condition (7) for the stream function at $r = 1$ must be replaced by the following:

$$\begin{aligned} \psi &= V_0 z + \psi_1, \quad 0 \le z \le z_0, \\ \psi &= V_0 z_0 + \psi_1, \quad z_0 \le z \le z_k . \end{aligned} \tag{10}$$

The main effect in this case is that by setting the appropriate inflow velocity, it is possible to influence the boundaries of the reverse flow zones, up to their complete elimination. Examples of the calculated flows are shown in Fig. 2.

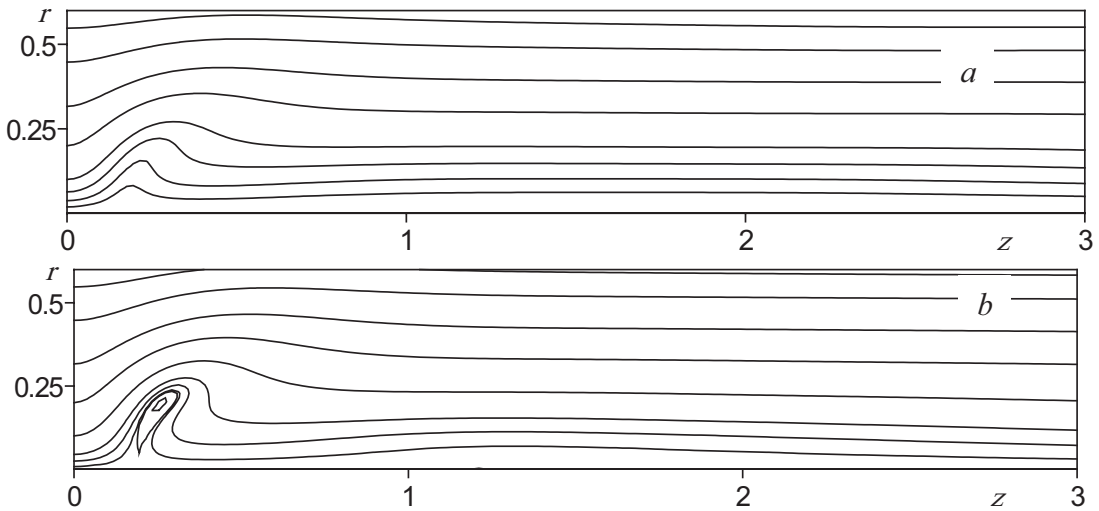


Figure 2. Streamlines for Re=150, G=2.6, $z_0 = 2.5$, V_0=0.01, 0.03 (a, b)

To study the swirling flow in an unbounded medium (without solid walls), a coordinate transformation was used in system (1)-(4), refining the mesh in the near-axis region of the flow, and instead of r, a variable y was introduced by the following transformation:

$$y = \frac{1}{a}\ln(1 + r/b), \quad r \in [0, r_k], \quad y \in [0, 1], \tag{11}$$

where a and b are constants. A characteristic pattern of separated flows is shown in Fig. 3. In this case, the front part of the recirculation zone becomes more pointed, its diameter relative to its length decreases, and overall, its shape corresponds more closely to the bubble-type vortex breakdown observed in experiments [8].

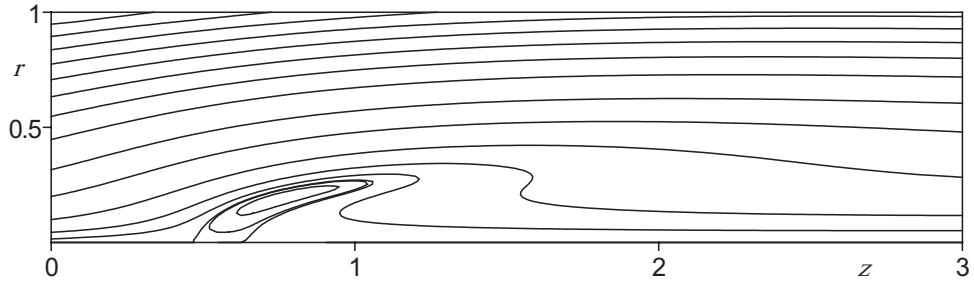


Figure 3. Streamlines for Re=750, G=0.95

The problem of the interaction of two axisymmetric swirling flows is relevant in connection with the modeling of flows in combustion chambers and gas turbines [2], vortex chambers, and gas curtains [9]. We will consider the case where the flow is organized as follows. Two coaxial flows, separated by a thin annular partition — an inner non-swirling flow and an outer swirling flow — enter a cylindrical channel and interact intensively within it.

For the calculations of the interaction between the axial and annular swirling flows at the inlet $z = 0$, velocity profiles with a uniform distribution and the following values were specified:

$$\begin{aligned} &U_0 = 1,\ V_{\varphi 0}(r) = 0,\ 0 \le r \le r_0, \\ &U_1 = 2.25, V_{\varphi 0}(r) = W_1 = 1, r_0 \le r \le r_1, \end{aligned} \tag{12}$$

in which it was adopted that $r_0 = 0.25,\ r_1 = 0.5$ for $R = 1$.

The most important properties of the flows discovered during the study are the emergence of a near-axis recirculation zone upon reaching a critical swirl rate, the formation downstream of this zone of a secondary recirculation region, and the development of an annular recirculation zone due to the splitting of the first zone by the inner jet flow. Characteristic streamline patterns are presented in Fig. 4.

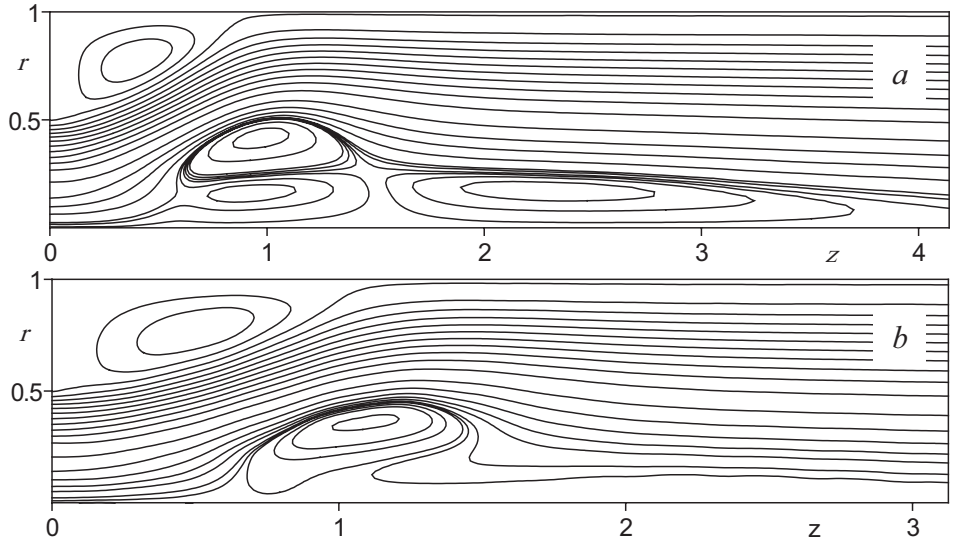


Figure 4. Streamlines for Re=150, G=2.25 (a), 2.75 (b)

Coaxial swirling flows are used in vortex combustion chambers [1]. The resulting near-axis recirculation zone serves as a kind of flame holder and is an example of vortex breakdown [8]. Consider the flow in an axisymmetric channel, at the inlet of which two coaxially swirling flows are supplied: an inner flow ($0 \le r \le r_0$) and an outer flow ($r_0 \le r \le r_1$). The

rotation can occur in either the same or opposite directions. The velocity distribution at $z = 0$ is specified as follows:

$$V_{z0}(r)=\begin{cases}1, & 0\le r\le r_{c1},\\ 1-k_1(r-r_{c1})^2, & r_{c1}\le r\le 1,\\ V_z^*-k_2(r-r_{c2})^2, & 1\le r\le r_{c2},\\ V_z^*, & 1\le r\le r_{c2},\\ V_z^*-k_3(r-r_{c3})^2, & r_{c3}\le r\le r_k,\end{cases} \quad (13)$$

$$V_{\varphi 0}(r)=\begin{cases}s_1 r, & 0\le r\le r_{a1},\\ 1-s_2(r-r_{a1})^2, & r_{a1}\le r\le r_{a2},\\ 1-s_3(r-r_{a2})^2, & r_{a2}\le r\le 1,\\ V_\varphi^*-s_4(r-r_{a3})^2, & 1\le r\le r_{a3},\\ \dfrac{Ar_k}{r}[1-\exp(-B(r/r_k)^2)], & r_{a3}\le r\le r_{a4},\\ b_0+b_1 r+b_2 r^2, & r_{a4}\le r\le r_k.\end{cases}$$

where $r_k = r_1/r_0 = 4$, $A = 0.554$, $B = 8$, $r_{c1} = 0.94$, $r_{c2} = 1.06$, $r_{c3} = 3.94$, $r_{a1} = 0.9$, $r_{a2} = 0.94$, $r_{a3} = 1.6$, $r_{a4} = 3.94$.

The solution of the boundary value problem (1)-(4) with the given distribution (13) depends on four parameters: the Reynolds number Re, the swirl parameter G, and the initial velocity values of the outer flow V_z^* and V_φ^*. Flow calculations were performed in the parameter range: $30 \le \mathrm{Re} \le 500$, $0 \le G \le 3$, $0.1 \le V_z^* \le 0.8$, $-1.6 \le V_\varphi^* \le 1.4$. An example of the flow calculation for the case of initial swirl in opposite directions is shown in Fig. 5. The two-cell structure of the recirculation zone (Fig. 5b) has been noted for bubble-type vortex breakdown in experiments [11] and numerical studies [12]. The calculations established that moderate swirl of the external flow in both the same and opposite directions can lead to both a reduction in the size of the near-axis recirculation zone (up to its complete disappearance at $V_\varphi^* > 0$) and an increase in its size. Strong swirl of the external flow $|V_\varphi^*| > 1$ always leads to an increase in the size of the recirculation zone.

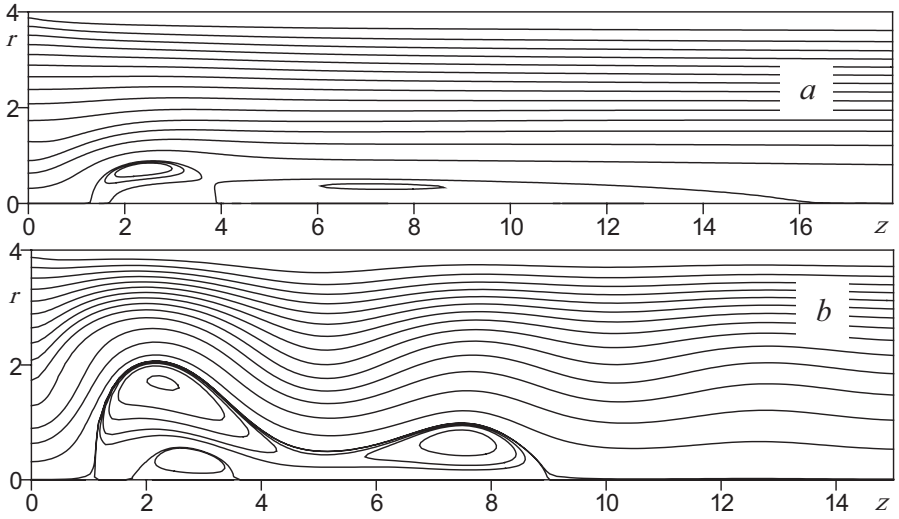


Figure 5. Streamlines for $\mathrm{Re} = 250$, $G = 1.8$, $V_z^* = 0.3$, $V_\varphi^* = -0.1, -0.8$ *(a, b)*

Let us consider the possibility of describing experimentally studied turbulent flows using the above-proposed model of swirling flows based on the concept of effective parameters. The experiments [13] were conducted on an aerodynamic stand, the working section of which was a plexiglass tube with a diameter of D = 14.5 cm. The inner jet was supplied into the measured test section from a copper tube with an outer diameter of 3.86 cm and an inner

diameter of 3.43 cm. The Reynolds number, based on the average flow velocity U_{cp} and the tube diameter D, was $\mathrm{Re} = 2.5 \cdot 10^5$.

We introduce into consideration the effective values of the turbulent viscosity coefficients ν_{tz} and $\nu_{t\varphi}$ in the longitudinal and azimuthal directions. Experiments [2] have shown that strong anisotropy of turbulent viscosity is observed in the flow, and $\nu_{t,z} / \nu_{t,\varphi} \approx 4$.

We define the turbulent value of the Reynolds number Re_{tz} as follows:

$$\mathrm{Re}_{tz} = \frac{U_{cp}\, R}{\nu_{t,z}} = \frac{1}{\chi}\sqrt{\frac{8}{\lambda}}, \qquad (14)$$

where U_{cp} is the average flow velocity, λ is the hydraulic resistance coefficient, and χ is a universal constant.

Based on the available experimental data, the hydraulic resistance coefficient along the pipe length is calculated using the formula of A.D. Altshul:

$$\lambda = 0.11\left(\frac{k_э}{D} + \frac{68}{\mathrm{Re}}\right)^{0.25} = $$
$$= 0.11\left(\frac{0.02}{145} + \frac{68}{2.5 \cdot 10^5}\right)^{0.25} = 0.015,$$

where $k_э = 0.02$ mm – коэффициент шероховатости полированного оргстекла. Используя значение универсальной постоянной для воздуха $\chi = 0.07$, из (14) находим $\mathrm{Re}_{tz} = 330$. Пересчитывая полученное число Рейнольдса в соответствии с характерными величинами – максимальной скорости внутренней струи U_0 в начальном сечении $z = 0$ и радиусу r_0, получим:

where $k_э = 0.02$ mm is the roughness coefficient of polished plexiglass. Using the value of the universal constant for air $\chi =$ 0.07, from (14) we find $\mathrm{Re}_{tz} = 330$. Recalculating the obtained Reynolds number in accordance with the characteristic values – the maximum velocity of the inner jet U_0 at the initial section z = 0 and the radius r_0 – we obtain:

$$\mathrm{Re}_{tz} = 330 \frac{U_0}{U_{cp}} \frac{r_0}{r_1} = 117.9.$$

In the experiments [13], integral swirl parameters for the inner and outer flows (S_0 and S_1, respectively) were used, defined by the relations:

$$S_j = \frac{\int_{r'}^{r''} V_z V_\varphi r^2 dr}{r'' \int_{r'}^{r''} V_z^2\, r\, dr}, \qquad j = 0; 1, \quad (15)$$

$$j = 0: \; r_j' = 0, \, r_j'' = r_0; \quad j = 1: \; r_j' = r_0, \, r_j'' = r_1.$$

In the series of experiments, the ratio $V_z^* = U_1 / U_0$ of the average axial velocities at the chamber inlet and the swirl parameter S_0 of the inner flow varied insignificantly: $V_z^* = 0.69 - 0.74$; $S_0 = 0.59 - 0.71$. Recirculation zones were observed for five cases under consideration, in which the values of the initial swirl of the outer flow were:

$$S_1 = -0.38, -0.19, 0, 0.21, 0.42. \qquad (16)$$

To conduct a comparison with the experiments, we take the average values of the inner jet parameters $V_z^* = 0.7$, $S_0 = 0.66$. Substituting the specified initial velocity distribution (13) into (15) considering (16), we find the effective swirl parameters for the calculation $G = 0.763$ and:

$$V_\varphi^* = -0.408, -0.25, 0, 0.27, 0.43. \qquad (17)$$

We determine, by analogy with [14], the effective values of the flow parameters using the expressions:

$$G_* = G\frac{\nu_{tz}}{\nu_{t\varphi}} = 0.763 \cdot 4 \approx 3, \qquad (18)$$

$$\mathrm{Re}_* = \mathrm{Re}_{tz}\frac{\nu_{t\varphi}}{\nu_{tz}} = \frac{117.9}{4} \approx 30. \qquad (19)$$

Taking this into account, the numerical solution of the boundary value problem (1)-(4), (13) for comparison with the experiment [13] was carried out for $\mathrm{Re}_* = 30$, $G_* = 3$, $V_z^* = 0.7$, and the values of V_φ^* from (17).

The calculated and experimental distributions of the axial velocity $V_z(0,z)$ along the channel length for the cases studied in [13] are presented in Fig. 6. The good agreement confirms the possibility of using the proposed model for calculating turbulent flows.

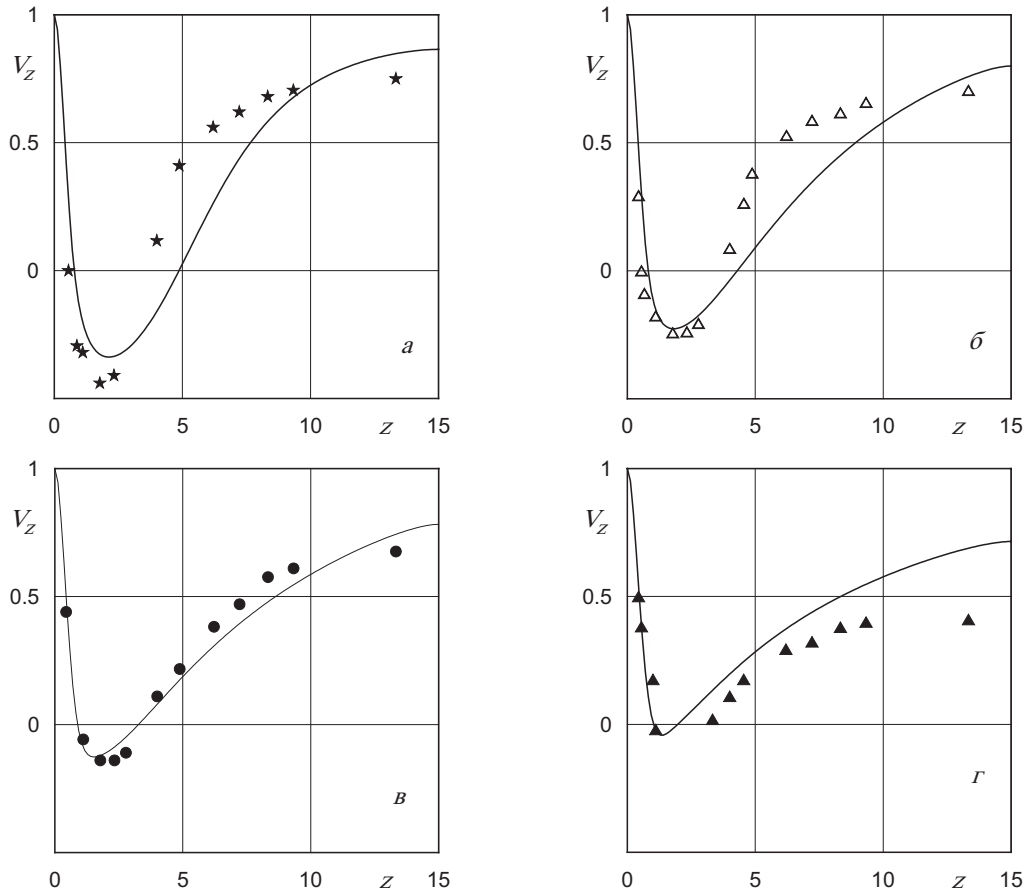


Figure 6. Comparison of the calculated (solid curves) and experimental [13] distributions of the velocities V_z at the channel axis; $S_1 = -0.38, -0.19, 0, 0.21$ (a–d)

The influence of the outer flow swirl V_φ^* on the diameter d_0 of the near-axis recirculation zone and the value of the maximum reverse flow velocity V_b is shown in Fig. 7 (calculated curves 1 and 2). An increase in the swirl of the outer flow in the opposite direction relative to the inner flow leads to an increase in the diameter d_0 of the recirculation zone and the reverse flow velocity V_b. In the case of the flows rotating in the same direction, an increase in the swirl of the outer flow leads to a decrease in the values of d_0 and V_b. The obtained calculated results are in good agreement with the experimental data [13] for all five investigated cases of varying outer flow swirl.

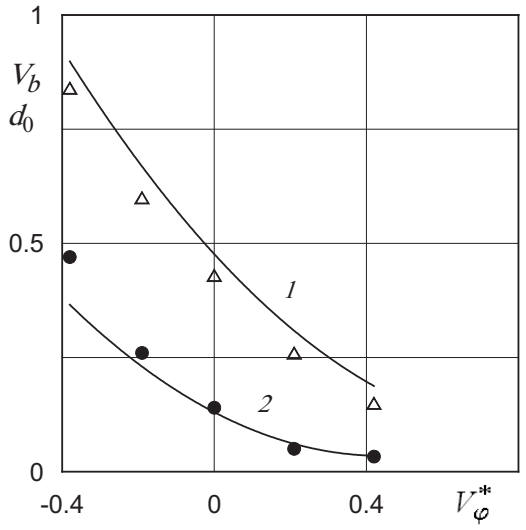


Figure 7. Comparison of calculated and experimental [13] dependencies of the recirculation zone diameter (curve 1 and experimental points) and the reverse flow velocity (curve 2 and experimental points) on the outer flow swirl

5. CONCLUSIONS

Based on the complete system of Navier-Stokes equations, mathematical modeling of swirling flows of various configurations has been carried out. For the numerical solution of the boundary value problems, a software package has been developed that allows for the efficient calculation of the structure of separated flows. Detailed streamline patterns were obtained, the range of parameters within which recirculation zones form in the flow was determined, and the internal structure of the separation zones was investigated. A comparison of the presented calculations with experimental data using the method of effective parameters demonstrates the applicability of the obtained results for the qualitative description of turbulent separated flows.

СПИСОК ЛИТЕРАТУРЫ

1. **Гупта А., Лилли Д., Сайред Н.** Закрученные потоки. М.: Мир, 1987. 588 с.
2. **Кутателадзе С.С., Волчков Э.П., Терехов В.И.** Аэродинамика и тепломассообмен в ограниченных вихревых потоках. Новосибирск: Институт теплофизики, 1987. 283 с.
3. **Ахметов В.К., Волшаник В.В., Зуйков А.Л., Орехов Г.В.** Моделирование и расчет контрвихревых течений. Монография. М.: Изд-во АСВ, 2012. 252 с.
4. **Волшаник В.В., Зуйков А.Л., Мордасов А.П.** Закрученные потоки в гидротехнических сооружениях. М.: Энергоатомиздат, 1990. 280 с.
5. **Животовский Б.А.** Водосбросные и сопрягающие сооружения с закруткой потока. М.: Изд-во РУДН, 1995. 190 с.
6. **Самарский А.А., Николаев Е.С.** Методы решения сеточных уравнений. М.: Наука, 1978. 592 с.
7. **Leonard B.P.** A stable and accurate convective modeling procedure based on quadratic upstream interpolation // Comp. Meth. Appl. Mech. and Eng. 1979. V. 19. № 1. P. 59–98.
8. **Лейбович С.** Распад вихря // Вихревые движения жидкости. М.: Мир., 1979. С. 160-196.
9. **Волков Э.П., Гаврилов Е.И., Дужих Ф.П.** Газоотводящие трубы ТЭЦ и АЭС. М.: Энергоатомиздат, 1987. 278 с.
10. **Lucca-Negro O., O'Doherty T.** Vortex breakdown: a review. Progress in Energy and Combustion Science. 2001. V. 27. P. 431-481.
11. **Faler J.H., Leibovich S.** An experimental map of the internal structure of a vortex breakdown // J. Fluid Mech. 1978. V. 86. № 2. P. 313-335.
12. **Spall R.E., Gatski T.B., Ash R.L.** The structure and dynamics of bubble-type vortex breakdown // Proc. Roy. Soc. London. Ser. A. 1990. V. 429. № 1877. P. 613-637.
13. **Vu B.T., Gouldin F.C.** Flow measurements in a model swirl combustor // AIAA J. 1982. V. 20. № 5. P. 642-651.

14. **Ахметов В.К., Шкадов В.Я.** Взаимодействие струи с кольцевым закрученным потоком // Известия РАН. Механика жидкости и газа. 1995. № 2. С. 39-46.

REFERENCES

1. **Gupta A.K, Lilley D.G, Syred N.** Swirl Flows 1984 (Abacus Press)
2. **Kutateladze S.S., Volchkov E.P., Terekhov V.I.** Aerodynamics and heat and mass exchange in bounded vortex flows. Novosibirsk: Institute of thermophysics, 1987. 283 p. (in Russian).
3. **Ahmetov V.K., Volshanik V.V., Zujkov A.L., Orekhov G.V.** Modelirovanie i raschet kontrvikhrevykh techenij. Monografiya. M.: Izd-vo ASV, 2012. 252 s.
4. **Volshanik V.V., Zujkov A.L., Mordasov A.P.** Zakruchennye potoki v gidrotekhnicheskikh sooruzheniyakh. M.: Ehnergoatomizdat, 1990. 280 s.
5. **Zhivotovskij B.A.** Vodosbrosnye i sopryagayushchie sooruzheniya s zakrutkoj potoka. M.: Izd-vo RUDN, 1995. 190 c.
6. **Samarskij A.A., Nikolaev E.S.** Metody resheniya setochnykh uravnenij. M.: Nauka, 1978. 592 s.
7. **Leonard B.P.** A stable and accurate convective modeling procedure based on quadratic upstream interpolation // Comp. Meth. Appl. Mech. and Eng. 1979. V. 19. № 1. P. 59–98.
8. **Leibovich S.** The structure of vortex breakdown // Annual review of fluid mechanics. 1978. V. 10. P. 221-246.
9. **Volkov E.P., Gavrilov E.I., Duzhikh F.P.** Gazootvodyashchie truby TEHC i AEHS. M.: Ehnergoatomizdat, 1987. 278 s.
10. **Lucca-Negro O., O'Doherty T.** Vortex breakdown: a review. Progress in Energy and Combustion Science. 2001. V. 27. P. 431-481.
11. **Faler J.H., Leibovich S.** An experimental map of the internal structure of a vortex breakdown // J. Fluid Mech. 1978. V. 86. № 2. P. 313-335.
12. **Spall R.E., Gatski T.B., Ash R.L.** The structure and dynamics of bubble-type vortex breakdown // Proc. Roy. Soc. London. Ser. A. 1990. V. 429. № 1877. P. 613-637.
13. **Vu B.T., Gouldin F.C.** Flow measurements in a model swirl combustor // AIAA J. 1982. V. 20. № 5. P. 642-651.
14. **Akhmetov V.K., Shkadov V.Ya.** Interaction between a jet and an annular swirling stream // Fluid Dynamics. 1995. V. 30. № 2. P. 188-194.

Vadim K. Akhmetov, Doctor of Science, Professor, Department of Computer Science and Applied Mathematics, Moscow State University of Civil Engineering, 26, Yaroslavskoe Shosse, Moscow, 129337, Russia, e-mail: vadim.akhmetov@gmail.com

Ахметов Вадим Каюмович, доктор технических наук, профессор кафедры информатики и прикладной математики Национального исследовательского Московского государственного строительного университета, 129337, г. Москва, Ярославское шоссе, д. 26, e-mail: vadim.akhmetov@gmail.com

International Journal for Computational Civil and Structural Engineering, 22(1) 74–85 (2026)

DOI:10.22337/2587-9618-2026-22-1-74-85

APPLICATION OF COMPUTER VISION TO DETECT DEFECTS IN WELDS

Marina E. Dement'eva

National Research Moscow State University of Civil Engineering, Moscow, RUSSIA

Abstract: In the context of increasing wear and tear of utility pipelines, improving the quality of diagnostics of their technical condition, as well as improving the quality of control over construction and repair work, is of particular importance. Timely detection of defects and damage helps prevent emergency situations and negative socio-economic and environmental consequences. Traditional methods of visual and instrumental control have a number of disadvantages, in particular, high labor intensity, long information processing time, and insufficient accuracy. This problem can be solved by using computer vision to identify and classify damage, which will improve the quality of defect detection, reduce the likelihood of human error, and speed up the diagnostic process. However, different levels of readiness of the developed machine learning algorithms require additional research to confirm the effectiveness of their use in professional fields, for example, when inspecting structures, which justifies the relevance of this study. The object of the study was the YOLO family of computer vision models capable of identifying various classes of defects. The aim of the study was to train the YOLOv5, YOLOv8, and YOLO11 detection algorithms and to perform a comparative analysis of their speed and accuracy of data processing using weld defects as an example. The results of the experimental studies show that the use of the latest version of the model does not lead to significant improvements in the quality of defect detection compared to previous versions. The results presented in the work allow us to assess the feasibility of using the new YOLO11 model to detect defects in radiographic images. Based on the experiments, researchers using computer vision methods to control the quality of welds can make an informed decision about whether to use this model or use previous versions of the algorithms.

Keywords: machine learning, lifecycle management, YOLO, radiography, predictive exploitation

ПРИМЕНЕНИЕ КОМПЬЮТЕРНОГО ЗРЕНИЯ ДЛЯ ОБНАРУЖЕНИЯ ДЕФЕКТОВ В СВАРНЫХ ШВАХ

М.Е. Дементьева

Национальный исследовательский Московский государственный строительный университет, г. Москва, РОССИЯ

Аннотация: В условиях растущего износа трубопроводов коммунальной инфраструктуры особую значимость приобретает повышение качества диагностирования их технического состояния на этапе эксплуатации, а также повышение качества контроля строительных и ремонтно-восстановительных работ. Своевременное выявление дефектов и повреждений позволяет предупредить возникновение аварийных ситуаций и предотвратить негативные социально-экономические и экологические последствия. Применяемые традиционные методы визуального и инструментального контроля имеют ряд недостатков, в частности, высокую трудоемкость, длительное время обработки информации, недостаточную точность. Решение данной проблемы возможно путем применения компьютерного зрения для выявления и классификации повреждений, что позволит повысить качество обнаружения дефектов, снизить вероятность человеческих ошибок, а также ускорить сам процесс диагностирования. Однако разный уровень готовности разрабатываемых алгоритмов машинного обучения требует дополнительных исследований, которые подтвердили бы эффективность их применения в профессиональных областях, например, при обследовании сооружений, что обосновывает актуальность данного исследования. Объектом исследования данной статьи являлись модели компьютерного зрения семейства YOLO, способные определять различные классы дефектов. Целью исследования стало обучение алгоритмов детекции YOLOv5, YOLOv8 и YOLO11 и сравнительный анализ скорости и точности обработки ими данных на примере дефектов сварных швов. Результаты экспериментальных исследований показывают, что применение последней версии модели не приводит к заметным

улучшениям качества детекции дефектов по сравнению с предыдущими версиями. Практическая значимость исследования заключается в том, что представленные в работе результаты позволяют выполнить оценку целесообразности использования новой модели YOLO11 для обнаружения дефектов на примере радиографических снимков. На основе проведенных экспериментов исследователи, использующие методы компьютерного зрения для контроля качества сварных швов, могут принять взвешенное решение о том, стоит ли применять эту модель или же использовать предыдущие версии алгоритмов.

Ключевые слова: машинное обучение, управление жизненным циклом, YOLO, радиография, предикативная эксплуатация

INTRODUCTION

According to Rosstat, the average wear and tear of utility networks in the country corresponds to an unsatisfactory technical condition. An increase in emergency situations is recorded, leading to a decrease in the quality of utilities, loss of resources, deterioration of the environmental situation and an increase in operating costs. Consequently, the quality of diagnostic measures during construction, repair, as well as during operational control directly determines the safety and uninterrupted functioning of the country's utility infrastructure. Particular attention should be paid to quality control of butt joints, where stress is most often concentrated, sealing elements wear out, and corrosion occurs. In our country, pipelines with welded seams are widely used, not only in utility infrastructure systems, but also for transporting gas, oil and other aggressive liquids. Given the difficult operating conditions, welded seams become one of the main sources of problems leading to accidents with serious socio-economic consequences.

To detect weld defects and prevent accidents, various methods of both visual and instrumental non-destructive testing are used [1-3]. The radiographic testing method has high accuracy and reliability of results compared to other methods. Defects in welds are determined during the study of welded joint images. However, this work is characterized by high labor intensity; therefore, automated radiographic scanning methods of welded joints are widely used in production. In this case, the main difficulty lies in processing and interpreting the radiography results, which requires exceptional attention and concentration of the specialist checking the images. Some defects may be barely noticeable even in high-quality images. In this case, there is a high probability that a non-destructive testing laboratory specialist will miss the defect.

Therefore, one of the ways to increase the reliability of weld diagnostics results, as well as the speed of data processing on radiographic images, is to use computer vision models to detect defects [4-6]. The latest scientific achievements in the field of artificial intelligence and parallel computing open up new opportunities for the use of computer vision models in various fields [7, 8], including construction and operation, to detect defects in welds [9, 10]. At the same time, different levels of technological readiness and market maturity of high-tech areas, as well as gaps in legislative regulation dictate the need to study emerging new products from the point of view of their effectiveness for practical application in the real sector of the economy.

Therefore, the objects of this study were the models of the well-known YOLO computer vision architecture, in particular YOLOv5, YOLOv8 and YOLO11. The hypothesis of the study was the assumption based on the developer’s data about the increase in the efficiency of the YOLO11 model compared to previous versions, considered on the example of processing weld inspection materials. The goal of the study was to perform a comparative analysis of the accuracy and speed of the YOLO family of models in solving the problem of detecting defects in welds on X-ray images. To achieve this goal, a list of research tasks was formed:

1) Preparing a training and test set of images with defects in welds;
2) Conducting an experiment to train YOLOv5, YOLOv8 and YOLO11 models on the training dataset;
3) Processing the results of the experiment and comparing the results of the models on the test dataset using standard metrics for assessing the quality of their work.

Literature Review

Improvement of the automated quality control system for welded joints can be based on both machine learning methods [11-13] and methods based on pixel brightness and geometric characteristics of welds [9, 14]. A review of studies of the most well-known machine learning algorithms allows us to assess their advantages and disadvantages for solving specialized problems. For example, the use of the SVM machine learning algorithm allows us to achieve fairly high accuracy, but small defects often remain undetected by the model [15]. The use of the AdaBoost algorithm has shown that it does not allow us to achieve high accuracy in detecting construction defects [16]. With the development of deep learning, convolutional models have increasingly been used to detect defects in welds [17, 18]. Quite high accuracy is observed when using the Faster R-CNN model, but the low image processing speed (7-10 frames per second) does not allow the model to be used to process a video stream [13, 19].

The YOLO deep learning model debuted in 2015 and has gained widespread adoption due to its high detection speed and the large number of versions released fairly quickly. The main difference between YOLO models and previous generation solutions [13, 19] is that they solve the detection problem in one stage. The model determines a set of bounding boxes based on the original image, while older approaches relied on pre-selecting candidate boxes from the image before feeding them to the model.

The model's operating principle is based on image processing by three consecutive blocks: Backbone, Neck, and Head [20]. Backbone transforms the image into a set of feature maps, which represent visual patterns of different levels. Neck simultaneously analyzes high-level and low-level patterns containing spatial and semantic information and obtains features for the final prediction of bounding boxes. The Head block is responsible for predicting bounding boxes and objects in them based on the features extracted by the Neck block. Each block, in turn, consists of standard layers used in computer vision: convolution layers (Conv) with batch normalization (BatchNorm) and activation functions (SiLU, Sigmoid, Softmax, etc.), pooling layers (MaxPooling), residual connections, etc.

And if the first YOLOv1 model solved only the detection problem, then subsequent models began to recognize more classes, with each modification the architecture of the model became more complex [19, 21-24]. Thus, in the YOLOv5 model [20] the emphasis was placed on optimizing computing resources, so it does not achieve such a high quality as its predecessors, but it works much faster, which allowed it to be used in real time.

In the YOLOv8 model, the architecture was optimized towards compactness. A significant change is the division of each branch of the Head block into two parts (Decoupled Head), one of which predicts the coordinates of the bounding box, and the other the class of the object located inside the box. This architectural change improves the convergence of the model and increases the quality of predictions. In [13, 25], a study of the YOLOv8 model for detecting defects in X-ray images was conducted, in [26], a technique for improving the quality of detection of this model was proposed.

The new YOLO11 model was presented in October 2024 [27, 28]. Modifications in this version affected both the optimization of computing blocks and the addition of quality improvement mechanisms [29]. A significant innovation was the addition of a new C2PSA (Cross Stage Partial with Spatial Attention) block with a spatial attention mechanism. Potentially,

due to focusing on the most significant areas of the image, this block should increase the accuracy of object detection. For the latest version of the YOLO11 model, no studies were conducted on the quality of its operation in detecting defects in welded seams on X-ray images, which justifies the relevance of this study.

METHODS

Dataset

The dataset provided by the authors [19] was used to train the neural networks. The dataset is available at *https://github.com/huangyebiaoke/steel-pipe-weld-defect-detection* and is distributed under the GPL-3.0 license, which permits the use of data with a link to the original source. The dataset contains 3408 X-ray images of defects in pipeline welds.

The images represent 8 types of defects: slag inclusion, weld pores, crack, undercut, and build-up, lack of weld fusion, weld cavity, and arc rupture. Examples of images of each type of defect are shown in Fig. 1.

The number of images of each type of defect is given in Table 1. The weld seam in the images has different inclination to the image boundaries and different zoom levels. All images in the data set are marked.

Since training neural networks requires a large amount of data, the original data was supplemented with images obtained by transforming the original images, which is a common practice in training computer vision models.

The following transformations were used: horizontal and vertical reflection, rotation relative to the central point of the image within (-15°…+15°), brightness change in the range (-15%…+15%), and noise introduction for up to 1.05% of the image pixels. Several transformations can be applied to one image at once. Transformations preserve the original structure and content of images, since the changes are simple geometric and color transformations. Such image processing allows increasing the diversity in the dataset while preserving key visual features for training the model, which improves its ability to recognize and process real data, since it becomes more resistant to "extra" details in the image. After the addition, the dataset size was 7794 images. The Roboflow service was used to transform the images.

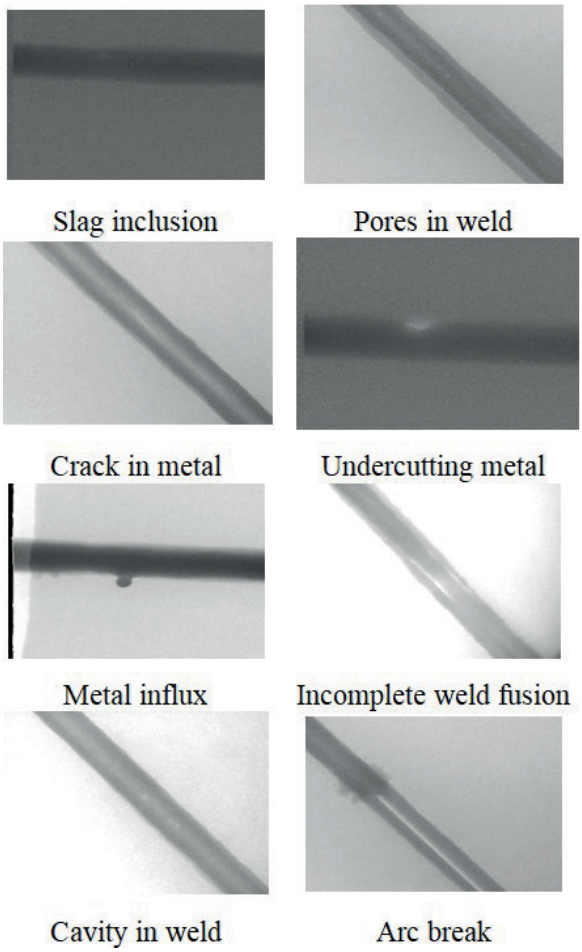


Figure 1. Examples of weld defects in images

Table 1. Number of images in the dataset for each type of defect

Name of defect	Number of images
Pores in weld	1339
Undercutting metal	35
Arc break	531
Crack in metal	119
Cavity in weld	613
Metal influx	219
Slag inclusion	136
Incomplete weld fusion	416

To speed up model training, the number of channels in the images was reduced from three (red, green and blue) to one (grayscale), which allows for faster model training without losing quality, since all images in the set are black and white. Also, to increase the speed of model training, the image size was reduced to 640×640 pixels.

Configuration of the experimental stand

The online services Google Colab and Roboflow were used to train the models, one Tesla T4 graphics processor with 16 GB of RAM was used. The following libraries were used to train the models: Ultralytics, Roboflow, IPython.

Three models were trained in the study: YOLOv5, YOLOv8 and YOLO11. YOLOv5 was trained to correctly compare the results of the models due to the lack of accurate data on image transformations in the training sample in the study [19]. The following versions of the models were selected due to the close number of parameters: YOLOv5m – 21.2 million, YOLOv8m – 25.9 million, YOLO11l – 25.3 million.

When training the models, the data were divided into training and validation sets in the following proportions: 10.4:1. The number of images in each set was: 6987 images for training, 672 images for validation, and 335 images for testing the model. The images were divided into groups in such a way that each group contained images of each type of defect. Each model was trained for 32 epochs (complete training cycles for all data). This number of epochs was chosen because it corresponded to the maximum duration of a session in the Google Colab service. The AdamW optimizer [30] was used for training. The parameters used in training the models are given in Table 2.

Table 2. Values of model parameters during training

Parameter	Value
learning rate	0.000833
momentum	0.9
batch size	16
warmup steps	3
dropout	0.0

Evaluation criteria

To determine the accuracy and completeness, the following object detection outcomes are introduced:

True Positive (*TP*) – correctly performed detection, i.e. the frame suggested by the model quite accurately coincides with the real frame established during image marking. The criterion for coincidence is the *IoU* (Intersection over union) area intersection coefficient:

$$IoU = \frac{Intersection\ area}{Union\ area} \tag{1}$$

where *Intersection area* is the area of intersection of the true and predicted frames; *Union area* is the area of union of the true and predicted frames.

At an *IoU* threshold of 50%, a model prediction is classified as *True Positive* if the calculated *IoU* value for that prediction is at least 50%.

False Positive (*FP*) – incorrectly performed detection, the model predicted an object where it does not exist, or the true and predicted frames do not match well enough and the *IoU* is below the threshold.

False Negative (*FN*) – incorrectly performed detection, the model did not detect the object in the image.

Next, the precision and recall indicators are calculated. Precision shows what proportion of objects predicted by the model are actually correct:

$$Precision = \frac{TP}{TP + FP} \tag{2}$$

where *TP* is the number of true positives; *FP* is the number of false positives.

Recall measures what proportion of all real objects in the image were correctly detected by the model:

$$Recall = \frac{TP}{TP + FN} \tag{3}$$

where *FN* is the number of missed objects in the image.

Next, the average precision for each defect class is calculated – Average Precision (*AP*). Among the class precisions, there is the mean Average Precision (*mAP*):

$$mAP = \frac{1}{k}\sum_{i}^{k} Precision_i \cdot Recall_i \qquad (4)$$

where *k* is the number of classes.

The standard metrics *mAP50* and *mAP50-95* were chosen as criteria for evaluating the performance of computer vision models. *mAP50* is the average accuracy among all classes, which is calculated at a fixed threshold of the *IoU* intersection rate ≥ 50%. *mAP50-95* is the average accuracy among all classes in the *IoU* range from 50% to 95% with a step of 5%. These indicators allow us to determine the ability of the model to detect objects of different classes, taking into account the accuracy and completeness of detection.

Using these metrics allows us to objectively compare models by assessing both their ability to accurately determine both the boundaries of a defect and the total number of correct and incorrect predictions.

RESULTS AND DISCUSSION

Comparison of model indicators

Based on the results of training the models over 32 epochs, graphs of changes in mAP50 and mAP50-95 were constructed on the validation sample (see Fig. 2 and 3).

Since in practice it is advisable to detect defects in welds at an *IoU* threshold of 50% or less, a more objective metric for the operation of models is *mAP50*. For comparison of models, metrics determined on the validation sample are provided, since it was not used in training.

Analyzing the graphs, we can conclude that after training, all models show very close results, while the *mAP* fluctuations during training are the smallest for the YOLO11 model. Also, the *mAP50* graph indicates that 32 epochs are sufficient for training and comparing models, since after the 25th epoch, there is a slight increase in the metric. Among the models considered, the highest defect detection speed was achieved by the YOLOv5 model. A comparison of the models' performance speed is given in Table 3.

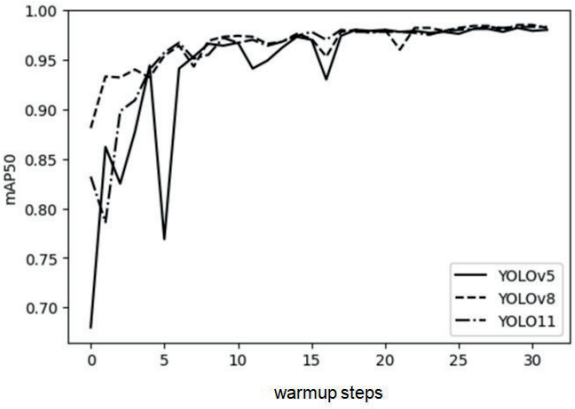


Figure 2. mAP50 values during validation during training

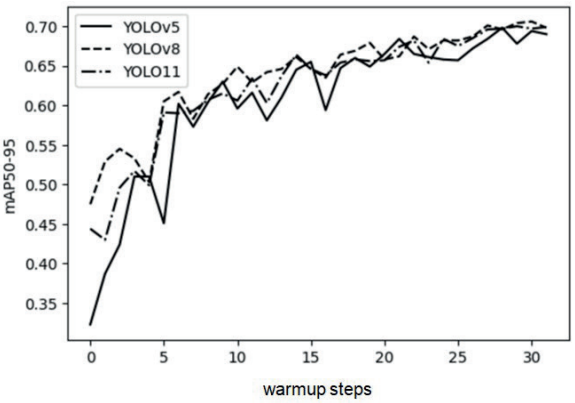


Figure 3. mAP50-95 values during validation during training

Table 3. Model operating speed

Model	Image processing time, msec	Processing frequency, images/sec
YOLOv5	16.4	61.0
YOLOv8	27.3	33.6
YOLO11	24.8	40.4

All models demonstrate an image processing rate of more than 30 images per second, which

indicates the possibility of using any of them for video stream processing. The optimization of the YOLO11 model compared to YOLOv8 allows achieving a higher image processing rate. Table 4 shows the metrics calculated for the best-performing YOLO11 model training epoch.

Table 4. Best validation scores for the YOLO11 model

Name of defect (identifier)	*AP50*	*AP50-95*
Pores in weld (0)	0.933	0.437
Undercutting metal (1)	0.995	0.583
Arc break (2)	0.975	0.909
Crack in metal (3)	0.970	0.636
Cavity in weld (4)	0.979	0.812
Metal influx (5)	0.995	0.742
Slag inclusion (6)	0.995	0.662
Incomplete weld fusion (7)	0.994	0.749

Analyzing the results of the experiment, we can note the low accuracy of detection of pores in the weld, which may be due to their small size and low image clarity. For other defects, fairly close values of detection completeness and high accuracy are observed.

Figures 4-7 show examples of defect detection by the YOLO11 model in images from the test sample. In the upper left part of the frame around the defect in the image, the defect identifier (its number from 0 to 7) and the confidence of the model in determining this defect are indicated. It can be noted that the model quite clearly determines the position and boundaries of defects.

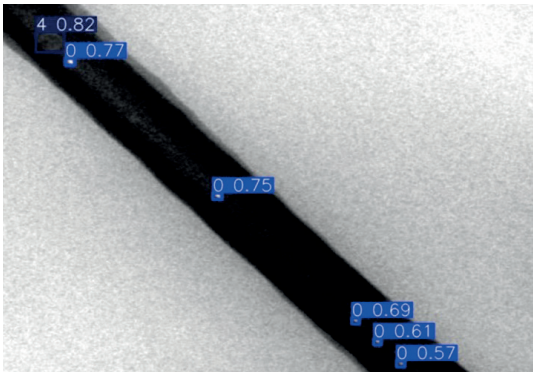


Figure 4. Detection by the model of a cavity (4) and pores in weld (0)

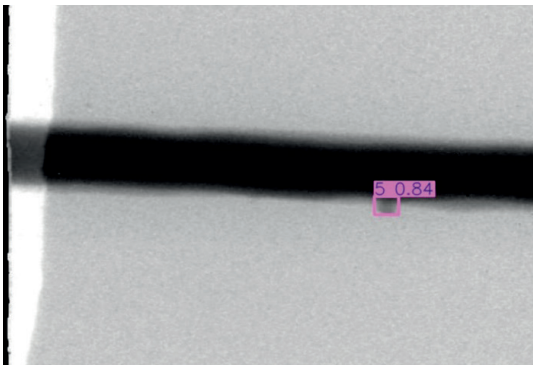


Figure 5. Detection of metal influx (5) by the model

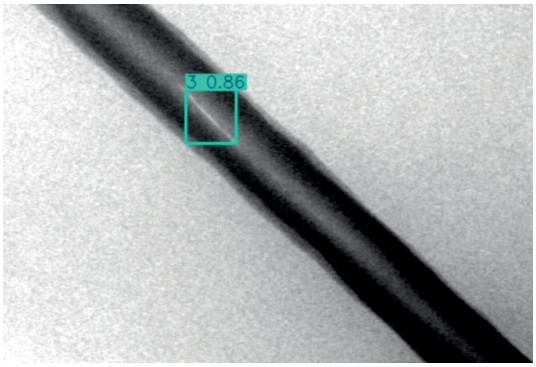


Figure 6. Detection of a crack in metal (3) by the model

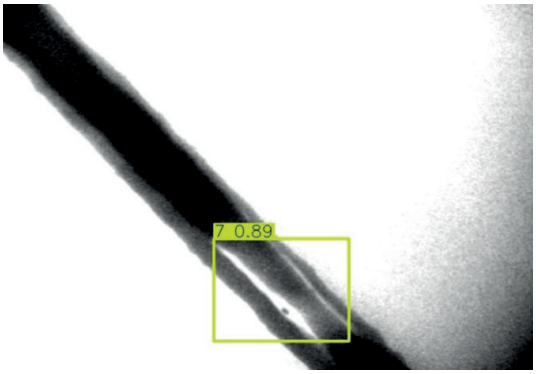


Figure 7. Detection of Incomplete weld fusion (7) by the model

In Tables 5 and 6 shows a comparison of the training results of the models.

The YOLOv8 model showed the greatest stability in class recognition. The training results show a more balanced detection of defects, since there is not such a big difference between the most poorly identified defects (pores in the weld and cracks) and the rest of the defects.

Table 5. Comparison of models by class recognition stability

Name of defect	*AP50*		
	YOLOv5	YOLOv8	YOLO11
Pores in weld	0.935	0,969	0.933
Undercutting metal	0.995	0.986	0.995
Arc break	0.986	0.983	0.975
Crack in metal	0.977	0.954	0.970
Cavity in weld	0.989	0.978	0.979
Metal influx	0.995	0.995	0.995
Slag inclusion	0.995	0.995	0.995
Incomplete weld fusion	0.994	0.995	0.994

Table 6. Comparison of mAP50 metrics based on model training results

Model	*mAP50*
YOLOv5	0.983
YOLOv8	0.985
YOLO11	0.979

Having analyzed the results of model training, we can conclude that the YOLO11 version shows slightly worse results, demonstrating the lowest *mAP50* value. The YOLOv5 and YOLO11 models are similar in *mAP50* metric values for each type of defect. The worst results shown by YOLO11 compared to other models may be due to the fact that this model relies on a spatial attention mechanism when forming a prediction, which allows it to focus on the most important areas of the image. In our case, it is impossible to distinguish the foreground or background in the image, and the defect can be anywhere along the seam. Also, the low quality of the model can be affected by modifications to the architecture aimed at increasing its speed.

CONCLUSION

1) Weld defect images were prepared for training the models, and geometric and color transformations were performed on the images to increase the diversity in the data set;
2) YOLOv5, YOLOv8 and YOLO11 models were trained for 32 epochs;
3) After training the models, a comparison of their performance results was carried out based on the standard metrics *mAP50*, *mAP50-95*, and a comparison of the image processing speed of each model was also performed.
The hypothesis put forward in the study, which is that the YOLO11 model will demonstrate better results in processing weld defect images than its predecessors, is partially refuted. The study shows that the best *mAP50* indicator in defect detection is achieved by the YOLOv8 algorithm. At the same time, the YOLO11 algorithm works slightly worse than other models, which may be due to the fact that the improvements made in the model cannot realize their potential in weld defect images. It is worth noting that the YOLO11 algorithm works 9% faster than the YOLOv8 algorithm.
Quality control of welded joints is carried out not only at the construction stage, but also at the operation stage. Regular automated control of welded joints can allow more accurate determination of the mechanism of change in the operational parameters of pipelines. Systematic acquisition of data on corrosion and defect formation in pipelines and their processing using effective computer vision algorithms will allow a transition to predictive operation, forecasting the service life of equipment and structures.

REFERENCES

1. **Shaloo M., Schnall M., Klein T., Huber N., Reitinger B.** (2022) A Review of Non-Destructive Testing (NDT) Techniques for Defect Detection: Application to Fusion Welding and Future Wire Arc Additive Manufacturing Processes. *Materials*, vol. 15, no. 10, pp. 3697. DOI: 10.3390/ma15103697

2. **Zhukovsky E.A., Khoroshev V.N.** (2005) Modern equipment for non-destructive quality control of welded joints of pipelines by radiographic method. *Russian journal of heavy machinery*, no. 9, pp. 8–10.
3. **Kazantsev I., Lemahieu I., Salov G.I., Denys R.** (2002) Statistical detection of defects in radiographic images in nondestructive testing. *Signal Processing*, vol. 82, no. 5, pp. 791–801. DOI: 10.1016/S0165-1684(02)00158-5
4. **Valavanis I., Kosmopoulos D.** (2010) Multiclass defect detection and classification in weld radiographic images using geometric and texture features. *Expert. Syst. Appl*., vol. 37, Is. 12, pp. 7606–7614. DOI: 10.1016/j.eswa.2010.04.082
5. **Boaretto N., Centeno T.M.** (2017) Automated detection of welding defects in pipelines from radiographic images DWDI. *NDT and Int.*, vol. 86, pp. 7–13. DOI: 10.1016/j.ndteint.2016.11.003
6. **Hou W., Zhang D., Wei Y., Guo J., Zhang X.** (2020) Review on computer aided weld defect detection from radiography images. *Appl. Sci.*, vol. 10(5), p. 1878. DOI: 10.3390/app10051878
7. **Garisto D.** (2024) How cutting-edge computer chips are speeding up the AI revolution. *Nature*, vol. 630, no. 8017, pp. 544–546. DOI: 10.1038/d41586-024-01544-0
8. **Andriyanov N.A., Dementiev V.E., Tashlinskii A.G.** (2022) Detection of objects in the images: from likelihood relationships towards scalable and efficient neural networks. *Computer Optics,* vol. 46, Is. 1, pp. 139–159. DOI: 10.18287/2412-6179-CO-922
9. **Yemelyanova M.G., Smailova S.S., Baklanova O.E.** (2023) Detection of surface defects in welded joints during visual inspections using machine vision methods. *Computer optics*, vol. 47, no. 1, pp. 112–117. DOI: 10.18287/2412-6179-CO-1137
10. **Fan X., Gao X., Liu G., Ma N., Zhang Y.** (2021) Research and prospect of welding onitoring technology based on machine vision. J. *Adv. Manuf. Technol.*, vol. 115, pp. 3365–3391. DOI: 10.1007/s00170-021-07398-4
11. **Gordeev D.V.** (2018) Application of machine vision for searching and detection of surface defects of weld seam. *Juvenis Scientia*, no. 3. pp. 4–5.
12. **Praveen Kumar R., Deivanathan R., Jegadeeshwaran R.** (2021) Welding defect identification with machine vision system using machine learning. *J. of Phys.: Conf. Ser.*, vol. 1716, p. 12023. DOI: 10.1088/1742-6596/1716/1/012023
13. **Sun J., Li C., Wu X.J., Palade V., Fang W.** (2019) An effective method of weld defect detection and classification based on machine vision. *IEEE Trans. Industr. Inform.*, vol. 15, no. 12, pp. 6322–6333. DOI: 10.1109/TII.2019.2896357
14. **Muravyov S.V., Pogadaeva E.Y.** (2020) Computer-aided recognition of defects in welded joints during visual inspections based on geometric attributes. *Russian Journal of Nondestructive Testing*, vol. 56, no. 3, pp. 259–267. DOI: 10.1134/S1061830920030055
15. **Shao J., Shi H., Du D., Wang L., Cao H.** (2011) Automatic weld defect detection in real-time X-ray images based on support vector machine. *Proc. 4th Int. Congr. Image Signal Process*., vol. 4, pp. 1842–1846. DOI: 10.1109/CISP.2011.6100637
16. **Duan F., Yin S., Song P., Zhang W., Zhu C., Yokoi H.** (2019) Automatic Welding Defect Detection of X-Ray Images by Using Cascade AdaBoost With Penalty Term. *IEEE Access*, vol. 7, pp. 125929–125938. DOI: 10.1109/ACCESS.2019.2927258
17. **Yaping L., Weixin G.** (2019) Research on X-ray welding image defect detection based on convolution neural network. *IOP Conf. Series: J. Phys. Conf. Ser.*, vol. 1237, Is. 3, p. 032005. DOI 10.1088/1742-6596/1237/3/032005
18. **Wang X., He F., Huang X.** (2024) A new method for deep learning detection of

defects in X-ray images of pressure vessel welds. *Sci Rep*., vol. 14, pp. 6312. DOI: 10.1038/s41598-024-56794-9

19. **Yang D., Cui Y., Yu Z., Yuan H.** (2021) Deep Learning Based Steel Pipe Weld Defect Detection. *Applied Artificial Intelligence*, vol. 35, no. 15, pp. 1237–1249. DOI:10.48550/arXiv.2104.14907
20. **Terven J., Córdova-Esparza D.-M., Romero-González J.-A.** (2023) A Comprehensive Review of YOLO Architectures in Computer Vision: From YOLOv1 to YOLOv8 and YOLO-NAS. *Machine Learning and Knowledge Extraction*, vol. 5(4), pp. 1680–1716. DOI: 10.3390/make5040083
21. **Cherkasov S., Ivanov M., Ivanov A.** (2023) Detection of Defects in Welded Joints Based on Data from the Computer Vision System Using YOLOv5. *Int. Ural Conf. on Electrical Power Eng. (UralCon)*, Magnitogorsk, Russian Federation, pp. 780–784, DOI: 10.1109/UralCon59258.2023.10291074
22. **Guo J., Dong L., Xu H.** (2024) Welding Image Defect Detection Based on YOLOv5. *4th Int. Conf. on Neural Networks, Information and Communication (NNICE)*, Guangzhou, China, pp. 469–472. DOI: 10.1109/NNICE61279.2024.10498851
23. **Gao A., Fan Z., Li A., Le Q., Wu D., Du F.** (2023) YOLO-Weld: A Modified YOLOv5-Based Weld Feature Detection Network for Extreme Weld Noise. *Sensors*, vol. 23(12), pp. 5640. DOI: 10.3390/s23125640
24. **Pan K., Hu H., Gu P.** (2023) WD-YOLO: A More Accurate YOLO for Defect Detection in Weld X-ray Images. *Sensors*, vol. 23(21), pp. 8677. DOI: 10.3390/s23218677
25. **Zhou J., Zhang W., Sui X., Chen Y.** (2024) Welding defect detection based on YOLOv8. *J. Phys.: Conf. Ser.,* vol. 2816, p. 012045. DOI: 10.1088/1742-6596/2816/1/012045
26. **Chen J., Liu J.** (2023) Enhancing Welding Defect Detection: An Improved YOLOv8 Model with Feature Augmentation and Scale Fusion. *IEEE 11th Joint Int. Inf. Tech. and Artificial Intell. Conf. (ITAIC),* Chongqing, China, pp. 1619–1622. DOI: 10.1109/ITAIC58329.2023.10408771
27. **Sulake N.R.** (2025) A Comprehensive Guide to YOLOv11 Object Detection. URL:https://www.analyticsvidhya.com/blog/2024/10/yolov11-object-detection/
28. **Ultralytics.** (2025) Ultralytics YOLO11. URL:https://docs.ultralytics.com/ru/models/yolo11
29. **Khanam R., Hussain M.** (2024) YOLOv11: An Overview of the Key Architectural Enhancements. *eprint arXiv*, DOI: 10.48550/arXiv.2410.17725
30. **Loshchilov I., Hutter F.** (2019) Decoupled Weight Decay Regularization. *ICLR*, DOI: 10.48550/arXiv.1711.05101

СПИСОК ЛИТЕРАТУРЫ

1. **Shaloo M., Schnall M., Klein T., Huber N., Reitinger B.** A Review of Non-Destructive Testing (NDT) Techniques for Defect Detection: Application to Fusion Welding and Future Wire Arc Additive Manufacturing Processes // Materials. 2022. vol. 15. № 10. p. 3697. DOI: 10.3390/ma15103697
2. **Жуковский Е.А., Хорошев В.Н.** Современная аппаратура для неразрушающего контроля качества сварных соединений трубопроводов радиографическим методом // Тяжелое машиностроение. 2005. № 9. С. 8–10.
3. **Kazantsev I., Lemahieu I., Salov G.I., Denys R.** Statistical detection of defects in radiographic images in nondestructive testing // Signal Processing. 2002. vol. 82. № 5. pp. 791–801. DOI: 10.1016/S0165-1684(02)00158-5
4. **Valavanis I., Kosmopoulos D.** Multiclass defect detection and classification in weld

radiographic images using geometric and texture features // Expert. Syst. Appl. 2010. vol. 37. Is. 12. pp. 7606–7614. DOI: 10.1016/j.eswa.2010.04.082
5. **Boaretto N., Centeno T.M.** Automated detection of welding defects in pipelines from radiographic images DWDI // NDT and Int. 2017. vol. 86: pp. 7–13. DOI: 10.1016/j.ndteint.2016.11.003
6. **Hou W., Zhang D., Wei Y., Guo J., Zhang X.** Review on computer aided weld defect detection from radiography images // Appl. Sci. 2020. vol. 10(5): p. 1878. DOI: 10.3390/app10051878
7. **Garisto D.** How cutting-edge computer chips are speeding up the AI revolution // Nature. 2024. T. 630. № 8017. C. 544–546. DOI: 10.1038/d41586-024-01544-0
8. **Andriyanov N.A., Dementiev V.E., Tashlinskii A.G.** Detection of objects in the images: from likelihood relationships towards scalable and efficient neural networks // Computer Optics. 2022. vol. 46. Is. 1. pp. 139–159. DOI: 10.18287/2412-6179-CO-922
9. **Емельянова М.Г., Смаилова С.С., Бакланова О.Е.** Обнаружение поверхностных дефектов сварных соединений при визуальном контроле методами машинного зрения // Компьютерная оптика. 2023. Т. 47. № 1. С. 112–117. DOI: 10.18287/2412-6179-CO-1137
10. **Fan X., Gao X., Liu G., Ma N., Zhang Y.** Research and prospect of welding monitoring technology based on machine vision // J. Adv. Manuf. Technol. 2021. vol. 115. pp. 3365–3391. DOI: 10.1007/s00170-021-07398-4
11. **Гордеев Д.В.** Применение машинного зрения для поиска и обнаружения поверхностных дефектов сварных соединений // Juvenis Scientia. 2018. № 3. С. 4–5.
12. **Praveen Kumar R., Deivanathan R., Jegadeeshwaran R.** Welding defect identification with machine vision system using machine learning // J. of Phys.: Conf. Ser. 2021. vol. 1716. p. 12023. DOI: 10.1088/1742-6596/1716/1/012023
13. **Sun J., Li C., Wu X.J., Palade V., Fang W.** An effective method of weld defect detection and classification based on machine vision // IEEE Trans. Industr. Inform. 2019. vol. 15. no. 12: pp. 6322–6333. DOI: 10.1109/TII.2019.2896357
14. **Muravyov S.V., Pogadaeva E.Y.** Computer-aided recognition of defects in welded joints during visual inspections based on geometric attributes // Russian Journal of Nondestructive Testing. 2020. vol. 56. no. 3. pp. 259–267. DOI: 10.1134/S1061830920030055
15. **Shao J., Shi H., Du D., Wang L., Cao H.** Automatic weld defect detection in real-time X-ray images based on support vector machine // Proc. 4th Int. Congr. Image Signal Process. 2011. vol. 4. pp. 1842–1846. DOI:10.1109/CISP.2011.6100637
16. **Duan F., Yin S., Song P., Zhang W., Zhu C., Yokoi H.** Automatic Welding Defect Detection of X-Ray Images by Using Cascade AdaBoost With Penalty Term // IEEE Access. 2019. vol. 7. pp. 125929–125938. DOI: 10.1109/ACCESS.2019.2927258
17. **Yaping L., Weixin G.** Research on X-ray welding image defect detection based on convolution neural network // IOP Conf. Series: J. Phys. Conf. Ser. 2019. vol. 1237. Is. 3. p. 032005. DOI 10.1088/1742-6596/1237/3/032005
18. **Wang X., He F., Huang X.** A new method for deep learning detection of defects in X-ray images of pressure vessel welds // Sci Rep. 2024. vol. 14. pp. 6312. DOI: 10.1038/s41598-024-56794-9
19. **Yang D., Cui Y., Yu Z., Yuan H.** Deep Learning Based Steel Pipe Weld Defect Detection // Applied Artificial Intelligence. 2021. vol. 35. no. 15. pp. 1237–1249. DOI:10.48550/arXiv.2104.14907
20. **Terven J., Córdova-Esparza D.-M., Romero-González J.-A.** A Comprehensive

Review of YOLO Architectures in Computer Vision: From YOLOv1 to YOLOv8 and YOLO-NAS // Machine Learning and Knowledge Extraction. 2023. vol. 5(4). pp. 1680–1716. DOI: 10.3390/make5040083
21. **Cherkasov S., Ivanov M., Ivanov A.** Detection of Defects in Welded Joints Based on Data from the Computer Vision System Using YOLOv5 // Int. Ural Conf. on Electrical Power Eng. (UralCon), Magnitogorsk, Russian Federation. 2023. pp. 780–784. DOI: 10.1109/UralCon59258.2023.10291074
22. **Guo J., Dong L., Xu H.** Welding Image Defect Detection Based on Yolov5 // 4th Int. Conf. on Neural Networks, Information and Communication (NNICE), Guangzhou, China. 2024. pp. 469–472. DOI: 10.1109/NNICE61279.2024.1049885
23. **Gao A., Fan Z., Li A., Le Q., Wu D., Du F.** YOLO-Weld: A Modified YOLOv5-Based Weld Feature Detection Network for Extreme Weld Noise // Sensors. 2023. vol. 23(12). pp. 5640. DOI: 10.3390/s23125640
24. **Pan K., Hu H., Gu P.** WD-YOLO: A More Accurate YOLO for Defect Detection in Weld X-ray Images // Sensors. 2023. vol. 23(21). pp. 8677. DOI: 10.3390/s23218677
25. **Zhou J., Zhang W., Sui X., Chen Y.** Welding defect detection based on YOLOv8 // J. Phys.: Conf. Ser., 2024. vol. 2816. p. 012045. DOI: 10.1088/1742-6596/2816/1/012045
26. **Chen J., Liu J.** Enhancing Welding Defect Detection: An Improved YOLOv8 Model with Feature Augmentation and Scale Fusion // IEEE 11th Joint Int. Inf. Tech. and Artificial Intell. Conf. (ITAIC). Chongqing, China. 2023. pp. 1619–1622. DOI: 10.1109/ITAIC58329.2023.10408771
27. **Sulake N.R.** A Comprehensive Guide to YOLOv11 Object Detection. 2025. URL:https://www.analyticsvidhya.com/blog/2024/10/yolov11-object-detection/
28. **Ultralytics.** Ultralytics YOLO11. 2025. URL:https://docs.ultralytics.com/ru/models/yolo11
29. **Khanam R., Hussain M.** YOLOv11: An Overview of the Key Architectural Enhancements // eprint arXiv. 2024. DOI: 10.48550/arXiv.2410.17725
30. Loshchilov I., Hutter F. Decoupled Weight Decay Regularization // ICLR, 2019. DOI: 10.48550/arXiv.1711.05101

Marina Evgen'evna Dement'eva - PhD in Technical Sciences, Associate Professor, Assistant Professor Department of Housing and Utilities Sector, National Research Moscow State University of Civil Engineering (MGSU), 26, Yaroslavskoe shosse, Moscow, 129337, Russia, 7dem@mail.ru, +7 916 353 18 31

Марина Евгеньевна Дементьева – кандидат технических наук, доцент, доцент кафедры Жилищно-коммунального комплекса, Федеральное государственное бюджетное образовательное учреждение высшего образования «Национальный исследовательский Московский государственный строительный университет» (НИУ МГСУ), д. 26, Ярославское шоссе, г. Москва, 129337, Россия, 7dem@mail.ru, +7 916 353 18 31

DOI:10.22337/2587-9618-2026-22-1-86-91

SIMULATION OF THE OPERATION OF A PRESSURE PIPELINE WITH AN INTERNAL LINING OF A PROTECTIVE COATING

Vladimir A. Orlov, Sergey P. Zotkin, Maria A. Bolshakova
National Research Moscow State University of Civil Engineering, Moscow, RUSSIA

Abstract. The article presents the results of alternative methods for determining the hydraulic characteristics of a deteriorated pressure pipeline with a Subcote FLP spray-on protective coating applied to its inner surface. The results were processed using automated programs, with an ultimate goal of determining and comparing a number of hydraulic characteristics, resulting in energy indicators of pipeline's performance during water transportation. Approaches are presented for identifying the dynamics of possible transformations of certain pipeline hydraulic parameters, specifically, hydraulic friction coefficients and equivalent roughness, when using the studied protective coating after its service over a certain time interval and with changing ambient temperature conditions. Dependencies for changes in these coefficients, and their impact on the pipeline's performance energy indicators during long-distance water transportation were obtained by calculations.

Keywords: pipelines, coatings, hydraulic indicators, light imaging, mathematical modeling, temperature parameters, energy saving

МОДЕЛИРОВАНИЕ РАБОТЫ НАПОРНОГО ТРУБОПРОВОДА С ВНУТРЕННЕЙ ОБЛИЦОВКОЙ ЗАЩИТНЫМ ПОКРЫТИЕМ

Владимир А. Орлов, Сергей П. Зоткин, Мария А. Большакова
Национальный исследовательский Московский государственный строительный университет, г. Москва, РОССИЯ

Аннотация. Приведены результаты альтернативных методов по определению гидравлических характеристик ветхого напорного трубопровода с нанесенным на его внутреннюю поверхность напыляемого защитного покрытия Subcote FLP. Обработка результатов производилась с использованием автоматизированных программ, где конечным итогом являлось определение и сопоставительный анализ ряда гидравлических характеристик с выходом на энергетические показатели работы трубопровода при транспортировке по нему воды. Приведены подходы к выявлению динамики возможной трансформации некоторых гидравлических показателей трубопровода, в частности, коэффициентов гидравлического трения и эквивалентной шероховатости при использовании исследуемого защитного покрытия после его эксплуатации в определенном временном интервале и при изменении температурных условий окружающей среды. Расчетным путем получены зависимости изменения этих коэффициентов и произведена оценка влияния их на энергетические показатели работы трубопровода в период его работы по транспортировке воды на большие расстояния.

Ключевые слова: трубопроводы, защитные покрытия, гидравлические показатели, светоскопия, математическое моделирование, температурные параметры, энергосбережение

INTRODUCTION

Given the significant wear and tear of pipeline networks, where, in particular, according to data from the Ministry of Regional Development, over 40% of water supply networks require prompt repair, the question of the effectiveness of new trenchless repair technologies is becoming extremely relevant [1, 2]. An analysis of global experience in the operation and restoration of utility networks of water supply and sanitation systems shows that the most promising solution to the problem of extending their service life is rehabilitation through the application of internal protective coatings of various types, including polymer spray coatings (PSCs). Unlike metal and

ceramic linings, polymer coatings have a hydrophobic surface, which positively affects the hydrodynamics inside the pipe and prevents the formation of surface contaminants [3]. Based on an analysis of literature sources [4, 5], it can be concluded that such protective coatings are promising materials for pipeline protection.

To demonstrate the effectiveness of various types of polymer protective coatings, as well as to study the possible transformation of their hydraulic properties over time (in particular, the degree of surface roughness), and the impact of temperature conditions on this process, it is necessary to conduct full-scale studies under dynamic conditions using appropriate models and proven methodological approaches. Automated programs are used to speed up calculations and potentially predict the resulting basic hydraulic and energy parameters.

According to available certificates of conformity, protective polymer spray coatings do not alter the composition of the pumped fluid, maintaining a high level of reliability in water supply pipeline networks and reducing the negative impact on the urban environment during repairs. During pipeline rehabilitation using PSCs, despite a layer thickness of only 3–8 mm, it is possible to effectively seal various defects and increase pipeline wear resistance. Thus, the internal surfaces of restored pipelines generally become less rough, which improves the hydraulic characteristics of water supply and wastewater disposal pipeline networks.

METHODS

A steel pipeline coated with a protective Subcote FLP coating applied to its inner surface was used for comprehensive hydraulic studies, including modeling of the parameters under study using automated software and modern light-profiling and profilometry equipment.

Subcote FLP coating has sanitary and epidemiological expert approval No. 77.01.12.P.014303.09.11 dated September 22, 2011, issued by the Moscow Office of the Federal Service for Surveillance on Consumer Rights Protection and Human Wellbeing, permitting its application to the inner surface of pipelines in drinking water systems.

The study involved physical testing (on a large-scale 10-meter-long and a small-scale 1-meter-long test bench) and then mathematical modeling of the pipeline's performance with the protective coating to determine its hydraulic characteristics at the same ambient temperature (20°C) using appropriate automated software [6, 7]. Hydraulic bench testing of the initial protective coating sample on a steel pipeline and processing of the results using automated calculation systems were conducted in the laboratory of the Department of Water Supply and Sanitation on a large-scale pressure rig (Fig. 1). The small-scale gravity rig was made in the form of an open steel inclined trough (gutter) with a nominal diameter of 100 mm with a thin layer of the coating being tested applied to it (Fig. 2), along which a mini-flow of water moved in the form of a lens at the end (Fig. 3) [8].



Figure 1. General view of a large-scale hydraulic test rig with 10 m long pipes with a nominal diameter of 100 mm made of various materials (the fourth pipe from the top is a steel pipe with a protective Subcote FLP coating)

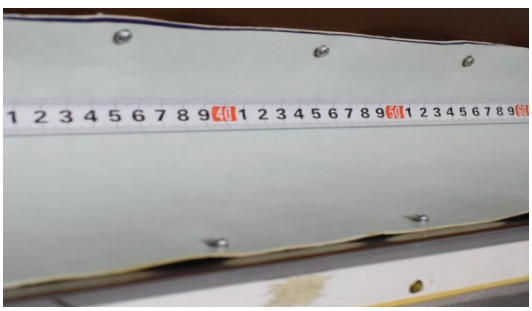


Figure 2. Detail of the top view of a 1 m long open inclined gutter with Subcote FLP coating applied to it

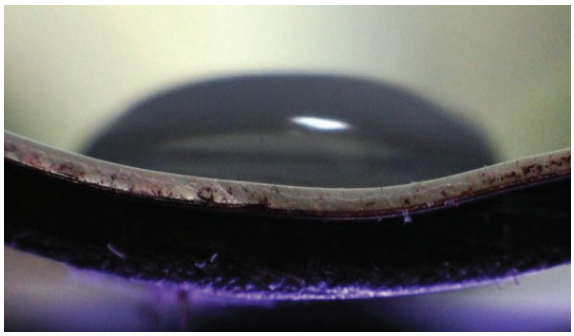


Figure 3. A fragment of the end section of a sloped gutter with a Subcote FLP protective coating and a mini-flow of moving water

To expand the experimental range, i.e., simulating extended water presence duration in pipelines and flumes, as well as elevated ambient temperatures, a special compact setup was developed. It consisted of a cylindrical vessel containing 1 liter of water, mounted on a magnetic stirrer. A rectangular coating sample of specified dimensions was immersed into the vessel and firmly secured. The coating samples were positioned at the periphery of the cylindrical vessel. The angular velocity of the stirrer armature was converted to linear velocity at the sample boundary at the vessel periphery. This design allowed for monitoring potential roughness changes in the protective coating samples during their prolonged immersion in water, and also at different temperatures. It should also be noted that chlorine was added to the water in the cylindrical vessel, providing a disinfectant effect. This allowed for the potential chemical interaction of the resulting chlorides with the test samples to be assessed. Thus, the process of water transportation through a long pipeline was simulated in a cylindrical vessel mounted on a magnetic stirrer, with chlorine consumption analyzed.

In parallel, light (optical) microscopy experiments were conducted on these samples using an Olympus GX53 inverted electron microscope (Japan), which provides high-quality images difficult to achieve using conventional optical microscopy methods.

The roughness of the samples was also studied using a SEITRONIK PSh 8-3 (SS) profilograph-profilometer, which allows roughness parameters to be determined digitally on a microprocessor unit. In both cases, experiments were conducted over different time intervals.

The objectives of the study, when conducting research using the listed above alternative methods, included comparing the obtained hydraulic parameters for identity and the degree of their discrepancy. The final result of the study was the calculation of possible energy losses during water transportation as a result of potential changes in the hydraulic characteristics of the protective coating samples over time. In general, the combination of methods and measuring instruments used made it possible to obtain a preliminary picture of the possible transformation of the hydraulic parameters of protective coatings over time.

RESULTS AND DISCUSSION

Below are the hydraulic test data for each of alternative method and a comparative analysis.

The results of automated processing of hydraulic tests of protective coatings on large and small rigs at an ambient temperature of 20°C showed similar results. Specifically, the average value of the hydraulic friction coefficient λ for the Subcote FLP coating on the large rig was 0.01772, while on the small rig it was 0.0181, i.e., there is a difference of only 2.14%, indicating a high degree of reliability of the obtained results.

Based on electron microscopy and profilometer studies, the following equivalent roughness coefficients ke were obtained:

- 0.03716 mm (light microscopy)
- 0.0386 mm (profilometry).

Using Prandtl's formula (1), the hydraulic resistance coefficients λ were calculated for a pipeline with a Subcote FLP protective coating as follows [9]:

$$\frac{1}{\sqrt{\lambda}} = 2 \cdot \lg \frac{d}{k_e} + 1{,}14 \quad (1)$$

where λ is the hydraulic resistance coefficient of the pipeline; d is the internal diameter of the pipeline with protective coating (mm); ke is the

equivalent roughness coefficient of the pipeline (mm) equal to
- 0.01563 (light microscopy)
- 0.01575 (profilometry).

The difference in the results was only 3.73%.

Thus, the results of experiments on hydraulic test benches and the data from light microscopy and profilometry can be considered reliable for determining the hydraulic friction coefficients and equivalent roughness, where, for example, the discrepancy between the largest absolute value (ke=0.0181 mm) and the smallest (ke=0.0163 mm) did not exceed 13.6%.

When modeling the evolution of hydraulic parameters under tangential water flow conditions in a cylindrical vessel with samples in a prolonged contact with water, the following dependencies for the equivalent roughness coefficient were obtained (Fig. 4).

The graph in Figure 4 clearly demonstrate the decrease in the equivalent roughness coefficient ke: the higher the dose of chlorine introduced and the longer the sample is exposed to the cylindrical vessel, the lower the equivalent roughness value. This trend can be explained, for example, by incrustation, which in this situation should be considered a positive phenomenon, as it ultimately contributes to a reduction in the hydraulic friction coefficient λ by smoothing out microroughness depressions, i.e., roughness peaks.

A reduction in the hydraulic friction coefficient automatically leads to a reduction in energy costs during water transportation through pressure pipelines. This is confirmed by the graphs in Figure 5, where the calculation of electricity consumption E (kW h per year) was carried out using formula (2)

$$E=0,81\cdot Q3\cdot l\cdot \lambda \cdot 24\cdot 365 / (d\ 5\cdot \eta p), \quad (2)$$

where Q is the flow rate of water supplied by the pipeline (m3/s), at which the flow velocity is 1 (m/s); d is the internal diameter of the pipeline (m); l is the length of pipeline section (m) ; λ is the coefficient of hydraulic friction; ηp is the efficiency of the pumping unit (0.95); 24 is the number of hours the pump operates per day (h); 365 is the number of days in a year.

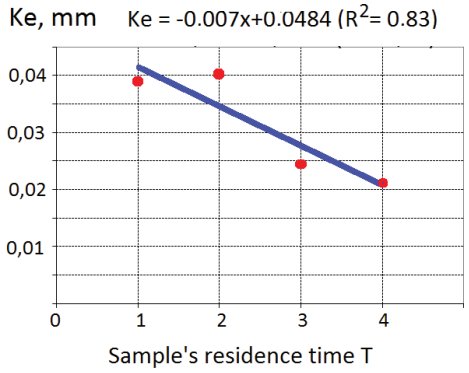


Figure 4. Graph of the change in the equivalent roughness coefficient ke (mm) as a function of the sample's presence time T in a cylindrical vessel with a stirrer (Points along the abscissa axis: 1 - for the initial sample T = 0 min; 2 - after treatment in 167 min with a single dose of chlorine at 0.5 mg/l; 3 - after treatment in 334 min with a single dose of chlorine; 4 - after treatment in 167 min with a double dose of chlorine)

The graph in Figure 5 illustrates the reduction in energy consumption depending on the duration and dose of chlorine introduced into the water.

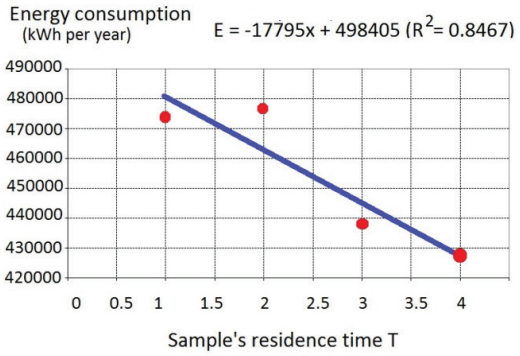


Figure 5. Graph of the change in energy consumption (E) (kWh per year) as a function of the sample's presence time T in a cylindrical vessel with a stirrer (Points on the abscissa axis: 1 - initial sample T = 0 min; 2 - treatment after 167 min with a single dose of chlorine; 3 – treatment after 334 min with a single dose of chlorine; 4 – treatment after 167 min with a double dose of chlorine)

Single-run pilot experiments conducted using a magnetic stirrer system to examine the effect of ambient temperature on changes in the roughness

of protective coating walls also revealed a tendency toward a decrease in the equivalent roughness coefficient as water temperature increased from 20 to 500°C. Therefore, the obtained results allow us to draw a reasonable preliminary conclusion regarding the need for continued experimental modeling studies across wide temperature ranges and durations of water presence in the water supply network to confirm the hypotheses regarding the transformation of the roughness of protective pipeline coatings during pipeline operation. For these purposes, a comprehensive and detailed analysis of the chemical composition of water and coating samples over time is envisaged.

CONCLUSIONS

1. The results of a study of the hydraulic characteristics of pipelines coated with Subcote FLP using alternative methods as well as promising methodological approaches for determining the possible transformation of equivalent roughness parameters and other parameters during long-term pipeline operation and changing temperature conditions are presented.
2. The experimental results demonstrate the validity of using various methods to determine the set of characteristics required by designers for pipes coated with protective coatings.
3. The focus of subsequent research will be on analyzing and establishing strict patterns of changes in the chemical composition of water and samples of Subcote FLP protective coatings and other types of polymer spray-on protective pipeline coatings, in particular, Scotchkote 169 HB, which has also found wide application in trenchless pipeline renovation.

REFERENCES

1. **Primin O.G.** Utechki vody. // Izdatel'stvo MISI-MGSU 2022. 167 p.
2. **Baymukanov M.A.** O vazhnosti analiza sostoyaniya vodoprovodnykh setey RF // Polimernyye truby. 2016. T. 5 (14). pp. 26–29.
3. **Zhuangzhu Luo, Zhaozhu Zhang, Wenjing Wang, Weimin Liu** Effect of polytetrafluoroethylene gradient-distribution on the hydrophobic and tribological properties of polyphenylene sulfide composite coating. Surface and Coatings Technology, Volume 203, Issues 10-11. 25 February 2009. Pages 1516-1522.
4. **Nabil Anagreh, Lutz Dorn, Christine Bilke-Krause** Low-pressure plasma pretreatment of polyphenylene sulfide (PPS) surfaces for adhesive bonding. International Journal of Adhesion and Adhesives, Volume 28, Issues 1-2. January-March 2008. Pages 16-22.
5. **Jinghui Yang, Tao Xu, Ai Lu, Qin Zhang, Hong Tan, Qiang Fu** Preparation and properties of poly (p-phenylene sulfide)/multiwall carbon nanotube composites obtained by melt compounding. Composites Science and Technology, Volume 69, Issue 2. February 2009. Pages 147-153.
6. **Orlov V.A., Zotkin S.P.** Programma analiza gidravlicheskikh kharakteristik napornykh truboprovodov // Svidetel'stvo o gosudarstvennoy registratsii programmy dlya EVM № 2013610520 ot 09.01.2012.
7. **Orlov V.A., Zotkin S.P., Dezhina I.S., Pelipenko A.A.** Programma rascheta stepeni gidrofobnosti i gidravlicheskikh parametrov trub i ikh zashchitnykh pokrytiy // Svidetel'stvo o gosudarstvennoy registratsii programmy dlya EVM № RU 2017612281 ot 20.02.2017.
8. **Dezhina I.S.** Povysheniye transportiruyu-shchey sposobnosti samotechnykh truboprovodov s uchetom gidrofobnosti i rel'yefa ikh poverkhnosti // Avtoreferat kand. diss. M. FGBOU VO «Natsional'nyy issledovatel'skiy Moskovskiy gosudarstvennyy stroitel'nyy universitet. 2021. 23. p.
9. **Prodous O.A.** Prognozirovaniye poter' napora v truboprovodakh iz raznykh polimernykh materialov // Vodosnabzheniye i sanitarnaya tekhnika. 2018. № 11. pp. 60-64.

СПИСОК ЛИТЕРАТУРЫ

1. **Примин О.Г.** Утечки воды. // Издательство МИСИ-МГСУ. 2022. 167 с..
2. **Баймуканов М.А.** О важности анализа состояния водопроводных сетей РФ // Полимерные трубы. 2016. Т. 5 (14). С. 26–29.
3. **Zhuangzhu Luo, Zhaozhu Zhang, Wenjing Wang, Weimin Liu** Effect of polytetrafluoroethylene gradient-distribution on the hydrophobic and tribological properties of polyphenylene sulfide compositecoating. Surface and Coatings Technology, Volume 203, Issues 10-11. 25 February 2009. Pages 1516-1522.
4. **Nabil Anagreh, Lutz Dorn, Christine Bilke-Krause** Low-pressure plasma pretreatment of polyphenylene sulfide (PPS) surfaces for adhesive bonding. International Journal of Adhesion and Adhesives, Volume 28, Issues 1-2. January-March 2008. Pages 16-22.
5. **Jinghui Yang, Tao Xu, Ai Lu, Qin Zhang, Hong Tan, Qiang Fu** Preparation and properties of poly (p-phenylene sulfide)/multiwall carbon nanotube composites obtained by melt compounding. Composites Science and Technology, Volume 69, Issue 2. February 2009. Pages 147-153.
6. **Орлов В.А., Зоткин С.П.** Программа анализа гидравлических характеристик напорных трубопроводов // Свидетельство о государственной регистрации программы для ЭВМ № 2013610520 от 09.01.2012.
7. **Орлов В.А., Зоткин С.П., Дежина И.С., Пелипенко А.А.** Программа расчета степени гидрофобности и гидравлических параметров труб и их защитных покрытий // Свидетельство о государственной регистрации программы для ЭВМ № RU 2017612281 от 20.02.2017.
8. **Дежина И.С.** Повышение транспортирующей способности самотечных трубопроводов с учетом гидрофобности и рельефа их поверхности // Автореферат канд. дисс. М. ФГБОУ ВО «Национальный исследовательский Московский государственный строительный университет. 2021. 23 с.
9. **Продоус О.А.** Прогнозирование потерь напора в трубопроводах из разных полимерных материалов // Водоснабжение и санитарная техника. 2018. № 11. с. 60-64.

Orlov Vladimir A., Professor, Doctor of Technical Sciences; National Research Moscow State University of Civil Engineering (NRU MGSU), Russia, 129337, Moscow, 26 Yaroslavskoe Shosse; E-mail: OrlovVA@mgsu.ru.

Орлов Владимир Александрович, профессор, доктор технических наук; Федеральное государственное бюджетное образовательное учреждение высшего образования «Национальный исследовательский Московский государственный строительный университет» (НИУ МГСУ), Россия, 129337, Москва, Ярославское шоссе, 26; E-mail: OrlovVA@mgsu.ru.

Zotkin Sergey P., Professor, Candidate of Technical Sciences; Russia, National Research Moscow State University of Civil Engineering (NRU MGSU), Russia, 129337, Moscow, 26 Yaroslavskoe Shosse; E-mail: ZotkinSP@mgsu.ru.

Зоткин Сергей Петрович, профессор, кандидат технических наук; Россия, Федеральное государственное бюджетное образовательное учреждение высшего образования «Национальный исследовательский Московский государственный строительный университет» (НИУ МГСУ), 129337, Москва, Ярославское шоссе, 26; E-mail: ZotkinSP@mgsu.ru.

Bolshakova Maria A., PhD student; National Research Moscow State University of Civil Engineering (NRU MGSU), Russia, 129337, Moscow, 26 Yaroslavskoe Shosse; E-mail: haritonova_mariy@mail.ru.

Большакова Мария Анатольевна, аспирант; Федеральное государственное бюджетное образовательное учреждение высшего образования «Национальный исследовательский Московский государственный строительный университет» (НИУ МГСУ), Россия, 129337, Москва, Ярославское шоссе, 26; E-mail: haritonova_mariy@mail.ru

International Journal for Computational Civil and Structural Engineering, 22(1) 92–103 (2026)

DOI:10.22337/2587-9618-2026-22-1-92-103

MATHEMATICAL MODEL OF OPTIMIZATION OF THE TRANSPARENT PARTITION THICKNESS IN THE TROMBE WALL HEAT EXCHANGE SYSTEM

Ivan K. Andrianov, Elena K. Chepurnova, Sergey A. Kostikov

Institute of Machine Science and Metallurgy of the Far Eastern Branch of the Russian Academy of Sciences of the Khabarovsk Federal Research Center of the Far Eastern Branch of the Russian Academy of Sciences, Komsomolsk-na-Amure, RUSSIA

Abstract: The study is devoted to the issue of mathematical modeling of effective heat transfer in a blood clot wall, which is a structural element of passive solar heating of buildings. The problem of optimization the geometry of the transparent partition wall of the Thrombus, partially absorbing and transmitting solar energy, is considered in the work. The air temperature in the air layer is selected as the optimization objective function. A mathematical model for optimizing the wall thickness of a transparent partition, at which the maximum air temperature in the gap is reached, is built in the work. The model was constructed using the equations of thermal balance, the Bouguer-Lambert-Beer lawlaw, and the necessary and sufficient conditions for the extremum of the objective function. The determining ratios take into account the processes of convective and radiant heat transfer. The numerical calculation method is implemented using the implicit differentiation method and the Newton iterative method. The optimal values of the wall thickness of a transparent partition, at which the maximum value of the air temperature in the wall layer of the Thrombus is reached, as well as the corresponding temperatures of the partition and the surface of a massive wall coated with a phase transition material, are obtained based on the constructed mathematical model. The constructed graphical dependences of the air temperature in the gap on the wall thickness of the transparent partition clearly demonstrate the presence of a maximum of the objective function. The optimal values of the wall thickness of the transparent partition and the air temperature in the interlayer decrease with increasing absorption coefficient of the glass partition material according to the results of numerical experiments. The constructed mathematical model and numerical calculation method will make it possible to increase the efficiency of heat transfer in the Thrombus wall by reducing heat energy losses when choosing the optimal thickness of the glass partition.

Keywords: Trombe wall, system of passive heating, solar radiation, convective heat exchange, radiant heat exchange, optimization, implicit differentiation

МАТЕМАТИЧЕСКАЯ МОДЕЛЬ ОПТИМИЗАЦИИ ТОЛЩИНЫ СТЕНКИ ПРОЗРАЧНОЙ ПЕРЕГОРОДКИ В СИСТЕМЕ ТЕПЛООБМЕНА СТЕНЫ ТРОМБА

И.К. Андрианов, С.А. Костиков, Е.К. Чепурнова

Институт машиноведения и металлургии Дальневосточного отделения Российской академии наук Федерального государственного бюджетного учреждения науки Хабаровского Федерального исследовательского центра Дальневосточного отделения Российской академии наук, г. Комсомольск-на-Амуре, РОССИЯ

Аннотация: Исследование посвящено вопросу математического моделирования эффективного теплопереноса в стене Тромба, представляющей собой конструктивный элемент пассивного солнечного отопления зданий. В работе рассматривается проблема оптимизации геометрии прозрачной перегородки стены Тромба, частично поглощающей и пропускающей солнечную энергию. В качестве целевой функции оптимизации выбрана температура воздуха в воздушной прослойке. Построена математическая модель оптимизации толщины стенки прозрачной перегородки, при которой достигается максимальная температура воздуха в зазоре. Построение модели проводилось с использованием уравнений теплового баланса, закона Бугера-Ламберта-Бера, необходимого и достаточного условий экстремума целевой функции. Определяю-

щие соотношения учитывают процессы конвективного и лучистого теплообмена. Численная методика расчета реализована с использованием метода неявного дифференцирования и итерационного метода Ньютона. На основании построенной математической модели получены оптимальные значения толщины стенки прозрачной перегородки, при которых достигается максимальное значение температуры воздуха в прослойке стены Тромба, а также соответствующие значения температур перегородки и поверхности массивной стены с покрытием из материала с фазовым переходом. Построенные графические зависимости температуры воздуха в прослойке от толщины стенки прозрачной перегородки наглядно демонстрируют наличие максимума целевой функции. Согласно результатам численных экспериментов при увеличении коэффициента поглощения материала стеклянной перегородки, оптимальные значения толщины ее стенки и температуры воздуха в прослойке уменьшаются. Построенная математическая модель и численная методика расчета позволят повысить эффективность теплопереноса в стене Тромба за счет снижения потерь тепловой энергии при выборе оптимальной толщины стеклянной перегородки.

Ключевые слова: стена Тромба, системы пассивного отопления, солнечное излучение, конвективный теплообмен, лучистый теплообмен, оптимизация, неявное дифференцирование

1. INTRODUCTION

Today, research on the use of heat exchange systems based on renewable energy sources is becoming increasingly common in civil and structural engineering. One such system is the Trombe wall, which operates by accumulating solar energy. The operating principle of this system is as follows: the flow of solar radiation, passing through a transparent partition, is absorbed by a solid wall, which is coated with a dark coating of a phase-change material. The absorbed thermal energy is then transferred to the air space between the transparent partition and the solid wall [1-3]. In practice, the Trombe wall is used as a source of passive heating in the design of residential structures.

In recent years, various approaches to optimizing the Trombe wall have become widespread, reflected primarily in foreign studies. The most comprehensive discussion of modern trends in Trombe wall optimization is provided in [4]. In addition, the main optimization issues addressed in the study of heat transfer in a Trombe wall should be noted: the choice of coatings and phase-change materials that ensure the best heat transfer in the Trombe wall [5, 6]; modeling the operating conditions of the Trombe wall to ensure optimal thermal comfort [7]; reducing energy consumption and heat losses in the Trombe wall [8, 9]; optimizing the geometry and introducing new design solutions in the Trombe wall [10, 11]; developing software to control the heat transfer process in the Trombe wall [12, 13]. According to the conducted analysis, most of the studied Trombe wall optimization problems are solved by trying out various configurations using either numerical methods, in particular the finite element method, or with the help of full-scale experiments. A few works are devoted to mathematical modeling of heat transfer in the Trombe wall, in particular the works [3, 14]. Some issues related to improving thermal efficiency in construction, as well as the use of phase-change materials, are discussed in [15-20].

One unexplored issue remains the mathematical modeling of the optimal thickness of the transparent partition in a Trombe wall. Today, a wide variety of glass blocks, double-glazed windows are used as transparent partitions in Trombe walls, each with varying degrees of light transmittance, which affects the amount of solar energy absorbed by the transparent partition. The challenge of optimizing the thickness of the transparent partition stems from the fact that, on the one hand, it acts as a thermal barrier: the thicker the transparent partition wall, the more light it absorbs, and the higher its temperature. On the other hand, as the thickness of the transparent partition wall increases, the intensity of solar radiation transmitted through the partition and incident on the solid wall with a phase-change material coating decreases. Since one of the main functions of a Trombe wall is to heat the air in the air gap between the transparent partition and the solid wall, the development of a mathematical model for optimizing the thickness of the

transparent partition, ensuring the maximum air temperature in the air gap of the Trombe wall, is relevant.

When conducting mathematical modeling of the optimal wall thickness of a transparent partition in the heat transfer system of a Trombe wall, we will use the following assumptions:

– the boundary surfaces of the transparent partition and the solid wall are flat, the width of the air gap and the thickness of the transparent partition are constant,

– the intensity of solar radiation incident on the Trombe wall is constant over the period of time under consideration,

– the reflection of solar radiation on the outer surface of the transparent partition is negligible,

– the boundary surfaces of the transparent partition and the solid wall are isothermal in the studied region,

– the air temperature and the heat transfer coefficient on the outer surface of the transparent partition remain constant over the studied period of time,

– the air temperature field in the studied region of the air gap is uniform,

– the temperature of the outer surface of the solid wall with a coating made of a phase-change material does not exceed the melting point of the material,

– heat transfer through the solid wall with a coating made of a phase-change material is excluded.

2. METHODS

Let us consider the heat balance equations for a transparent partition, air in the air gap and a solid wall with a coating made of a phase-change material [3]:

$$Q_{\text{gl}}^{+} - Q_{\text{gl}}^{-} = c_{\text{gl}}\rho_{\text{gl}}\delta S\left(T_{\text{gl}}^{(\tau)} - T_{\text{gl}}^{(0)}\right), \quad (1)$$

$$Q_{\text{air}}^{+} - Q_{\text{air}}^{-} = c_{\text{air}}\rho_{\text{air}}bS\left(T_{\text{air}}^{(\tau)} - T_{\text{air}}^{(0)}\right), \quad (2)$$

$$Q_{\text{wl}}^{+} - Q_{\text{wl}}^{-} = c_{\text{wl}}m_{\text{wl}}\left(T_{\text{wl}}^{(\tau)} - T_{\text{wl}}^{(0)}\right), \quad (3)$$

where $Q_{\text{gl}}^{+}, Q_{\text{gl}}^{-}$ – the amounts of heat supplied to and removed from the transparent partition, $Q_{\text{air}}^{+}, Q_{\text{air}}^{-}$ – the amounts of heat supplied to and removed from the air in the air gap, $Q_{\text{wl}}^{+}, Q_{\text{wl}}^{-}$ – the amounts of heat supplied to and removed from the massive wall with a coating made of phase-change material, $c_{\text{gl}}, c_{\text{air}}, c_{\text{wl}}$ – the specific heat capacities of the transparent partition, air in the duct, and phase-change material, $\rho_{\text{gl}}, \rho_{\text{air}}$ – the densities of the transparent partition, air in the duct, m_{wl} – the mass of the phase-change material, δ – the thickness of the transparent partition, b – the width of the air duct, $T_{\text{gl}}^{(0)}, T_{\text{air}}^{(0)}, T_{\text{wl}}^{(0)}$ – the initial temperatures of the transparent partition, air in the duct, and phase-change material, $T_{\text{gl}}^{(\tau)}, T_{\text{air}}^{(\tau)}, T_{\text{wl}}^{(\tau)}$ – temperatures of the transparent partition, air in the channel, material with a phase transition after time τ.

We will describe the attenuation of the luminous flux when light radiation passes through the wall of a transparent partition based on the Bouguer-Lambert-Beer law:

$$I = I_0 e^{-\mu\delta}, \quad (4)$$

where I_0 – the intensity of the light flux incident on the transparent partition, I – the intensity of the light flux passed through the transparent partition, μ – the absorption coefficient of the medium.

Heat supply and removal (Fig. 1) is ensured by radiant and convective heat exchange, taking into account the relationship (4):

$$Q_{\text{gl}}^{+} = I_0\left(1 - e^{-\mu\delta}\right)S\tau + \alpha_{\text{gl}}^{+}\left(T_{\text{air}}^{(\tau)} - T_{\text{gl}}^{(\tau)}\right)S\tau + \varepsilon\sigma\left(\left(T_{\text{wl}}^{(\tau)}\right)^4 - \left(T_{\text{gl}}^{(\tau)}\right)^4\right)S\tau,$$

$$Q_{\text{gl}}^{-} = \varepsilon\sigma\left(\left(T_{\text{gl}}^{(\tau)}\right)^4 - T_{\text{out}}{}^4\right)S\tau + \alpha_{\text{gl}}^{-}\left(T_{\text{gl}}^{(\tau)} - T_{\text{out}}\right)S\tau,$$

$$Q_{\text{air}}^{+} = \alpha_{\text{wl}}\left(T_{\text{wl}}^{(\tau)} - T_{\text{air}}^{(\tau)}\right)S\tau,$$

$$Q_{\text{air}}^{-} = \alpha_{\text{gl}}^{+}\left(T_{\text{air}}^{(\tau)} - T_{\text{gl}}^{(\tau)}\right)S\tau,$$

$$Q_{\text{wl}}^{+} = I_0 e^{-\mu\delta}S\tau,$$

$$Q_{\text{wl}}^{-} = \varepsilon\sigma\left(\left(T_{\text{wl}}^{(\tau)}\right)^4 - \left(T_{\text{gl}}^{(\tau)}\right)^4\right)S\tau + \\ +\alpha_{\text{wl}}\left(T_{\text{wl}}^{(\tau)} - T_{\text{air}}^{(\tau)}\right)S\tau,$$

where $T_{\text{out}}^{(\tau)}$ – the outside air temperature, $\alpha_{\text{gl}}^{+}, \alpha_{\text{gl}}^{-}$ – the heat transfer coefficients on the boundary inner and outer surfaces of the transparent partition, α_{wl} – the heat transfer coefficient on the surface of a massive wall with a coating made of a phase-change material, S – the area of the surface under study, ε is the effective emissivity, σ – the Stefan-Boltzmann constant.

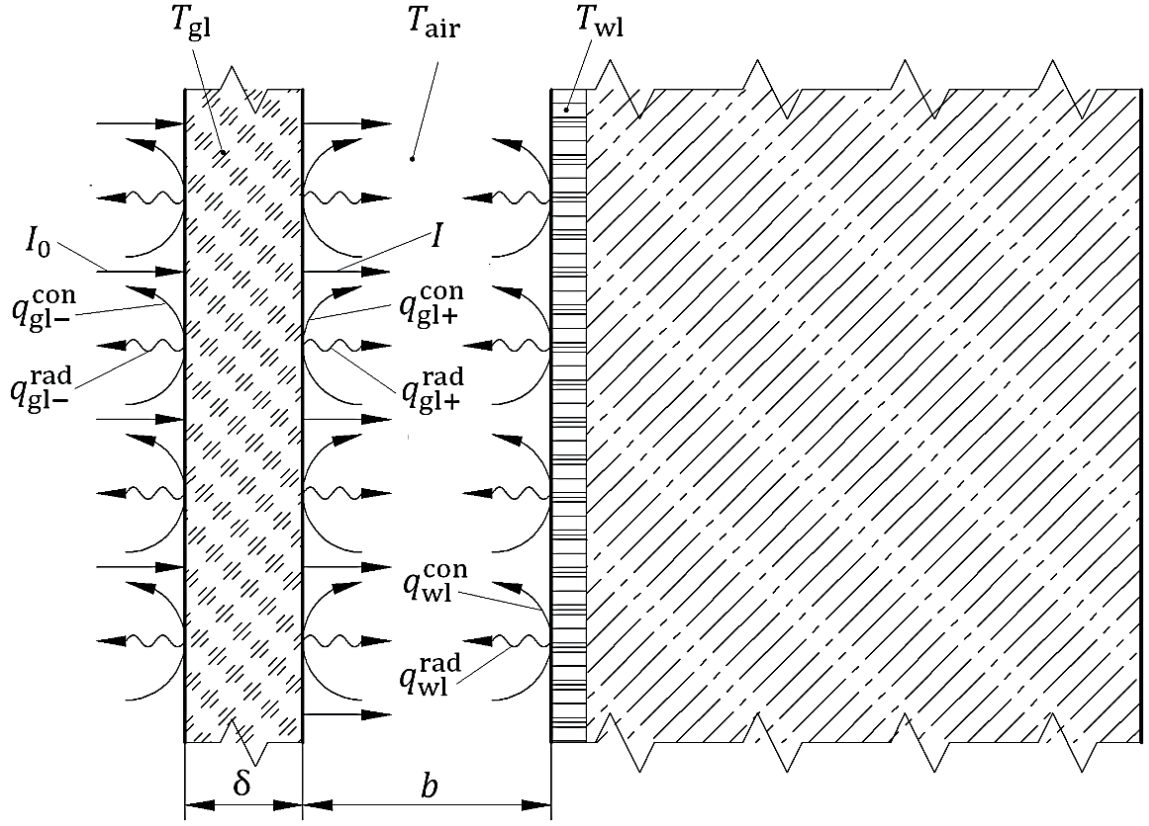


Figure 1. Diagram of the heat exchange process in the Trombe wall (q_{gl-}^{rad} , q_{gl+}^{rad}, q_{wl}^{rad} – specific radiant heat flux on the outer and inner surfaces of the transparent partition and on the surface of the massive wall; q_{gl-}^{con} , q_{gl+}^{con}, q_{wl}^{con} – specific convective heat flux on the outer and inner surfaces of the transparent partition and on the surface of the massive wall)

When constructing the optimization model, we will consider an unconstrained optimization problem. The objective function will be the air temperature in the air gap between the transparent partition and the solid wall coated with a phase-change material, and the optimization variable will be the wall thickness of the transparent partition. Thus, the mathematical formulation of the air optimization problem in the gap, taking into account heat balance equations (1) –(3) and the Bouguer-Lambert-Beer law, will take the form:

$$T_{\text{air}}^{(\tau)} = T_{\text{air}}^{(\tau)}\left(\delta, T_{\text{wl}}^{(\tau)}(\delta), T_{\text{gl}}^{(\tau)}(\delta)\right) \rightarrow \max, \quad (5)$$

$$\Phi_1\left(\delta, T_{\text{air}}^{(\tau)}(\delta), T_{\text{wl}}^{(\tau)}(\delta), T_{\text{gl}}^{(\tau)}(\delta)\right) = 0, \quad (6)$$

$$\Phi_2\left(T_{\text{air}}^{(\tau)}(\delta), T_{\text{wl}}^{(\tau)}(\delta), T_{\text{gl}}^{(\tau)}(\delta)\right) = 0, \quad (7)$$

$$\Phi_3\left(\delta, T_{\text{air}}^{(\tau)}(\delta), T_{\text{wl}}^{(\tau)}(\delta), T_{\text{gl}}^{(\tau)}(\delta)\right) = 0, \quad (8)$$

where $\Phi_1 = c_{\text{gl}}\rho_{\text{gl}}\delta\left(T_{\text{gl}}^{(\tau)} - T_{\text{gl}}^{(0)}\right) - I_0\left(1 - e^{-\mu\delta}\right)\tau - \varepsilon\sigma\left(\left(T_{\text{wl}}^{(\tau)}\right)^4 - \left(T_{\text{gl}}^{(\tau)}\right)^4\right)\tau + +\varepsilon\sigma\left(\left(T_{\text{gl}}^{(\tau)}\right)^4 - \left(T_{\text{out}}^{(\tau)}\right)^4\right)\tau + +\alpha_{\text{gl}}^{-}\left(T_{\text{gl}}^{(\tau)} - T_{\text{out}}^{(\tau)}\right)\tau - \alpha_{\text{gl}}^{+}\left(T_{\text{air}}^{(\tau)} - T_{\text{gl}}^{(\tau)}\right)\tau,$

$\Phi_2 = c_{\text{air}}\rho_{\text{air}}b\left(T_{\text{air}}^{(\tau)} - T_{\text{air}}^{(0)}\right) - -\alpha_{\text{wl}}\left(T_{\text{wl}}^{(\tau)} - T_{\text{air}}^{(\tau)}\right)\tau + \alpha_{\text{gl}}^{+}\left(T_{\text{air}}^{(\tau)} - T_{\text{gl}}^{(\tau)}\right)\tau,$

$\Phi_3 = c_{\text{wl}}m_{\text{wl}}\left(T_{\text{wl}}^{(\tau)} - T_{\text{wl}}^{(0)}\right) - I_0 e^{-\mu\delta}S\tau + +\varepsilon\sigma\left(\left(T_{\text{wl}}^{(\tau)}\right)^4 - \left(T_{\text{gl}}^{(\tau)}\right)^4\right)S\tau + \alpha_{\text{wl}}\left(T_{\text{wl}}^{(\tau)} - T_{\text{air}}^{(\tau)}\right)S\tau.$

To find the optimal value for the transparent partition wall thickness, we use the necessary extremum condition: $\left.\partial T_{\text{air}}/\partial\delta\right|_{\delta=\delta^*} = 0$, where δ^* – the optimal value for the transparent partition wall thickness. According to the system of equations (5) – (8), the air temperature in the air gap is not explicitly expressed in terms of the wall thickness. Therefore, we use the implicit differentiation method:

$$\frac{d\Phi_1}{d\delta} = \frac{\partial\Phi_1}{\partial\delta} + \frac{\partial\Phi_1}{\partial T_{\text{air}}}\frac{\partial T_{\text{air}}}{\partial\delta} + + \frac{\partial\Phi_1}{\partial T_{\text{wl}}}\frac{\partial T_{\text{wl}}}{\partial\delta} + \frac{\partial\Phi_1}{\partial T_{\text{gl}}}\frac{\partial T_{\text{gl}}}{\partial\delta}, \quad (9)$$

$$\frac{d\Phi_2}{d\delta} = \frac{\partial\Phi_2}{\partial\delta} + \frac{\partial\Phi_2}{\partial T_{\text{air}}}\frac{\partial T_{\text{air}}}{\partial\delta} + + \frac{\partial\Phi_2}{\partial T_{\text{wl}}}\frac{\partial T_{\text{wl}}}{\partial\delta} + \frac{\partial\Phi_2}{\partial T_{\text{gl}}}\frac{\partial T_{\text{gl}}}{\partial\delta}, \quad (10)$$

$$\frac{d\Phi_3}{d\delta} = \frac{\partial\Phi_3}{\partial\delta} + \frac{\partial\Phi_3}{\partial T_{\text{air}}}\frac{\partial T_{\text{air}}}{\partial\delta} + + \frac{\partial\Phi_3}{\partial T_{\text{wl}}}\frac{\partial T_{\text{wl}}}{\partial\delta} + \frac{\partial\Phi_3}{\partial T_{\text{gl}}}\frac{\partial T_{\text{gl}}}{\partial\delta}. \quad (11)$$

Solving the system of equations (9) – (11) taking into account the conditions:

$$\left.\partial T_{\text{air}}/\partial\delta\right|_{\delta=\delta^*} = 0 \text{ and } d\Phi_1/d\delta = 0, \quad d\Phi_2/d\delta = 0, d\Phi_3/d\delta = 0,$$

according to equations (6) – (8), and excluding $\partial T_{\text{wl}}/\partial\delta$, $\partial T_{\text{gl}}/\partial\delta$, we move on to the equation for $\delta = \delta^*$:

$$\Phi_4\left(\delta^*, T_{\text{air}}^{(\tau)}(\delta^*), T_{\text{wl}}^{(\tau)}(\delta^*), T_{\text{gl}}^{(\tau)}(\delta^*)\right) = 0, \quad (12)$$

where

$$\Phi_4 = \frac{\partial\Phi_1}{\partial\delta} - \frac{\partial\Phi_1}{\partial T_{\text{wl}}^{(\tau)}}\frac{\partial\Phi_3}{\partial\delta}\Big/\frac{\partial\Phi_3}{\partial T_{\text{wl}}^{(\tau)}} + + \left(\frac{\partial\Phi_1}{\partial T_{\text{gl}}^{(\tau)}} - \frac{\partial\Phi_1}{\partial T_{\text{wl}}^{(\tau)}}\frac{\partial\Phi_3}{\partial T_{\text{gl}}^{(\tau)}}\Big/\frac{\partial\Phi_3}{\partial T_{\text{wl}}^{(\tau)}}\right)\cdot \cdot\left[\frac{\partial\Phi_2}{\partial T_{\text{wl}}^{(\tau)}}\frac{\partial\Phi_3}{\partial\delta}\Big/\frac{\partial\Phi_3}{\partial T_{\text{wl}}^{(\tau)}}\right]\Big/\left(\frac{\partial\Phi_2}{\partial T_{\text{gl}}^{(\tau)}} - -\frac{\partial\Phi_2}{\partial T_{\text{wl}}^{(\tau)}}\frac{\partial\Phi_3}{\partial T_{\text{gl}}^{(\tau)}}\Big/\frac{\partial\Phi_3}{\partial T_{\text{wl}}^{(\tau)}}\right),$$

$\partial\Phi_1/\partial\delta = c_{\text{gl}}\rho_{\text{gl}}\left(T_{\text{gl}}^{(\tau)} - T_{\text{gl}}^{(0)}\right) - -\mu I_0 e^{-\mu\delta}\tau, \quad \partial\Phi_1/\partial T_{\text{wl}}^{(\tau)} = -4\varepsilon\sigma\left(T_{\text{wl}}^{(\tau)}\right)^3\tau,$

$\partial\Phi_1/\partial T_{\text{gl}}^{(\tau)} = c_{\text{gl}}\rho_{\text{gl}}\delta + 8\varepsilon\sigma\left(T_{\text{gl}}^{(\tau)}\right)^3\tau + +\left(\alpha_{\text{gl}}^{-} + \alpha_{\text{gl}}^{+}\right)\tau, \partial\Phi_2/\partial T_{\text{wl}}^{(\tau)} = -\alpha_{\text{wl}}\tau,$

$\partial\Phi_2/\partial T_{\text{gl}}^{(\tau)} = -\alpha_{\text{gl}}^{+}\tau,$

$\partial\Phi_3/\partial T_{\text{gl}}^{(\tau)} = -4\varepsilon\sigma\left(T_{\text{gl}}^{(\tau)}\right)^3 S\tau,$

$\partial\Phi_3/\partial T_{\text{wl}}^{(\tau)} = c_{\text{wl}}m_{\text{wl}} + 4\varepsilon\sigma\left(T_{\text{wl}}^{(\tau)}\right)^3 S\tau + +\alpha_{\text{wl}}S\tau, \quad \partial\Phi_3/\partial\delta = \mu I_0 e^{-\mu\delta}S\tau.$

Thus, the optimization problem is reduced to solving the system of equations (6) – (8), (12) for $\delta = \delta^*$. We introduce the vector of unknown parameters: $\mathbf{x} = \left\{\delta, T_{\text{air}}^{(\tau)}, T_{\text{wl}}^{(\tau)}, T_{\text{gl}}^{(\tau)}\right\}$. To calculate the system of nonlinear equations, we use Newton's iterative method, then the linearized system of equations (6) – (8), (12) will take the form:

$$\sum_{j=1}^{4}\frac{\partial\Phi_i(\mathbf{x}^k)}{\partial x_j}\Delta x_j^{k+1} + \Phi_i(\mathbf{x}^k) = 0, i = \overline{1,4}, \quad x_j^{k+1} = \Delta x_j^{k+1} + x_j^k, \quad (13)$$

where k – the iteration number.

The condition for the termination of the iterative process can be represented as: $\max\limits_{1\le j\le 4}\left|x_j^{k+1}-x_j^k\right|\le \Delta\varepsilon$, where $\Delta\varepsilon$ – the specified accuracy of the numerical calculation.

The solution to the system of linear equations (13) will be the values: $\delta^*, T_{\text{air}}^{(\tau)}(\delta^*), T_{\text{wl}}^{(\tau)}(\delta^*), T_{\text{gl}}^{(\tau)}(\delta^*)$, at which the air temperature in the air gap reaches the optimal value:

$$\max T_{\text{air}}^{(\tau)}\left(\delta, T_{\text{wl}}^{(\tau)}(\delta), T_{\text{gl}}^{(\tau)}(\delta)\right) = T_{\text{air}}^{(\tau)}\left(\delta^*, T_{\text{wl}}^{(\tau)}(\delta^*), T_{\text{gl}}^{(\tau)}(\delta^*)\right).$$

In order to estimate the obtained optimal value to the maximum, we will use the sufficient condition for the extremum $\partial^2 T_{\text{air}}/\partial\delta^2|_{\delta=\delta^*}<0$. By solving the system of equations (9) – (11), we obtain an equation for finding $\partial T_{\text{air}}/\partial\delta$in implicit form:

$$\Phi_5\left(\delta, T_{\text{air}}^{(\tau)}(\delta), T_{\text{wl}}^{(\tau)}(\delta), T_{\text{gl}}^{(\tau)}(\delta)\right)=0, \quad (14)$$

where

$$\Phi_5=\frac{\partial\Phi_1}{\partial\delta}+\frac{\partial\Phi_1}{\partial T_{\text{air}}^{(\tau)}}\frac{\partial T_{\text{air}}^{(\tau)}}{\partial\delta}-\frac{\partial\Phi_1}{\partial T_{\text{wl}}^{(\tau)}}\left(\frac{\partial\Phi_3}{\partial\delta}+\frac{\partial\Phi_3}{\partial T_{\text{air}}^{(\tau)}}\frac{\partial T_{\text{air}}^{(\tau)}}{\partial\delta}\right)\Big/\frac{\partial\Phi_3}{\partial T_{\text{wl}}^{(\tau)}}+\left(\frac{\partial\Phi_1}{\partial T_{\text{gl}}^{(\tau)}}-\frac{\partial\Phi_1}{\partial T_{\text{wl}}^{(\tau)}}\frac{\partial\Phi_3}{\partial T_{\text{gl}}^{(\tau)}}\Big/\frac{\partial\Phi_3}{\partial T_{\text{wl}}^{(\tau)}}\right)\cdot\left[\frac{\partial\Phi_2}{\partial T_{\text{wl}}^{(\tau)}}\left(\frac{\partial\Phi_3}{\partial\delta}+\frac{\partial\Phi_3}{\partial T_{\text{air}}^{(\tau)}}\frac{\partial T_{\text{air}}^{(\tau)}}{\partial\delta}\right)\Big/\frac{\partial\Phi_3}{\partial T_{\text{wl}}^{(\tau)}}-\frac{\partial\Phi_2}{\partial T_{\text{air}}^{(\tau)}}\frac{\partial T_{\text{air}}^{(\tau)}}{\partial\delta}\right]\Big/\left(\frac{\partial\Phi_2}{\partial T_{\text{gl}}^{(\tau)}}-\frac{\partial\Phi_2}{\partial T_{\text{wl}}^{(\tau)}}\frac{\partial\Phi_3}{\partial T_{\text{gl}}^{(\tau)}}\Big/\frac{\partial\Phi_3}{\partial T_{\text{wl}}^{(\tau)}}\right),$$

$$\frac{\partial\Phi_1}{\partial T_{\text{air}}^{(\tau)}}=-\alpha_{\text{gl}}^{+}\tau,\frac{\partial\Phi_3}{\partial T_{\text{air}}^{(\tau)}}=-\alpha_{\text{wl}}S\tau,$$

$$\frac{\partial\Phi_2}{\partial T_{\text{air}}^{(\tau)}}=c_{\text{air}}\rho_{\text{air}}b+\left(\alpha_{\text{wl}}+\alpha_{\text{gl}}^{+}\right)\tau.$$

We introduce the notation $T_{\text{air}}^{(\tau)\prime}=\partial T_{\text{air}}^{(\tau)}/\partial\delta$. To check the sufficient condition for the extremum to be maximal, we use the implicit differentiation method. Then, taking into account that $d\Phi_5/d\delta=0$, we obtain an equation for calculating $\partial T_{\text{air}}^{(\tau)\prime}/\partial\delta$:

$$\frac{\partial\Phi_5}{\partial\delta}+\frac{\partial\Phi_5}{\partial T_{\text{air}}^{(\tau)\prime}}\frac{\partial T_{\text{air}}^{(\tau)\prime}}{\partial\delta}+\frac{\partial\Phi_5}{\partial T_{\text{wl}}^{(\tau)}}\frac{\partial T_{\text{wl}}}{\partial\delta}+\frac{\partial\Phi_5}{\partial T_{\text{gl}}^{(\tau)}}\frac{\partial T_{\text{gl}}^{(\tau)}}{\partial\delta}=0, \quad (15)$$

where

$$\frac{\partial T_{\text{wl}}^{(\tau)}}{\partial\delta}=-\left(\frac{\partial\Phi_3}{\partial\delta}+\frac{\partial\Phi_3}{\partial T_{\text{air}}^{(\tau)}}\frac{\partial T_{\text{air}}^{(\tau)}}{\partial\delta}+\frac{\partial\Phi_3}{\partial T_{\text{gl}}^{(\tau)}}\frac{\partial T_{\text{gl}}^{(\tau)}}{\partial\delta}\right)\Big/\frac{\partial\Phi_3}{\partial T_{\text{wl}}^{(\tau)}},$$

$$\frac{\partial T_{\text{gl}}^{(\tau)}}{\partial\delta}=\left[\frac{\partial\Phi_2}{\partial T_{\text{wl}}^{(\tau)}}\left(\frac{\partial\Phi_3}{\partial\delta}+\frac{\partial\Phi_3}{\partial T_{\text{air}}^{(\tau)}}\frac{\partial T_{\text{air}}^{(\tau)}}{\partial\delta}\right)\Big/\frac{\partial\Phi_3}{\partial T_{\text{wl}}^{(\tau)}}-\frac{\partial\Phi_2}{\partial T_{\text{air}}^{(\tau)}}\frac{\partial T_{\text{air}}^{(\tau)}}{\partial\delta}\right]\Big/\left(\frac{\partial\Phi_2}{\partial T_{\text{gl}}^{(\tau)}}-\frac{\partial\Phi_2}{\partial T_{\text{wl}}^{(\tau)}}\frac{\partial\Phi_3}{\partial T_{\text{gl}}^{(\tau)}}\Big/\frac{\partial\Phi_3}{\partial T_{\text{wl}}^{(\tau)}}\right)$$

The solution to equation (15) for $\delta=\delta^*$ is $\partial^2 T_{\text{air}}/\partial\delta^2|_{\delta=\delta^*}$. Due to nonlinearity, the numerical solution to equation (15) can be found using Newton's method, similar to the system of equations (13).

To establish the dependence of the temperature change: $T_{\text{air}}^{(\tau)}, T_{\text{wl}}^{(\tau)}, T_{\text{gl}}^{(\tau)}$with a change in δ, we consider the numerical solution of the system of equations (6) - (8) with a vector of unknown parameters $\mathbf{x}=\left\{T_{\text{air}}^{(\tau)}, T_{\text{wl}}^{(\tau)}, T_{\text{gl}}^{(\tau)}\right\}$ for a given set of values of the thickness of the transparent partition $\boldsymbol{\delta}=\{\delta_l\}, l=\overline{1,n}$. Applying Newton's method for the numerical solution of the system

of equations (6) - (8), we obtain the following iterative scheme for a fixed value of the partition thickness $\delta = \delta_l, l = \overline{1,n}$:

$$\sum_{j=1}^{4} \frac{\partial \Phi_i(\mathbf{x}^k, \delta_l)}{\partial x_j} \Delta x_j^{k+1} + \Phi_i(\mathbf{x}^k, \delta_l) = 0, \quad (16)$$

$$x_j^{k+1} = \Delta x_j^{k+1} + x_j^k, i = \overline{1,3}, j = \overline{1,4}\ l = \overline{1,n}.$$

The condition for the termination of the iterative process: $\max\limits_{1 \le j \le 3} \left| x_j^{k+1} - x_j^k \right| \le \Delta\varepsilon$. The initial approximations of the sought temperatures in the iterative processes (13) and (16) will be determined by the given values at the initial moment of time: $T_{\text{air}}^{(0)}, T_{\text{wl}}^{(0)}, T_{\text{gl}}^{(0)}$.

3. RESULTS

Based on the constructed mathematical models, we will carry out a numerical calculation using the mathematical package Mathcad 15.0 with the following input data: $\mu = 1{,}05$, $I_0 = 350\ \text{W/m}^2$, $\tau = 300$ s, $\sigma = 5{,}67 \cdot 10^{-8}\ \text{W/(м}^2 \cdot \text{K}^4)$, $\varepsilon = 0{,}3$, $\alpha_{\text{gl}}^{+} = 8\ \text{W/(m}^2 \cdot \text{K)}$, $\alpha_{\text{gl}}^{-} = 23\ \text{W/(m}^2 \cdot \text{K)}$, $\alpha_{\text{wl}} = 8\ \text{W/(m}^2 \cdot \text{K)}$, $c_{\text{wl}} = 3000\ \text{J/(kg} \cdot \text{K)}$, $c_{\text{gl}} = 840\ \text{J/(kg} \cdot \text{K)}$, $c_{\text{air}} = 1005\ \text{J/(kg} \cdot \text{K)}$, $S = 1\ \text{m}^2$, $b = 0{,}1$ m, $m_{wl} = 7{,}2$ kg, $\rho_{\text{air}} = 1{,}5\ \text{kg/m}^3$, $\rho_{\text{gl}} = 2500\ \text{kg/m}^3$, $T_{\text{wl}}^{(0)} = 293$ K, $T_{\text{gl}}^{(0)} = 293$ K, $T_{\text{air}}^{(0)} = 293$ K, $T_{\text{out}}^{(0)} = 288$ K, $\Delta\varepsilon = 0{,}01$.

We will consider a glass partition as a transparent partition. We will conduct a series of calculations for various values of the glass absorption coefficient: $\mu_1 = \mu, \mu_2 = 5\mu, \mu_3 = 10\mu, \mu_4 = 20\mu$. We will take the initial approximation of the optimal glass wall thickness in the iterative process (13) as $\delta^0 = 1$ mm.

According to the numerical solution of the optimization problem (5) – (8) for different values of the absorption coefficient of the glass, the following optimal values were obtained, presented in Table 1.

To estimate the temperature changes of the glass partition, the air in the air gap, and the surface of a solid wall coated with a phase-change material for various values of a given set of glass partition thicknesses: δ={2,4,…,12,15,25,50, …,100} mm, numerical solutions of the system of equations (6)–(8) were obtained. Graphical dependences of the change in the desired temperatures on the glass partition thickness are presented in Fig. 2.

Table 1. Results of calculating the optimal parameters in problem (5) – (8)

Absorption coefficient, $\mu_i(\mu), i = \overline{1,4}$	Optimal parameters			
	δ^*, mm	T_{air}^*, °C	T_{wl}^*, °C	T_{gl}^*, °C
$\mu_1 = \mu$	53,89	21,96	24,23	19,80
$\mu_2 = 5\mu$	23,04	21,76	23,96	19,68
$\mu_2 = 10\mu$	15,87	21,67	23,78	19,66
$\mu_2 = 20\mu$	10,93	21,58	23,55	19,69

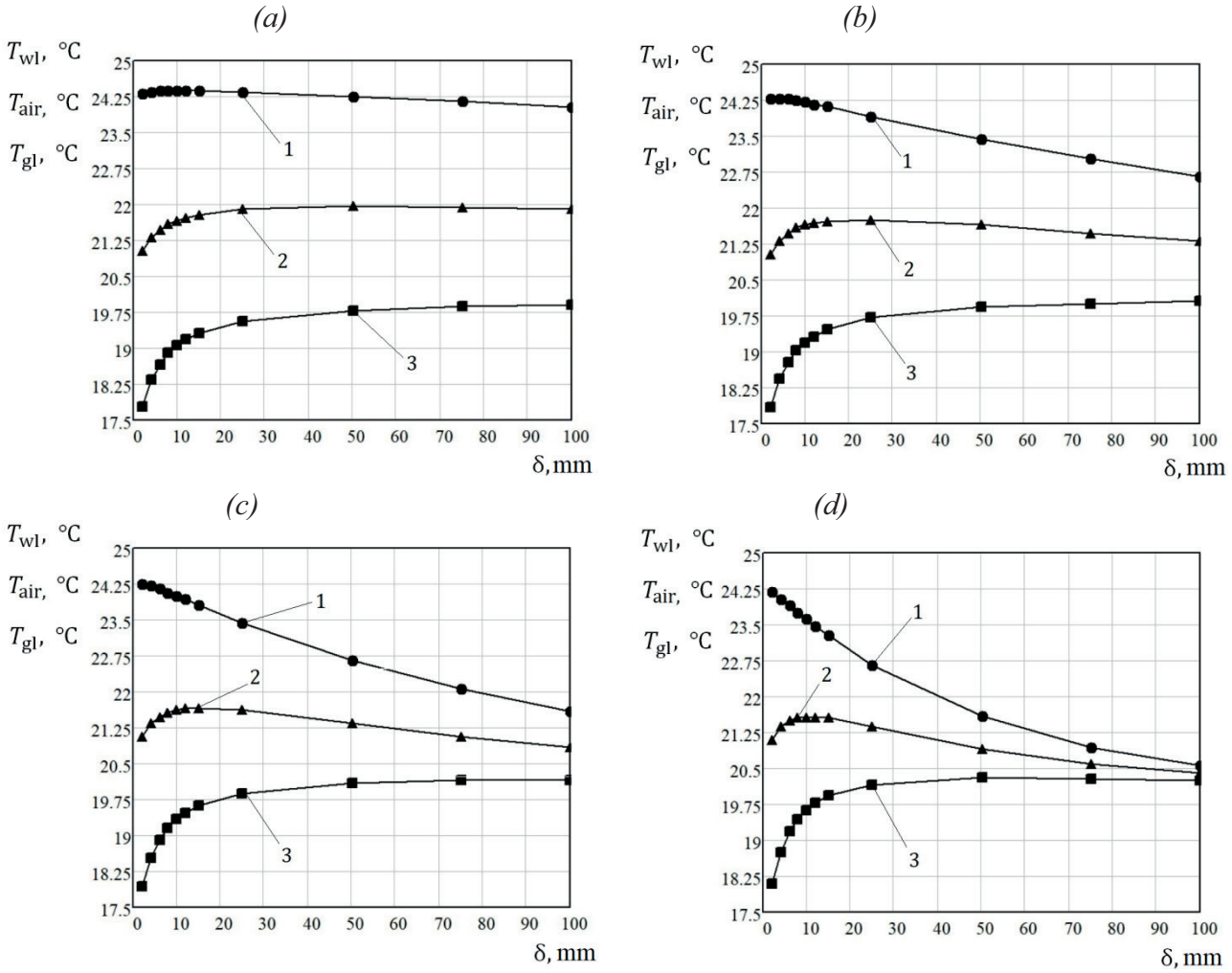


Figure 2. Dependence of the temperatures of a solid wall (1), air in the air gap (2), glass partition (3) on the thickness of the glass partition with absorption coefficients: $\mu_1 = \mu$ *(a),* $\mu_2 = 5\mu$ *(b),* $\mu_3 = 10\mu$ *(c),* $\mu_4 = 20\mu$ *(d)*

4. DISCUSSION

According to the results presented in Table 1, optimal values for the glass partition thickness were obtained for achieving the maximum air temperature in the Trombe wall air gap, as well as the corresponding temperatures of the glass partition and the surface of the solid wall coated with a phase-change material. As the glass partition's absorption coefficient increases, the optimal thickness and the maximum air temperature in the Trombe wall air gap decrease.

The graphical dependencies presented in Figure 2 clearly demonstrate the presence of a maximum on the curve of the air temperature in the Trombe wall air gap as a function of the glass partition thickness. Moreover, the optimal values in the graphs in Figure 2 correspond to the values obtained in Table 1, confirming the accuracy of the numerical calculations performed according to the constructed mathematical model. Based on the results presented in Figure 2, it can be concluded that as the thickness of the transparent partition increases, the air temperature in the air gap initially increases, then reaches a maximum value, and then decreases; With an increase in the absorption coefficient of the glass partition, all other things being equal, the maximum point on the curve of the dependence for the air tempera-

ture in the air gap shifts “to the left”, i.e. the optimal values of the thickness of the transparent partition are achieved at smaller values.

5. CONCLUSION

This paper develops a mathematical model for calculating the optimal wall thickness of a transparent partition in a Trombe wall, achieving the maximum air temperature in the air gap between a solid wall coated with a phase-change material and the transparent partition. The mathematical model takes into account heat balance conditions for convective and radiative heat transfer, as well as the Bouguer-Lambert-Beer law. The numerical solution to the optimization problem was constructed using the implicit differentiation method and Newton's iterative method. Numerical experiments yielded optimal temperatures for the glass partition, the air in the air gap, and the surface of the solid wall coated with a phase-change material. These temperatures were also plotted as a function of the wall thickness of the transparent partition in the Trombe wall. According to the obtained results, as the absorption coefficient of the glass partition used as a transparent partition in the Trombe wall increases, the optimal wall thickness and the maximum air temperature in the air gap decrease. It should be noted that in practice, a transparent partition can be a single-chamber glass unit with an effective thickness of 25 mm. A transparent partition can also be a glass block with an effective thickness ranging from 75 mm to 100 mm.

ACKNOWLEDGEMENTS

The research was funded by the Russian Science Foundation grant №25-29-01248, https://rscf.ru/project/25-29-01248/.

REFERENCES

1. **Bryzgalin V.V., Soloviev A.K.** (2018). Use of passive solar heating systems as an element of a passive house. *Vestnik MGSU*, *13*(4), 472–481. https://doi.org/10.22227/1997-0935.2018.4.472-481
2. **Bi Z.** (2024). Use of Trombe walls to improve energy efficiency in Harbin, Shenyang and Changchun during heating periods. *Ekonomika Stroitel’stva*, (12), 588–591.
3. **Kostikov S.A., Grinkrug M.S., Gordin S.A., Yiqiang J.** (2023). Numerical study of thermal characteristics of a new Trombe wall design with glass blocks for cold climatic conditions. *Teploenergetika*, (12), 90–100. https://doi.org/10.56304/S004036362312007X
4. **Xiao Yu., Yang Q., Fei F., et al**. (2024). Review of Trombe wall technology: Trends in optimization. *Renewable and Sustainable Energy Reviews*, *200*, 114503. https://doi.org/10.1016/j.rser.2024.114503
5. **Zhou Ya., Zhu J., Zhang Yu., et al**. (2024). Structure and regional optimization of a phase change material Trombe wall system. *Energy*, *305*, 132273. https://doi.org/10.1016/j.energy.2024.132273
6. **Martínez A., Alonso C., Martín-Consuegra F., et al**. (2021). Experimental analysis of a prototype for a thermochromic Trombe wall. *Building Research and Information*, *49*(7), 777–794. https://doi.org/10.1080/09613218.2021.1905502
7. **Bensafi M., Bayram M., Osra O., et al**. (2023). Optimization of thermal comfort in buildings via analysis of a Trombe wall for enhanced energy efficiency. *Thermal Science*, *27*(4 Part B), 3423–3432. https://doi.org/10.2298/tsci2304423b
8. **Zhu Na., Deng R., Hu P., et al**. (2021). Coupling optimization study of key influencing factors on PCM Trombe wall for year-round thermal management. *Energy*, *236*, 121470. https://doi.org/10.1016/j.energy.2021.121470
9. **Samiev K. A., Halimov A. S., Fayziev Sh. Sh**. (2022). Multiobjective optimization of integration of the Trombe wall in buildings using a full factorial experiment. *Applied*

Solar Energy, *58*(1), 127–136. https://doi.org/10.3103/s0003701x22010169

10. **Bevilacqua P., Bruno R., Gallo S., & Szyszka J.** (2024). A validated multi-physic model for the optimization of an innovative Trombe Wall for winter use. *Journal of Building Engineering*, *86*, 108915. https://doi.org/10.1016/j.jobe.2024.108915
11. **Zamora B., Kaiser A. S.** (2009). Thermal and dynamic optimization of the convective flow in Trombe Wall shaped channels by numerical investigation. *Heat and Mass Transfer*, *45*(11), 1393–1407. https://doi.org/10.1007/s00231-009-0509-6
12. **Hashemi S. H., Dinmohammad M., Hashemi S. A.** (2021). Optimization of Trombe wall system parameters using TWsim software. *Modeling Earth Systems and Environment*, *7*(2), 917–924. https://doi.org/10.1007/s40808-020-00929-0
13. **Kostikov S. A.** (2021). Optimization of design solutions for Trombe wall. In *Aktual'nye problemy informatsionno-telekommunikatsionnykh tekhnologii i matematicheskogo modelirovaniya v sovremennoi nauke i promyshlennosti: Materialy I Mezhdunarodnoi nauchno-prakticheskoi konferentsii molodykh uchenykh* (pp. 158–161). Komsomolsk-on-Amur: Komsomolsk-on-Amur State University. https://doi.org/10.17084/978-5-7765-1488-3-2021-158
14. **Kostikov S. A.** (2021). Prediction of thermal load of a combined building heating system based on mathematical modeling. In S. I. Sukhorukov, A. S. Gudim, & N. N. Lyubushkina (Eds.), *Proizvodstvennye tekhnologii budushchego: ot sozdaniya k vnedreniyu: Materialy IV Mezhdunarodnoi nauchno-prakticheskoi konferentsii* (pp. 276–280). Komsomolsk-on-Amur: Komsomolsk-on-Amur State University.
15. **Tusnina V. M.** (2023). Numerical analysis of thermal efficiency of external walls with heat-conducting inclusions. *International Journal for Computational Civil and Structural Engineering*, *19*(1), 155–167. https://doi.org/10.22337/2587-9618-2023-19-1-155-167
16. **Fedosov S. V., Anisimova N. K., Shchepochkina Yu. A., Shishkov Yu. V.** (2011). Non-stationary heat transfer in two-layer unlimited plate at combined boundary conditions of the second and fourth types. *International Journal for Computational Civil and Structural Engineering*, *7*(1), 33–38.
17. **Nevskii S. A., Kormyshev V. E., Simonov Y. N., Konovalov S. V.** (2020). Simulation of phase transformations in high carbon pearlite steel at various cooling rates. *CIS Iron and Steel Review*, *20*, 55–60. https://doi.org/10.17580/cisisr.2020.02.12.
18. **Zhu N., Li S., Hu P., Lei F., Deng R**. (2019). Numerical investigations on performance of phase change material Trombe wall in building. *Energy*, *187*(C).
19. **Andrianov I. K.** (2025). On the formulation of the problem of optimizing the thickness of the transparent partition wall in the Trombe wall heat exchange system. In *Prikladnaya matematika i fundamental'naya informatika: Materialy XV Mezhdunarodnoi molodezhnoi nauchno-prakticheskoi konferentsii s elementami nauchnoi shkoly* (pp. 10–11). Omsk: Omsk State Technical University.
20. **Zhao J., Ma X., Zhang Q.** (2025). Buildings' thermal performance and energy efficiency for sustainable construction. *Buildings*, *15*(18), 3410

СПИСОК ЛИТЕРАТУРЫ

1. **Брызгалин В. В., Соловьев А. К.** Использование пассивных систем солнечного отопления как элемента пассивного дома. Вестник МГСУ, 2018, Т. 13, № 4(115), С. 472–481. DOI: 10.22227/1997-0935.2018.4.472-481.
2. **Би Ж.** Использование Стен Тромба для повышения энергоэффективности в го-

роде Харбин, Шэньян и Чанчунь в периоды отопления. Экономика строительства, 2024, № 12, С. 588–591.

3. **Костиков С. А., Гринкруг М. С., Гордин С. А., Yiqiang J.** Численное исследование тепловых характеристик стены Тромба новой конструкции со стеклоблоком для холодных климатических условий. Теплоэнергетика, 2023, № 12, С. 90–100. DOI: 10.56304/S004036362312007X.
4. **Xiao Yu., Yang Q., Fei F. et al**. Review of Trombe wall technology: Trends in optimization. Renewable and Sustainable Energy Reviews, 2024, Vol. 200, P. 114503. DOI: 10.1016/j.rser.2024.114503.
5. **Zhou Ya., Zhu J., Zhang Yu. et al**. Structure and regional optimization of a phase change material Trombe wall system. Energy, 2024, Vol. 305, P. 132273. DOI: 10.1016/j.energy.2024.132273.
6. **Martínez A., Alonso C., Martín-Consuegra F. et al.** Experimental analysis of a prototype for a thermochromic Trombe wall. Building Research and Information, 2021, Vol. 49, No. 7, P. 777–794. DOI: 10.1080/09613218.2021.1905502.
7. **Bensafi M., Bayram M., Osra O. et al.** Optimization of thermal comfort in buildings via analysis of a Trombe wall for enhanced energy efficiency. Thermal Science, 2023, Vol. 27, No. 4 Part B, P. 3423–3432. DOI: 10.2298/tsci2304423b.
8. **Zhu Na, Deng R., Hu P. et al.** Coupling optimization study of key influencing factors on PCM Trombe wall for year-round thermal management. Energy, 2021, Vol. 236, P. 121470. DOI: 10.1016/j.energy.2021.121470.
9. **Samiev K. A., Halimov A. S., Fayziev Sh. Sh.** Multiobjective optimization of integration of the Trombe wall in buildings using a full factorial experiment. Applied Solar Energy, 2022, Vol. 58, No. 1, P. 127–136. DOI: 10.3103/s0003701x22010169.
10. **Bevilacqua P., Bruno R., Gallo S., Szyszka J.** A validated multi-physic model for the optimization of an innovative Trombe Wall for winter use. Journal of Building Engineering, 2024, Vol. 86, P. 108915. DOI: 10.1016/j.jobe.2024.108915.
11. **Zamora B., Kaiser A. S.** Thermal and dynamic optimization of the convective flow in Trombe Wall shaped channels by numerical investigation. Heat and Mass Transfer, 2009, Vol. 45, No. 11, P. 1393–1407. DOI: 10.1007/s00231-009-0509-6.
12. **Hashemi S. H., Dinmohammad M., Hashemi S. A.** Optimization of Trombe wall system parameters using TWsim software. Modeling Earth Systems and Environment, 2021, Vol. 7, No. 2, P. 917–924. DOI: 10.1007/s40808-020-00929-0.
13. **Костиков С. А.** Оптимизация конструктивных решений для стены Тромба. В кн.: Актуальные проблемы информационно-телекоммуникационных технологий и математического моделирования в современной науке и промышленности: Материалы I Международной научно-практической конференции молодых учёных, Комсомольск-на-Амуре, 20–25 марта 2021 года. Комсомольск-на-Амуре: Комсомольский-на-Амуре государственный университет, 2021, С. 158–161. DOI: 10.17084/978-5-7765-1488-3-2021-158.
14. **Костиков С. А.** Прогнозирование тепловой нагрузки комбинированной системы теплоснабжения здания на основе математического моделирования. В кн.: Производственные технологии будущего: от создания к внедрению: Материалы IV Международной научно-практической конференции, Комсомольск-на-Амуре, 16–26 февраля 2021 года / Редколлегия: С. И. Сухоруков (отв. ред.), А. С. Гудим, Н. Н. Любушкина. Комсомольск-на-Амуре: Комсомольский-на-Амуре государственный университет, 2021, С. 276–280.
15. **Tusnina V. M.** Numerical analysis of thermal efficiency of external walls with heat-conducting inclusions. International Journal for Computational Civil and Structural Engineering, 2023, Vol. 19, No. 1, P. 155–167. DOI: 10.22337/2587-9618-2023-19-1-155-167.

16. **Федосов С. В., Анисимова Н. К., Щепочкина Ю. А., Шишков Ю. В.** Нестационарный теплообмен в двухслойной неограниченной пластине при комбинированных граничных условиях второго и четвёртого типов. International Journal for Computational Civil and Structural Engineering, 2011, Vol. 7, No. 1, P. 33–38.
17. **Nevskii S. A., Kormyshev V. E., Simonov Y. N., Konovalov S. V.** Simulation of phase transformations in high carbon pearlite steel at various cooling rates. CIS Iron and Steel Review, 2020, Vol. 20, P. 55–60. DOI: 10.17580/cisisr.2020.02.12.
18. **Zhu N., Li S., Hu P., Lei F., Deng R.** Numerical investigations on performance of phase change material Trombe wall in building. Energy, 2019, Vol. 187(C).
19. **Андрианов И. К.** К постановке задачи об оптимизации толщины стенки прозрачной перегородки в системе теплообмена стены Тромба. В кн.: Прикладная математика и фундаментальная информатика: Материалы XV Международной молодёжной научно-практической конференции с элементами научной школы, Омск, 19–24 мая 2025 года. Омск: Омский государственный технический университет, 2025, С. 10–11.
20. **Zhao J., Ma X., Zhang Q.** Buildings' thermal performance and energy efficiency for sustainable construction. Buildings, 2025, Vol. 15, No. 18, P. 3410. DOI: 10.3390/buildings15183410.

Ivan K. Andrianov, Ph.D. in engineering sciences, associate professor, senior researcher, Institute of Machine Science and Metallurgy, Far Eastern Branch of the Russian Academy of Sciences (IMiM FEB RAS – a separate subdivision of the Khabarovsk Federal Research Center, FEB RAS), 1 Metallurgov St., Komsomolsk-on-Amur, Khabarovsk Krai, 681005, Russia, e-mail: ivan_andrianov_90@mail.ru,

Иван Константинович Андрианов, кандидат технических наук, доцент, старший научный сотрудник, Институт машиноведения и металлургии Дальневосточного отделения Российской академии наук Федерального государственного бюджетного учреждения науки Хабаровского Федерального исследовательского центра Дальневосточного отделения Российской академии наук (ИМиМ ДВО РАН - обособленное подразделение ХФИЦ ДВО РАН), дом 1, ул. Металлургов, Хабаровский край, г. Комсомольск-на-Амуре, 681005, Россия, ivan_andrianov_90@mail.ru.

Elena K. Chepurnova, junior researcher, Institute of Machine Science and Metallurgy, Far Eastern Branch of the Russian Academy of Sciences (IMiM FEB RAS – a separate subdivision of the Khabarovsk Federal Research Center, FEB RAS), 1 Metallurgov St., Komsomolsk-on-Amur, Khabarovsk Krai, 681005, Russia, e-mail: el.chep@bk.ru.

Елена Константиновна Чепурнова, младший научный сотрудник, Институт машиноведения и металлургии Дальневосточного отделения Российской академии наук Федерального государственного бюджетного учреждения науки Хабаровского Федерального исследовательского центра Дальневосточного отделения Российской академии наук (ИМиМ ДВО РАН - обособленное подразделение ХФИЦ ДВО РАН), дом 1, ул. Металлургов, Хабаровский край, г. Комсомольск-на-Амуре, 681005, Россия, el.chep@bk.ru.

Sergey A. Kostikov, junior researcher, Institute of Machine Science and Metallurgy, Far Eastern Branch of the Russian Academy of Sciences (IMiM FEB RAS – a separate subdivision of the Khabarovsk Federal Research Center, FEB RAS), 1 Metallurgov St., Komsomolsk-on-Amur, Khabarovsk Krai, 681005, Russia, e-mail: 300gloof@mail.ru.

Сергей Александрович Костиков, младший научный сотрудник, Институт машиноведения и металлургии Дальневосточного отделения Российской академии наук Федерального государственного бюджетного учреждения науки Хабаровского Федерального исследовательского центра Дальневосточного отделения Российской академии наук (ИМиМ ДВО РАН - обособленное подразделение ХФИЦ ДВО РАН), дом 1, ул. Металлургов, Хабаровский край, г. Комсомольск-на-Амуре, 681005, Россия, 300gloof@mail.ru.

DOI:10.22337/2587-9618-2026-22-1-104-117

NONLINEAR DYNAMIC ANALYSIS OF THE STEEL-RUBBER VIBRATION ISOLATORS WITH PERFORATION

Vladimir L. Mondrus [1], Dmitry K. Sizov [2], Timofei M. Kvasnikov [1]
[1] National Research Moscow State University of Civil Engineering, Moscow, RUSSIA
[2] OOO "Vibroseismozastchita", Moscow, RUSSIA

Abstract: The paper presents a comparative study of nonlinear dynamic analyses of perforated and non-perforated steel–rubber vibration isolators. Particular emphasis is placed on the nonlinear response of rubber, incorporating hyperelasticity (via the Mooney–Rivlin model) and viscoelasticity (through a Prony series), under static preloading conditions. The computational methodology is implemented in Python, integrating the finite element method (FEM), the Newmark-β time integration scheme for dynamic equilibrium, and a Newton–Raphson iterative solver enhanced with line search.

Keywords: vibration isolation, steel-rubber vibration isolator with holes, Mooney–Rivlin model, Prony series, Newmark-β method

НЕЛИНЕЙНЫЙ ДИНАМИЧЕСКИЙ АНАЛИЗ ПЕРФОРИРОВАННЫХ РЕЗИНОМЕТАЛЛИЧЕСКИХ ВИБРОИЗОЛЯТОРОВ

В.Л. Мондрус [1], Д.К. Сизов [2], Т.М. Квасников [1]
[1] Национальный исследовательский Московский государственный строительный университет (НИУ МГСУ), г. Москва, РОССИЯ
[2] ООО «Вибросейсмозащита», г. Москва, РОССИЯ

Аннотация: В статье представлены результаты сравнения нелинейного динамического анализа резинометаллических виброизоляторов с перфорациями и без. Особое внимание уделяется нелинейному поведению резины с учётом гиперупругости (модель Муни-Ривлина), вязкоупругости (ряды Прони) при статическом предварительном нагружении. Расчётная методика реализована с помощью языка программирования Python с применением метода конечных элементов, схемы Ньюмарка и итерационного алгоритма Ньютона-Рафсона с line search

Ключевые слова: виброизоляция, резинометаллический виброизолятор с отверстиями, модель Муни-Ривлина, ряды Прони, метод Ньюмарка-β

1. INTRODUCTION

Vibrations generated by underground rail transport pose a serious threat to the serviceability of buildings located in close proximity to subway tunnels. These vibrations propagate through the soil and are transmitted to building structures via their foundations. The spectral composition of the excitation is determined by several mechanisms: the relative motion of the train car body and its suspension system, wheel bounce on the rails, and the resistance to motion caused by the wheel-rail contact surface.

Introducing perforations into the structure of a vibration isolator allows for the tuning of its dynamic characteristics and broadening of its isolation band. However, this significantly complicates the calculation of its stress-strain state. Furthermore, rubber exhibits pronounced hyperelastic and viscoelastic behavior, which necessitates the use of advanced numerical analysis methods that account for large deformations, nonlinear

material models, and the interaction between prestress and dynamic loading.

The objective of this work is the nonlinear dynamic analysis of three types of rubber-metal vibration isolators. The methodology is based on a multi-step calculation procedure: a static analysis with a preload representing the load from a portion of the building, followed by a dynamic analysis employing the Newton-Raphson algorithm with line search and implicit Newmark time integration.

The computational core of the code, written in the Python programming language, utilizes the NumPy and SciPy libraries. The NumPy library provides efficient storage for dense arrays and enables vectorized operations, while the scipy.sparse module is used to store the global stiffness and mass matrices, which are highly sparse in finite element analysis (FEA) problems. To solve the systems of linear algebraic equations at each Newton-Raphson iteration, efficient direct solvers available in scipy.sparse.linalg are employed.

The general implementation algorithm in Python is as follows:

Mesh generation was performed directly in Python, with the capability to export in VTK format for subsequent validation in ParaView. The domain was discretized using cubic HEX8 elements. Based on this data, a material class is created, defining functions to compute the internal force vector and tangent stiffness matrices, incorporating the hyperelastic Mooney-Rivlin model and viscoelasticity implemented via Prony series. The next step is the global assembly procedure, which sums the contributions of individual finite elements into the overall sparse system matrix.

A key stage prior to the dynamic analysis is the preliminary static calculation, where the load is applied in increments, and the nonlinear system of equations at each step is solved using the Newton-Raphson method. This allows for the determination of the initial deformed state and the updating of the tangent stiffness matrix to account for the resulting geometric nonlinearity.

The computational process concludes with the application of the Newmark-β method for dynamic analysis. At each time step t_{n+1}, a nonlinear system of dynamic equilibrium equations is formulated and solved using the iterative Newton-Raphson method. Within each iteration, the current kinematic parameters are estimated using the Newmark relationships, after which the geometry, stresses, and tangent stiffness matrix are updated. Upon achieving convergence, the material history is updated, and the results are saved for post-processing [1-4].

2. RESEARCH METHODS

Initial Excitation and Isolator Geometry

The challenge of correctly selecting the resonant frequency of a vibration isolator requires a deep understanding of the spectral composition of the excitation generated by a shallow subway system. The analysis was performed by processing data obtained from a three-channel vibration meter (sensors Kn1, Kn2, Kn3) in octave frequency bands from 2 to 250 Hz, located near the "Akademicheskaya" subway station. Processing of the experimental data showed (Figure 2) that the spectrum of the vibration signal has a distinctly uneven character with several key peaks. The highest energy saturation of the signal was recorded in the low-frequency range, which is characteristic of the impact of rolling stock on the soil mass. The dominant peak is in the octave band with a center frequency of 31.5 Hz, where vibration levels reach maximum values (~72 dB). This frequency can be critical for a number of vibration isolation tasks (especially for the natural frequencies of floors and walls), creating a high risk of structural resonance.

In addition to the main peak, significant vibration levels were recorded in the 16 Hz and 63 Hz bands. Specifically, the component at 16 Hz, with a level of about 65 dB, presents a particular challenge for isolation, as it requires the use of vibration isolators with extremely low stiffness.

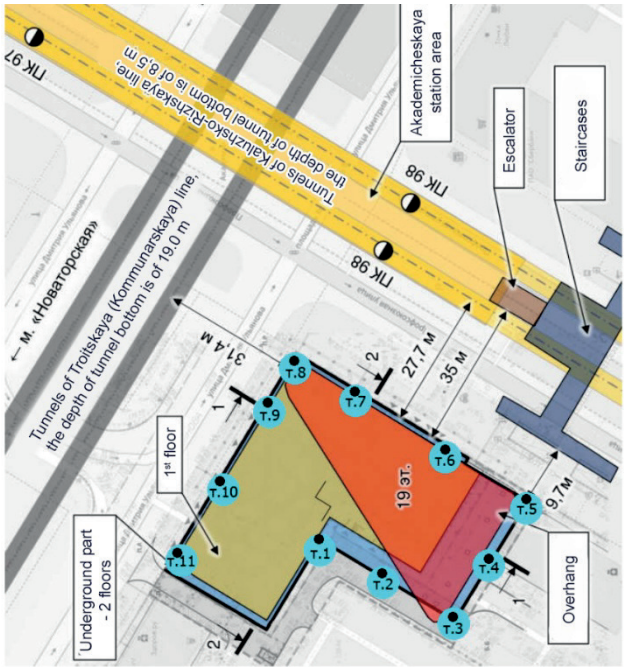


Figure 1. Gauges placement

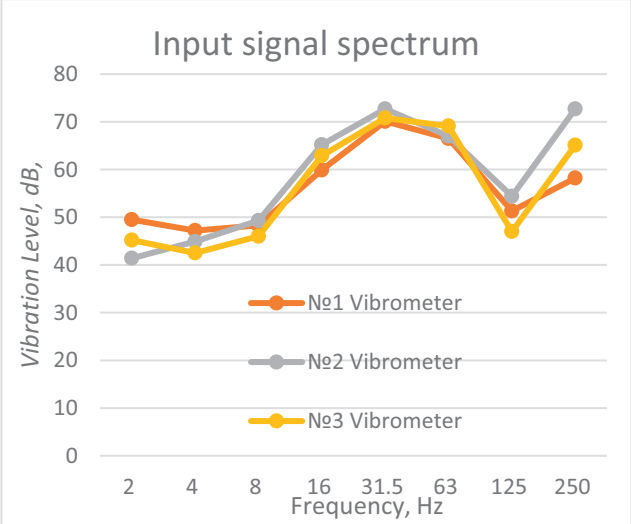


Figure 2. Diagram of the input frequencies spectrum according to gauge indications

Determining the first natural frequency of the system is essential for preventing resonant phenomena. If the first natural frequency of the system is close to the external excitation frequencies, this will lead to a sharp increase in vibration amplitude, intensification of the vibratory impact on structural elements, and potential material failure. [5]

Three variants of the vibration isolator were modeled: a classic rubber-metal type without holes (Type A, Fig. 3, 6), a version with a central through-hole (Type B, Fig. 4, 7), and a modification featuring a central hole plus four additional holes arranged diagonally (Type C, Fig. 5, 8).

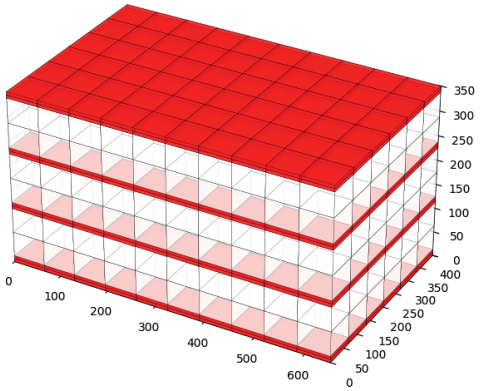


Figure 3. Finite element model of a rubber-metal vibration isolator 650x400x350mm without opening

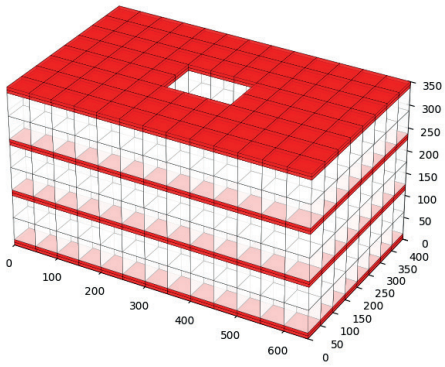


Figure 4. Finite element model of a rubber-metal vibration isolator 650x400x350mm with central opening

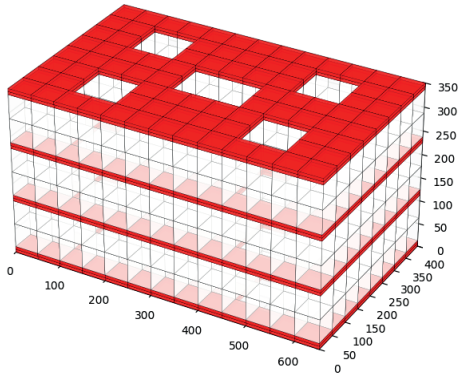


Figure 5. Finite element model of a rubber-metal vibration isolator 650x400x350mm with five openings

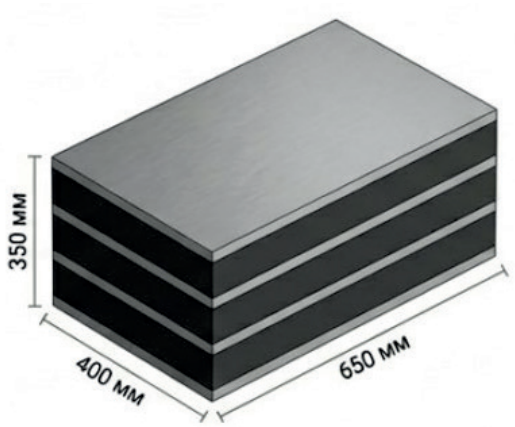


Figure 6. 3D view of a rubber-metal vibration isolator 650x400x350mm without opening

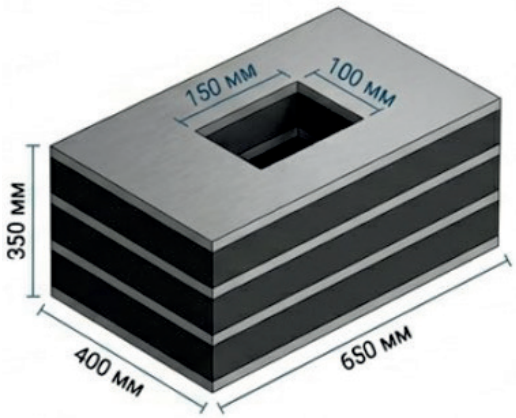


Figure 7. 3D view of a rubber-metal vibration isolator 650x400x350mm with central opening

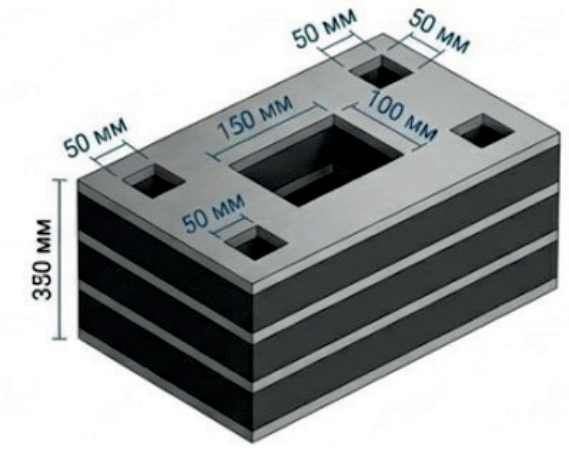


Figure 8. 3D view of a rubber-metal vibration isolator 650x400x350mm with five openings

The overall dimensions of the vibration isolator are 650 × 400 × 350 mm. The structure consists of alternating layers: steel plates with a thickness of 12.5 mm and rubber layers with a thickness of 100 mm.

The dimensions of the central hole are set at 150 × 100 mm, while the dimensions of the staggered holes are set at 50 × 50 mm.

The steel plates are defined by the following parameters: $E = 2 \cdot 10^{11}$ Pa, $\nu = 0.3$, and a density of $\rho = 7000$ kg/m³.

Hyper elastic behavior

The hyper elastic behavior of the rubber is described using the strain energy density function in the Mooney-Rivlin model:

$$W = C_{10}(I_1 - 3) + C_{01}(I_2 - 3) + \frac{1}{D_1}(J_{el} - 1)^2 \quad (1)$$

where:

$I_1 = tr(C)$ is the first invariant of the right Cauchy-Green deformation tensor

$I_2 = \frac{1}{2}[(tr(C))^2 - tr(C^2)]$ is the second invariant

$J_{el} = \sqrt{\det(C)}$ is the volumetric tension

$C_{10} = 0.35$ MPa and $C_{01} = 0.12$ MPa are the material constants.

The first sum describes the deviatoric part of the energy, while the second considers the volumetric part associated with compressibility.

Two-parameter Mooney-Rivlin model (N=1, C_{11}=0) is as follows:

$$W = C_{10}(I_1 - 3) + C_{01}(I_2 - 3) \quad (2)$$

This model is preferable to the simplest neo-Hookean model, since the presence of the term with C_{01} allows one to describe the effect of rubber softening under moderate deformations [6].

Viscoelasticity

The hyper elastic model describes the static behavior of the rubber. However, one of the key functions of a vibration isolator is damping, which in polymers has a viscoelastic nature. This leads to the stress depending not only on the strain, but also on the strain rate and the loading

history. The hyper elastic part describes the equilibrium response; viscoelastic effects are accounted for as deviations from it and contribute to both the static and dynamic response. [7]
In the frequency domain, this is expressed through the complex shear modulus as follows

$$G^*(w) = G'(w) + iG''(w) \quad (3)$$

where G' is the storage modulus (elastic component), and G'' is the loss modulus (viscous component). The tangent of the mechanical loss angle (loss coefficient)

$$tan\delta = G''/G' \quad (4)$$

For the numerical analysis in the time domain, which is necessary for solving nonlinear dynamic problems using Newmark's method, the frequency dependence is transformed into a shear relaxation function $G(t)$. The most convenient approximation is the expansion into Prony series (generalized Maxwell model).
The hyper elastic Mooney-Rivlin model describes the static behavior of rubber; however, a critically important characteristic of a vibration isolator is its damping capacity, which in rubbers has a distinctly viscoelastic nature. These processes cause the stress-strain state to depend not only on the current strain, but also on the entire loading history.
For numerical modeling in the time domain, the frequency dependence of the complex shear modulus $G^*(w)$ is approximated by the shear relaxation function $G(t)$. In the present work, the generalized Maxwell model is used, which is mathematically expressed through Prony series. [8, 9]
The shear relaxation function $G(t)$ is defined by the expression:

$$G(t) = G_0\left[1 - \sum_{k=1}^{N} g_k(1 - e^{-t/\tau_k})\right] \quad (5)$$

where:

- G_0 is the instantaneous shear modulus at t=0, related to the hyper elastic constants by the relation:

$$G_0 = 2(C_{10} + C_{01}) \quad (6)$$

- g_k is the dimensionless relaxation weighting coefficient ($g_k = G_k / G_0$), characterizing the contribution of the k^{th} branch to the overall reduction in rigidity;
- τ_k is the creep times;
- N is the order of the series, i.e., the number of Maxwell branches [10].

The long-term shear modulus (G_∞), which determines the rigidity of rubber after the relaxation processes are completed, is related to the instantaneous modulus by the ratio:

$$G_\infty = G_0[1 - \sum_{k=1}^{N} g_k)] \quad (7)$$

The coefficients are adopted on the basis of identification for high-damping rubbers: $g_1 = 0.436$, $g_2 = 0.058$, $g_3 = 0.005$, $\tau_1 = 9.85$ c, $\tau_2 = 98.5$ c, $\tau_3 = 985.2$ c. [11]

Combined Hyper elastic - Viscoelastic Model for Calculating Stress and the Tangent Stiffness Matrix

In the present study, the hyper elastic and viscoelastic models are used within a unified visco-hyperelastic formulation. The hyper elastic part (Mooney–Rivlin model) defines the equilibrium contribution to the strain energy and determines the static (long-term) stress-strain state, while the viscoelastic part in the form of Prony series describes the deviations from this equilibrium response over time. In practice, this is implemented as follows: at each solution step, based on the known strain tensor, the equilibrium stresses and the material tangent matrix are first computed using the Mooney–Rivlin model (considering G_∞). Subsequently, the non-equilibrium contributions from each branch of the Prony series are added to them. These contributions are determined by their own relaxation equations (internal variables dependent on the strain history). As a result, the total stress tensor represents the sum of the hyper elastic and all viscoelastic components, and the tangent stiffness matrix ($K_{tangent}$) is formed as a superposition of the material stiffness from the Mooney–Rivlin model and additional derivatives

from all branches of the Prony series. This approach ensures the correct accounting of both the instantaneous nonlinear stiffness of the material and the time-dependent relaxation and damping under dynamic loading [12].

Software Architecture and System State Transfer

To implement the numerical modeling in Python, an architecture employing a single class was applied, ensuring the preservation of the system state throughout the entire calculation. Avoiding two independent calculations (static and dynamic) circumvents the difficulties associated with the correct transfer of internal variables describing the history of viscoelastic deformation. Instead, the model implements two sequential solution methods: static and dynamic, both operating on unified variables and classes.

Upon completion of the static loading stage F_{static}, the system records the displacement field, the updated configuration of the mesh nodes, as well as the stress and strain tensors at each integration point. It is important not only to save the tangent stiffness matrix $K_{tangent}$ but also the complete tensor field of stresses. These stresses are responsible for the "geometric stiffness" effect, which modifies the system's response. Omitting information about the initial stresses while preserving only the matrix K would lead to an incorrect calculation of internal forces in subsequent steps of the dynamic analysis.

The transition from statics to dynamics is implemented in Python as a change of solver without recreating the vibration isolator model. The converged solution obtained in the Newton-Raphson loop is accepted as the initial condition t=0 for Newmark's method. This ensures the continuity of the viscoelastic memory: the creep parameters (Prony series terms) accumulated during the static phase are passed as the initial state for the first step of the dynamic calculation.

Accounting for Geometric Nonlinearity

To correctly account for geometric nonlinearity, the stiffness matrix (K) must be recalculated at each time step based on the current nodal coordinates ($x = X + u$). This implies constructing the strain-displacement matrix (B) based on the deformed geometry rather than the original configuration.

The algorithm for a dynamic step includes the following operations:

1. Calculation of total displacements (the sum of static and current dynamic displacements) and updating the coordinates.
2. Updating the matrix (B) and computing the current stresses.
3. Forming the geometric component of the stiffness matrix (K_{geo}), which depends on the current stress-strain state.

The total tangent stiffness matrix is defined as the superposition of the material and geometric components:

$$K_{tangent} = K_{material} + K_{geo} \quad (8)$$

The presence of the component (K_{geo}), reflecting the influence of compressive stresses in the rubber, is critically important for correctly modeling the change in the frequencies of the rubber-metal vibration isolator under load [13].

Structure of the Software Implementation

The practical implementation of the model is built according to a modular scheme:

- **StaticSolver:** Performs the solution of the nonlinear static problem, returning the deformed mesh, the matrix ($K_{tangent}$), the stress field, and the state of the viscoelastic process.
- **State:** A module that receives all current data after each iteration (mesh, matrix K, material properties, internal variables).
- **DynamicSolver:** Conducts the dynamic analysis based on the data from the State module, adds inertial masses to the corresponding degrees of freedom, and implements the numerical time integration procedure using Newmark's method.

The primary requirement is the strict transfer of the mesh and stiffness to the dynamic module.

Applying the load to the top surface exclusively through mass is a necessary condition for generating correct inertial forces, without which a nonlinear dynamic analysis of the vibration isolation is impossible..

3. STATIC ANALYSIS

The static load F_{static} = 2000 kN, simulating the weight of a portion of the building, is applied to the top plate of the vibration isolator as a uniformly distributed load. Given the pronounced geometric nonlinearity (large deformations) and the physical nonlinearity of the hyper elastic material, applying the full load in a single step is impossible due to convergence problems.
To address this issue, an incremental loading procedure was implemented: F_{static} = 2000 kN was divided into 1000 equal substeps (ΔF = 2 kN). At each substep, the equilibrium of the system was sought using the iterative Newton-Raphson method, with a convergence criterion based on the relative norm of the force residual set to 10^{-5}.

Analysis of the Stress-Strain State
As a result of the static calculation, the field of prestresses and the updated (deformed) mesh geometry were obtained. It is this stressed state that determines the tangent stiffness matrix ($K_{tangent}$), which is recorded and passed as the initial condition for the subsequent dynamic analysis [14].

Numerical Implementation of the Nonlinear System Solution using the Newton-Raphson Algorithm
The solution of the system of nonlinear equilibrium equations was carried out using the Newton-Raphson method, incorporating a line search procedure to enhance the stability of the iterative process. The load application procedure was discretized: at each stage, an increment of ΔF = 2 kN was applied, totaling 1000 substeps until the full load value was reached. [15]
During the iterative process, the Jacobian matrix (tangent stiffness matrix) was updated at each step:

$$J = \frac{\partial R}{\partial u} \tag{9}$$

The force residual vector (R) was defined as the difference between the external loads and the internal reaction forces of the system:

$$R = F_{ext} - F_{int}(u) \tag{10}$$

The computational algorithm within each loading substep was implemented according to the following scheme:

1. Residual Calculation. The current force imbalance vector is determined as follows:

$$R_i = F_{ext} - F_{int}(u_i) \tag{11}$$

2. Convergence Check. The norm of the residual is evaluated against the relative convergence tolerance ε_{rel}:

$$\frac{\|R_i\|}{\|F_{ext}\|} < \varepsilon_{rel} \tag{12}$$

where the convergence tolerance is taken as $\varepsilon_{rel} = 10^{-5}$

3. Solving the Linearized System. The displacement increment vector is computed as follows:

$$J_i \Delta u_i = R_i \tag{13}$$

4. Line Search (State Update). The current nodal coordinates are corrected using a step size α:

$$u_{i+1} = u_i + \alpha \Delta u_i \tag{14}$$

The backtracking method was used to determine the parameter α. In cases where the full algorithm step (α = 1) did not lead to a decrease in the residual, a step reduction algorithm with a factor of 0.5 was activated.

Algorithm Efficiency
Analysis of the numerical simulation results demonstrated the high efficiency of the specified algorithm:

- The number of Newton-Raphson iterations per loading substep decreased from 18–22 to 7–12.
- Cases of solution divergence in situations requiring step damping ($\alpha < 0.3$) were eliminated.

Transfer to Dynamic Analysis

The modeling of the inertial properties of the system is carried out by modifying the global matrices and vectors before initializing the dynamic loop. During the static calculation stage, the external force vector (F_{ext}) is formed, simulating the gravitational load on the top nodes, and the system of equilibrium equations is solved, with inertial terms excluded from these equations [16].

Before starting the dynamic step, a procedure for redefining the system of equations is performed:

1. The components of the external force vector (F_{ext}) corresponding to the static pressure are zeroed out, as this load transitions into the category of inertial forces.
2. The global mass matrix (M) is modified. The calculated equivalent mass is distributed among the corresponding nodes of the top face of the isolator.

In the Python code, this is implemented by adding lumped masses to the diagonal entries of the global matrix.

The equation of motion is written as a balance of inertial and internal forces:

$$M\ddot{u} + F_{int}(u, \dot{u}, history) = 0 \qquad (15)$$

The internal force vector (F_{int}) includes stresses from both the hyper elastic Mooney-Rivlin model and the viscoelastic model. An explicit damping matrix C is not used, as energy dissipation arises automatically in the calculation of F_{int} due to the dependence of stresses on the strain history. The damping of viscoelastic materials is strongly frequency-dependent. The Rayleigh matrix ($C = \alpha M + \beta K$) assumes damping proportional to mass or stiffness, which provides a very rough, non-physical approximation of the frequency dependence [17, 18].

4. DYNAMIC ANALYSIS

Numerical integration of the equations of motion was performed using the implicit Newmark scheme. The parameters $\beta = 0.25$ and $\gamma = 0.5$ were used, corresponding to the constant average acceleration scheme, which ensures stability and the absence of numerical dissipation.

The time integration step was set to $\Delta t = 10^{-4}$ s. The choice of step size is justified by the accuracy criterion for reproducing wave processes:

$$f_{max}\Delta t < 0.1 \qquad (16)$$

where f_{max} = 31.5 Hz is the upper bound of the frequency range of the external excitation.

The kinematic parameters of the system at the new time step (n+1) are determined through the recurrence relations:

Displacement prediction

$$u_{n+1} = u_n + \Delta t\dot{u}_n + \left(\frac{1}{2} - \beta\right)\Delta t^2\ddot{u}_n + \beta\Delta t^2\ddot{u}_{n+1} \qquad (17)$$

Velocity prediction

$$\dot{u}_{n+1} = \dot{u}_n + (1-\gamma)\Delta t\ddot{u}_n + \gamma\Delta t\ddot{u}_{n+1} \qquad (18)$$

To solve the nonlinear system of dynamic equilibrium equations at each time step, the iterative Newton–Raphson method was employed.

Linearization of the equation

$$M\ddot{u} + F_{int}(u, \dot{u}, history) = 0 \qquad (19)$$

within the framework of the Newmark scheme leads to the formation of an effective stiffness matrix:

$$K_{eff} + K_{tangent} + \frac{1}{\beta\Delta t^2}M \qquad (20)$$

where the tangent matrix is as follows:

$$K_{tangent} = \frac{\partial F_{int}}{\partial u} \qquad (21)$$

It includes:

- the material component from the equilibrium stress (Mooney–Rivlin),
- the material contributions from all branches of the Prony series,
- the geometric stiffness resulting from pre-existing stresses.

The damping matrix (C) is not formed explicitly, as the energy dissipation properties of the system are fully accounted for within the nonlinear vector (F_{int}) [19].

The line search procedure is activated if the norm of the residual at the new iteration increases compared to the previous one or decreases insufficiently rapidly (by less than a specified tolerance).

$$\|R_{i+1}\| > \|R_i\| \tag{22}$$

5. RESULTS AND DISCUSSION

Vibration Isolator Settlement

At the moment of load application from the weight of the building portion (t=0), the vertical settlement (u_z) values of the top face of the vibration isolator were obtained. The introduction of perforation expectedly reduced the vertical stiffness of the element, leading to an increase in static deformation:

- Type A (No perforation): Settlement amounted to -10.2 mm. The vibration isolator demonstrates maximum stiffness.
- Type B (1 central hole): Settlement increased to -14.5 mm. The reduction in cross-sectional area led to a moderate increase in settlement.
- Type C (5 holes: 1 center + 4 staggered): Settlement amounted to -22.1 mm. Significant perforations substantially reduced the stiffness of the vibration isolator, providing the softest response to the static load.

Displacement Time History

At time t=0, the settlements start from the static settlement values (-10.2, -14.5, and -22.1 mm, respectively), rather than from zero, which confirms the correct transfer of the stress-strain state from the Static module to the Dynamic module.

Spectral Analysis and Determination of Natural Frequencies

To identify the dynamic characteristics of the vibration isolators in their working (compressed) state, the time histories of vertical displacements ($u_z(t)$), obtained from numerical simulation of the system's free damped vibrations after being displaced from the static equilibrium position, were processed.

Dynamic Analysis

The dynamic analysis of the loaded system revealed a dependence between the perforation types and the dynamic characteristics of the vibration isolator:

- **Type A (Solid):** The spectral peak was recorded at a frequency of **9.50 Hz**.
- **Type B (1 hole):** The introduction of a central channel led to a slight decrease in stiffness, with a frequency of **9.43 Hz**. This minimal difference (less than 1%) is explained by the fact that removing material from the center reduced the vertical stiffness of the system, but simultaneously decreased the associated oscillating mass of the rubber, resulting in the stiffness-to-mass ratio remaining practically unchanged.
- **Type C (5 holes):** The maximum reduction in dynamic stiffness was recorded for the configuration with five holes. The frequency shifted to **8.06 Hz** (a reduction of ~15% relative to Type A).

The significant frequency drops for Type C by 1.44 Hz relative to the solid specimen. This confirms the effectiveness of perforation for reducing support stiffness without loss of stability.

Vibration Isolation Efficiency

The evaluation of vibration protection properties was carried out for the dominant frequency of the external excitation f_{ext} = 31.5 Hz, corresponding to the maximum spectral density of the signal generated by the subway.

According to the theory of linear vibration isolation, the transmission ratio (TR) is determined by the ratio of the excitation frequency to the natural frequency of the system [20]:

$$\eta = f_{ext}/f_n \quad (23)$$

Effective isolator operation is ensured under the condition:

$$\eta > \sqrt{2} \quad (24)$$

Comparative Efficiency Calculation:
For Type A (Solid):
Frequency ratio η = 31.5 / 9.50 ≈ 3.32.
The system is in the vibration isolation zone. The theoretical transmission ratio is TR ≈ 0.10.
For Type B (1 hole):
Frequency ratio η = 31.5 / 9.43 ≈ 3.34.
The indicators are practically identical to the solid vibration isolator. A hole only in the central zone had a minimal impact on the global vertical mode, providing only a symbolic gain in isolation efficiency (less than 1%).
For Type C (5 holes):
Due to the significant reduction in natural frequency, the ratio η increased to 31.5 / 8.06 ≈ 3.91. The increase in frequency detuning leads to a decrease in the theoretical transmission ratio to TR ≈ 0.07. This provides an additional reduction in vibration levels compared to the base variant.

Analysis of Time Histories
Numerical simulation in the time domain confirmed the modal analysis data. For all isolator types, a significant suppression of acceleration amplitudes is observed. However, Type C demonstrates qualitatively different response dynamics: due to its "softer" structure and frequency of 8.06 Hz, it provides deeper filtering not only of the fundamental harmonic (31.5 Hz) but also effectively suppresses the high-frequency "noise" (63 Hz and above), which is partially transmitted by the stiffer models A and B.

Influence of Perforation on Dynamic Characteristics
The analysis showed that introducing perforation into the body of the vibration isolator is an effective tool for controlling stiffness without changing the overall dimensions of the isolator. A comparative analysis of the three configurations under a static load F_{stat} = 2000 kN revealed the following patterns:

1. Stiffness Reduction: The transition from the isolator without holes (Type A) to the perforated structure with five holes (Type C) led to an increase in static settlement from 10.2 mm to 22.1 mm. This indicates a reduction in the vertical static stiffness of the system by more than a factor of two.
2. The natural frequency of the loaded vibration isolator system shifted from 9.50 Hz (Type A) to 8.06 Hz (Type C). The reduction of 1.44 Hz is significant, as it allows for increased detuning from the dominant excitation frequencies.

Effectiveness of Vibration Protection in the Frequency Spectrum Excited by Subway Trains
Analysis of the transmission ratio (TR) for the main excitation frequency of 31.5 Hz (peak of the vibration spectral density) demonstrated the high efficiency of the proposed solution:

$$TR \sim \left|\frac{1}{1-\eta^2}\right|, \text{где } \eta = \frac{f_{ext}}{f_n} \quad (25)$$

For all isolator types, the condition for post-resonance operation is met:

$$\eta = f_{ext}/f_n \quad (26)$$

The frequency ratio is η ≈ 3.3 for the solid block and increases to η ≈ 3.9 for the perforated one (Type C). The calculated transmission ratio for Type C was TR ≈ 0.07, corresponding to a vibration level reduction of 23 dB. This surpasses the performance of the solid vibration isolator (TR ≈ 0.10, 20 dB) and confirms the feasibility of using perforation [21].

Nonlinear Effects
Accounting for geometric nonlinearity and material hyperelasticity allowed for the identification of the rubber "stiffening" effect under large deformations. Ignoring this effect would lead to an incorrect assessment of vibration isolation efficiency and errors in predicting resonant frequencies.

6. CONCLUSIONS

This work presents a nonlinear dynamic simulation of a rubber-metal vibration isolator subjected to a static load from a building and dynamic excitation caused by vibrations from a shallow underground railway. The main conclusions of the study are as follows:

1. The introduction of a system of five vertical holes (1 central + 4 peripheral) allows for a reduction in the natural frequency of the vibration isolator to 8.06 Hz. This ensures reliable protection against the critical frequency range (31.5 Hz – 63 Hz).
2. The developed configuration provides a transmission ratio of TR ≈ 0.07 at the dominant frequency. In the frequency range of 31.5–63 Hz, characteristic of vibrations from shallow subway systems, a reduction in vibration levels by more than a factor of 10 is achieved for a building located near a shallow underground railway.
3. It is demonstrated that the application of simplified linear models is inadmissible when using rubber-metal vibration isolators. The use of the Mooney-Rivlin model and the consideration of large displacements revealed a significant difference between the actual dynamic stiffness and linear extrapolation, confirming the necessity of employing the developed algorithm (Newmark method + Newton-Raphson iterations).

The contribution of this study in practice lies in substantiating the choice of the vibration isolator configuration (Type C), which provides an optimal balance between load-bearing capacity (up to 2000 kN) and the required effective compliance for suppressing low-frequency vibrations generated by trains in shallow subway systems.

7. ACKNOWLEDGEMENT

The work was funded by the Ministry of Science and Higher Education of the Russian Federation, project No. FSWG-2023-0004.

REFERENCES

1. **M. Kaliske, H. Rothert** (1997) Formulation and implementation of three-dimensional viscoelasticity at small and finite strains. Computational Mechanics 19 228-239. https://doi.org/10.1007/s004660050171
2. **Hamid Reza Ghoreishy** (2012) Determination of the parameters of the Prony series in hyper-viscoelastic material models using the finite element method. Materials & Design Volume 35, 791-797. https://doi.org/10.1016/j.matdes.2011.05.057
3. **Li Z., Lou J** (2011) Simulation on Performance of Rubber Isolator Based on ANSYS. 2nd International Conference on Mechanic Automation and Control Engineering, MACE 2011 - Proceedings. DOI:10.1109/MACE.2011.5987260
4. **A.J.M. Ferreira, J.M.A.C. Sá, A.T. Marques** (2003) Nonlinear Finite Element Analysis of Rubber Composite Shells ISSN 0556-171X. Проблемы прочности, № 3, УДК 539.4. DOI: 10.1023/A:1024656604257
5. **Mondrus V.L., Sizov D.K., Kvasnikov T.M.** (2023) Raschet rezinometallicheskih vibroizolyatorov s otverstiyami v sisteme vibrozashchity zdanij s pomoshch'yu programmnogo kompleksa, realizuyushchego metod konechnyh elementov [Finite Element Modelling of Rubber-Metal Vibration Isolators with Holes for the Vibration Protection System of Buildings]// ZHelezobetonnye konstrukcii. [Reinforced concrete structures]4(4):43-51. (In Russian) https://doi.org/10.22227/2949-1622.2023.4.43-51
6. **H. Sugihardjo, Y. Lesmana** (2018) FE Model of Low Grade Rubber for Modeling Housing's Low-Cost Rubber Base Isolators. Civil Engineering Journal. 4. 24. https://doi.org/10.28991/cej-030966
7. **Nidhal Jridi, M. Arfaoui** (2018) The capability of three separable finite-strain viscoelastic models to predict response of a filled

rubber material. Mechanics & Industry, Volume 19, Number 5. https://doi.org/10.1051/meca/2018014
8. **Wang, Rui & Li, Shiqi & Song, Shaoyun**. (2007). A Viscohyperelastic Constitutive Model for Rubber Used in Vibration Isolation. Noise & Vibration Worldwide. 38. 12-19. DOI 10.1260/095745607783360262.
9. **Hedayati Dezfuli, Farshad & Alam, M. Shahria.** (2012). Material Modeling of High Damping Rubber in Finite Element Method. Proceedings, Annual Conference - Canadian Society for Civil Engineering. 3.
10. **Tapia Romero, Manuel Alejandro & Gomez, Mariamne & Lugo, Luis**. (2020). Prony series calculation for viscoelastic behavior modeling of structural adhesives from DMA data. Ingeniería Investigación y Tecnología. 21. 1-10. DOI 10.22201/fi.25940732e.2020.21n2.014.
11. **Wu, Yifeng & Wang, Hao & Li, Aiqun.** (2016). Parameter Identification Methods for Hyperelastic and Hyper-Viscoelastic Models. Applied Sciences. 6. 386. DOI 10.3390/app6120386.
12. **Kartik Srinivas** (2020) Hyperelastic and Viscoelastic Characterization of Polymers and Rubber Materials Advanced Scientific and Engineering Services (AdvanSES)
13. **Lee, W.-S & Youn, Sung-Kie.** (2004). Topology optimization of rubber isolators considering static and dynamic behaviours. Structural and Multidisciplinary Optimization. 27. 284-294. DOI 10.1007/s00158-004-0376-1.
14. **Beijers, Clemens & de Boer, Andre.** (2003). Numerical modelling of rubber vibration isolators. Tenth International Congress on Sound and Vibration, Stockholm, Sweden
15. **Chip Fricke** (2013) Nonlinear Analysis Using Femap with NX Nastran. FEMAP SYMPOSIUM 2013 Mission Critical Design and Analysis
16. Rahnavard, Rohola & Craveiro, Hélder & Napolitano, Rebecca. (2020). Static and dynamic stability analysis of a steel-rubber isolator with rubber cores. Structures. 26. 441-455. DOI 10.1016/j.istruc.2020.04.048.
17. **Johnson & Chen** (2003) An Approximate Dissipation Function for Large Strain Rubber Thermo-Mechanical Analyses. NASA/TM-2003-212430
18. **Simo & Hughes** (1998) Computational Inelasticity. Springer-Verlag NewYork, In
19. **Bathe, K.J.** (1996). Finite Element Procedures. PRENTICE HALL, Upper Saddle River, New Jersey 07458
20. **Schaefer R.J**. (2001) Chapter 33 Mechanical Properties of Rubber
21. **Dashevskij M.A., Mondrus V.L., Motorin V.V.** (2017) Effektivnaya vibrozashchita verhnego stroeniya puti metropolitena [Effective vibration protection of the superstructure of the subway track]/ / Academia. Arhitektura i stroitel'stvo. [Academia. Architecture and construction.]. №4.

СПИСОК ЛИТЕРАТУРЫ

1. **Kaliske M., Rothert H.** Formulation and implementation of three-dimensional viscoelasticity at small and finite strains // 1997. Computational Mechanics. 19. P. 228–239. DOI: 10.1007/s004660050171.
2. **Ghoreishy H.R.** Determination of the parameters of the Prony series in hyper-viscoelastic material models using the finite element method // 2012. Materials & Design. 35. P. 791–797. DOI: 10.1016/j.matdes.2011.05.057.
3. **Li Z., Lou J.** Simulation on performance of rubber isolator based on ANSYS // 2011. 2nd International Conference on Mechanic Automation and Control Engineering (MACE 2011): Proceedings. DOI: 10.1109/MACE.2011.5987260.
4. **Ferreira A.J.M., Sá J.M.A.C., Marques A.T.** Nonlinear finite element analysis of rubber composite shells // 2003. Проблемы прочности. № 3. УДК 539.4. DOI: 10.1023/A:1024656604257.

5. **Мондрус В.Л., Сизов Д.К., Квасников Т.М.** Расчет резинометаллических виброизоляторов с отверстиями в системе виброзащиты зданий с помощью программного комплекса, реализующего метод конечных элементов // Железобетонные конструкции. 2023,4(4):43-51 https://doi.org/10.22227/2949-1622.2023.4.43-51
6. **Sugihardjo H., Lesmana Y.** FE model of low grade rubber for modeling housing's low-cost rubber base isolators // 2018. Civil Engineering Journal. 4. P. 24. DOI: 10.28991/cej-030966.
7. **Jridi N., Arfaoui M**. The capability of three separable finite-strain viscoelastic models to predict response of a filled rubber material // 2018. Mechanics & Industry. 19. № 5. DOI: 10.1051/meca/2018014.
8. **Wang R., Li S., Song S**. A viscohyperelastic constitutive model for rubber used in vibration isolation // 2007. Noise & Vibration Worldwide. 38. P. 12–19. DOI: 10.1260/095745607783360262.
9. **Hedayati Dezfuli F., Alam M.S.** Material modeling of high damping rubber in finite element method // 2012. Proceedings, Annual Conference - Canadian Society for Civil Engineering. 3.
10. **Tapia Romero M.A., Gomez M., Lugo L.** Prony series calculation for viscoelastic behavior modeling of structural adhesives from DMA data // 2020. Ingeniería Investigación y Tecnología. 21. P. 1–10. DOI: 10.22201/fi.25940732e.2020.21n2.014.
11. **Wu Y., Wang H., Li A**. Parameter identification methods for hyperelastic and hyper-viscoelastic models // 2016. Applied Sciences. 6. P. 386. DOI: 10.3390/app6120386.
12. **Srinivas K.** Hyperelastic and viscoelastic characterization of polymers and rubber materials // 2020. Advanced Scientific and Engineering Services (AdvanSES).
13. **Lee W.-S., Youn S.-K.** Topology optimization of rubber isolators considering static and dynamic behaviours // 2004. Structural and Multidisciplinary Optimization. 27. P. 284–294. DOI: 10.1007/s00158-004-0376-1.
14. **Beijers C., de Boer A.** Numerical modelling of rubber vibration isolators // 2003. Tenth International Congress on Sound and Vibration, Stockholm, Sweden.
15. **Beijers C., de Boer A.** Numerical modelling of rubber vibration isolators // 2003. Tenth International Congress on Sound and Vibration, Stockholm, Sweden.
16. **Rahnavard R., Craveiro H., Napolitano R.** Static and dynamic stability analysis of a steel-rubber isolator with rubber cores // 2020. Structures. 26. P. 441–455. DOI: 10.1016/j.istruc.2020.04.048.
17. **Johnson, Chen.** An approximate dissipation function for large strain rubber thermo-mechanical analyses // 2003. NASA/TM-2003-212430.
18. **Simo, Hughes**. Computational inelasticity // 1998. Springer-Verlag, New York.
19. **Bathe K.J.** Finite element procedures // 1996. Prentice Hall, Upper Saddle River, New Jersey 07458.
20. **Schaefer R.J.** Chapter 33 mechanical properties of rubber // 2001.
21. **Дашевский М.А., Мондрус В.Л., Моторин В.В.** Эффективная виброзащита верхнего строения пути метрополитена // Academia. Архитектура и строительство. 2017. №4.

Mondrus Vladimir Lvovich – Doctor of Technical Sciences, Professor, Corresponding Member. RAASN, Professor of the Department of Structural and Theoretical Mechanics, Institute of Industrial and Civil Engineering, National Research Moscow State University of Civil Engineering (NRU MGSU). 405, 26 Yaroslavskoe highway, Moscow, 129337, Russia. E-mail: mondrusvl@mgsu.ru

Мондрус Владимир Львович – д.т.н., профессор, член корр. РААСН, профессор кафедры строительной и теоретической механики, институт Промышленного и гражданского строительства, Национальный Исследовательский Московский Государственный Строительный Университет (НИУ МГСУ). 405, 26 Ярославское шоссе, Москва, 129337, Россия. E-mail:mondrusvl@mgsu.ru

Sizov Dmitry Konstantinovich – Ph.D., Vibroseysmozashchita LLC,6 st. Bratislavskaya, Moscow, 109341, Russia. E-mail: newfff@mail.ru

Kvasnikov Timofei Mikhailovich - 4rd year graduate student of the Department of Structural and Theoretical Mechanics, Institute of Industrial and Civil Engineering, National Research Moscow State University of Civil Engineering (NRU MGSU). 405, 26 Yaroslavskoe shosse, Moscow, 129337, Russia. E-mail: tima.kvasnikov@gmail.com, https://orcid.org/0000-0002-7836-4918

Сизов Дмитрий Константинович – к.т.н., ООО «Вибросейсмозащита»,ул. Братиславская, 6, Москва, 109341,Россия. E-mail: newfff@mail.ru

Квасников Тимофей Михайлович -аспирант 4 курса кафедры строительной и теоретической механики, институт Промышленного и гражданского строительства, Национальный Исследовательский Московский Государственный Стро-ительный Университет (НИУ МГСУ). 405, 26 Ярославское шоссе, Москва, 129337, Россия. E-mail: tima.kvasnikov@gmail.com, https://orcid.org/0000-0002-7836-4918

International Journal for Computational Civil and Structural Engineering, 22(1) 118–132 (2026)

DOI:10.22337/2587-9618-2026-22-1-118-132

HIGHER-MODE EFFECTS IN GLASS PANE RESPONSE TO CLOSE-RANGE BLAST: A FINITE ELEMENT AND SDOF MODEL COMPARISON

Ilham Nurhuda [1], ***Nelson T.K. Lam*** [2]

[1] Diponegoro University, Semarang, INDONESIA
[2] The University of Melbourne, Melbourne, AUSTRALIA

Abstract: The structural performance of glass panes under blast-induced pressures is commonly analyzed using single-degree-of-freedom (SDOF) models, which assume that the response is governed by the fundamental mode of vibration. However, in close-range explosion scenarios where the load duration is significantly shorter than the natural period of the glass pane, higher-mode effects can become significant. To enhance the blast resistance of glass panels, it is important to understand their behavior under a wide range of explosion scenarios, including close-range blasts. Unlike previous studies that have primarily focused on long-distance explosions with relatively long load durations, this study investigates the dynamic response of glass panes under short-duration blast loads. The investigation is conducted using calibrated finite element (FE) simulations on glass panes with varying dimensions and thicknesses, subjected to different blast intensities. Key response parameters examined include deflection shapes, bending stresses, and shear stresses. Results indicate that while the SDOF model can reasonably predict the maximum deflection of glass panes, it significantly underestimates peak bending and shear stresses in short-duration blast scenarios. A power-law relationship is proposed to quantify the discrepancy between SDOF and FE stress predictions as a function of the load duration-to-natural period ratio. These findings reveal the limitations of conventional SDOF models and highlight the need to account for higher-mode effects in the design of glazing systems exposed to close-in explosions.

Keywords: glass pane, close-range explosion, finite element, SDOF, higher modes

ВЛИЯНИЕ ВЫСШИХ ФОРМ КОЛЕБАНИЙ НА ОТКЛИК СТЕКЛЯННЫХ ПАНЕЛЕЙ ПРИ БЛИЖНИХ ВЗРЫВАХ: СРАВНЕНИЕ МОДЕЛЕЙ МКЭ И SDOF

Ильхам Нурхуда [1], ***Нельсон Т.К. Лам*** [2]

[1] Университет Дипонегоро, Семаранг, ИНДОНЕЗИЯ
[2] Мельбурнский университет, Мельбурн, АВСТРАЛИЯ

Аннотация: Поведение стеклянных панелей при взрывных воздействиях обычно описывается моделями SDOF, основанными на фундаментальной форме колебаний. Однако при ближних взрывах с короткой длительностью импульса значимыми становятся высшие формы. В работе с использованием метода конечных элементов исследован динамический отклик панелей различной толщины и размеров при кратковременных нагрузках. Рассмотрены прогибы, изгибные и касательные напряжения. Показано, что модель SDOF удовлетворительно предсказывает максимальный прогиб, но существенно занижает пиковые напряжения. Для оценки расхождений предложена степенная зависимость от отношения длительности импульса к собственному периоду колебаний. Результаты выявляют ограничения классических моделей SDOF и необходимость учёта высших форм при проектировании остекления, подверженного ближним взрывам.

Ключевые слова: стеклянная панель, ближний взрыв, метод конечных элементов, модель SDOF, высшие формы колебаний

1. INTRODUCTION

Buildings such as government offices, hotels, and commercial facilities are often potential targets of terrorist attacks. These types of structures frequently incorporate large glass panes in their façades, which are widely recognized as the most vulnerable components during an explosion [1], [2]. Evidence from past terrorist incidents shows that buildings designed in accordance with modern codes of practice generally experienced limited structural damage. However, extensive damage to surrounding glass façades was frequently observed. Flying glass fragments from shattered panes have been identified as one of the primary causes of injury [3], [4].

The behaviour of glass panes subjected to explosions can be analysed numerically using the finite element method (FEM), as demonstrated in previous studies [5], [6]. However, FEM analyses typically require considerable time and computational resources for both modelling and simulation. Therefore, for practical purposes, simplified single-degree-of-freedom (SDOF) models are often used as an alternative [7], [8], [9], [5]. Given that blast pressures generated by long-distance explosions generally have longer durations than those from close-range blasts, the response of the glass pane in such cases is often dominated by the fundamental mode of vibration. As a result, SDOF models can be effectively employed to estimate the response of glass panes under long-duration blast loading, offering a more practical alternative to complex numerical simulations.

Long distance explosion scenarios are generally valid in situations where security measures have precluded the possibility of a large explosion (generated by a car bomb or trick bomb, for example) to be detonated at close range to a protected target. However, the target, or part of it, could still be susceptible to attacks by the use of smaller explosion devices at close range. Examples of such "minor" blast scenarios include the parcel bomb incident in Paris in 2007 and the grenade attack on the US embassy in Greece in the same year. This paper focuses on the dynamic behaviour of glass panes when subject to close-range explosions in which blast pressures of much shorter duration and higher peak overpressure are generated. With load duration shorter than that of the fundamental natural period of glass panes, higher modes effects can become significant and need to be taken into account in the strength evaluation.

This paper investigates the influence of higher vibration modes on the dynamic response of glass panes. The response parameters of interest include displacement, normal (bending) stress, and transverse shear stress within the glass panes. The main contributions of this paper are as follows: (1) validation of finite element (FE) modeling under short-duration loading; (2) a comparative analysis of the responses obtained from calibrated FE simulations and SDOF models across varying ratios of load duration (td) to the natural period (T) of the glass panes; and (3) derivation of correction formulae for SDOF stress estimates under higher-mode influence.

2. METHODOLOGY

2.1. Geometry of Glass Panes

This study examines the behavior of glass panes supported on two opposite sides, a configuration commonly found in façade walls, interior partitions, and display windows. This type of support typically results in a relatively long fundamental natural period compared to the duration of a blast load.

Table 1. Dimension of glass panes

Pane Dimensions (mm)	Glass Thickness (mm)
500 x 500	4
1000 x 1000	10
1000 x 1000	4
2000 x 2000	19

The glass panes were analyzed in three size categories: small (500 mm x 500 mm), medium (1000 mm x 1000 mm), and large (2000 mm x 2000 mm). The thickness of each pane was

selected to meet wind load requirements in accordance with the AS 1288 standard [10], ensuring structural adequacy under normal service conditions. The detailed pane dimensions and thicknesses are listed in Table 1.

2.2. Finite Element (FE) Modelling and Verification

In this study, the dynamic behaviour of the glass panes was studied analytically using LS-DYNA, an explicit, non-linear 3D finite element analysis (FEA) code [11]. The glass panes were modelled using shell elements. Figure 1a shows a finite element (FE) model of a glass pane supported on 2 sides. The X, Y, and Z axes in Figure 1a are the global axes in the FE model which are used as a reference for calculating the distribution of blast pressure and internal forces in the glass pane. Point O denotes the centre of the pane, while Point A is located at the support such that line OA is parallel to the X-axis. Figure 1b shows a typical shell element. Notations r, s, and t in Figure 1b refer to local axes in a shell element, and a_k denotes the element thickness at node k.

The shell elements used in this analysis considered both large deformation and transverse shear in the elements [12], [11], [13]. Annealed glass was used throughout the study. The glass material was modelled as a linearly elastic isotropic material with Young's modulus = 68,500 MPa, Poisson's ratio = 0.23 and density = 2,500 kg/m^3.

The analysis procedure was verified against results from physical experiments. Physical tests were conducted on a glass pane of size 1000 mm x 1000 mm x 5 mm, which was simply supported along two parallel edges. The glass pane was subject to an impact load from an elastic ball with a diameter of 27 mm. The elastic ball was dropped from a heigh of 1400 mm onto the centre of the pane. An accelerometer was attached to the ball to record its acceleration during impact. The deflection of the glass pane was measured using linear variable displacement transducers (LVDTs) positioned beneath the glass. The test set-up is illustrated in Figure 2.

The impact load, illustrated in Figure 3, was calculated by multiplying the measured acceleration by the combined mass of the elastic ball and the attached accelerometer. The duration of the impact loading, also shown in Figure 3, was approximately 3 milliseconds, significantly shorter than the fundamental natural period of vibration of the glass pane (T = 84 ms). This impact duration is consistent with test results reported in the literature for a single loading cycle (Zhang et al., 2025). Since the load duration was much shorter than the fundamental period, the dynamic response of the glass pane was strongly influenced by higher vibration modes, as evidenced in Figure 4.

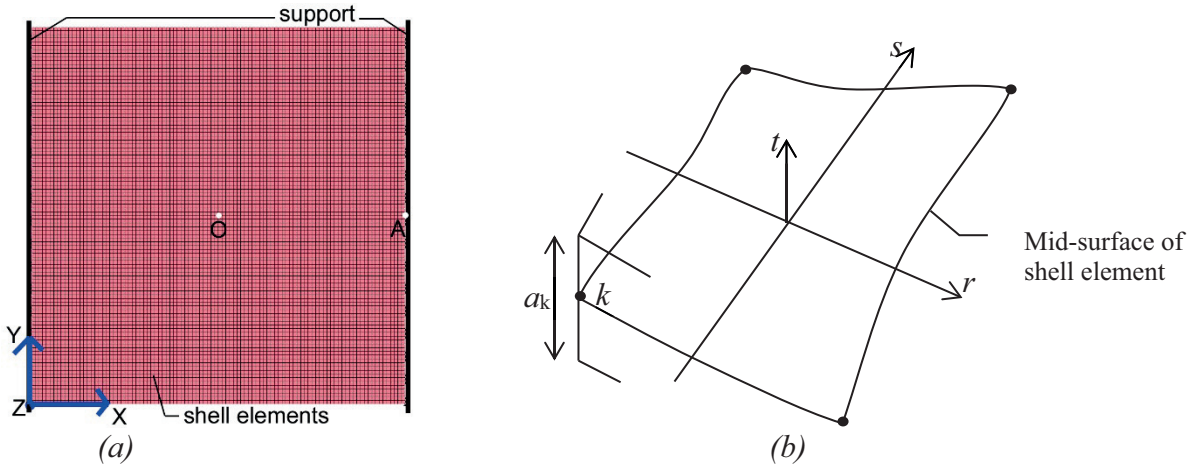


Figure 1. Finite element model (a) FE model for glass panes supported on 2 sides, (b) Shell element [15]

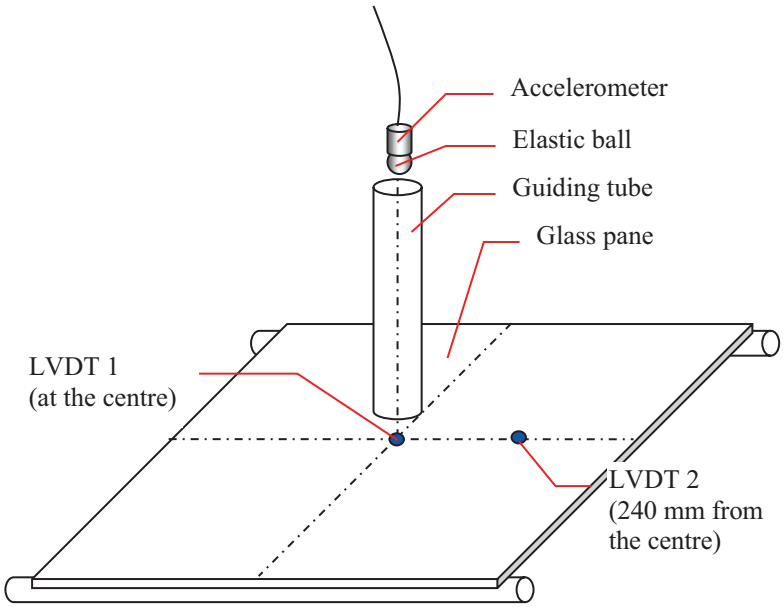


Figure 2. The physical test set up

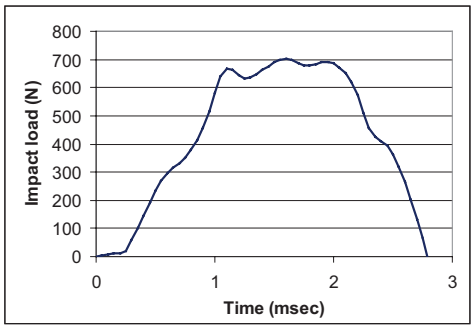
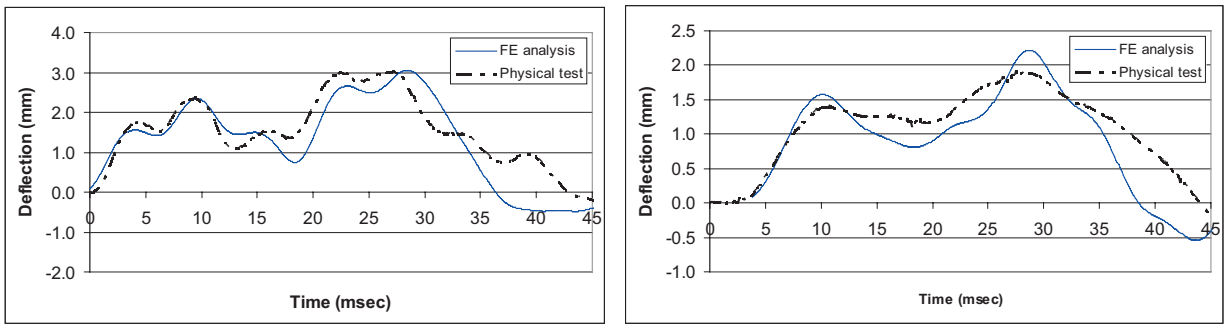


Figure 3. Impact load



(a) *(b)*

Figure 4. Deflections of the glass pane (a) at LVDT 1, (b) at LVDT 2 (refer Figure 2)

Figure 4 presents a comparison between deflections obtained from the physical experiment and those predicted by the finite element (FE) analyses. As shown, the FE predictions align well with the experimental observations, particularly during the early phase of the response. However, in the physical test, the glass pane experienced multiple impacts due to the ball bouncing upon contact (Zhang et al., 2025). Since this aspect of the experiment was not incorporated into the FE model, the numerical predictions could not fully match the measured deflections throughout the entire response. Nevertheless, the applicability of the developed FE models for simulating the dynamic behaviour of glass panes has been successfully verified.

2.3. SDOF Model Formulation and Assumptions

Analysis using a representative finite element (FE) model can provide accurate predictions of a structure's dynamic behaviour. However, such analysis requires sophisticated FE software, such as LS-DYNA. Simpler methods, such as single-degree-of-freedom (SDOF) models, have been widely used to predict structural responses under blast loading. SDOF models have been shown to provide reasonable estimates when the explosion originates from a long distance [7]. However, their applicability to glass panes subjected to close-range explosions remains uncertain and warrants further investigation to evaluate the accuracy of the results obtained from SDOF-based analyses.

In SDOF model analyses, the dynamic properties of the structure are characterized by its equivalent mass (m*), equivalent stiffness (k*), and equivalent damping (c) as shown in Figure 5a. The applied loads must also be transformed into an equivalent force Methods for calculating these SDOF parameters are well documented in the literature [8], [16], [17]. In this study, the SDOF parameters representing the glass pane were calculated using Rayleigh's method, which is based on the principle of conservation of energy. The blast induced pressure was defined by Eq 1, and the deflection shape function of the glass pane was of the sinusoidal form as defined by Eq 2 forming part of the Rayleigh's method. The equivalent mass (m*) and equivalent stiffness (k*) representing the glass pane were calculated according to the deflection shape function using Eqs 3 – 6. Once these parameters were obtained, the fundamental natural period of vibration of the glass pane (T) could be estimated.

$$p(x,y,t) = pr(t).\left[\frac{R^2}{\left(x-\frac{a}{2}\right)^2+\left(y-\frac{b}{2}\right)^2+R^2}\right] + pi(t)\left[1-\frac{R}{\sqrt{\left(x-\frac{a}{2}\right)^2+\left(y-\frac{b}{2}\right)^2+R^2}}\right]^2 \quad (1)$$

$$\psi(x,y) = sin\frac{\pi x}{a} \quad (2)$$

for plates supported on 2 parallel sides

$$\psi(x,y) = sin\frac{\pi x}{a}\ sin\frac{\pi y}{b}$$

for plates supported on 4 sides

$$m^* = \int_0^a \int_0^b m.\ \psi(x,y)^2 dx.dy \quad (3)$$

$$k^* = D\int_0^a \int_0^b \begin{Bmatrix} s \\ -2(1-\nu).t \end{Bmatrix} dxdy \quad (4)$$

$$s = \left[\frac{\partial^2\psi(x,y)}{\partial x^2}+\frac{\partial^2\psi(x,y)}{\partial y^2}\right]^2$$

$$t = \left[\frac{\partial^2\psi(x,y)}{\partial x^2}\frac{\partial^2\psi(x,y)}{\partial y^2}-\left(\frac{\partial^2\psi(x,y)}{\partial x\partial y}\right)^2\right]$$

$$D = Eh^3/12(1-\nu^2) \quad (5)$$

$$p*(t) = \int_0^a \int_0^b p(x,y,t).\ \psi(x,y)dx.dy \quad (6)$$

where $\psi(x,y)$ is the deflection shape function, p* is the equivalent force, x and y are coordinates on the glass pane measured from the bottom left corner of the pane (see Figure 1a), a and b are the width and length of the pane, h is the thickness, t is time, $p(x,y,t)$ is the blast pressure function, $pr(t)$ is the reflected pressure at time t, $pi(t)$ is the incident pressure at time t, R is the distance from the explosive to the centre of the target, m is mass per unit area, E is Young's modulus, and ν is Poisson's ratio.

For glass panes supported on all four sides, membrane action has been found to dominate under large deflections [17]. An SDOF model that incorporates the contribution of membrane stiffness is shown in Figure 5b, and its equation of motion is presented in Equation 7. The displacement x(t) in Equation 7 can be solved numerically using the Central Difference Method for step-by-step time integration.

$$m*\ddot{x}(t) + c.\dot{x}(t) + k*.x(t) = p*(t) \quad (7)$$

where $x(t)$, $\dot{x}(t)$, and $\ddot{x}(t)$ are the displacement, velocity, and acceleration at the centre of glass plates, and c is damping coefficient.

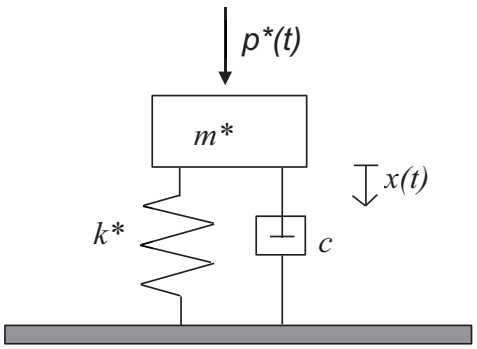


Figure 5. SDOF model

2.4. Blast Loading Model and Scenarios

Blast pressures result from the instantaneous release of energy during explosive detonation. The magnitude of the blast loading is typically quantified in terms of the equivalent TNT weight

of the explosive [18], [4], [19], [2]. For explosives other than TNT, their weight can be converted into an equivalent TNT weight using Equation 8 [19].

$$W_{TNT} = W_{EXP}.(Q_{EXP}/Q_{TNT}) \quad (8)$$

where W_{TNT} is the equivalent TNT charge weight, W_{EXP} is the weight of the explosive, Q_{EXP} is the mass specific energy of the detonated explosive, and Q_{TNT} is the mass specific energy of TNT.

An explosion produces hot gases that expand rapidly, displacing the surrounding air and generating blast waves in the atmosphere. As the blast wavefront reaches the ground, it is reflected, and the interaction between the incident and reflected waves results in even higher pressures. When the blast wave strikes a target, its expansion is constrained, causing a sudden rise in pressure on the target surface, as illustrated in Figure 6.

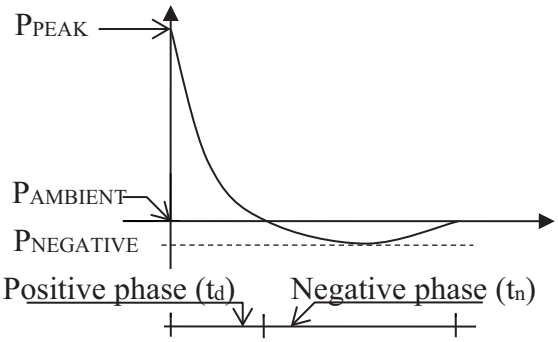


Figure 6. Typical pressure-time history

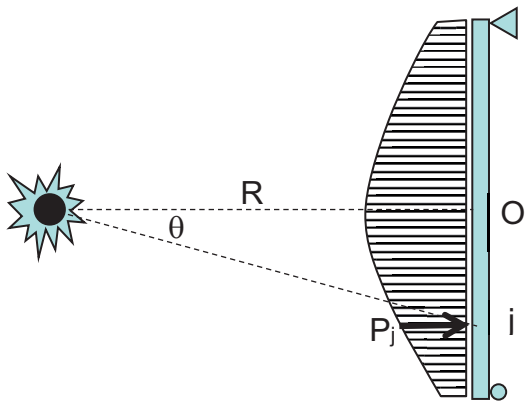


Figure 7. Distribution of blast pressure

The blast-induced pressure then gradually decreases to ambient levels at time t_d, marking the end of the positive phase. Following this, the pressure may drop below ambient, creating a negative (suction) phase, before returning to normal atmospheric conditions. Since the negative phase typically reduces the target's deflection, its effect can be neglected, as is done in this study.

The blast pressure parameters illustrated in Figure 6 depend on various factors, including charge weight (expressed as equivalent TNT weight), stand-off distance, the location of the detonation (in air or on the surface), and the presence of obstacles between the explosive and the target. Methods for estimating blast pressure–time histories are well-documented in the literature [19]. Existing analytical approaches can generally be grouped into two main categories: (1) analytical methods that use empirical formulae and charts, and (2) numerical simulations, such as computational fluid dynamics (CFD), which are computationally expensive and thus better suited for modelling blast effects on structures with complex geometries or in complicated environments [20], [21]. Blast scenarios involving structures with regular geometry in standard environments, analytical methods based on formulae and graphs are typically sufficient [13], [19].

In this study, the ConWep method [22] was used to model the blast-induced pressures on the glass panes. ConWep is based on empirical test data and analytical approximations, and has been widely adopted by both researchers and practitioners. Furthermore, it has been shown to provide reliable predictions of blast effects [23].

The distribution of blast-induced pressure on the surface of a target is significantly influenced by the stand-off distance. At long stand-off distances, the distance from the explosive charge to any point on the planar target is nearly uniform, resulting in a small angle of incidence (θ), as illustrated in Figure 7. Under such conditions, the blast pressure can be reasonably assumed to be uniformly distributed across the target surface. However, at short stand-off distances, this

uniform pressure assumption is no longer valid due to the increased variation in angle and distance. In this study, the distribution of the blast load, $P_j(t)$, on the glass panes is calculated using Equation 9 [24].

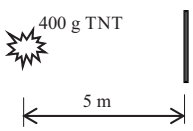
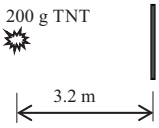
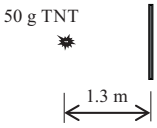
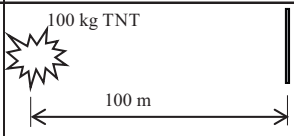
	Scenario A	Scenario B	Scenario C	Scenario D
				
P_i	26.51 kPa	37.48 kPa	79.81 kPa	5.53 kPa
P_r	58.57 kPa	85.77 kPa	208.4 kPa	11.27 kPa
td	3.1 ms	2.284 ms	1.188 ms	28.12 ms
Glass Panes	500 mm x 500 mm x 4 mm (td/T = 0.12)	1000 mm x 1000 mm x 4 mm (td/T = 0.02) 1000 mm x 1000 mm x 10 mm (td/T =0.05)	2000 mm x 2000 mm x 19 mm (td/T = 0.01)	2000 mm x 2000 mm x 19 mm (td/T = 0.32)

Figure 8. Blast scenarios

$$P_j(t) = Pr_o(t).\cos^2(\theta) + Pi_o(t).(1-\cos(\theta))^2 \quad (9)$$

where $Pr_o(t)$ and $Pi_o(t)$ are the reflected and incident pressures respectively at point "O" as defined by ConWep, and θ is the angle of incidence as illustrated in Figure 7.

This investigation focused on analysing the effects of explosions generated by handheld bombs, such as grenades and parcel bombs, at close range to the target. The equivalent TNT weights in these scenarios ranged from 50 to 400 grams. In this study, explosives were positioned directly in front of the centre of the glass panes at four different stand-off distances: 1.3 m, 3.2 m, 5.0 m, and 100 m. Details of the blast scenarios are presented in Figure 8. Scenario D represents a case where a glass pane responds to a long-range explosion at a stand-off distance of 100 m, included for comparison purposes.

3. RESULTS AND DISCUSSIONS

3.1. Deflection of Glass Panes

Figure 9a presents the displacement-time history at the centre of a glass pane measuring 500 mm x 500 mm x 4 mm, subjected to blast-induced pressure with a duration of 3.1 ms (scenario A) or corresponding to a td/T ratio of 0.12. Figure 9b presents results for a glass pane of size 1000 mm x 1000 mm x 10 mm under a blast pressure duration of 2.3 ms (scenario B), or td/T = 0.05. Figures 9c and 9d present results of glass panes of identical size (2000 mm x 2000 mm x 19 mm) but subjected to different blast scenarios. The glass pane in Figure 9c was exposed to a close-range explosion, while the one in Figure 9d experienced a long-range explosion. Across Figures 9a – 9d, it is consistently observed that a decrease in the td/T ratio increases the contributions of higher modes, as indicated by the wavy broken lines in the figures.

Results from the finite element (FE) analysis are presented alongside predictions from the SDOF models in Figures 9a–9d. The SDOF model used in the analyses did not include membrane stiffness (Figure 4a). Figures 9a–9d demonstrate that the deflection profiles obtained from the SDOF model without accounting for higher-mode effects can still be representative of the actual behaviour, particularly when the td/T ratio is not less than 0.05. However, when the td/T ratio becomes smaller (as shown in Figure 9c), the accuracy of the SDOF model predictions may diminish. Furthermore, Figure 9c illustrates that higher-mode effects can lead to noticeable reduction in the maximum deflection of the glass pane.

Since the parameters defining the SDOF generalization are based on an assumed deflection shape, it is important to compare this

assumed sinusoidal function with deflection profiles obtained from finite element (FE) analyses. Figure 10a shows the normalized deflection shape of the glass pane, as computed from the FE analysis (along the OA section defined in Figure 1a) at the moment of maximum deflection.

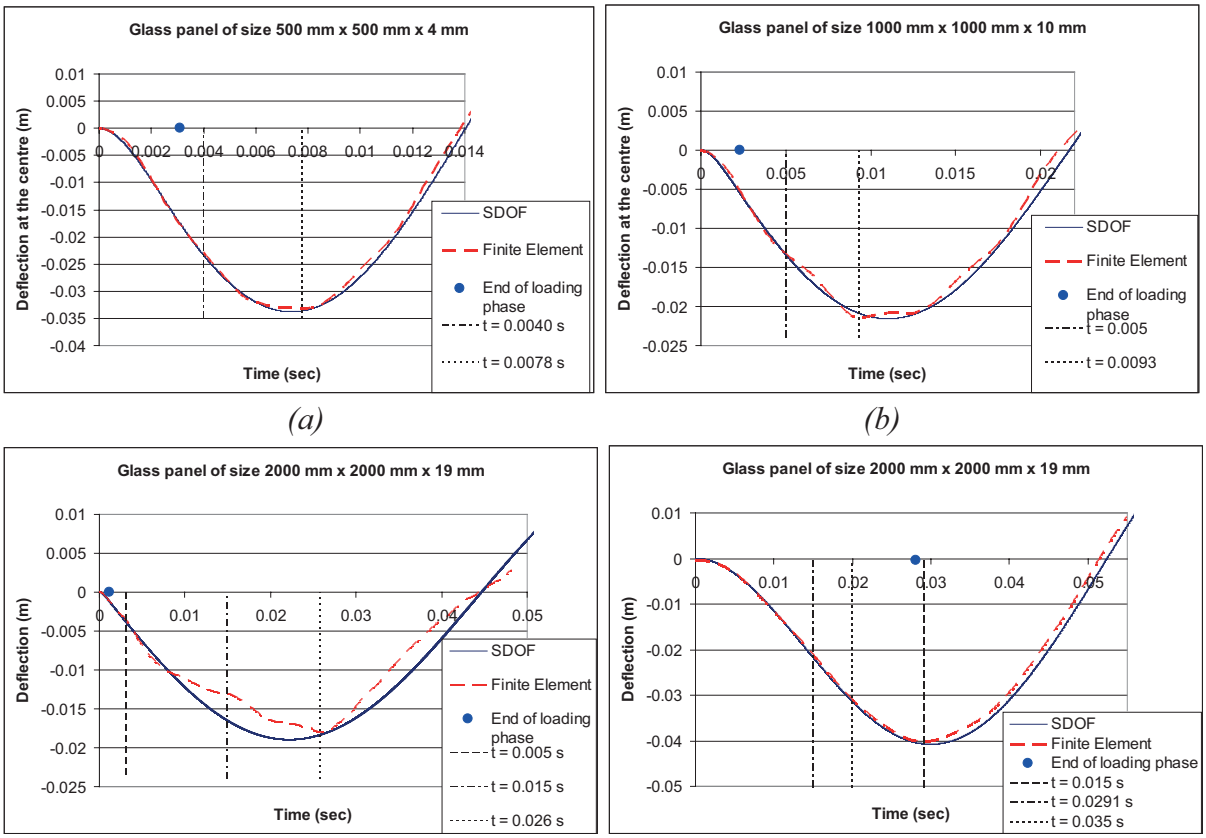


Figure 9. Deflection-time history of glass panes (a) td/T = 0.12, (b) td/T = 0.05, (c) td/T = 0.01, (d) td/T = 0.32

Figures 10b–10d present deflection shapes at other time instances, as indicated in the respective legends. Overall, the sinusoidal deflection shape assumed in the SDOF generalization shows reasonable agreement with the FE results. However, a noticeable discrepancy is observed in Figure 10c, where the td/T ratio is very small (0.01).

3.2. Bending Stress

The strength of glass is commonly evaluated based on the major principal stresses estimated on the surface of the glass pane [13], [25], [16], [26]. For glass panes supported on two parallel sides, these stresses are primarily governed by bending. Figures 11a–11c present the time history of the maximum bending stresses at the centre of the glass pane. The results reveal a highly fluctuating time-history of bending stress, in contrast to the more predictable deflection response. This fluctuation is indicative of the significant influence of higher vibration modes on the bending stress.

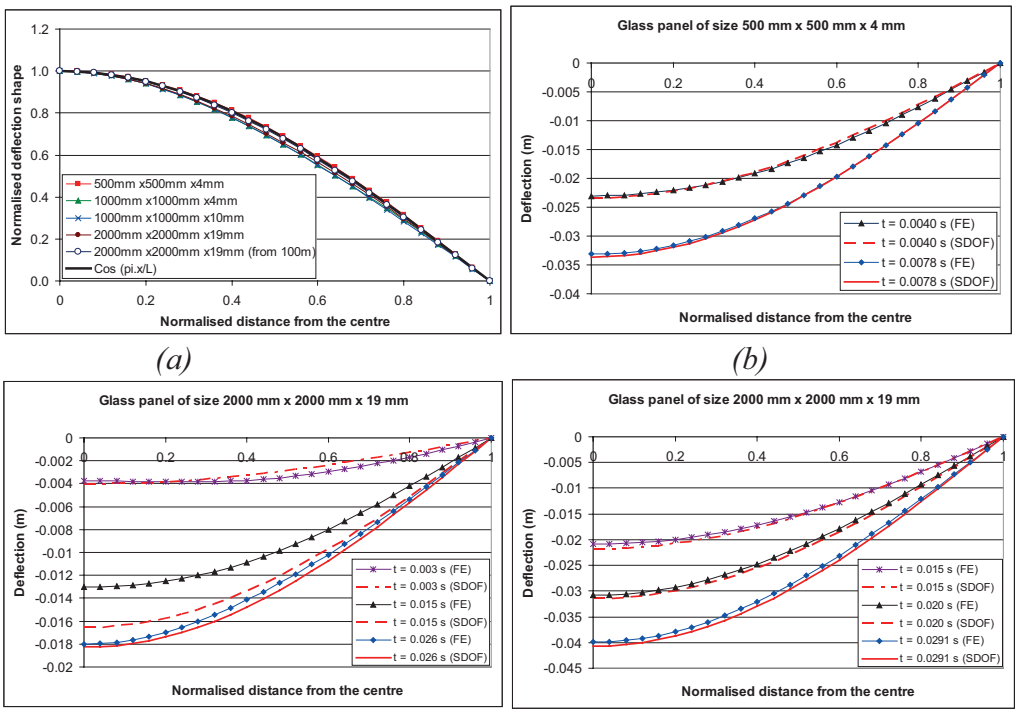


Figure 10. Deflection shape along section OA (a) Maximum deflection shape for different glass panes (b) 500 mm x 500 mm x 4 mm glass pane (td/T = 0.12), (c) 2000 mm x 2000 mm x 19 mm glass pane (td/T = 0.01), (d) 2000 mm x 2000 mm x 19 mm glass pane (td/T = 0.32)

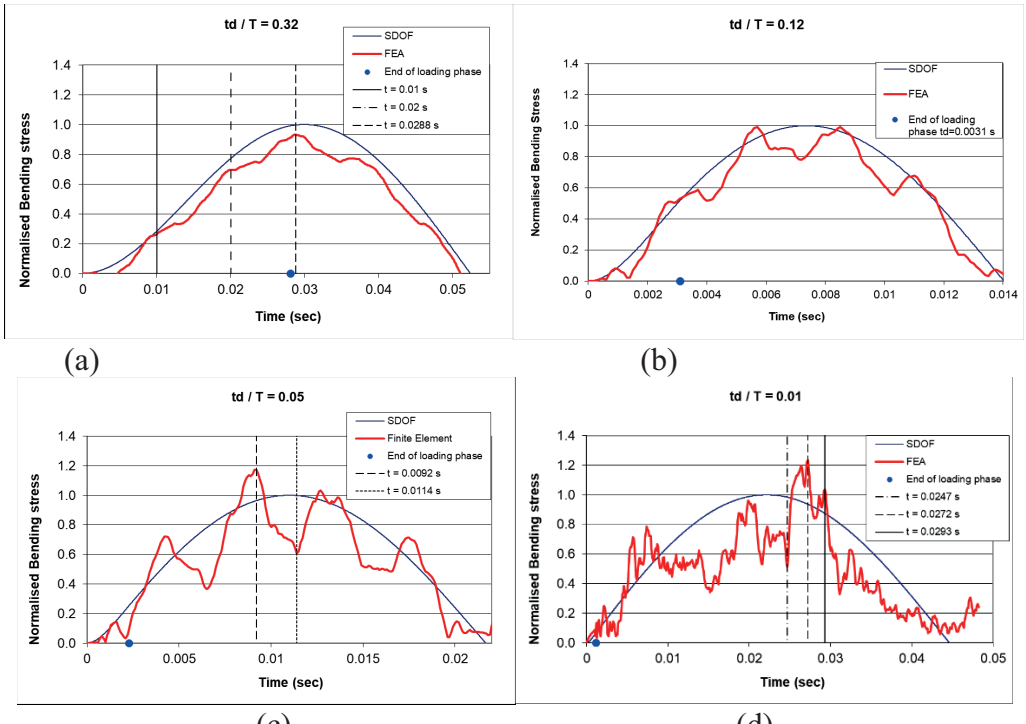


Figure 11. Time history of the normalized bending stress at the centre of (a) a glass pane measuring 2000 mm x 2000 mm x 19 mm, with td/T=0.32, (b) a glass pane measuring 500 mm x 500 mm x 4 mm, with td/T=0.12; (c) a glass pane measuring 1000 mm x 1000 mm x 10 mm, with td/T=0.05, (d) a glass pane measuring 2000 mm x 2000 mm x 19 mm, with td/T=0.01

Figure 11a demonstrates good correlation between the predictions of the generalized SDOF model and those from the finite element (FE) analysis. In blast scenarios with lower td/T ratios (Figures 11b and 11c), the maximum stress values predicted by the generalized SDOF model are significantly lower than those obtained from the FE analysis. While SDOF analysis offers the advantages of simplicity and lower computational cost, some limitations in accuracy have been identified. As shown in Figure 11, the magnitude of stress fluctuations increases as the td/T ratio decreases. Therefore, the accuracy of the SDOF model can be improved by modifying its results to account for higher-mode effects, whose significance has been shown to depend on the td/T ratio. The discrepancy between the FE and SDOF predictions of bending stress can be expressed as the ratio σ_{FEA} / σ_{SDOF}. Figure 12 illustrates that this ratio increases as the td/T ratio decreases. Furthermore, the relationship between σ_{FEA} and σ_{SDOF} can be modelled using the power function presented in Equation 8, which is valid for rectangular glass panes supported on two sides with td/T values ranging between 0.01 and 0.12.

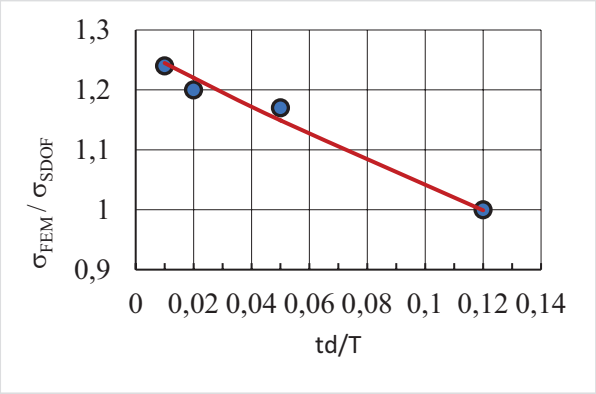
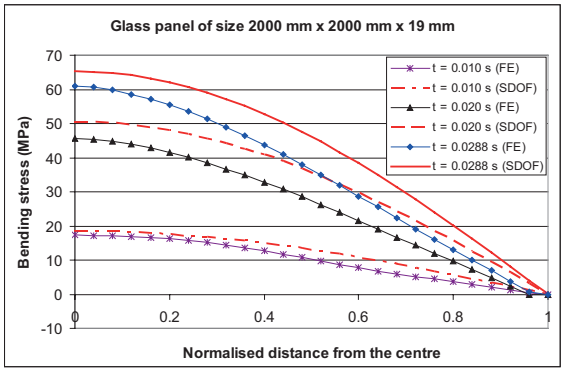


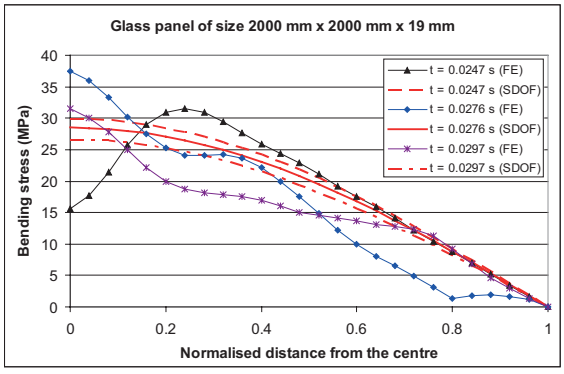
Figure 12. Relationship between $\sigma_{FEA}/\sigma_{SDOF}$ and td/T.

$$\sigma_{FEA} = 1.27\ \sigma_{SDOF}.e^{-2(td/T)} \qquad (8)$$

The probabilistic strength of glass depends on the effective area of the glass pane, which is influenced by the surface stress distribution [27]. Under dynamic conditions, surface stresses vary over time, as illustrated in Figures 13a–13b, and can be difficult to predict. Discrepancies between estimates from the SDOF analysis and those from the finite element (FE) analysis are particularly pronounced when the td/T ratio is small. Even at td/T = 0.32 (Figure 13a), notable differences remain. For glass panes subjected to close-range explosions (i.e., small td/T ratios), the time-dependent variation of surface stress must be considered when calculating the probabilistic strength of the glass. However, detailed considerations of failure probability are beyond the scope of this paper.



(a)



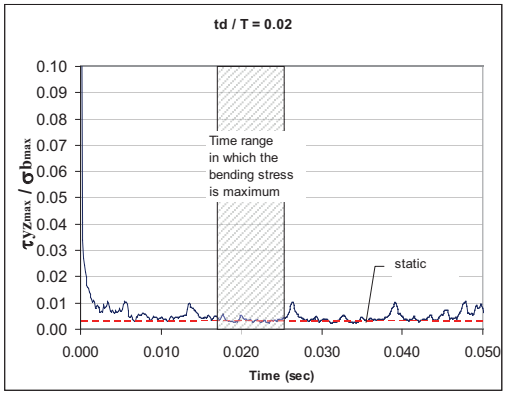
(b)

Figure 13. Maximum bending stress profile along section OA in: (a) glass panes of size 2000 mm x 2000 mm x 19mm (td/T=0.32), (b) glass panes of size 2000 mm x 2000 mm x 19mm (td/T=0.01)

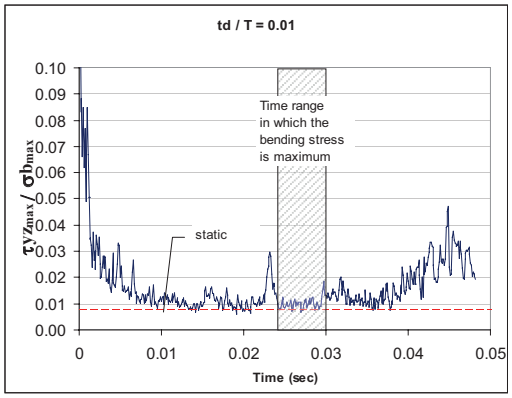
3.3. Transverse Shear Stress

In glass panes subjected to static loading, the effect of transverse shear stress is often neglected. This is because, under static conditions, the

magnitude of transverse shear stress in thin glass panes is typically much smaller than that of the principal (bending) stresses. However, under dynamic loading, the bending moment stress profile varies with time, and its slope can be significantly steeper than that in static loading. Since transverse shear stress is related to the rate of change of bending moment, its magnitude under dynamic conditions can become substantial. The significance of transverse shear stress in dynamically loaded glass panes is illustrated in Figure 14, where its intensity is expressed as the ratio of maximum transverse shear stress to maximum bending stress (τyz_{max} / σb_{max}).



(a)



(b)

Figure 14. Time history of the ratio of maximum shear stress to the maximum major principal stress (a) in glass pane of size 1000 mm x 1000 mm x 4 mm, (b) in glass pane of size 2000 mm x 2000 mm x 19 mm

Figures 14a and 14b present the time histories of the ratio τyz_{max} / σb_{max} for td/T = 0.02 and 0.01, respectively. The shaded regions in both figures indicate the time intervals during which the bending stress reaches its maximum. During these periods of peak bending stress, the ratio τyz_{max} / σb_{max} is generally low and comparable to values observed under static loading conditions. However, the figures also show that the ratio τyz_{max} / σb_{max} increases as the td/T ratio decreases, emphasizing the growing significance of transverse shear stress in short-duration blast loading scenarios.

Figures 14a and 14b show that the ratio τyz_{max} / σb_{max} is very high during the initial stage of the response. At this early phase, the magnitude of the transverse shear stress can reach levels comparable to the bending stress (i.e., τyz_{max} / $\sigma b_{max} \approx 1$). This indicates that, in cases where the explosion occurs at close range, the glass pane may fail due to excessive shear stress. However, it is important to note that such high shear stress levels occur only for a very brief duration, on the order of microseconds.

4. CONCLUSIONS

The findings of this study confirm the significant influence of higher vibration modes on the dynamic response of glass panes subjected to close-range blast loading. The following key conclusions are drawn:

1. The finite element (FE) models have been shown to accurately simulate the short-duration dynamic response of glass panes, particularly during the critical early phase of loading. Despite minor discrepancies caused by multiple impacts in the physical experiment, the overall agreement confirms the capability and validity of the FE models for use in this application.
2. Comparative analysis between calibrated finite element (FE) simulations and single-degree-of-freedom (SDOF) models demonstrates that SDOF models can effectively estimate the maximum deflection at the centre of glass panes, provided their limitations are acknowledged.
3. Higher-mode effects were found to significantly influence the displacement, normal (bending) stress, and transverse shear stress in

glass panes, particularly under short-duration loading conditions (i.e., low td/T ratios). A correction formula was developed to improve SDOF stress estimates by accounting for the influence of higher vibration modes. This correction enhances the accuracy of SDOF predictions in short-duration blast scenarios involving glass panes supported on two sides. Furthermore, the simulations indicate that the SDOF model provides reasonably accurate results when td/T > 0.1.

4. At the early stage of response, very high transverse shear stress was observed, particularly near the centre of the pane. If the explosion occurs at close range, this intense shear stress, although short-lived, may cause shear failure.

ACKNOWLEDGEMENTS

The authors gratefully acknowledge Prof. Emad Gad for his valuable guidance and input during the development of the research underlying this study.

REFERENCES

1. **X. Zhang and C. Bedon,** "Vulnerability and Protection of Glass Windows and Facades under Blast: Experiments, Methods and Current Trends," *Int. J. Struct. Glass Adv. Mater. Res.*, vol. 1, no. 2, pp. 10–23, Feb. 2017, doi: 10.3844/sgamrsp.2017.10.23.
2. **C. Bedon** *et al.*, "Performance of structural glass facades under extreme loads – Design methods, existing research, current issues and trends," *Constr. Build. Mater.*, vol. 163, pp. 921–937, Feb. 2018, doi: 10.1016/j.conbuildmat.2017.12.153.
3. **H.S. Norville, Natalie Harvill, Edward J. Conrath, and Sheryll Shariat,** "Glass-Related Injuries in Oklahoma City Bombing," *J. Perform. Constr. Facil.*, vol. 13, no. 2, pp. 50–56, May 1999.
4. **S. Das Adhikary**, "Review of Glazing and Glazing Systems under Blast Loading," *Pract. Period. Struct. Des. Constr.*, vol. 21, no. 1, Feb. 2016, doi: 10.1061/(asce)sc.1943-5576.0000264.
5. **L. Figuli, Z. Zvaková, and C. Bedon,** "Design and Analysis of Blast Loaded Windows," *Procedia Eng.*, vol. 192, pp. 177–182, 2017, doi: 10.1016/j.proeng.2017.06.031.
6. **J. Rudshaug, K.O. Aasen, O.S. Hopperstad, and T. Børvik**, "A physically based strength prediction model for glass," *Int. J. Solids Struct.*, vol. 285, p. 112548, Dec. 2023, doi: 10.1016/j.ijsolstr.2023.112548.
7. **K. Fischer and I. Häring**, "SDOF response model parameters from dynamic blast loading experiments," *Eng. Struct.*, vol. 31, no. 8, pp. 1677–1686, Aug. 2009, doi: 10.1016/j.engstruct.2009.02.040.
8. **K. Lee and J. Shin**, "Equivalent single-degree-of-freedom analysis for blast-resistant design," *Int. J. Steel Struct.*, vol. 16, no. 4, pp. 1263–1271, Dec. 2016, doi: 10.1007/s13296-016-0073-0.
9. **S. Chen, X. Chen, G.-Q. Li, and Y. Lu,** "A theoretical study on the P-I diagram of framed monolithic glass window subjected to blast loading," *Eng. Struct.*, vol. 150, pp. 497–510, Nov. 2017, doi: 10.1016/j.engstruct.2017.07.055.
10. AS1288, *Glass in building-Selection and installation*, Sydney, NSW., 2006.
11. **J.O. Hallquist,** *LS-DYNA Theory Manual*. Livermore, CA: Livermore Software Technology Corporation, 2006.
12. **T. Belytschko, J.I. Lin, and C.-S. Tsay**, "Explicit algorithms for the nonlinear dynamics of shells," *Comput. Methods Appl. Mech. Eng.*, vol. 42, no. 2, Feb. 1984.
13. **J. Wei, M.S. Shetty, and L.R. Dharani,** "Failure analysis of architectural glazing subjected to blast loading," *Eng. Fail. Anal.*, vol. 13, no. 7, pp. 1029–1043, Oct. 2006, doi: 10.1016/j.engfailanal.2005.07.010.
14. **R. Zhang, X. Zhai, X. Zhou, P. Li, and X. Zhi**, "Experimental and numerical study of annealed glass subjected to low-velocity

impact: Simulation of windborne debris impact," *J. Build. Eng.*, vol. 106, p. 112504, Jul. 2025, doi: 10.1016/j.jobe.2025.112504.
15. **M.L. Bucalem and K.J. Bathe,** "Finite Element Analysis of Shell Structures," *Arch. Comput. Methods Eng.*, vol. 4, no. 1, pp. 3–61, 1997.
16. **N.T.K. Lam, E.F. Gad, I. Nurhuda, and I. Calderone**, "Impact Resistance of Annealed Glass Panels," *J. Perform. Constr. Facil.*, vol. 25, no. 5, pp. 422–432, Oct. 2011, doi: 10.1061/(asce)cf.1943-5509.0000181.
17. **A.W.D.Q.R. Reis, R.B. Burgos, and M.F.F.D. Oliveira,** "Nonlinear Dynamic Analysis of Plates Subjected to Explosive Loads," *Lat. Am. J. Solids Struct.*, vol. 19, no. 1, 2022, doi: 10.1590/1679-78256706.
18. **T. Krauthammer and A. Altenberg,** "Negative phase blast e!ects on glass panels," *Int. J. Impact Eng.*, vol. 24, pp. 1–17, 2000.
19. **A. Ullah, F. Ahmad, H.-W. Jang, S.-W. Kim, and J.-W. Hong**, "Review of analytical and empirical estimations for incident blast pressure," *KSCE J. Civ. Eng.*, vol. 21, no. 6, pp. 2211–2225, Sep. 2017, doi: 10.1007/s12205-016-1386-4.
20. **O.R. Hansen, P. Hinze, D. Engel, and S. Davis,** "Using computational fluid dynamics (CFD) for blast wave predictions," *J. Loss Prev. Process Ind.*, vol. 23, no. 6, pp. 885–906, Nov. 2010, doi: 10.1016/j.jlp.2010.07.005.
21. **D. Mohotti, K. Wijesooriya, and S. Weckert,** "A simplified approach to modelling blasts in computational fluid dynamics (CFD)," *Def. Technol.*, vol. 23, pp. 19–34, May 2023, doi: 10.1016/j.dt.2022.11.006.
22. TM5-1300, *Structures to Resist the Effects of Accidental Explosions*. Washington, DC: US Department of Army, 1990.
23. **X. Nian, Q. Xie, X. Kong, Y. Yao, and K. Huang,** "Experimental and numerical study on protective effect of RC blast wall against air shock wave," *Def. Technol.*, vol. 31, pp. 567–579, Jan. 2024, doi: 10.1016/j.dt.2022.11.005.
24. **G. Randers-Pehrson and K.A. Bannister,** *Airblast Loading Model for DYNA2D and DYNA3D*. Army Research Laboratory, 1997.
25. **M.D. Netherton and M.G. Stewart,** "The effects of explosive blast load variability on safety hazard and damage risks for monolithic window glazing," *Int. J. Impact Eng.*, vol. 36, no. 12, pp. 1346–1354, Dec. 2009, doi: 10.1016/j.ijimpeng.2009.02.009.
26. **I. Nurhuda, N.T.K. Lam, H. Jiang, and E.F. Gad**, "Simulation of Crack Propagation in Glass Panels Using Finite Element Analysis," *Aust. J. Struct. Eng.*, vol. 12, no. 3, pp. 225–236, 2011.
27. **I. Nurhuda, N.T.K. Lam, E.F. Gad, and I. Calderone**, "Estimation of strengths in large annealed glass panels," *Int. J. Solids Struct.*, vol. 47, no. 18–19, pp. 2591–2599, 2010.

СПИСОК ЛИТЕРАТУРЫ

1. **X. Zhang and C. Bedon,** "Vulnerability and Protection of Glass Windows and Facades under Blast: Experiments, Methods and Current Trends," *Int. J. Struct. Glass Adv. Mater. Res.*, vol. 1, no. 2, pp. 10–23, Feb. 2017, doi: 10.3844/sgamrsp.2017.10.23.
2. **C. Bedon** *et al.*, "Performance of structural glass facades under extreme loads – Design methods, existing research, current issues and trends," *Constr. Build. Mater.*, vol. 163, pp. 921–937, Feb. 2018, doi: 10.1016/j.conbuildmat.2017.12.153.
3. **H.S. Norville, Natalie Harvill, Edward J. Conrath, and Sheryll Shariat,** "Glass-Related Injuries in Oklahoma City Bombing," *J. Perform. Constr. Facil.*, vol. 13, no. 2, pp. 50–56, May 1999.
4. **S. Das Adhikary**, "Review of Glazing and Glazing Systems under Blast Loading," *Pract. Period. Struct. Des. Constr.*, vol. 21, no. 1, Feb. 2016, doi: 10.1061/(asce)sc.1943-5576.0000264.
5. **L. Figuli, Z. Zvaková, and C. Bedon,** "Design and Analysis of Blast Loaded Windows," *Procedia Eng.*, vol. 192, pp.

177–182, 2017, doi: 10.1016/j.proeng.2017.06.031.
6. **J. Rudshaug, K.O. Aasen, O.S. Hopperstad, and T. Børvik**, "A physically based strength prediction model for glass," *Int. J. Solids Struct.*, vol. 285, p. 112548, Dec. 2023, doi: 10.1016/j.ijsolstr.2023.112548.
7. **K. Fischer and I. Häring**, "SDOF response model parameters from dynamic blast loading experiments," *Eng. Struct.*, vol. 31, no. 8, pp. 1677–1686, Aug. 2009, doi: 10.1016/j.engstruct.2009.02.040.
8. **K. Lee and J. Shin**, "Equivalent single-degree-of-freedom analysis for blast-resistant design," *Int. J. Steel Struct.*, vol. 16, no. 4, pp. 1263–1271, Dec. 2016, doi: 10.1007/s13296-016-0073-0.
9. **S. Chen, X. Chen, G.-Q. Li, and Y. Lu,** "A theoretical study on the P-I diagram of framed monolithic glass window subjected to blast loading," *Eng. Struct.*, vol. 150, pp. 497–510, Nov. 2017, doi: 10.1016/j.engstruct.2017.07.055.
10. AS1288, *Glass in building-Selection and installation*, Sydney, NSW., 2006.
11. **J.O. Hallquist,** *LS-DYNA Theory Manual*. Livermore, CA: Livermore Software Technology Corporation, 2006.
12. **T. Belytschko, J.I. Lin, and C.-S. Tsay**, "Explicit algorithms for the nonlinear dynamics of shells," *Comput. Methods Appl. Mech. Eng.*, vol. 42, no. 2, Feb. 1984.
13. **J. Wei, M.S. Shetty, and L.R. Dharani,** "Failure analysis of architectural glazing subjected to blast loading," *Eng. Fail. Anal.*, vol. 13, no. 7, pp. 1029–1043, Oct. 2006, doi: 10.1016/j.engfailanal.2005.07.010.
14. **R. Zhang, X. Zhai, X. Zhou, P. Li, and X. Zhi**, "Experimental and numerical study of annealed glass subjected to low-velocity impact: Simulation of windborne debris impact," *J. Build. Eng.*, vol. 106, p. 112504, Jul. 2025, doi: 10.1016/j.jobe.2025.112504.
15. **M.L. Bucalem and K.J. Bathe,** "Finite Element Analysis of Shell Structures," *Arch. Comput. Methods Eng.*, vol. 4, no. 1, pp. 3–61, 1997.
16. **N.T.K. Lam, E.F. Gad, I. Nurhuda, and I. Calderone**, "Impact Resistance of Annealed Glass Panels," *J. Perform. Constr. Facil.*, vol. 25, no. 5, pp. 422–432, Oct. 2011, doi: 10.1061/(asce)cf.1943-5509.0000181.
17. **A.W.D.Q.R. Reis, R.B. Burgos, and M.F.F.D. Oliveira,** "Nonlinear Dynamic Analysis of Plates Subjected to Explosive Loads," *Lat. Am. J. Solids Struct.*, vol. 19, no. 1, 2022, doi: 10.1590/1679-78256706.
18. **T. Krauthammer and A. Altenberg,** "Negative phase blast e!ects on glass panels," *Int. J. Impact Eng.*, vol. 24, pp. 1–17, 2000.
19. **A. Ullah, F. Ahmad, H.-W. Jang, S.-W. Kim, and J.-W. Hong**, "Review of analytical and empirical estimations for incident blast pressure," *KSCE J. Civ. Eng.*, vol. 21, no. 6, pp. 2211–2225, Sep. 2017, doi: 10.1007/s12205-016-1386-4.
20. **O.R. Hansen, P. Hinze, D. Engel, and S. Davis,** "Using computational fluid dynamics (CFD) for blast wave predictions," *J. Loss Prev. Process Ind.*, vol. 23, no. 6, pp. 885–906, Nov. 2010, doi: 10.1016/j.jlp.2010.07.005.
21. **D. Mohotti, K. Wijesooriya, and S. Weckert,** "A simplified approach to modelling blasts in computational fluid dynamics (CFD)," *Def. Technol.*, vol. 23, pp. 19–34, May 2023, doi: 10.1016/j.dt.2022.11.006.
22. TM5-1300, *Structures to Resist the Effects of Accidental Explosions*. Washington, DC: US Department of Army, 1990.
23. **X. Nian, Q. Xie, X. Kong, Y. Yao, and K. Huang,** "Experimental and numerical study on protective effect of RC blast wall against air shock wave," *Def. Technol.*, vol. 31, pp. 567–579, Jan. 2024, doi: 10.1016/j.dt.2022.11.005.
24. **G. Randers-Pehrson and K.A. Bannister,** *Airblast Loading Model for DYNA2D and DYNA3D*. Army Research Laboratory, 1997.
25. **M.D. Netherton and M.G. Stewart,** "The effects of explosive blast load variability on

safety hazard and damage risks for monolithic window glazing," *Int. J. Impact Eng.*, vol. 36, no. 12, pp. 1346–1354, Dec. 2009, doi: 10.1016/j.ijimpeng.2009.02.009.
26. **I. Nurhuda, N.T.K. Lam, H. Jiang, and E.F. Gad**, "Simulation of Crack Propagation in Glass Panels Using Finite Element Analysis," *Aust. J. Struct. Eng.*, vol. 12, no. 3, pp. 225–236, 2011.
27. **I. Nurhuda, N.T.K. Lam, E.F. Gad, and I. Calderone**, "Estimation of strengths in large annealed glass panels," *Int. J. Solids Struct.*, vol. 47, no. 18–19, pp. 2591–2599, 2010.

Ilham Nurhuda, Dr., Senior Lecturer, Department of Civil Engineering, Diponegoro University (Undip). Jl. Prof. Soedarto, S.H., Tembalang, Semarang, 50275, Indonesia. E-mail: ilham@live.undip.ac.id.

Nelson T.K. Lam, Professor, Department of Infrastructure Engineering, The University of Melbourne (UniMelb), Grattan Street, Parkville, Victoria, 3010, Australia. E-mail: ntkl@unimelb.edu.au

Илхам Нурхуда, д.т.н., старший преподаватель, кафедра гражданского строительства, Университет Дипонегоро (Undip). Ул. Проф. Соедарто, S.H., Тембаланг, Семаранг, 50275, Индонезия. E-mail: ilham@live.undip.ac.id.

Нельсон Т.К. Лам, д.т.н., профессор, кафедра инженерии инфраструктуры, Мельбурнский университет (UniMelb), Граттан-стрит, Парквилл, Виктория, 3010, Австралия. E-mail: ntkl@unimelb.edu.au

International Journal for Computational Civil and Structural Engineering, 22(1) 133–143 (2026)

DOI:10.22337/2587-9618-2026-22-1-133-143

DETERMINATION OF THE SOIL RESISTANCE VALUE FOR THE FOUNDATION DESIGN OF RECONSTRUCTED BUILDINGS

Anatolii I. Polishchuk [1], Shuhong Wang [2], Nadezhda S. Nikitina [3], Maxim B. Marinichev [1]

[1] Kuban State Agrarian University named after I. T. Trubilin, Krasnodar, RUSSIA
[2] Northeastern University, Shenyang 110819, Liaoning, CHINA
[3] National Research Moscow State University of Civil Engineering, Moscow, RUSSIA

Abstract: The calculation of bases and foundations of reconstructed buildings on sandy and clayey soils requires taking into account the value of the design resistance of the soil R. It is known that in the process of long-term operation of buildings, soil under the footings becomes compacted due to pressure from the foundations, and their properties usually improve. Over this period, the value of R also increases, and in the following we will call it the calculated resistance of the compacted foundation soil R_{comp}. The authors have analyzed known methods of determining R_{comp}, published by Russian scientists over the past 50 years.

The purpose of this work was to refine the method for determining the value of the design resistance of the compacted soil R_{comp} for the design of foundations for reconstructed buildings. Among the considered ones, the most effective is the engineering method of determining R_{comp} based on the recommendations for calculating the value of R according to the formula (5.7) of SP 22.13330.2016, which is supplemented by coefficients that take into account changes in the physical and strength characteristics of soils. The greatest increase in the value of R to R_{comp} (by 45-60%) is observed for shallow foundations on clayey low-plastic soils, while the smallest increase occurs in cases of ground water saturation during the operation of the building (by 20-25%). However, if the additional loading p from the foundation is insignificant ($p/R \leq 0.6$-0.7), then the value of R (for uncompacted soil) decreases by 10-15% and more. The greatest compaction effect for clay soils during the building's operational life occurs when the pressure at the footings p is 80% or more of the calculated soil resistance R ($p \geq 0.8\ R$). All these factors must be considered when determining the reserve strength of the foundations of reconstructed buildings.

Keywords: design resistance of the foundation soil, shallow foundations, compaction of the base by pressure from the foundations, improvement of soil properties

ОПРЕДЕЛЕНИЕ РАСЧЕТНОГО СОПРОТИВЛЕНИЯ ГРУНТА ОСНОВАНИЯ ПРИ ПРОЕКТИРОВАНИИ ФУНДАМЕНТОВ РЕКОНСТРУИРУЕМЫХ ЗДАНИЙ

А.И. Полищук [1], Ш. Ванг [2], Н.С. Никитина [3], М.Б. Мариничев [1]

[1] Кубанский государственный аграрный университет им. И. Т. Трубилина, г. Краснодар, РОССИЯ
[2] Северо-восточный университет, г. Шэньян, КИТАЙ
[3] Национальный исследовательский Московский государственный строительный университет, г. Москва, РОССИЯ

Аннотация. Расчет оснований и фундаментов реконструируемых зданий на песчаных и глинистых грунтах в России предусматривает использование величины расчетного сопротивления грунта основания R. При этом установлено, что в процессе длительной эксплуатации зданий (сооружений) происходит уплотнение грунтов основания давлением от фундаментов, и их свойства обычно улучшаются. За этот период происходит также увеличение значения R, которое для условий реконструкции зданий принято называть расчетным сопротивлением уплотненного грунта основания $R_{уп}$. Авторами проанализированы известные методы определения $R_{уп}$, опубликованные в работах отечественных ученых за последние 50 лет (с 1971 г.). Сравнительный анализ показал, что методы расчета $R_{уп}$ в настоящее время нуждаются в дальнейшем развитии. Цель работы заключалась в уточнении метода определения расчетного сопротивления уплотненного грунта основания $R_{уп}$ для проектирования фундаментов реконструируемых зданий. Из числа рассмотренных наиболее эффективным является инженерный метод разработанный в

ТГАСУ (Томск), получивший свое развитие в период с 2007 по 2021 гг. Метод учитывает не только улучшение свойств грунтов под подошвой фундаментов за счет постепенного догружения давлением от здания, но и их ослабление (ухудшение), вызванное обводнением основания в период его эксплуатации. Рассматриваемый метод определения $R_{уп}$ базируется на рекомендациях к вычислению значения R по формуле (5.7) СП 22.13330.2016 (Россия), в которую вносятся дополнения в виде коэффициентов, учитывающих изменения физических и прочностных характеристик грунтов. Например, наибольшее повышение значения R до $R_{уп}$ (на 45-60%) наблюдается для фундаментов мелкого заложения на глинистых грунтах тугопластичных, а наименьшее – для случая обводнения этих грунтов в период эксплуатации здания (на 20-25%). Если же догружение грунта основания давлением p от фундамента незначительно ($p/R \leq 0{,}6$-$0{,}7$), то значение R (неуплотненного грунта) понижается на 10-15% и более. Следует также заметить, что наибольший эффект уплотнения глинистых грунтов основания за период эксплуатации зданий происходит в том случае, когда давление по подошве фундаментов p составляет 80% и более от расчетного сопротивления естественного гранта основания R ($p \geq 0{,}8\ R$). Все это необходимо учитывать при определении резерва прочности основания фундаментов реконструируемых зданий, в каждом конкретном случае, в зависимости от вида (разновидности) грунта, срока их эксплуатации.

Ключевые слова: реконструкция зданий, расчетное сопротивление грунта основания, фундаменты мелкого заложения, уплотнение основания давлением от фундаментов, улучшение свойств грунта

INTRODUCTION

In Russia, when calculating the bases and foundations of reconstructed buildings on sandy and clayey soils for the second group of limit states, the parameter of design soil resistance R is used in accordance with SP 22.13330.2016. It is known that during the long-term operation of buildings, the foundation soils become compacted under the pressure from the foundations, and their properties usually improve (P. A. Konovalov, 1986; A. I. Polishchuk et al., 1997, and others). Due to the compaction of the soil and the improvement of its properties, there is also an increase in the parameter R, which for the conditions of reconstruction of buildings is usually called the calculated resistance of the compacted soil of the foundation R_{comp}. The authors of the article have analyzed known methods for determining the parameter R_{comp}, published in the works of: B. I. Dalmatov et al. (1985–1990), V. A. Zurnadzhi & M. P. Filatova (1970), P. A. Konovalov et al. (1986–2011), A.V. Pilyagin (2005–2017), A. I. Polishchuk et al. (1997–2023), A. G. Roitman et al. (1971–1990), N. G. Smolenskaya et al. (1979), E. A. Sorochan & Yu. I. Dvorkina (1976–1986), V. M. Ulitsky et al. (1986–1993), G. I. Shvetsov & I. V. Noskov et al. (1991–2002), V. B. Shvets, V. V. Lushnikov et al. (1981–1995) and others [1, 2, 13–18]. The comparative analysis showed that the current methods for calculating R_{comp} require further development.

This work aimed to substantiate a method for evaluating the design resistance of compacted subsoil (R_{comp}) to support foundation design in building reconstruction projects. This article was prepared with the participation of T.N. Gutnik.

DESIGN METHODOLOGY AND THEORETICAL APPROACHES

Currently, existing regulatory documents contain limited information on methods for determining the design bearing capacity of compacted foundation soils (R_{comp}) for building reconstruction projects. This results in frequent use of natural soil characteristics obtained from geotechnical investigations for new construction when designing (assessing loading conditions for) shallow foundations on sandy and clayey soils. In such cases, the improvement (change) in soil properties due to long-term compaction under foundation loads is frequently neglected. Let us consider the main methods used in Russia for determining the R_{comp} parameter at the stage of justifying design solutions for foundation systems of reconstructed buildings.

When designing foundations for reconstructed buildings, parameter R [Method (5.7) of SP 22.13330.2016] is frequently used as for new construction conditions. However, at the same time, prior to the design process, during the preparation of a report on the technical condition of a reconstructed building, an engineering and geological survey is conducted at the site (either fully or partially, as a means of verification), including a survey of existing foundations and their foundations. During this stage, samples of compacted soils are collected from under the bases of foundations to determine their physical and mechanical properties. The properties of the soil thus determined allow for the calculation of the R_p parameter, which is used to assess the loading capacity of the foundations under consideration. This method can be described as experimental method. The physico-mechanical properties of foundation soils for reconstructed buildings can also be determined through alternative methods such as geophysical surveys, sounding, or penetration tests. The determination of the R_p parameter based on actual soil characteristics established experimentally during foundation investigations, readers may refer to works by P.A. Konovalov, E.A. Sorochan, Yu.I. Dvorkina, A.I. Polishchuk et al., V.M. Ulitsky et al., and A.G. Roitman et al. [1,3,5,6,10,12,14, etc.]. The experimental method for determining the R_{comp} parameter discussed above is based on current regulatory documents, has undergone verification, and has proven effective in the design practice of foundations for reconstructed buildings. However, its implementation requires a significant amount of time-consuming preparatory work related to collecting samples, soil samples taken from under the foundation base and determination of their physical, strength, and deformation characteristics under specified loading conditions.

The experience of increasing loads on building structures, including foundations, due to the addition of extra floors has shown that the soils supporting the foundations often have a reserve of strength. These issues were first addressed in scientific publications as early as the 1930s [1, 9, 12, 16, 17]. However, these publications provided only general recommendations regarding potential additional loading of existing foundations and subsoils without specific quantitative guidelines. For example, Professor P. A. Konovalov (1980) suggested that increased ground pressure during building reconstruction should be determined based on the allowable pressure R (used for new building design) with enhancement factors ranging from 1.1 to 1.5 depending on soil type [1]. In the 1941 building regulations, which were developed for construction under military conditions, it was recommended that the R - value be increased by 40% during reconstruction, provided that there were no cracks were observed in walls or other structural elements due to differential foundation settlement. In subsequent regulatory documents, the pressure on the foundations varies from 20% to 25% depending on the duration of their operation and the absence of defects, provided that they are at least 20 years old. The 1974 (SNIP P-15-74) and 1983 (SNIP 2.02.01-83*) documents on the design of foundations for buildings and structures no longer contain any recommendations regarding potential increases in R for soils beneath existing buildings [11].

In 1970, V.A. Zurnadzhi and M.P. Filatova proposed a method for determining the increased allowable ground pressure $R^{и}$, in their work [4]. According to the authors, their method should be considered as preliminary, and the following formula was provided:

$$R^{и} = K_з \cdot \sigma_p, \quad (1)$$

where: σ_p – design soil pressure beneath an existing building, kPa;

$K_з$ – the increasing coefficient is determined depending on the type of soil, its humidity, the calculated pressure at the base of the foundation σ_p and the operating time of the building.

According to the tabular data [4] for loess–like loams with a humidity from 5 to 20%, a design pressure of σp from 100 to 300 kPa, and building service life of 5-25 years, the enhancement factor values ($K_з$) vary within

1.0-1.4. If the base contains sands of various sizes and densities, regardless of their humidity, at σp from 100 to 400 kPa and the service life of the building from 5 to 25 years or more, the k_s values range from 1.1 to 1.5.

For cases where data on the actual soil characteristics in the compacted area under the foundation base is unavailable, P. A. Konovalov and A. G. Roitman, (1970-1972) and later E. V. Polyakov and V. K. Sokolov (1972) developed a method for determining parameter *R'*, which takes into account the compression (pre-consolidation) effect of foundation soils during construction maintenance. The equation developed by P. A. Konovalov and A. G. Roitman is as follows:

$$R' = R \cdot m \cdot k_s, \quad (2)$$

where: *R'* - calculated ground resistance of the base, taking into account the effect of compression (compaction) of the base by pressure from the foundation of the reconstructed building, kPa;

R – the calculated resistance of the soil of the base during its natural occurrence (unconsolidated state), determined by SP 22.13330.2016, kPa;

m – the coefficient that takes into account the change in the physico–mechanical properties of the soils (the degree of compression of the soils) of the foundation under the foundation during the period of operation of the building;

k_s – a coefficient that takes into account the degree of realization (using) of the maximum precipitation of the foundation during the period of operation of the building (determined by the ratio of the calculated precipitation at a pressure equal to the calculated to the maximum allowable precipitation). The values of the *k* coefficient for different types (varieties) of soils are determined according to the tables (P. A. Konovalov, 2011).

The coefficient *m* in formula (2) depends on the ratio of the foundation pressure before vertical extension p_0 to the design soil resistance *R*.

At $p_0/R \geq 0.8$ (more than 80%), the coefficient $m = 1.3$, at $p_0/R = 0.7$-0.8 (equal to 70-80%), the coefficient $m = 1.15$, at $p_0/R \leq 0.7$ (less than 70%), the coefficient $m = 1$.

The ratio p_0/R equaling 1 signifies the complete utilization of the calculated soil resistance in the foundation for calculations pertaining to the second group of limiting states [1, 14].

The formula of E.V. Polyakov and V.K. Sokolov for determining *R'* has the following form:

$$R' = kR, \quad (3)$$

where: R', R – the same as in formula (2);

k – the coefficient of increase in the resistance of the base soil, depending on the ratio p_0/R (here p_0 is the actual pressure on the base soils up to the superstructure, kPa); The values of the coefficient *k* vary from 1.0 to 1.5 and are taken according to the tables (P.A. Konovalov, 1980).

Formula (3) may be applied when the building being vertically extended has been in service for at least 3 years for sandy soils, 5 years for sandy loams, and 8 years for clayey soils. In contrast to the method of P. A. Konovalov and A.G. Roitman, formula (3) includes only a single coefficient *k*, which accounts for the amount of load/magnitude of pressure transmitted to the soil by the foundation. The difference between the two methods also lies in the absence of a parameter in formula (3) to account for changes in foundation settlement during the operation of the structure. The values for the *k* coefficient are derived from tables (P. A. Konovalov, 1980).

In AO TSNII Promzdaniy (Moscow), research was conducted (1965) into the strength characteristics of sand soils at the bases of existing buildings (operating period from 20 to 120 years). Based on the research findings, a linear correlation was identified between the strength properties of soil and the duration of its loading, followed by the development of empirical formulas for determining the angle of internal friction and specific cohesion of

sands at given time intervals after initial loading [5-7]. The considered methodology allowed:

- to determine design bearing capacity values of foundation soils accounting for their time-dependent consolidation;
- to address the issue of necessity for strengthening foundations and bases for the reconstruction of buildings, considering changes in strength properties of the soil.

Based on the data obtained by Yu.I. Dvorkin and E.A. Sorochan from AO TSNII Promzdaniy (1972), a method has been developed for calculating the calculated resistance of compacted soil in the foundation base for sandy soils. The proposed method takes into account the time-dependent improvement in the building properties of sandy soils and is determined using the following formula for foundation design:

$$R_{comp} = R \cdot K_E, \quad (4)$$

where: R – the calculated resistance of the soil of the base during its natural occurrence (unconsolidated state), determined by SP 22.13330.2016, kPa;

K_E – a coefficient accounting for the improvement of soil engineering properties, adopted from tabulated data (E. A. Sorochan, 1986).

In TSASU (Tomsk), researches were conducted (1997-2000) to evaluate the load on the clay foundation of reconstructed (long-operating), buildings led to the development of a method for determining the compacted soil resistance parameter R_{comp} (by author A.I. Polishchuk), considering its compressibility [8,9]. The method is based on formula (5.7) for calculating the designed resistance of natural soil base R, as per SP 22.13330.2016. Coefficients K_γ, K_c, K_φ, K_s are included in formula (5.7), taking into account changes in soil strength characteristics during compaction and wetting (soaking) during building operation. The formula, considering the accepted coefficients, takes the following form:

$$R_{comp} = \frac{\gamma_{c1}\gamma_{c2}}{k}\left[M_\gamma k_z b \gamma_{II} K_\gamma + M_q d_1 \gamma'_{II} + \left(M_q - 1\right) d_b \gamma'_{II} + M_c c_{II} \cdot K_c\right] \cdot K_{s,} \quad (5)$$

where: K_γ, K_c – coefficients that take into account the change in the characteristics of density p (specific gravity) and specific adhesion to the soil of the foundation under the foundation during the period of operation of the building (Table 1);

M_q, M_γ, M_c – coefficients accepted according to SP 22.13330.2016, depending on the characteristics of the angle of internal friction ($\bar{\varphi}_{II}$) of the foundation compacted by pressure from the operated building:

$$\bar{\varphi}_{II} = \varphi_{II} \cdot K_\varphi, \quad (6)$$

where: φ_{II} – the angle of internal friction of the natural (uncompacted) soil of the base, deg;

K_φ – the coefficient that takes into account the change in the characteristic of the angle of internal friction φII over the period of operation of the building (Table 1);

K_S – a coefficient that takes into account the degree of realization (use) of the maximum precipitation of the foundation during the period of operation of the building (Table 2).

The remaining designations in equation (5) are the same as in SP 22.13330.2016.

The values of the coefficients K_y, K_φ, K_c should be selected depending/based on the ratio of the average pressure along the sole of the exploited foundation p to the calculated resistance of the natural (unconsolidated) soil of the base R, which was assumed during the initial design of the facility (they were obtained experimentally for clay soils).At the same time, the coefficients K_y, K_φ, K_c were established as the ratio of the characteristics of compacted (pressure foundations) and natural soils with a building life of more than 15 years [9].

Table 1. Values of coefficients K_y, K_φ, K_c for determining the design resistance of the compacted soil of the R_{comp} base (data by A.I. Polishchuk)

№ п/п	The foundation soils of the reconstructed building	Parameter *p/R*	Coefficients		
			K_γ,	K_φ	K_c
1	Clayey soils with index $I_L \leq 0.5$ and building service life exceeding more 15 years	more 0,8 0,5-0,8 less than 0,5	1,07-1,17 1,03-1,05 1,0	1,10 1,05 1,0	1,6 1,32 1,05
2	Clayey soils with index $I_L > 0,5$ and building service life exceeding more 15 years	more 0,8 0,5-0,8 less than 0,5	1,05-1,15 1,0-1,05 1,0	1,08 1,04 1,0	1,45 1,25 1,05
3	Clayey soils with groundwater present at foundation level and building service life exceeding more 15 years	more 0,8 0,5-0,8 less than 0,5	1,03 1,03 1,0	0,97 0,88 0,8	1,3 1,06 0,85

Note. The use of coefficients K_y, K_φ, K_c is provided for soils that do not have specific unfavorable properties (subsidence, swelling, etc.); p is the average pressure along the sole of the foundation under consideration before the reconstruction of the building; R is the calculated resistance of the natural (uncompacted) soil of the base.

Table 2. Values of coefficient Ks for determining the design resistance of compacted foundation soil

№ п/п	Foundation soils regardless of density and moisture content	coefficient K_s when S/S_u	
		0,2	0,7
1	Coarse and medium sands	1,4	1,0
2	Fine sands	1,2	1,0
3	Silty sands	1,1	1,0
4	Cohesive (clayey) soils with index $I_L \leq 0$	1,2	1,0
5	Cohesive (clayey) soils with index $I_L \leq 0.5$ and building service life exceeding more 15 years	1,1	1,0
6	Cohesive (clayey) soils with index $I_L > 0,5$ and building service life exceeding more 15 years	1,07	1,0
7	Clayey soils with groundwater present at foundation level and building service life exceeding more 15 years	1,05	1,0

Note. 1. In Table 2, the following designations are used: S – is the settlement of the foundation under a pressure p at the sole, corresponding to the estimated resistance of the natural ground at the base (p=R); S_u – is the maximum permissible settlement for the type of structure under consideration. For medium-rise buildings, the K_z factor is estimated by interpolation based on the S/S_u ratio.
2. In Table 2, figures 1-5 present data on coefficients obtained by NIIOSP experts in collaboration with Moszhilniiproekt (P. A. Konovalov, A. G. Roitman, et al., [11], [14]). The values of K_s numbered 6 and 7 were proposed by A.I. Polishchuk.

RESULTS AND DISCUSSION

Analyzing the methods discussed above for determining the design resistance of compacted foundation soil at the R_{comp} reveals that all are applicable only to specific soil types (or varieties.

The method proposed by Yu. I. Dvorkin and E. A. Sorochan (1976–1982, 1986) is applicable only to sandy soils with different granulometric compositions and humidity.

The method by P.A. Konovalov and A.G. Roitman (1972-1980), as well as the method by E.V. Polyakov and V.K. Sokolov (1972), are applicable not only to sandy soils but also to cohesive (clayey) soils with a liquidity index $J_L \leq 0.5$ and building service life of at least 15 years.

According to the authors themselves, the method proposed by V. A. Zurnadzhi and M. P. Filatova (1970) should be considered only as preliminary.

The method developed at TGASU (1997-2000), unlike the previously described methods by P. A. Konovalov et al. (1972-1980), E. P. Polyakov et al. (1972), and V. A. Zurnadzhi et al. (1970), has a broader application range and is applicable to clayey soils ranging from hard to soft-plastic (plastic) consistency.

It should be noted that the method developed at TSASU 1997 - 2000 takes into account not only the improvement of soil properties beneath the foundations of reconstructed buildings as a result of compaction, but also the weakening caused by flooding during the operation of these buildings. For instance, the largest increase in R to R_p is seen for shallow foundations on clay soils with an $J_L \leq 0.5$, which is 45-60%, and the smallest increase is for the case where these soils are flooded during the operation, which is 20-25%. If the compression of foundation soil due to pressure from the foundation is negligible ($p/R \leq 0.6$-0.7), the value of R for unconsolidated soils decreases by 10-15% or more [2, 9].

It is also important to note that, in some cases, the actual pressure exerted at the base of the foundations of reconstructed buildings may be 20-30% of the calculated bearing capacity of the natural, unconsolidated soil. In such instances, the effect of the compressive load from the foundations on the base is negligible. The greatest impact of compression on the foundation soil during the operational life of the structure occurs when the pressure applied to the base of the foundation is equal to 80% or greater than 80% of the bearing capacity of the unconsolidated soil ($p \geq 0.8$ R).

All these factors must be considered when determining the required strength reserve for the foundations of reconstructed structures, taking into account the specific characteristics of the soil and the anticipated service life of the building [19-25].

CONCLUSION

1. It has been determined that for the design of foundations and shallow foundations (ribbon, isolated, dense) for reconstructed buildings, it is essential to determine the parameter of calculated resistance of compacted soil at the base of the structure. Engineering methods for calculating the R_p are based on recommendations from regulatory documents for calculating R for natural (uncompacted) foundations (in accordance with SP 22.13330.2016) that have been supplemented to account for changes in soil properties beneath foundations due to compaction during building operation.

2. A review of experimental and theoretical studies suggests that the methods currently used for determining R_{comp} are applicable to certain soil types (sands, clays, loams, and sandy loams) and have limited applicability. Of the domestic methods considered for determining R_{comp}, the most effective is the engineering approach proposed at TSASU, which considers not only the improvement of soil properties under foundations due to compaction, but also the weakening (deterioration) caused by soil flooding during building operation [8, 9]. This method has broader applicability, covering clays, loams, and sandy loams from hard to soft-plastic (plastic) consistency states.

3. For the design foundations of reconstructed buildings on clay soils, it is necessary to further develop methods for determining the R_{comp}. In particular, this requires the development of a method for calculating the resistance of compacted soil R_{comp} for foundations with various shapes of the base in plan (e.g., T-shaped, trapezoidal, etc.), as well as foundations with a partially deepened slab along the perimeter.

REFERENCES

1. **Konovalov P.** A Foundations and foundations of reconstructed buildings. 4th, Redesign. et. M.: VNIINTPI, 2000. – 318 p.
2. **Polischuk A.I., Lobanov A.A.** Assessment of loading of foundations of reconstructed buildings using personal computers. –

Tomsk: Publishing house of Tom. University of Tomsk, 1996. – 134 p.
3. **Ulitsky V.M., Shashkin A.G., Shashkin K.G.** Geotechnical Support of Urban Development (Practical Guide to Designing Buildings and Underground Structures in Conditions of Dense Construction): "StroyizdatSevero-Zapad", Georeconstruction Group - St. Petersburg. 2010.
4. **Zurnadzhi V.A., Filatova M.P.** Strengthening foundations and foundations in the repair of buildings. Moscow: Stroyizdat, 1970. 96 p.
5. **Sorochan E.A.** Foundations of Industrial Buildings. – Moscow: Stroyizdat, 1986. – 303 p.
6. **Dvorkin Y.I.** On assignment of pressure on sandy foundations during reconstruction of buildings// Foundations, Foundations and Mechanics of Soils.1982. № 4. p. 23-24.
7. **Sorochan E.A., Dvorkin Y.I.** On the assignment of pressure on the foundation during reconstruction of structures // Foundations, Foundations and Soil Mechanics. 1976. № 2. p. 8-9.
8. **Polischuk A.I.** Appointment of design resistance of foundation soil when designing foundations of reconstructed buildings Foundations, Foundations and Soil Mechanics. – 2000. – № 3. - p. 6-10.
9. **Polischuk A.I.** Fundamentals of designing and construction of foundations of reconstructed buildings. – Northampton: STT, 2007. – 476 p.
10. **Roitman A.G., Smolenskaya N.G.** Repair and Reconstruction of Residential and Public Buildings. Moscow: Stroyizdat, 1978. 319 p.
11. **Konovalov P.A.** Foundations and foundations of reconstructed buildings. 4th, Redesign. et. M.: VNIINTPI, 2000. 318 p.
12. **Plevkov V.S.** Restoration and strengthening of building structures of emergency and reconstructe d buildings / Plevkov V. S., Malganov A. I., Polishchuk A.I. Atlas of schemes and drawings. – Tomsk, 1990.
13. **Yushube S.V.** Method of making drill-injection piles in seasonally freezing soil / Yushube S. V., Polishchuk A. I., Fursov V. V. The patent for the invention RU 2150550 C1, 10.06.2000. Application №99101576/03 of 25.01.1999.
14. **Smolenskaya N.G.** Methodology of Inspection and Design of Foundations and Foundations during Major Repair, Reconstruction and Superstructure of Buildings / N.G. Smolenskaya, R.G. Komissarchik, B.N. Ershov et al. – Moscow; Stroyizdat, 1972. – 111c.
15. **Polishchuk A.I.** Foundations and bases, underground structures: textbook / A. I. Polishchuk, M. B. Marinichev; edited by A. I. Polishchuk. – 3rd ed. reprint. and additional – Krasnodar: KubGAU, 2024. – 612 p.
16. **Ilyichev V.A**. Handbook of geotechnics: foundations, foundations and underground structures / under the general editorship of V.A. Ilyichev and R.A. Mangushev. Chapter
17. **Mangushev R.A., Osokin A.I., Usmanov R.A.** Construction and reconstruction of foundations and foundations on weak and structurally unstable soils / Ed. by R.A. Mangushev: Monograph. – St. Petersburg: Publishing house "Lan", 2018. – 460 p.
18. **Tsytovich N.A.** Mechanics of soils. Fourth edition, newly revised and expanded. Moscow: Gosstoroizdat, 1963. – 636 p.
19. **Marinichev M.B., Nikitina N.S., Polishchuk A.I.** Development of methods for designing pile foundations for multi-storey civil buildings constructed on macroporous subsidence soils // International Journal for Computational Civil and Structural Engineering. 2024. Vol. 20 (3). Pp. 206–217. DOI 10.22337/2587-9618-2024-20-3-206-217.
20. **Nikitina N.S., Polishchuk A.I., Marinichev M.B., Ipatova D.O.** Development of the stages of designing pile foundations on subsiding soils for multi-storey residential buildings // Modern

methods of designing, underground construction and reconstruction of foundations and foundations (GFAC 2024): collection of theses of the National (All-Russian) Scientific and Technical Institute. conf. s mezhdunar. participation dedicated to the 90th anniversary of the Department of Geotechnics (Mechanics of Soils, Bases and Foundations, Engineering Geology). St. Petersburg, October 23–25, 2024. St. Petersburg: SPbGASU, 2024. Pp. 91–92.

21. **Malyshev M.V., Nikitina N.S.** Computing foundation settlements for a nonlinear relationship between stresses and strains in the soils // Soil Mechanics and Foundation Engineering. 1982. № 2. C. 21-24.
22. **Shuhong Wang, Bowen Han, Jianhui Jiang, Natalia Telyatnikova.** Machine learning and FEM-driven analysis and optimization of deep foundation pits in coastal area: A case study in Fuzhou soft ground. Underground Space, 2025, 22(3): 55-76 DOI:10.1016/j.undsp.2024.11.001.
23. **Xiu Z., Wang S., Ji Y**. *et al.* Experimental investigation on liquefaction and post-liquefaction deformation of stratified saturated sand under cyclic loading. *Bull Eng Geol Environ* 79, 2313–2324 (2020). https://doi.org/10.1007/s10064-019-01696-8
24. **Wang Dongsheng, Wang Shuhong, Zhan g Ze, Ding Peng,** Study of the Mechanical Behavior of Retaining Structures and Adjacent Buildings during the Excavation of Deep and Long Pits, *Shock and Vibration*, 2024, 7242422, 16 pages, 2024. https://doi.org/10.1155/2024/7242422.
25. **Shuhong Wang, Bo Yang, Furui Dong, Marinichev Maxim and Ze Zhang** // Determination of the influence of the disturbance caused by traversing cross-type deep foundation pit excavations/ Sustainability 2023, 15, 1130. https://doi.org/10.3390/su15021130.

СПИСОК ЛИТЕРАТУРЫ

1. **Коновалов П.А**. Основания и фундаменты реконструируемых зданий. – М.: Стройиздат, 1980. – 136 с.
2. **Полищук А. И., Лобанов А. А.** Оценка загружения оснований фундаментов реконструируемых зданий с использованием персональных ЭВМ. – Томск: Изд-во Том. Ун-та, 1996. – 134 с.
3. **Улицкий В.М., Шашкин А.Г., Шашкин К.Г.** Геотехническое сопровождение развития городов (практическое пособие по проектированию зданий и подземных сооружений в условиях плотной застройки): «СтройиздатСеверо–Запад», Группа компаний «Георекнструкция» – СПб. 2010.
4. **Зурнаджи В.А., Филатова М.П.** Усиление оснований и фундаментов при ремонте зданий. М.: Стройиздат, 1970. 96 с.
5. **Сорочан Е.А.** Фундаменты промышленных зданий. – М.: Стройиздат, 1986. – 303 с.
6. **Дворкин Ю.И.** О назначении давления на песчаные основания при реконструкции зданий// Основания, фундаменты и механика грунтов.1982. № 4. С. 23–24.
7. **Сорочан Е.А., Дворкин Ю.И.** О назначении давления на основание при реконструкции сооружений// Основания, фундаменты и механика грунтов. 1976. № 2. С. 8–9.
8. **Полищук А.И.** Назначение расчетного сопротивления грунта основания при проектировании фундаментов реконструируемых зданий. Основания, фундаменты и механика грунтов. - 2000. - № 3. -С. 6-10.
9. **Полищук А.И.** Основы проектирования и устройства фундаментов реконструируемых зданий. – Нортхэмптон: STT, 2007. – 476 с.
10. **Ройтман А. Г., Смоленская Н.Г.** Ремонт и реконструкция жилых и общественных зданий. М.: Стройиздат, 1978. 319 с.

11. **Коновалов П.А.** Основания и фундаменты реконструируемых зданий. 4-е изд., перераб. и доп. М.: ВНИИНТПИ, 2000. 318 с.
12. Восстановление и усиление строительных конструкций аварийных и реконструируемых зданий / Плевков В.С., Мальганов А.И., Полищук А.И. Атлас схем и чертежей. – Томск, 1990.
13. Способ изготовления буроинъекционной сваи в сезоннопромерзающем грунте / Ющубе С.В., Полищук А.И., Фурсов В.В. Патент на изобретение RU 2150550 C1, 10.06.2000. Заявка №99101576/03 от 25.01.1999.
14. Методика обследования и проектирования оснований и фундаментов при капитальном ремонте, реконструкции и надстройке зданий / Н.Г. Смоленская, Р.Г. Комиссарчик, Б.Н. Ершов и др. – М.;Стройиздат, 1972. – 111с.
15. Основания и фундаменты, подземные сооружения: учебник / А.И. Полищук, М.Б. Мариничев; под ред. А.И. Полищука. – 3-е изд. перераб. и доп. – Краснодар: КубГАУ, 2024. - 612 с.
16. Справочник геотехника: основания, фундаменты и подземные сооружения / под общ. ред. В.А. Ильичева и Р.А. Мангушева. Глава 16. Усиление оснований и фундаментов реконструируемых зданий (авторы А.И. Полищук, М.Б. Мариничев, А.А. Петухов). В двух томах, Т2. – М.: Изд-во АСВ, 2024. С. 255-292 (на английском языке).
17. **Мангушев Р.А., Осокин А.И., Усманов Р.А.** Устройство и реконструкция оснований и фундаментов на слабых и структурно-неустойчивых грунтах / Под ред. Р.А. Мангушева: Монография. – СПб.: Изд-во «Лань», 2018. – 460 с.
18. **Цытович Н.А.** Механика грунтов. Издание четвертое, вновь переработанное и дополненное. –М.: Госсторойиздат, 1963. – 636 с.
19. **Marinichev M. B., Nikitina N. S., Polishchuk A. I.** Development of methods for designing pile foundations for multi-storey civil buildings constructed on macroporous subsidence soils // International Journal for Computational Civil and Structural Engineering. 2024. Vol. 20 (3). Pp. 206–217. DOI 10.22337/2587-9618-2024-20-3-206-217.
20. **Никитина Н. С., Полищук А. И., Мариничев М. Б., Ипатова Д. О.** Развитие этапов проектирования свайных фундаментов на просадочных грунтах для многоэтажных жилых зданий // Современные методы проектирования, подземного строительства и реконструкции оснований и фундаментов (GFAC 2024): сб. тезисов Национальной (всерос.) науч.-техн. конф. с междунар. участием, посвященной 90-летию кафедры геотехники (механики грунтов, оснований и фундаментов, инженерной геологии). Санкт-Петербург, 23–25 октября 2024 г. СПб.: СПбГАСУ, 2024. С. 91–92.
21. **Малышев М.В.** Расчет осадок фундаментов при нелинейной зависимости между напряжениями и деформациями в грунтах / М.В. Малышев, Н.С. Никитина // Основания, фундаменты и механика грунтов. 1982. №2. С. 21-24.
22. **Shuhong Wang, Bowen Han, Jianhui Jiang, Natalia Telyatnikova.** Machine learning and FEM-driven analysis and optimization of deep foundation pits in coastal area: A case study in Fuzhou soft ground. Underground Space, 2025, 22(3): 55-76 DOI:10.1016/j.undsp.2024.11.001.
23. **Xiu Z., Wang S., Ji Y**. *et al.* Experimental investigation on liquefaction and post-liquefaction deformation of stratified saturated sand under cyclic loading. *Bull Eng Geol Environ* 79, 2313–2324 (2020). https://doi.org/10.1007/s10064-019-01696-8

24. **Wang Dongsheng, Wang Shuhong, Zhang Ze, Ding Peng,** Study of the Mechanical Behavior of Retaining Structures and Adjacent Buildings during the Excavation of Deep and Long Pits, *Shock and Vibration*, 2024, 7242422, 16 pages, 2024. https://doi.org/10.1155/2024/7242422.

25. **Shuhong Wang, Bo Yang, Furui Dong, Marinichev Maxim and Ze Zhang** // Determination of the influence of the disturbance caused by traversing cross-type deep foundation pit excavations/ Sustainability 2023, 15, 1130. https:// doi.org/10.3390/su15021130.

Anatolii Ivanovich. Polishchuk – Head of the department "Bases and Foundations" of the Kuban State Agrarian University named after I.T. Trubilin (Krasnodar), Honored Builder of the Russian Federation, Honorary Worker of Higher Professional Education of the Russian Federation, holder of the honorary diploma of the President of the Russian Federation, Doctor of Technical Sciences. (Russia, 350044, Krasnodar, Kalinina St., 13., E-mail: ofpai@mail.ru).

Shuhong Wang – Professor at the School of Resource Science and Civil Engineering at Northeastern University (Shenyang), Member of the China National Group of the International Society for Rock Mechanics (ISRM), Member of the Council of the Chinese Society for Rock Mechanics and Engineering Structures, Doctor of Engineering Sciences. Specialist in the field of engineering and geological surveys, rock mechanics, information. 3–11, Wenhua Road, Heping District, Shenyang, Liaoning, 110819, China

Nadezhda Sergeevna. Nikitina. Candidate of Technical Sciences, Professor of the Department of Soil Mechanics and Geotechnics; National Research Moscow State University of Civil Engineering (NRU MSUCE); Moscow, Russia, 129337, Yaroslavskoe shosse, 26; tel./fax: +7 (495) 287-49-14; e-mail: nsnikitina@mail.ru

Marinichev Borisovich Maxim– Professor of the Department of "Bases and Foundations" of the Kuban State Agrarian University named after I.T. Trubilin (Krasnodar), Honored Builder of the Kuban, Doctor of Technical Sciences. Russia, 350044, Krasnodar, Kalinina str., 13, E-mail: marinichev@list.ru.

Полищук Анатолий Иванович – профессор кафедры «Основания и фундаменты» Кубанского государственного аграрного университета им. И. Т. Трубилина (г. Краснодар), заслуженный строитель РФ, почетный работник высшего профессионального образования РФ, обладатель почетной грамоты Президента РФ, доктор технических наук. Россия, 350044, г. Краснодар, ул. Калинина, 13. Тел. +7 (918) 293-97-30, E-mail: ofpai@mail.ru.

Shuhong Wang – профессор Школы ресурсоведения и гражданского строительства Северо-восточного университета (г. Шэньян), Член Китайской национальной группы Международного общества по механике скальных пород (ISRM), член Совета Китайского общества по механике скальных пород и инженерным сооружениям, доктор технических наук. (Китай, провинция Ляонин, г. Шэньян, 110819, ул. Вэньхуа, 3-11)

Никитина Надежда Сергеевна – к.т.н., профессор кафедры «Механики грунтов и геотехники»; Национальный исследовательский Московский государственный строительный университет (НИУ МГСУ); г. Москва, Россия, 129337, Ярославское шоссе, д.26; тел./факс: +7(495) 287-49-14; e-mail: nsnikitina@mail.ru

Мариничев Максим Борисович – профессор кафедры «Основания и фундаменты» Кубанского государственного аграрного университета им. И. Т. Трубилина (г. Краснодар), заслуженный строитель Кубани, доктор технических наук. Россия, 350044, г. Краснодар, ул. Калинина, 13., E-mail: marinichev@list.ru.

International Journal for Computational Civil and Structural Engineering, 22(1) 144–156 (2026)

DOI:10.22337/2587-9618-2026-22-1-144-156

ANALYSIS OF THE PHYSICAL AND MECHANICAL PROPERTIES OF A FIBREGLASS COMPOSITE PIPE WITH BINDER MODIFIED BY PLASTICIZERS

Sergey V. Shashkin, Tatyana A. Matseevich

Moscow State University of Civil Engineering, Moscow, RUSSIA
Ishlinsky Institute for Problems in Mechanics of the Russian Academy of Sciences, Moscow, RUSSIA

Abstract: This paper considers an approach to improving the service performance of fiberglass composite pipelines under seismic conditions by modifying the thermosetting binder with plasticizing and toughening additives aimed at increasing fracture toughness and reducing the material's tendency to brittle failure under alternating-sign and impulse actions. The relevance of the study is driven by the fact that conventional pipeline materials (steel, reinforced concrete) have significant limitations when operated in seismically hazardous regions, whereas fiberglass reinforced plastics manufactured by continuous filament winding are characterized by high specific strength, corrosion resistance, and durability, but often demonstrate linear-elastic behavior up to failure. The object of the study was fiberglass composite pipes with a three-layer wall (surface, structurally reinforced, and liner layers). The following binder modifiers were considered: Polyplex; a modifier produced by JSC "Poliplast" (PoliPlast M); and a powder impact modifier of the "core–shell" type Clearstrength® XT100, introduced in different mass percentages. For each formulation, a series of repeated measurements was performed to ensure comparability and statistical evaluation of the results. The experimental program included determination of the initial specific ring stiffness and resistance to initial ring deflection, the initial hoop tensile strength and tensile modulus, the initial axial tensile strength and tensile modulus, as well as Charpy impact toughness in accordance with the applicable standards. Based on the combined indicators, the necessity for multi-criteria selection of binder composition is discussed, enabling preservation of the design stiffness–strength characteristics while improving the dynamic resistance of the material.

Keywords: fiberglass composite pipe, continuous winding, plasticizer, impact modifier, seismic resistance

ИССЛЕДОВАНИЕ ФИЗИКО-МЕХАНИЧЕСКИХ СВОЙСТВ ТРУБЫ ИЗ МОДИФИЦИРОВАННОГО ПЛАСТИФИКАТОРАМИ СТЕКЛОКОМПОЗИТА

С.В. Шашкин, Т.А. Мацеевич

Национальный исследовательский Московский государственный строительный университет, г. Москва, РОССИЯ
Институт Проблем Механики им. А.Ю. Ишлинского РАН, г. Москва, РОССИЯ

Аннотация: В работе рассмотрен подход к повышению работоспособности стеклокомпозитных трубопроводов в сейсмических условиях за счет модификации термореактивного связующего пластифицирующими и упрочняющими добавками, направленными на увеличение вязкости разрушения и снижение склонности материала к хрупкому разрушению при знакопеременных и импульсных воздействиях. Актуальность исследования обусловлена тем, что традиционные материалы трубопроводов (сталь, железобетон) обладают существенными ограничениями при эксплуатации в сейсмоопасных районах, тогда как стеклопластики, получаемые методом непрерывной намотки, характеризуются высокой удельной прочностью, коррозионной стойкостью и долговечностью, но при этом часто демонстрируют линейно-упругое поведение до момента разрушения. Объектом исследования являлись стеклокомпозитные трубы с трехслойной стенкой (поверхностный, структурно-армированный и футеровочный слои). В качестве модификаторов связующего рассмотрены Polyplex, модификатор АО «Полипласт» (ПолиПласт М) и порошковый модификатор ударной вязкости типа «ядро-оболочка» Clearstrength® XT100, вводимые в раз-

ных процентных соотношениях. Для каждого состава выполнялась серия повторных измерений, обеспечивающая сопоставимость и статистическую оценку результатов. Экспериментальная программа включала определение начальной удельной кольцевой жесткости и устойчивости к начальной кольцевой деформации, начального окружного предела прочности и модуля упругости при растяжении, начального осевого предела прочности и модуля упругости при растяжении, а также ударной вязкости по методу маятникового удара (Шарпи) в соответствии с действующими стандартами. На основе совокупности показателей обсуждается необходимость многокритериального подбора состава связующего, позволяющего одновременно сохранять расчетные жесткостно-прочностные характеристики и повышать динамическую стойкость материала.

Ключевые слова: стеклокомпозитная труба, непрерывная намотка, пластификатор, модификатор ударной вязкости, сейсмостойкость

INTRODUCTION

Modern trends in construction are characterized by continuously increasing complexity of architectural, planning, and structural solutions, driven by growing economic and social requirements. Under these conditions, the task of ensuring comprehensive safety of buildings and structures becomes particularly relevant; it goes beyond accounting for individual extreme actions and requires considering their combinations [1, 2]. The importance of the present research is additionally обусловлена by the implementation of the national project “Infrastructure for Life” [3], aimed at modernizing and improving the reliability of engineering and transport infrastructure facilities, including water supply, wastewater disposal, and other pipeline networks, whose serviceability largely determines the resilience of territorial systems.

For pipeline systems, which are critical infrastructure elements, the issue of combined actions is especially important. The high seismicity of a significant part of the territory of the Russian Federation (more than 26% of the area, including the Caucasus, Crimea, Altai, Sayan Mountains, Transbaikalia, Kamchatka, and the Kuril Islands) creates prerequisites for the realization of various scenarios of extreme impacts [4]. Statistical data confirm that regions with high seismic activity show an increased frequency of technogenic accidents, including damage to pipeline systems [5].

Traditional materials for pipelines—steel and reinforced concrete—have several serious disadvantages under seismic conditions: high mass, susceptibility to brittle fracture, and low corrosion resistance [6]. Composite materials, in particular fiberglass reinforced plastics manufactured by continuous filament winding, represent a promising alternative combining high specific strength, corrosion resistance, and durability [7–10].

However, conventional epoxy and polyester fiberglass composites are characterized by predominantly linear-elastic behavior up to the moment of brittle failure. This means that under complex alternating-sign and impulse loads typical of earthquakes, such structures cannot effectively redistribute peak stresses through plastic deformations, which increases the probability of sudden catastrophic failure [11]. In this context, the impact toughness becomes a critical controlled parameter, since it reflects the material’s energy absorption capacity under dynamic loading and its resistance to crack initiation and unstable crack propagation. Consequently, ensuring a stable and sufficiently high level of impact toughness is essential for preventing the transition from local damage accumulation to rapid, brittle, and system-level failure in seismic conditions.

Specialized studies on the seismic stability of pipelines are presented in [12–21]. The authors established that the main earthquake-related damage mechanisms for polymer composite pipelines are associated with:

- Stress concentrations in joint and branch zones [17];
- Failure under bending deformations [18];
- Loss of stability (buckling) of the pipe wall under compression [19];
- Fatigue failure under repeated cyclic actions [20, 21].

Study [22] raised the issue of predicting the physical and mechanical properties of polymer materials. The authors described a property prediction methodology; however, optimal compositions were not determined.

Thus, it is necessary to develop a composite pipe material with enhanced resistance to impact cyclic loads, while maintaining the required stiffness and strength characteristics for safe operation under combined extreme actions.

MATERIALS AND METHODS

The investigated object — a fiberglass composite pipe—consists of the following main components:

- **Binder:** unsaturated polyester resin on an orthophthalic base (PN-1 grade), isophthalic base (Depol X-400 grade), or vinyl ester base (Divinyl 911 grade);
- **Reinforcement:** fiberglass in the form of continuous and chopped E, ECR rovings;
- **Filler:** enriched quartz sand of grade VS-050-1;
- **Plasticizer.**

A plasticizer is a substance thermodynamically compatible with a polymer that reduces the density of intermolecular interactions in the polymer phase. This additive makes polymer materials less brittle and more ductile.

The following plasticizers were considered:

- **Polyplex** — a flexible unsaturated polyester resin modifier for UPR matrices.
- **Clearstrength® XT100 (Arkema)** — a powder "core–shell" impact modifier for thermosetting binders.
- **Flexible isophthalic UPR resin modifier (JSC "Poliplast")** — an isophthalic unsaturated polyester resin modifier for thermosetting binders used in continuous winding (PoliPlast M).

In addition, a number of auxiliary components were used in small amounts: cobalt octoates, methyl ethyl ketone peroxides, C-glass surface veils, and others.

Fiberglass composite pipes (Figure 1) were manufactured with plasticizer addition based on the need to increase the impact toughness of each specimen. For each formulation (Table 1), a series of at least three measurements was performed for the key indicators, enabling statistical assessment of result scatter.

The pipe cross-section consists of three layers: (1) surface layer, (2) structurally reinforced layer, and (3) liner layer. The surface and liner serve as protective layers for the external and internal pipe surfaces against weathering, UV radiation, and aggressive and/or abrasive service fluids, while the reinforced layers provide mechanical strength.



Figure 1. Specimens with modified binder

Table 1. Experimental series of binder formulations for a DN1000 pipe

Series	Plasticizer	Plasticizer content, wt.% of resin
Control	No plasticizer	0
PoliPlast M	UPR modifier (JSC "Poliplast")	10; 15; 20
Polyplex	Elastomeric additive (Polyplex Flexible)	10; 15; 20
Clearstrength XT100	"Core–shell" particles	10; 15; 20

For each formulation, a series of at least three measurements was performed for the key indicators, enabling statistical assessment of result scatter. The pipe cross-section (Figure 2) consists of three layers: (1) surface layer, (2) structurally reinforced layer, and (3) liner layer. The surface and liner protect the pipe from environmental impacts, UV exposure, and aggressive and/or abrasive fluids; the reinforced layers provide mechanical strength.

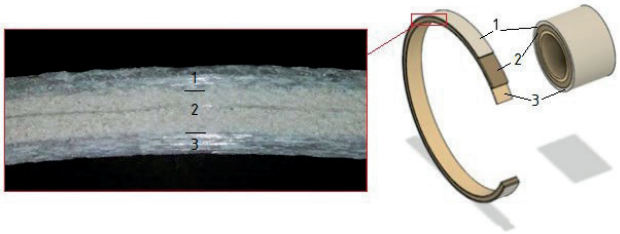


Figure 2. Wall structure of a fiberglass composite pipe

The specimen preparation scheme for the fiberglass composite pipes studied is shown in Figure 3. Specimens were cut from the manufactured pipe for: (1) impact toughness determination, (2) ring stiffness and resistance to initial ring deflection, (3) initial hoop tensile strength and tensile modulus, and (4) initial axial tensile strength and tensile modulus.

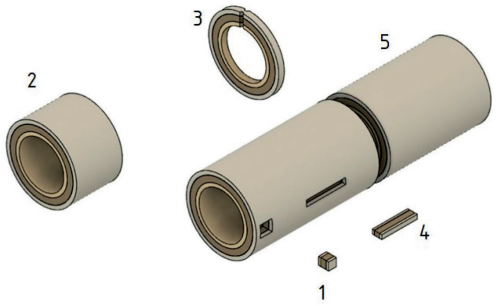


Figure 3. Specimen preparation scheme

RESULTS AND DISCUSSION

Determination of initial specific ring stiffness

Specimens for testing the initial specific ring stiffness by Method A specified in [23] and resistance to initial ring deflection according to [24] were rings cut from the fiberglass composite pipe with a width of 300 mm.
Test results are presented in Table 2. Plots of initial specific ring stiffness are shown in Figure 4.

Table 2. Initial specific ring stiffness SN, N/m²

Series	Plasticizer content, wt.% of resin	Meas. 1	Meas. 2	Meas. 3	Meas. 4	Average
Control	0	10682.5	10449.2	10738.0	10782.0	10702.5
PoliPlast M	10	10265.3	10782.6	10165.6	10433.9	10399.9
	15	10021.2	9669.0	10688.2	9602.5	10039.7
	20	10248.7	9894.3	9943.4	9661.9	9900.6
Polyplex	10	9936.4	9535.2	10067.0	9863.2	9694.0
	15	9516.1	9720.6	9639.4	9926.2	9664.3
	20	8604.2	9293.0	8692.2	9069.2	9070.2
Clearstrength XT100	10	11201.2	10099.9	10114.8	10161.7	10529.9
	15	10145.8	9651.3	10205.7	9488.2	9974.7
	20	10011.0	10431.3	10210.6	9409.9	9960.9

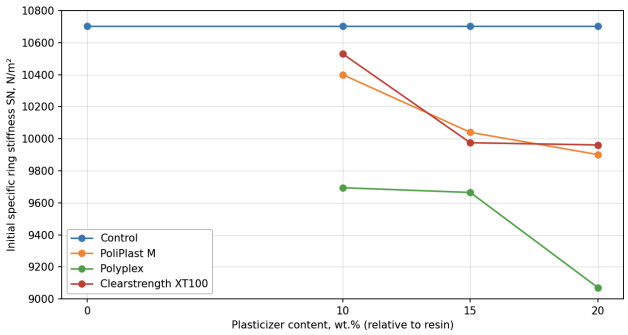


Figure 4. Plots of initial specific ring stiffness SN versus plasticizer content

Determination of initial hoop tensile strength and tensile modulus

Specimens for testing initial hoop tensile strength and tensile modules by Method B specified in [25] were cut from fiberglass composite pipes in the circumferential direction as rings 25 mm wide with a reduced section (stress concentrator) 10 mm wide.

Results are given in Table 3. Plots of initial hoop tensile strength and tensile modulus are shown in Figures 5 and 6.

Table 3. Results for initial hoop tensile strength and tensile modulus

Series	Plasticizer content, wt.% of resin	Specimen No	Initial hoop strength, MPa	Hoop tensile modulus, MPa
Control	0	1	205,3	16853
		2	204,3	16561
		3	205,6	16561
PoliPlast M	10	1	204,6	16236
		2	203,0	16041
		3	203,0	16041
	15	1	196,1	15450
		2	197,9	15564
		3	195,7	15464
	20	1	191,2	15252
		2	191,1	15134
		3	191,4	14980
Polyplex	10	1	194,4	15084
		2	191,2	14861
		3	191,7	15126
	15	1	190,1	15033
		2	189,0	15028
		3	189,7	14843
	20	1	184,8	13935
		2	182,2	14260
		3	182,6	14019
Clearstrength XT100	10	1	201,8	16179
		2	202,3	16195
		3	202,0	16041
	15	1	196,2	15300
		2	197,0	15352
		3	196,0	15452
	20	1	196,3	15467
		2	194,7	15226
		3	196,8	15419

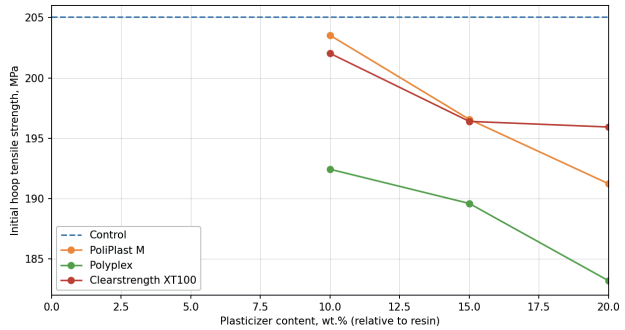


Figure 5. Initial hoop tensile strength versus plasticizer content

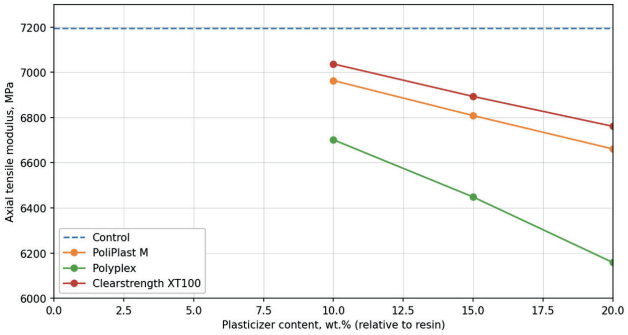


Figure 6. Initial axial tensile modulus versus plasticizer content

Testing of initial specific ring stiffness SN showed that introducing plasticizers into the binder generally reduces pipe ring stiffness compared with the control formulation (SN_avg = 10702.5 N/m²), and the reduction degree depends on the plasticizer type and content. Values closest to the control level were obtained for Clearstrength XT100 10% (SN_avg = 10529.9 N/m²; ~1–2% decrease) and PoliPlast M 10% (SN_avg = 10399.9 N/m²; ~3% decrease); PoliPlast M 15% maintains SN near the required level (SN_avg = 10039.7 N/m²). When increasing content to 20%, some formulations fall below SN = 10000 N/m² (PoliPlast M 20%—9900.6 N/m²; "PESU" 15–20%—9974.7–9960.9 N/m²), and the most pronounced stiffness drop is recorded for Polyplex (down to 9070.2 N/m² at 20%). Therefore, from the standpoint of maintaining ring stiffness within this section, formulations with 10% (PoliPlast M, Clearstrength XT100) and 15% (PoliPlast M) are the most preferable, whereas increasing content to 20% and using Polyplex are accompanied by a significant decrease in SN.

Determination of initial hoop tensile strength and tensile modulus

Specimens for testing initial axial tensile strength and tensile modulus were determined in accordance with Method B described in [26]; they were cut from fiberglass composite pipes in the axial direction as strips 25 mm wide and 450 mm long.

Results are presented in Table 4. Plots are shown in Figures 7 and 8.

Table 4. Results for initial axial tensile strength and tensile modulus

Series	Plasticizer content, wt.% of resin	Specimen No.	Initial axial strength, MPa	Axial tensile modulus, MPa
Control	0	1	103,5	7155
		2	102,6	7291
		3	102,9	7133
		4	103,9	7205
		5	103,4	7193
PoliPlast M	10	1	102,0	7010
		2	99,4	6885
		3	99,9	6926
		4	101,0	7036
		5	101,0	6961
	15	1	99,9	6865
		2	97,4	6743

		3	97,9	6783
		4	97,5	6794
		5	99,1	6858
	20	1	96,8	6684
		2	94,4	6565
		3	94,8	6605
		4	95,3	6753
		5	95,2	6697
Polyplex	10	1	98,8	6793
		2	96,4	6672
		3	96,9	6712
		4	96,3	6694
		5	96,0	6636
	15	1	95,7	6504
		2	93,4	6388
		3	93,8	6426
		4	94,7	6353
		5	96,8	6570
	20	1	91,6	6215
		2	89,3	6104
		3	89,7	6141
		4	89,6	6185
		5	92,7	6146
Clearstrength XT100	10	1	103,0	7118
		2	100,5	6991
		3	101,0	7033
		4	103,0	6977
		5	100,5	7066
	15	1	100,9	6973
		2	98,4	6849
		3	98,9	6891
		4	96,0	6907
		5	99,0	6846
	20	1	98,8	6829
		2	96,4	6707
		3	96,9	6748
		4	99,5	6715
		5	98,1	6806

Based on the average values (Figures 4.12 and 4.13), introducing the considered plasticizers leads to a decrease in axial tensile modulus and initial axial tensile strength. The most pronounced reduction is observed for the Polyplex formulation at 20% content, whereas the Clearstrength XT100 modifier better preserves strength characteristics with a moderate decrease in stiffness.

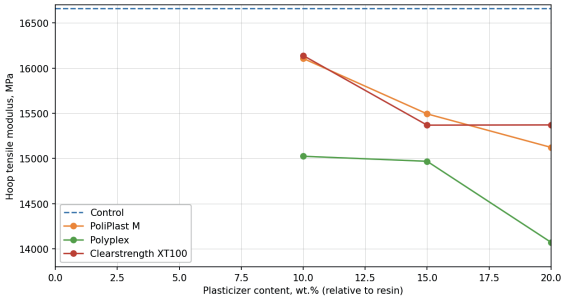


Figure 7. Initial axial tensile strength versus plasticizer content

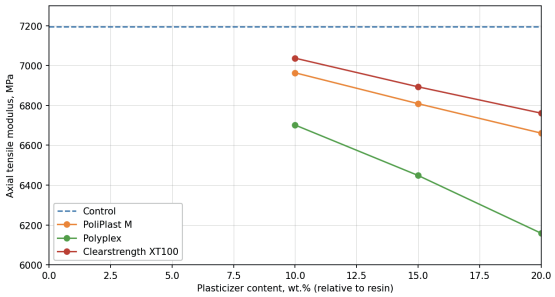


Figure 8. Axial tensile modulus versus plasticizer content

Determination of the impact toughness

Impact toughness was determined by the Charpy pendulum impact method on notched and/or unnotched specimens in accordance with [27]. To ensure comparability, the specimen size recommended by the standard was used: Type 2, length 80 mm, width 10.0 mm.
Test results are presented in Table 5. The impact toughness plot is shown in Figure 8.

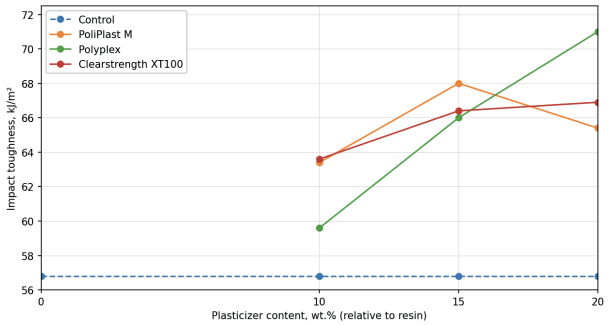


Figure 8. Impact toughness versus plasticizer content

Table 5. Charpy impact toughness, kJ/m²

Series	Plasticizer content, wt.% of resin	Meas. 1	Meas. 2	Meas. 3	Meas. 4	Average
Control	0	56,6	55,6	56,8	58,2	56,8
PoliPlast M	10	62,1	62,1	65,3	63,9	63,4
	15	67,6	69,4	67,6	67,6	68,0
	20	67,6	63,8	64,1	66,2	65,4
Polyplex	10	59,1	61,5	59,3	58,4	59,6
	15	68,7	65,7	66,2	63,5	66,0
	20	70,5	71,7	69,4	72,2	71,0
Clearstrength XT100	10	62,3	62,9	62,3	66,7	63,6
	15	67,0	65,1	68,5	64,8	66,4
	20	68,6	64,7	65,8	68,6	66,9

The most pronounced increase in impact toughness was obtained for the Polyplex series at 20% content: 71.0 kJ/m², corresponding to an increase of about 25% relative to the control level. For PoliPlast M, the maximum is achieved at 15% content (68.0 kJ/m², increase about 19.7%); with a further increase to 20%, the value decreases to 65.4 kJ/m² (increase about 15.1%), which can be interpreted as manifestation of an "over-toughening/over-plasticization" effect of the matrix and deterioration of interfacial interaction at excessive additive content. For Clearstrength XT100, a steady increase in impact toughness is observed with increasing content from 10 to 20% (up to 66.9 kJ/m², increase about 17.8%).

CONCLUSION

The performed study established that introducing plasticizing and elastomeric modifiers (including dispersed "core–shell" systems) into the thermosetting binder of fiberglass composite pipes is an effective tool for targeted increase in material impact toughness. Increasing this parameter is considered one of the determining factors in improving crack resistance and, consequently, the performance of pipe elements under seismic actions characterized by impulse nature and alternating-sign loading.

At the same time, it was revealed that the increase in impact toughness is accompanied by a decrease in stiffness–strength characteristics; the changes are systematic and dose-dependent and are governed by the nature of the plasticizer and its concentration in the matrix.

The maximum increase in impact toughness was recorded for the Polyplex formulation at 20% content; however, this series also exhibits the most pronounced decrease in ring stiffness, which limits its applicability where stiffness requirements are regulated. Formulations modified with PoliPlast M and Clearstrength XT100 demonstrate a more rational "toughness–stiffness" compromise: at moderate dosages, ring stiffness remains comparable to the control material, while a statistically significant increase in impact toughness is achieved.

The obtained data confirm the prospects of using plasticizing additives for purposeful modification of the viscoelastic response and for improving resistance to dynamic failure of fiberglass composite pipes under seismic activity.

ACKNOWLEDGEMENTS

The authors express their gratitude to "Innovative Pipe Solutions" LLC for providing equipment for specimen testing.

This work was supported by the Russian Science Foundation Grant No. 24–49–02002.

REFERENCES

1. **Shashkin S.V., Matseevich T.A., Antoshin V.A., Albagachiyev A.YU**. (2023) Primenimost′ metodov izgotovleniya stekloplastika pri stroitel′stve gorizontal′nykh yemkostey [Applicability of fiberglass manufacturing methods in the construction of horizontal tanks.]. Inzhenernyy vestnik Dona. № 5. p 738-750.
2. **Yuchenko L.V., Vaynberg M.V., Churayev A.A.** (2019) Ispol′zovaniye stekloplastikovykh trub v sel′skokhozyaystvennom vodosnabzhenii. [Use of fiberglass pipes in agricultural water supply.] Ekologiya i vodnoye khozyaystvo. №3. p. 77–92
3. Ukaz Prezidenta Rossiyskoy Federatsii ot 7 maya 2024 g. N 309 «O natsional′nykh tselyakh razvitiya Rossiyskoy Federatsii na period do 2030 goda i na perspektivu do 2036 goda» [Decree of the President of the Russian Federation dated 7 May 2024 No. 309 «On the National Development Goals of the Russian Federation for the Period up to 2030 and for the Longer Term up to 2036.»].
4. **Tamrazyan A.G., Chernik V.I.** (2024) Teplomassoperenos v zhelezobetonnykh kolonnakh pri ognevom vozdeystvii s uchetom stadii okhlazhdeniya [Heat and mass transfer in reinforced concrete columns under fire exposure considering the cooling stage.]. «Stroitel′stvo i rekonstruktsiya», № 3 (113), DOI: 10.33979/2073-7416-2024-113-3-72-82.
5. **Makhutov N.A. i soavt.** (2022) Bezopasnost′ morskikh truboprovodnykh i drugikh ob′′yektov pri uchete razdel′nogo i vzaimosvyazannogo spektra prirodnykh, tekhnogennykh i antropogennykh faktorov i ekstremal′nykh sostoyaniy [Safety of offshore pipelines and other facilities consider-

ing separate and interrelated spectra of natural, technogenic, and anthropogenic factors and extreme states.]. Morskaya nauka i tekhnika, vyp. 7. pp. 3–14.
6. **Kolbasin A.V., Garmashova L.V.** (2023) Sostoyaniye i perspektivy razvitiya trubnoy promyshlennosti Rossii. Ekonomika, predprinimatel′stvo i parvo. №7.
7. **Butovka D.V., Melent′yev I.V., Bezikov M.B.** (2025) Primeneniye stekloplastikovykh trub v sistemakh drenazha (na primere NTT DOR) [Application of fiberglass pipes in drainage systems (case study of NTT DOR).]. Gradostroitel′stvo i arkhitektura. №15(1). P 58-68
8. **Sebeay, T. A., & Ahmed, A.** (2023). Numerical Investigation into GFRP Composite Pipes under Hydrostatic Internal Pressure. Polymers, 15(5), 1110. https://doi.org/10.3390/polym15051110
9. **Seyit Mehmet Demet, Yusuf Kepir, Alper Gunoz, Harun Sepetcioglu, Mehmet Bagci, Memduh Kara.** (2026) Erosive wear behavior of FRP composite pipes under varying impingement angles, impact velocities and flow directions, International Journal of Pressure Vessels and Piping,Volume 219, Part A, https://doi.org/10.1016/j.ijpvp.2025.105657.
10. **Demet S. M., Kepir Y., Gunoz A., Sepetcioglu H., Bagci M., Kara M.** (2026) Erosive wear behavior of FRP composite pipes under varying impingement angles, impact velocities and flow directions International Journal of Pressure Vessels and Piping. Vol. 219. Art. 105657. DOI: 10.1016/j.ijpvp.2025.105657.
11. **Shashkin S.V., Matseevich T.A., Antoshin V.A., Albagachiyev A.YU.** (2024) Vliyaniye kolichestva poocheredno nanesennykh sloyev na dinamicheskiye svoystva steklokompozitnykh trub. Inzhenernyy vestnik Dona. № 8(116). pp. 615-628.
12. **Ancaș A.-D., Așchilean I. et al.** (2021) Experimental Study on the Behaviour of Seismic Actions on a Flexible Glass-Reinforced Plastic Structure Used in Water Transport Pipes. Materials.
13. **Dudchenko A.V., Dias D., Kuznetsov S.V.** (2021) Vertical wave barriers for vibration reduction Archive of Applied Mechanics (Ingenieur Archiv). T. 91. № 1. p. 257-276
14. **Tahamouli Roudsari M., Samet S. et all** (2017). Numerically Based Analysis of Buried GRP Pipelines under Earthquake Wave Propagation and Landslide Effects. Periodica Polytechnica Civil Engineering,
15. **Almahakeri M., Fam A., Moore I.D.** (2013) Longitudinal Bending and Failure of GFRP Pipes Buried in Dense Sand under Relative Ground Movement. Journal of Composites for Construction (ASCE).
16. **Zhenhao Lin, Shanqing Li**, (2024) Study on interfacial mechanical properties of bonded pipe joint under dynamic load, Heliyon, Volume 10, Issue 16. https://doi.org/10.1016/j.heliyon.2024.e36369.
17. **Davaasambuu K. et al.** (2025) Mechanisms and Performance of Composite Joints Through Adhesive and Interlocking Means—A Review. Journal of Composites Science (MDPI).
18. **Li Hong (Ed.)** (2021) Fiberglass Science and Technology: Chemistry, Characterization, Processing, Modeling, Application, and Sustainability. – Springer. p.555.
19. **Chen, J.; Liu, Z.; Wang, K.; Huang, J.; Li, K.; Nie, X.; Jiang, J.** (2018) Epoxidized castor oil-based diglycidyl-phthalate plasticizer: Synthesis and thermal stabilizing effects on poly(vinyl chloride). – Polymer Science, 2018. 135.
20. **Puyou Jia, Haoyu Xia, Kehan Tang, Yonghong Zhou,** (2018) Plasticizers Derived from Biomass Resources: A Short Review. – Polymer Science, p. 1303.
21. **Stern T., Marom G.** (2024) Fracture Mechanisms and Toughness in Polymer Nanocomposites: A Brief Review. Journal of Composites Science.
22. **Askadskiy A.A., Matseevich T.A.** (2020) Latest developments of models and calcula-

tion schemes for the quantitative analysis of the physical properties of polymers. Physics-Uspekhi. 2020. T. 63. № 2. C. 162-191.
23. **GOST R 55071–2012** Truby i detali iz reaktoplastov, armirovannykh steklovoloknom. Metody ispytaniy. Opredeleniye nachal′noy udel′noy kol′tsevoy zhestkosti [Pipes and fittings made of thermosetting plastics reinforced with glass fiber. Test methods. Determination of initial specific ring stiffness.].
24. **GOST R 55071–2012** Truby i detali iz reaktoplastov, armirovannykh steklovoloknom. Metody ispytaniy. Opredeleniye nachal′noy udel′noy kol′tsevoy zhestkosti [Pipes and fittings made of thermosetting plastics reinforced with glass fiber. Methods for determining resistance to initial ring deflection.].
25. **GOST R 54925–2012** Truby i detali iz reaktoplastov, armirovannykh steklovoloknom. Metody opredeleniya nachal′nogo okruzhnogo predela prochnosti pri rastyazhenii [Pipes and fittings made of thermosetting plastics reinforced with glass fiber. Methods for determining initial hoop tensile strength.].
26. **GOST R 54924-2017** Truby i detali iz reaktoplastov, armirovannykh steklovoloknom. Metody opredeleniya mekhanicheskikh kharakteristik pri osevom rastyazhenii [Pipes and fittings made of thermosetting plastics reinforced with glass fiber. Methods for determining mechanical properties under axial tension.].
27. **GOST 4647–2015** Plastmassy. Metody opredeleniya udarnoy vyazkosti po Sharpi [Plastics. Methods for determining Charpy impact strength.].

СПИСОК ЛИТЕРАТУРЫ

1. **Шашкин С.В., Мацеевич Т.А., Антошин В.А., Албагачиев А.Ю.** (2023) Применимость методов изготовления стеклопластика при строительстве горизонтальных емкостей. Инженерный вестник Дона. № 5. с. 738-750.
2. **Юченко Л.В., М.В. Вайнберг, А.А. Чураев** (2019) Использование стеклопластиковых труб в сельскохозяйственном водоснабжении. Экология и водное хозяйство. №3. С. 77-92.
3. Указ Президента Российской Федерации от 7 мая 2024 г. N 309 «О национальных целях развития Российской Федерации на период до 2030 года и на перспективу до 2036 года».
4. **Тамразян А.Г., Черник В.И.** (2024)**.** Тепломассоперенос в железобетонных колоннах при огневом воздействии с учетом стадии охлаждения. Строительство и реконструкция. № 3 (113), DOI: 10.33979/2073-7416-2024-113-3-72-82.
5. **Махутов и соавт.** (2022) Безопасность морских трубопроводных и других объектов при учете раздельного и взаимосвязанного спектра природных, техногенных и антропогенных факторов и экстремальных состояний. Морская наука и техника, вып. 7, с. 3–14.
6. **Колбасин А.В., Гармашова Е.П.** (2023) Состояние и перспективы развития трубной промышленности России. Экономика, предпринимательство и право. №7.
7. **Бутовка А.Н., Кретов Д.А. Морозова С.С.** (2025) Применение стеклопластиковых труб в системах дренажа (на примере НТТ ДОР). Градостроительство и архитектура. № 15(1). С. 55-68.
8. **Sebeay, T. A., & Ahmed, A.** (2023). Numerical Investigation into GFRP Composite Pipes under Hydrostatic Internal Pressure. Polymers, 15(5), 1110. https://doi.org/10.3390/polym15051110
9. **Seyit Mehmet Demet, Yusuf Kepir, Alper Gunoz, Harun Sepetcioglu, Mehmet Bagci, Memduh Kara.** (2026) Erosive wear behavior of FRP composite pipes under varying impingement angles, impact velocities and flow directions, International

Journal of Pressure Vessels and Piping,Volume 219, Part A, https://doi.org/10.1016/j.ijpvp.2025.105657

10. **Demet S. M., Kepir Y., Gunoz A., Sepetcioglu H., Bagci M., Kara M.** (2026) Erosive wear behavior of FRP composite pipes under varying impingement angles, impact velocities and flow directions International Journal of Pressure Vessels and Piping. Vol. 219. Art. 105657. DOI: 10.1016/j.ijpvp.2025.105657.
11. **Шашкин С.В., Т.А. Мацеевич, В.А. Антошин, Албагачиев А.Ю.** (2024) Влияние количества поочередно нанесенных слоев на динамические свойства стеклокомпозитных труб Инженерный вестник Дона. № 8(116). С. 615-628.
12. **Ancaș A.-D., Așchilean I. et al.** (2021) Experimental Study on the Behaviour of Seismic Actions on a Flexible Glass-Reinforced Plastic Structure Used in Water Transport Pipes. Materials.
13. **Dudchenko A.V., Dias D., Kuznetsov S.V.** (2021) Vertical wave barriers for vibration reduction Archive of Applied Mechanics (Ingenieur Archiv). T. 91. № 1. p. 257-276
14. **Tahamouli Roudsari M., Samet S. et al** (2017). Numerically Based Analysis of Buried GRP Pipelines under Earthquake Wave Propagation and Landslide Effects. Periodica Polytechnica Civil Engineering,
15. **Almahakeri M., Fam A., Moore I.D.** (2013) Longitudinal Bending and Failure of GFRP Pipes Buried in Dense Sand under Relative Ground Movement. Journal of Composites for Construction (ASCE).
16. **Zhenhao Lin, Shanqing Li**, (2024) Study on interfacial mechanical properties of bonded pipe joint under dynamic load, Heliyon, Volume 10, Issue 16. https://doi.org/10.1016/j.heliyon.2024.e36369.
17. **Davaasambuu K. et al.** (2025) Mechanisms and Performance of Composite Joints Through Adhesive and Interlocking Means—A Review. Journal of Composites Science (MDPI).
18. **Li Hong (Ed.)** (2021) Fiberglass Science and Technology: Chemistry, Characterization, Processing, Modeling, Application, and Sustainability. – Springer. p.555.
19. **Chen, J.; Liu, Z.; Wang, K.; Huang, J.; Li, K.; Nie, X.; Jiang, J.** (2018) Epoxidized castor oil-based diglycidyl-phthalate plasticizer: Synthesis and thermal stabilizing effects on poly(vinyl chloride). – Polymer Science, 2018. 135.
20. **Puyou Jia, Haoyu Xia, Kehan Tang, Yonghong Zhou,** (2018) Plasticizers Derived from Biomass Resources: A Short Review. – Polymer Science, p. 1303.
21. **Stern T., Marom G.** (2024) Fracture Mechanisms and Toughness in Polymer Nanocomposites: A Brief Review. Journal of Composites Science.
22. **Аскадский А.А., Мацеевич Т.А.** (2020) Новейшие разработки моделей и расчётных схем для количественного анализа физических свойств полимеров. Успехи физических наук. 2020. Т. 190. № 2. С. 179-210.
23. **ГОСТ Р 55071–2012** Трубы и детали из реактопластов, армированных стекловолокном. Методы испытаний. Определение начальной удельной кольцевой жесткости.
24. **ГОСТ Р 54926–2012** Трубы и детали из реактопластов, армированных стекловолокном. Методы определения устойчивости к начальной кольцевой деформации.
25. **ГОСТ Р 54925–2012** Трубы и детали из реактопластов, армированных стекловолокном. Методы определения начального окружного предела прочности при растяжении.
26. **ГОСТ Р 54924-2017** Трубы и детали из реактопластов, армированных стеклово-

локном. Методы определения механических характеристик при осевом растяжении.

27. **ГОСТ 4647–2015** Пластмассы. Методы определения ударной вязкости по Шарпи.

Sergey V. Shashkin — PhD student, National Research Moscow State University of Civil Engineering (NRU MSUCE), Junior Researcher at the Laboratory of Mechanics of Strength and Fracture of Materials and Structures, IPM RAS, 26 Yaroslavskoye Shosse, Moscow 129337, Russia, E-mail: forbic@list.ru; ORCID: 0000-0003-3334-8604

Tatyana A. Matseevich — Doctor of Physical and Mechanical Sciences, Professor, Department of Higher Mathematics NRU MSUCE, Leading Researcher at the Laboratory of Mechanics of Strength and Fracture of Materials and Structures, IPM RAS, 26 Yaroslavskoye Shosse, Moscow 129337, Russia, E-mail: Matseevichta@mgsu.ru; ORCID: 0000-0001-6292-0759.

Шашкин Сергей Владимирович – аспирант Национального исследовательского государственного строительного университета, младший научный сотрудник лаборатории механики прочности и разрушения материалов и конструкций ИПМ РАН, 129337, Ярославское шоссе, 26, Москва, Россия, E-mail: forbic@list.ru; ORCID: 0000-0003-3334-8604

Мацеевич Татьяна Анатольевна – доктор физико-механических наук, профессор кафедры высшей математики Национального исследовательского государственного строительного университета, ведущий научный сотрудник лаборатории механики прочности и разрушения материалов и конструкций ИПМ РАН, 129337, Ярославское шоссе, 26, Москва, Россия, Matseevichta@mgsu.ru; ORCID: 0000-0001-6292-0759.

International Journal for Computational Civil and Structural Engineering, 22(1) 157–168 (2026)

DOI:10.22337/2587-9618-2026-22-1-157-168

NUMERICAL SIMULATION OF DYNAMIC STRUCTURAL RESPONSE TO VIBRATIONS INDUCED BY RAILWAY TRANSPORT

Alexander M. Belostotsky, Alexander I. Nagibovich, Dmitry S. Dmitriev, Andrey A. Aul, Tatiana N. Vasileva

National Research Moscow State University of Civil Engineering, Moscow, RUSSIA
Research & Development Centre StaDyO, Moscow, RUSSIA

Abstract: This article presents numerical modeling results of prognosed dynamic response for load-bearing structural elements of constructing business complex building to railway transport vibration excitation. The transport vibrations are measured on existing pile foundation heads. The obtained response vibration acceleration evaluated by its spectra in accordance with Russian sanitary normative document.

Keywords: finite element method, vibration excitation, transport vibrations, dynamic analysis, modal analysis, dynamic response, response accelerogram, vibration comfort index

ЧИСЛЕННОЕ МОДЕЛИРОВАНИЕ ДИНАМИЧЕСКОГО ОТКЛИКА НЕСУЩИХ КОНСТРУКЦИЙ ЗДАНИЯ ОТ ВИБРАЦИОННОГО ВОЗДЕЙСТВИЯ РЕЛЬСОВОГО ТРАНСПОРТА

А.М. Белостоцкий, А.И. Нагибович, Д.С. Дмитриев, А.А. Аул, Т.Н. Васильева

Национальный исследовательский Московский государственный строительный университет, г. Москва, РОССИЯ
АО «Научно-исследовательский центр СтаДиО», г. Москва, РОССИЯ

Аннотация: В настоящей статье представлены результаты численного исследования прогнозируемого динамического отклика несущих конструкций строящегося здания Делового комплекса в г. Москва от вибрационного воздействия рельсового транспорта, определённого по результатам натурных измерений на оголовках свайного фундамента, и оценка комфортности пребывания людей в соответствии с российскими нормами.

Ключевые слова: метод конечных элементов, вибрационное воздействие, транспортные вибрации, динамический анализ, модальный анализ, динамический отклик, ответные акселерограммы, комфортность пребывания людей

1. INTRODUCTION

Currently building constructing and designing in railway influence area more often happens in metropolises with highly developed railway infrastructure. Besides this infrastructure extension leads to worsened exploiting building structures vibrational state due to new railway tracks laying closer to existing building and structures. Constructing and existing buildings and structures turn out to be under the rail transport vibration influence caused by land passenger and freight transportation trains, high-speed trains and underground. There are a few illustrations: residential complex Dominion in Moscow, Russia [1] arranged above shallow subways and the Xi'an Bell Tower in China also arranged above four shallow subways lied in 14 meters from Bell Tower foundation, as well [2].

It is known that the wheel and railway cuts impacts causes the railway transport vibration. Its spectrum and amplitude vary due to different railway construction and vibration waves propagation in the ground and also initial vibration amplitude may increase [3]. Railway transport vibration frequence mostly consists of impact excitation 25-50 Hz components [3].
Transformed transport vibration reaches buildings foundations and according to main vibration excitation frequence leads to various effects on buildings structural elements, such as steel structures fatigue resistance diminution (Bauschinger effect), cracking in concrete and masonry structures (see Fig. 1) [2], finish peeling. Periodic transport vibration leads to worsened well-being of people and equipment malfunctioning.

2. PROBLEM FORMULATION

Evaluation of constructing building load bearing structures dynamic response to vibrations induced by railway transport using numerical modeling approach is processed in 2 stages. The first stage consists of the following steps:
– measuring transport vibration excitation on pile foundation heads with further processing and evaluating;
– selecting smaller excerpt from the whole measured and processed vibration signal for usage as initial data at the next stage.
The second stage consists of the following steps:
– designing the finite element model of load bearing structures of a building;
– processing numerical research of load bearing structures dynamic response in building representative part;
– evaluating obtained in representative parts response structures vibrations according to limit vibration values given in Russian building codes and regulations.



Figure 1. The Xi'an Bell Tower foundation cracking due to periodic forced vibrations caused by underground railway transport

In the current paper the object of study is the constructing business complex building located in Moscow, Kulneva street and Kutuzovsky avenue intersection (see Fig. 2). Subject of research is the people residence vibration comfort for the premises of the object exposed to transport vibration excitation caused by land Moscow underground (Metro) trains and Moscow Central Ring (MCR) trains. Currently under construction building block lettered "B" (further "Block B") located in railway influence area. The smallest distance between MCR rail tracks and Block B vertical load bearing structures is equal to 22 meters (see Fig. a).
Beside location near railway tracks Block B has following characteristics:
– Block B building is constructed above already existing basement floor structures (5 floors deep). Vertical load bearing structures of Block B placed on existing piles and take only vertical load from existing basement flood slabs (see Fig.3);
– load bearing structures of the Block B are steel frame with steel decking monolithic reinforced concrete floor slabs and reinforced concrete structural cores;
– the maximum span between two load bearing columns rows is equal to 30 meters;
– the complex node connection between fourbranched steel part (above the ground) and reinforced concrete part with circle cross section

(below ground) (see Fig. 4). The underground concrete column part bear to pile grid.



Figure 2. The business complex render: a) an assembly view, b) the Block B render

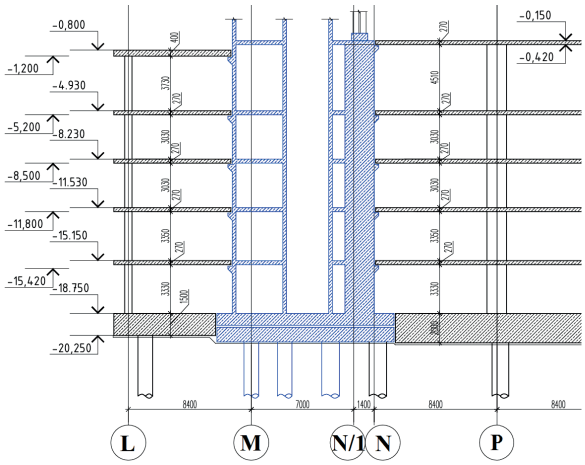
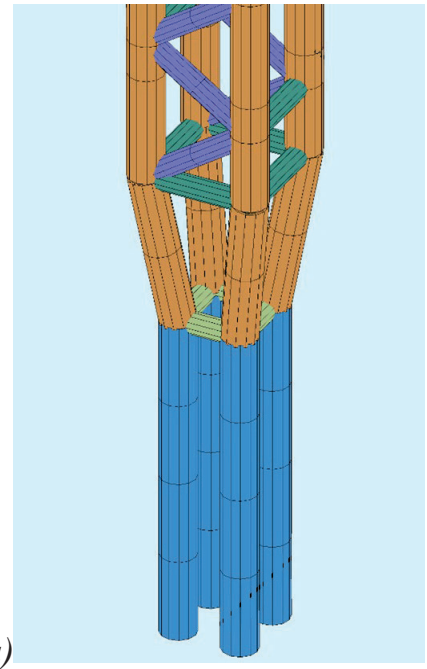


Figure 3. Cross-sectional plan of a five floors basement. New reinforced columns are colored in blue, existing load bearing structures are colored in black



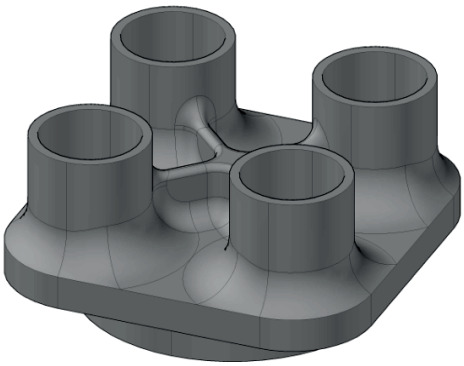
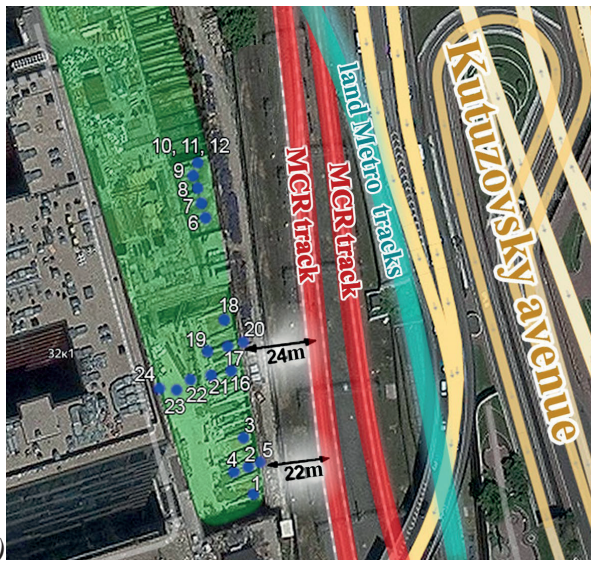


Figure 4. The fourbranched steel bearing column reinforced concrete bearing column node connection: a) an assembly view of column steel part, b) the connection part

3. STAGE 1. MEASURING VIBRATIONS

Taking in account the fact that Block B columns will bear to existing pile grid it was decided to take railway transport vibration measurements on the pile heads (see Fig 4). That provides the lack of need to conduct mathematical modelling of vibration waves propagation in soil mass between Block B pile foundation and railway tracks.

a)



b)



Figure 5. Vibration measurements.
a) Points of measurements location.
Constructing Block B contour is colored green;
b) An accelerometer position on a pile head

The measurements of railway transport vibration acceleration were conducted by experts Gecha V.Ia., Grabilin A.O., Derishev D.V. from CJSC «Moscow Engineering Agency» taking in account Russian standards [4]. The utilized accelerometers (see Fig. 5b) have from 0.05 up to 750 Hz frequence range and sensitivity in range 100 – 107 mV/ms^2. The vibration signals measurement and analyzation were made using LMS SCADAS Mobile system. The series of measurement were made. According to the LMS SCADAS Mobile ADC limits and characteristics the sampling rate for each measurement in series was chosen fs = 256 Hz with frequency step Δf = 0,001953 Hz. Therefore, sampled acceleration signal had Ns = 131 080 values. According to those characteristics the maximum duration of measured railroad transport vibration signals T = 256 s, the discretization step Δt = 2 ms. The measured in each point (see Fig. 5a) vibration acceleration signals consist of five recorded sequentially signals because the 256 seconds are barely enough to register at least one of Metro or MCR trains passes by nearest railway tracks. Total vibration acceleration signal duration is 1280 s which allowed to measure vibration from at least 5 Metro trains and 3 MCR trains passed in both directions. Railway transport vibration acceleration was measured in 3 directions (see Fig. 6).

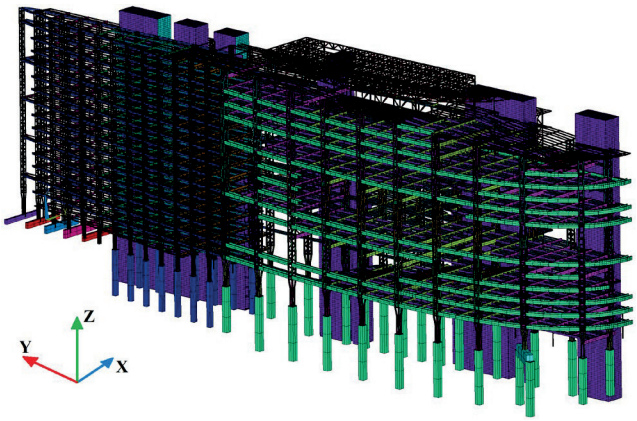


Figure 6. The Block B finite element model.
The direction axes of railway transport vibration excitation are located in the left bottom corner:
– X and Y direction: horizontal perpendicular and parallel to column rows respectively vibration components;
– Z direction: vertical vibration component

The following measured vibration excitation features were obtained based on its analysis results:
– all measured vibration acceleration signals have low-frequency (significantly lower than 1 Hz) components;
– some of the obtained acceleration signals recorded in few points have an unsignificant extraneous noise (lower than 50 dB);

– some of the obtained acceleration signals recorded in a few points have a significant noise from working vibration and impact equipment.

Measured railway transport vibration acceleration signals were filtered before further research. Filtration was obtained by extracting components with frequency from 1 to 200 Hz, the components with frequency lower then 1 Hz and higher then 200 Hz were deleted. Besides components of noise with 50 Hz frequency were cut too. Obtained in point 1 at the axis 35 pile head example of railway transport vibration acceleration signal before and after filtration presented on Figure 7.

The moments when MCR and Metro trains passing by Block B are easy to define on processed vibration acceleration signals. The 10 seconds and 50 seconds fragments for MCR and Metro trains with highest acceleration amplitude were chosen from filtered vibration accelerations signals (see Fig. 7, 10 seconds fragments highlighted pink, 50 seconds fragments highlighted yellow). 1/1 octave spectra were obtained for each of these 10 s and 50 s fragments for further railway transport vibration evaluation.

According to [5] the vibration evaluation must be proceeded with vibration logarithmic grade. This method is commonly used for experimental and numerical studies, as example [6]. The limits for our problem are designated for vibration acceleration logarithmic grade value *La* (in dB) for every of 2 – 63 Hz 1/1 octave band of vibration acceleration. The limit values for each 1/1 octave band took from [5] with amendment in «-10 dB» because the transport vibration excitation is inconstant or periodic excitation. The whole signal, 10 s and 50 s MCR and Metro fragments vibration acceleration obtained in point 1 octave spectra comparison with limit logarithmic grade values presented in Tables 1-3. As it shown for representative point 1, measured and filtered railway transport vibration acceleration octave spectra values do not exceed limit logarithmic grade values.

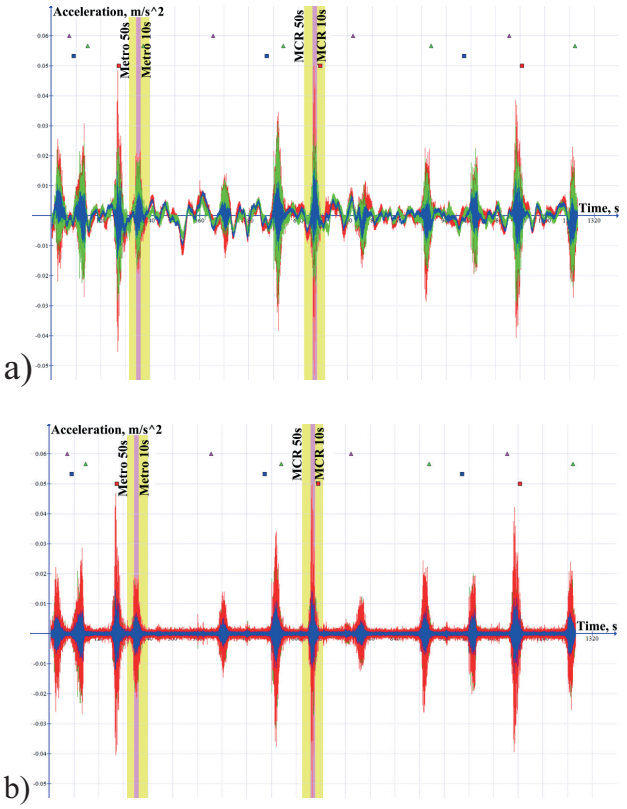


Figure 7. Acceleration history: a) measured; b) filtered. Fragments highlighted pink and yellow were used to obtain vibration signal spectra

Table 1. 1/1 octave spectra for measured in point 1 railway transport vibration acceleration. X direction

Hz	*2*	*4*	*8*	*16*	*31.5*	*63*	*125*
«Limit», dB	*70*	*71*	*73*	*79*	*85*	*91*	*-*
1280 s	*46*	*44*	*45*	*50*	*61*	*63*	*57*
MCR 10s	*39*	*39*	*47*	*56*	*68*	*71*	*68*
MCR 50s	*36*	*37*	*45*	*52*	*63*	*66*	*64*
Metro 10s	*20*	*20*	*25*	*36*	*50*	*52*	*38*
Metro 50s	*19*	*20*	*23*	*32*	*44*	*46*	*33*

Table 2. 1/1 octave spectra for measured in point 1 railway transport vibration acceleration. Y direction

Hz	*2*	*4*	*8*	*16*	*31.5*	*63*	*125*
«Limit», dB	*70*	*71*	*73*	*79*	*85*	*91*	*-*
1280 s	*49*	*47*	*51*	*56*	*63*	*65*	*57*
MCR 10s	*31*	*46*	*55*	*61*	*72*	*77*	*71*
MCR 50s	*44*	*45*	*52*	*58*	*66*	*71*	*64*
Metro 10s	*12*	*11*	*22*	*31*	*42*	*53*	*52*
Metro 50s	*22*	*25*	*30*	*38*	*47*	*47*	*32*

Table 3. 1/1 octave spectra for measured in point 1 railway transport vibration acceleration. Z direction

Hz	*2*	*4*	*8*	*16*	*31.5*	*63*	*125*
«Limit», dB	*70*	*71*	*73*	*79*	*85*	*91*	*-*
1280 s	*34*	*33*	*40*	*45*	*53*	*55*	*49*
MCR 10s	*44*	*41*	*45*	*50*	*61*	*65*	*60*
MCR 50s	*38*	*37*	*44*	*47*	*56*	*60*	*55*
Metro 10s	*11*	*22*	*31*	*42*	*53*	*52*	*38*
Metro 50s	*15*	*19*	*23*	*32*	*44*	*44*	*33*

The 20 seconds fragment with highest amplitude, that cut from measured and filtered railway transport vibration three-component acceleration history obtained in point 1 (630 – 650 seconds), was chosen for the second stage dynamic response research design data. Three components of chosen vibration acceleration fragment illustrated on Figure 8.

4. STAGE 2. STRUCTURAL DYNAMIC RESPONSE NUMERICAL MODELING

The finite element model utilized for Block B dynamic response analysis were designed in ANSYS Mechanical Software. It consists of spatial discretization of Block B above ground structural load bearing elements and below ground new reinforced concrete columns and structural cores). The reinforced concrete and steel columns and beams are modelled with the 3D 2-node beam BEAM188 finite elements (the element is based on Timoshenko beam theory which includes shear-deformation effects), the steel decking monolithic reinforced concrete floor slabs, walls and structural cores are spatially discretized with the elastic shell SHELL63 finite elements (has both bending and membrane capabilities). The FE model consisted of 846 158 nodes and 282 903 finite elements. Every node has 6 degrees of freedom.

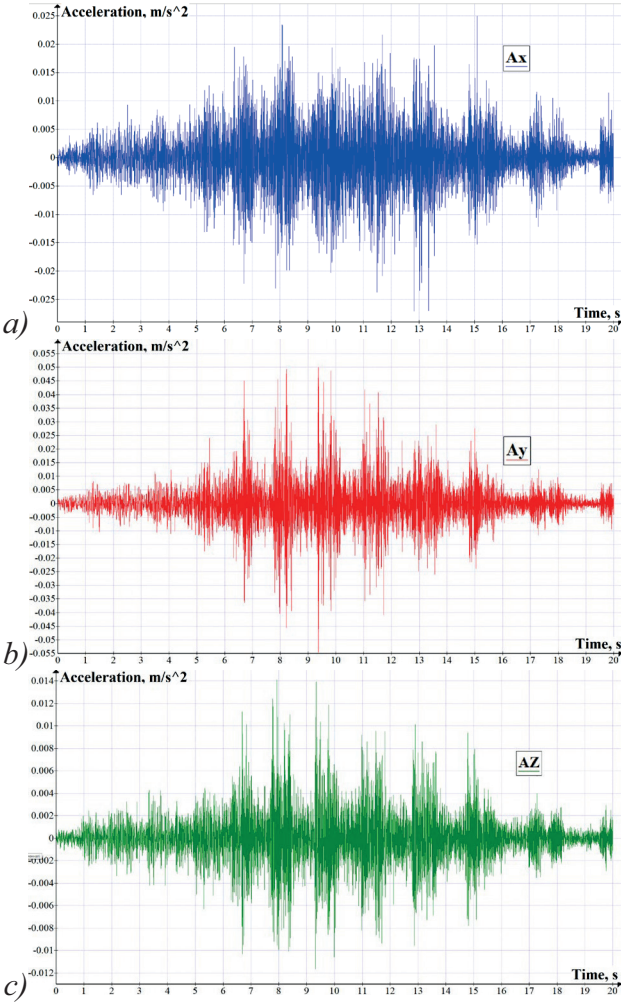


Figure 8. Three components of railway transport vibration acceleration 20 seconds history utilized for the next stage numerical research

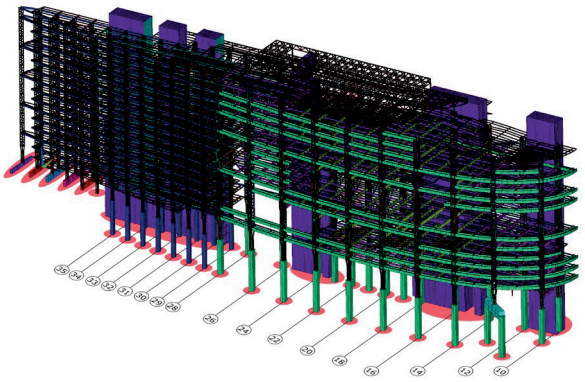
Element material properties are presented in Table 4.

Table 4. Material properties

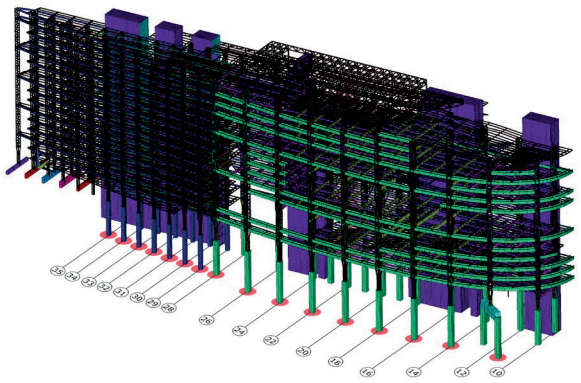
Material	Elastic Modulus E, GPa	Poisson's ratio ν	Density ρ, kg/m^3
Reinforced concrete	36	0.2	2500
Steel	206	0.3	7850

There were designed two options of railway transport vibration excitation (taken as the 20 seconds three-component acceleration history according to stage 1 measurements) distribution scheme to evaluate people residence vibration comfort for the premises of Block B. The first

load distribution scheme (further Option 1) illustrates the platform vibration load distribution, hence vibration acceleration history is simultaneously applied to the all of underground columns lowest nodes right where the reinforced concrete underground load bearing columns bear to the existing piles (see Fig. 9a). And the second load distribution scheme (further Option 2) illustrates the non-platform vibration load distribution, unlike Option 1, the vibration acceleration applies only to the closest to the railway tracks vertical underground load bearing structures lowest nodes (see Fig. 9b). Besides, it's expected that Block B structural elements dynamic response obtained with Option 1 will be higher due to soil railway transport vibration waves damping.



a)



b)

Figure 9. The railway transport vibration load distribution schemes. Nodes to which three-component vibration acceleration history applied to marked with red areas.
a) Option 1. Platform vibration load distribution scheme;
b) Option 2. Non-platform vibration load distribution scheme.

The numerical model of the Block B load bearing structures vibration dynamic response problem consists of finite element method semi-discrete equation of motion (see Eq.1). That equation solution can be conducted using direct implicit Newmark method updating equation step by step (see Eq. 2 and 3). The chosen for equations solving time step is equal to 0.002 s. Similar numerical modeling approaches to people residence vibration comfort for the premises of the object exposed to railway transport vibration excitation are presented in articles [1] and [7].

$$[M]\{\ddot{u}(t)\}+[C]\{\dot{u}(t)\}+ +\left([K]+\left[K_G\right]\right)\{u(t)\}=\{F(t)\}+\{R(u,\dot{u})\}, \quad (1)$$

where
$[M]$, $[C]$, $[K]$ и $[K_G]$ – the finite element model structural mass matrix, the structural damping matrix, and the linear (initial) and geometrical stiffness matrixes, respectively;
t – time;
$\{F(t)\}$ – the applied static and dynamic load vector;
$\{R(u,\dot{u})\}$ – the restored load vector utilized for material nonlinear equation solving;
$\{u(t)\}$ – the obtained general nodal displacement vector.
The Newmark time integration method is based on finite difference method. Each Δt time step following velocity and displacement vectors updated as it shown further (see Eq. 2 and 3).

$$\{\dot{u}_{n+1}\}=\{\dot{u}_n\}+\left[(1-\delta)\cdot\{\ddot{u}_n\}+\delta\cdot\{\ddot{u}_{n+1}\}\right]\cdot\Delta t \quad (2)$$

$$\{u_{n+1}\}=\{u_n\}+\{\dot{u}_n\}\cdot\Delta t+ +\left[\left(\frac{1}{2}-\alpha\right)\cdot\{\ddot{u}_n\}+\alpha\cdot\{\ddot{u}_{n+1}\}\right]\cdot\Delta t^2 \quad (3)$$

where
α, δ – Newmark's integration parameters chosen with the accuracy and stability conditions. The optimal parameters (δ = 0.5 and α = 0.25) satisfying to both conditions make the Newmark

constant average acceleration method unconditionally stable;

$$\Delta t = t_{n+1} - t_n;$$

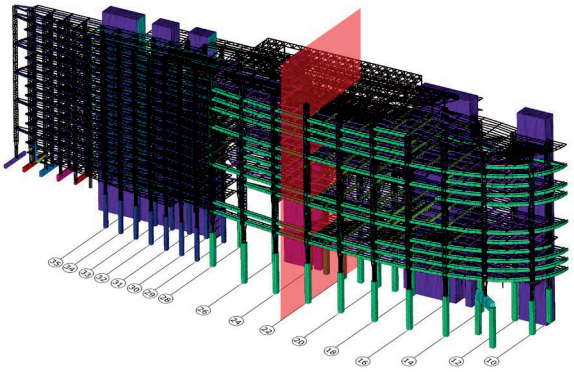
$\{u_n\}$ and $\{u_{n+1}\}$ – the vectors of nodal displacements at time t_n and t_{n+1} respectively;
$\{\dot{u}_n\}$ и $\{\dot{u}_{n+1}\}$ – the vectors of nodal velocity at time t_n and t_{n+1} respectively;
$\{\ddot{u}_n\}$ и $\{\ddot{u}_{n+1}\}$ – the vectors of nodal acceleration at time t_n and t_{n+1} respectively.

5. OPTION 1 (PLATFORM SCHEME) RESULTS

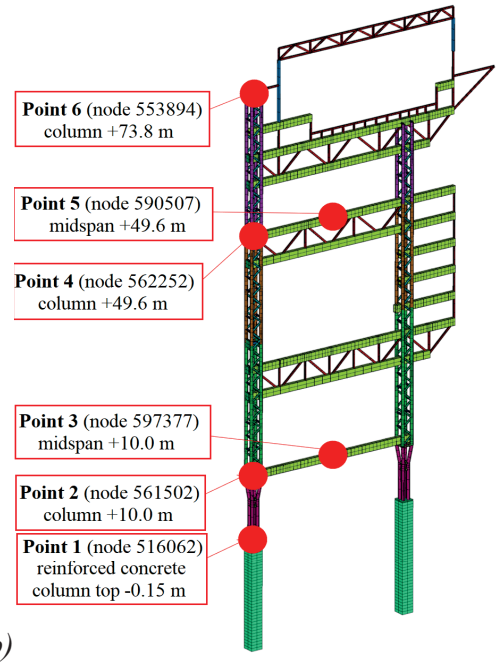
The Block B load bearing structures exposed to railway transport vibration specified by three-component vibration acceleration history dynamic response spectra obtained with numerical simulation are compared to limit values represented in [5]. According to this Russian regulation document the determined vibration response acceleration of the structural elements evaluation must be conducted using certain parameter (acceleration) spectral (frequency) analysis. Hence, the logarithmic grade parameter (vibration response acceleration) values must not exceed limit value for each of 1/1 octave bands, given in [5]. The limit logarithmic grade values have been taken with «-10 dB» amendment, due to the transport vibration excitation inconstant nature.
Logarithmic acceleration grade values *La* formula is given below (See Eq. 4). The *La* units are decibels (dB).

$$L_a = 20 \lg \frac{a}{1 \cdot 10^{-6}}, \qquad (4)$$

where
a – mean average vibration acceleration, m/s$^{2;}$
$1 \cdot 10^{-6}$ – reference vibration acceleration, m/s^2.
The steel frame by axis 22 (frame 22) was chosen as representative for numerical modeling results evaluating due to structural core absence by 22 axis and frame 22 structures span, that is the largest in whole Block B structure. The obtained Option 1 (see Fig. 9a) response vibration acceleration history for representative points in bearing and span areas of frame 22 (see Fig. 10) illustrated in Figure 11. Moreover, the obtained logarithmic grade response vibration acceleration values evaluation for some of these points given in Table 5.



a)



b)

Figure 10. The representative frame by axis 22. a) Its position in Block B finite element model marked red; b) The frame 22 structural elements. The representative points in which response vibration acceleration numerical modeling results obtained marked red.

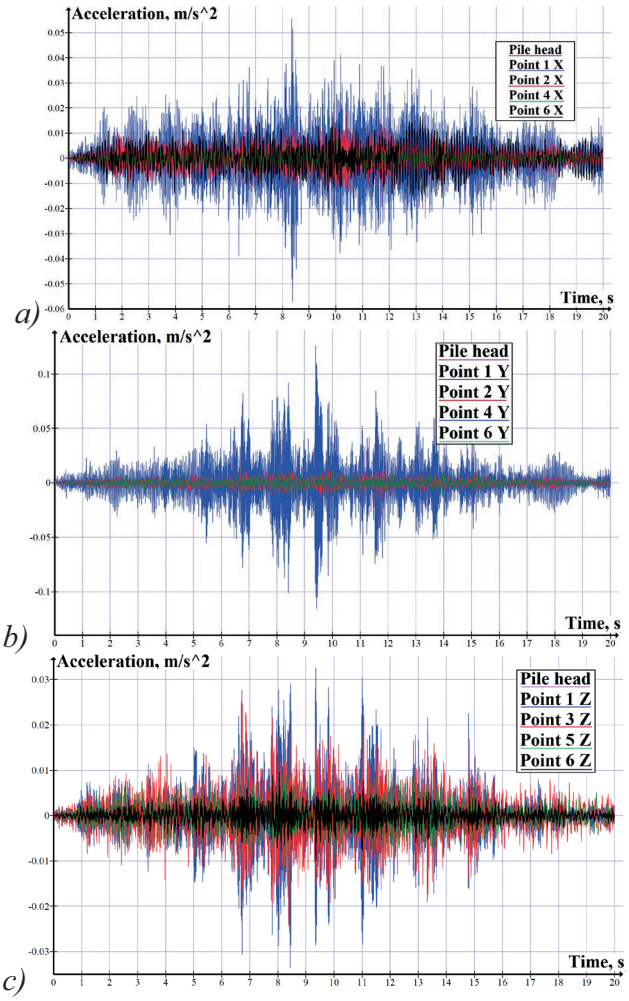


Figure 11. Frame 22 response vibration acceleration history:
a) Ax, points 1, 2, 4, 6. Ax_{max} = 0.0572 m/s^2
b) Ay, points 1, 2, 4, 6. Ay_{max} = 0.1255 m/s^2
c) Az, points 1, 3, 5, 6. Az_{max} = 0.0333 m/s^2

Table 5. The logarithmic grade vibration acceleration values at the representative frame 22 points for Option 1 load distribution scheme

Octave band geometric mean frequency, Hz	*Ax, point 1, dB*	*Ay, point 1, dB*	*Az, point 1, dB*	*Az, point 3, dB*	*Az, point 6, dB*	*Limit, dB*
2	40.41	35.79	32.67	35.41	47.53	70
4	59.40	44.05	36.32	60.83	58.32	71
8	51.84	61.90	46.15	68.35	74.48	73
16	75.97	80.52	52.86	68.07	69.85	79
31.5	71.92	74.93	69.67	71.47	68.91	85
63	80.87	86.97	77.06	71.79	59.20	91
125	73.40	70.26	60.98	50.08	29.12	-

*Note: values that exceed residence comfort limits values marked blue.

6. OPTION 2 (NON-PLATFORM SCHEME) RESULTS

The non-platform vibration excitation distribution scheme (Option 2) let us obtain the response vibration acceleration numerical modeling results that are closer to the real structural elements dynamic response due to transport vibration waves dissipation in soil.
The Figure 12 presents the obtained using Option 1 and Option 2 schemes vibration acceleration history comparison for the specific frame 22 representative points in which the residence comfort values those exceed limits were observed. The comparison of logarithmic grade response vibration acceleration values obtained using both platform and non-platform excitation distribution schemes given in Table 6.

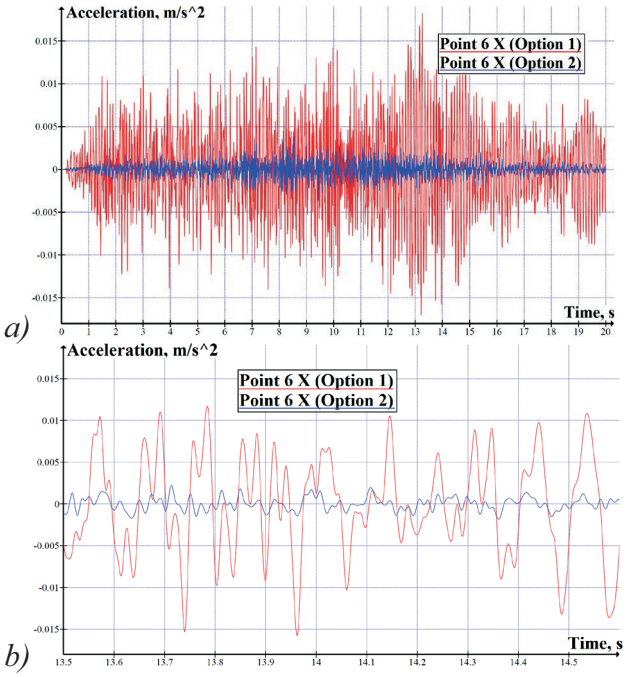


Figure 12. The response vibration acceleration history in X direction at point 6 of frame 22 obtained using Option 1 (platform) and Option 2 (non-platform) schemes.
a) The whole excitation duration response vibration acceleration history (20 seconds);
b) The 1.1 seconds fragment (13.5 – 14.6 s) where the vibration acceleration maximum amplitude was observed.

Table 6. The logarithmic grade vibration acceleration values at representative frame 22 6 point comparison for Option 1 and Option 2 load distribution schemes

Octave band geometric mean frequency, Hz	Ax, point 6, dB		Δ, %	Limit, dB
	Option 1 (platform scheme)	Option 2 (non-platform scheme)		
2	47.53	35.25	-25.84	70
4	58.32	52.56	-9.88	71
8	74.48	61.71	-17.15	73
16	69.85	55.81	-20.10	79
31.5	68.91	58.85	-14.60	85
63	59.20	63.53	+7.31	91
125	29.12	20.57	-29.36	-

*Note: values that exceed residence comfort limits values marked blue.

As expected, logarithmic grade values of response vibration acceleration spectra obtained with Option 2 railway transport excitation are within the limit people residence comfort values comparing to Option 1 response spectra exceeding limit logarithmic grade values.

CONCLUSION

Firstly, for the business complex Block B there were measured on existing pile heads and evaluated the vibrations induced by railway transport: land underground trains and MCR trains. Secondly, the Block B dynamic structural response to measured transport vibrations was obtained using finite element model and two vibration excitation distribution schemes: platform and non-platform. The results are described in more details below:

1. The measured on existing pile heads railway transport vibration acceleration octave spectra do not exceed the limit logarithmic grade ones taken according to [5]. For the further object dynamic response numerical research purposes, the 20 second fragment of the three-component acceleration history with maximum measured acceleration amplitude was selected.
2. The two transport distribution schemes were considered: platform (Option 1) and non-platform (Option 2). The Option 1 railway transport vibration acceleration spectra were obtained for the Block B representative steel frame by axis 22 points located in frame midspans and in load-bearing column areas. The vibration acceleration spectra of point 1 and 6 are exceeding limit logarithmic grade values, hence some of Block B premises are uncomfortable for people residence. However, expected the implausible results for Option 1 scheme.
3. The dynamic response spectra values obtained for Option 2 scheme more likely illustrating the real Block B dynamic response to vibration induced by railway transport are significantly less than limit logarithmic grade vibration acceleration values (reserve more than 10 dB).
4. The comparison of the frame 22 representative points railway vibration acceleration logarithmic grade values obtained for Option 1 and Option 2 schemes shows the expected lower values for Option 2 than Option 1 with 29.36% difference. Except the dynamic response vibration acceleration value for 1/1 octave band with 63 Hz central frequency, for this octave band the Option 2 value higher than Option 1 but yet lower than limit value.

REFERENCES

1. **Belostotsky, A., Aul, A., Nagibovich, A.** Numerical and experimental simulation vibrational state of bearing structures tall buildings, caused by the movement subway trains. // International Journal for Computational Civil and Structural Engineering. – 2011. – Vol.7, No.3. – P. 62-69.
2. **Lai J., Niu F., Wang K.** Dynamic effect of metro-induced vibration on the rammed earth base of the Bell Tower. // SpringerPlus – 2016. – Vol. 5 – №. 935.
3. **Dashevskij M.A.** Protection of buildings against vibrations induced by subway train

traffic // Doctoral thesis in engineering science. – Central Scientific-Research Institute of Building Structures named after V.A. Kucherenko, – Moscow, Russia. – 1991. – P. 456.
4. Code of practice 23-105-2004. Vibration assessment for design, construction and operation of metro units. – 2004.
5. Sanitary norms 2.2.4/2.1.8.566-96. The sanitary norms of industrial vibration, vibration of residential and public buildings. Минздрав России, – 1997.
6. **Dashevskij M.A., Mitroshin V.A., Mondrus V.L., Sizov D.K.** Impact of metro induced ground-borne vibration on urban development. // Magazine of Civil Engineering. – 2021. – Vol. 106, No. 6. – No. 10602.
7. **Belostotsky, A.,** Numerical and experimental simulation tall buildings vibrational state, caused by the movement subway trains. // Tall buildings, – 2015. – Vol.4, – P. 101-107.

СПИСОК ЛИТЕРАТУРЫ

1. **Белостоцкий А.М., Аул А.А., Нагибович А.И.** Расчетно-экспериментальное моделирование вибрационного состояния несущих конструкций многоэтажных зданий, вызванного движением поездов метрополитена. // International Journal for Computational Civil and Structural Engineering. – 2011. – Vol.7, No.3. – P. 62-69.
2. **Лай Ц., Ню Ф., Ван К**. Воздействие вибраций, вызванных работой метро, на Колокольную башню в Сиане // SpringerPlus – 2016. – Vol. 5 – №. 935.
3. **Дашевский М.А.** Защита зданий от вибраций, возбуждаемых движением поездов метрополитена // Диссертация на соискание ученой степени доктора технических наук. – Центральный научно-исследовательский и проектно-экспериментальный институт комплексных проблем строительных конструкций и сооружений им. В. А. Кучеренко (ЦНИИСК им. Кучеренко), – Москва, Россия. – 1991. – С. 456.
4. СП 23-105-2004. Оценка вибрации при проектировании, строительстве и эксплуатации объектов метрополитена., М., Госстрой России. – 2004.
5. СН 2.2.4/2.1.8.566-96. Производственная вибрация, вибрация в помещениях жилых и общественных зданий. Минздрав России, – 1997.
6. **Dashevskij M.A., Mitroshin V.A., Mondrus V.L., Sizov D.K.** Impact of metro induced ground-borne vibration on urban development. // Magazine of Civil Engineering. – 2021. – Vol. 106, No. 6. – No. 10602.
7. **Белостоцкий А.М.** Расчетно-экспериментальное моделирование вибрационного состояния высотных зданий, вызванного движением поездов метрополитена. Высотные здания, № 4, 2015, стр.101-107.

Alexander M. Belostotsky – DSc, Professor, Full Member of the Russian Academy of Architecture and Construction Sciences, Scientific adviser at Zolotov Research and Educational Center for Computational Modelling of the National Research Moscow State University of Civil Engineering; 129337, Russia, Moscow, Yaroslavskoe shosse, 26. General Director Scietific and Research Center StaDyO; 18, 3ya Ulitsa Yamskogo Polya, Moscow, 125040, E-mail: amb@stadyo.ru

Белостоцкий Александр Михайлович – д.т.н., профессор, академик РААСН, научный руководитель НОЦ КМ им. А.Б. Золотова Национального исследовательского Московского государственного строительного университета; 129337, Россия, г. Москва, Ярославское шоссе, д. 26. E-mail: amb@stadyo.ru

Alexander I. Nagibovich – CSc, Director at Zolotov Research and Educational Center for Computational Modelling of the National Research Moscow State University of Civil Engineering; 129337, Russia, Moscow, Yaroslavskoe shosse, 26. Leading calculation engineer at the Scientific and Research Center StaDyO; 18, The 3rd Yamskogo Polya st., Moscow, 125040, Russia. E-mail: nagibovich@yandex.ru

Dmitry S. Dmitriev - CSc, Senior Research Fellow of A.B. Zolotov REC SM of the National Research Moscow State University of Civil Engineering; 129337, Russia, Moscow, Yaroslavskoe shosse, 26. Deputy General Director for Computational Research of JSC Scietific Research Center StaDyO; 18, 3ya Ulitsa Yamskogo Polya, Moscow, 125040, Russia. E-mail: dmitriev.d.s@yandex.ru

Andrey A. Aul – Head of the sector at Zolotov Research and Educational Center for Computational Modelling of the National Research Moscow State University of Civil Engineering; 129337, Russia, Moscow, Yaroslavskoe shosse, 26. Leading calculation engineer at the Scientific and Re-search Center StaDyO; 18, The 3rd Yamskogo Polya st., Moscow, 125040, Russia. E-mail: stadyo@stadyo.ru

Tatiana N. Vasileva – engineer at Zolotov Research and Educational Center for Computational Modelling of the National Research Moscow State University of Civil Engineering; 129337, Russia, Moscow, Yaroslavskoe shosse, 26. Calculation engineer at the Scientific and Research Center StaDyO; 18, The 3rd Yamskogo Polya st., Moscow, 125040, Russia. E-mail: rabitfew@gmail.com

Нагибович Александр Игоревич – к.т.н., директор НОЦ КМ им. А.Б. Золотова Национального исследовательского Московского государственного строительного университета; 129337, Россия, г. Москва, Ярославское шоссе, д. 26. Ведущий инженер-расчетчик АО НИЦ СтаДиО; E-mail: nagibovich@yandex.ru

Дмитриев Дмитрий Сергеевич – к.т.н, старший научный сотрудник НОЦ КМ им. А.Б. Золотова Национального исследовательского Московского государственного строительного университета; 129337, Россия, г. Москва, Ярославское шоссе, д. 26. Заместитель генерального директора по расчетным исследованиям АО НИЦ СтаДиО. E-mail: dmitriev.d.s@yandex.ru

Аул Андрей Андреевич – заведующий сектором НОЦ КМ им. А.Б. Золотова Национального исследовательского Московского государственного строительного университета; 129337, Россия, г. Москва, Ярославское шоссе, д. 26. Ведущий инженер-расчетчик АО НИЦ СтаДиО; E-mail: stadyo@stadyo.ru

Васильева Татьяна Николаевна – инженер НОЦ КМ им. А.Б. Золотова Национального исследовательского Московского государственного строительного университета; 129337, Россия, г. Москва, Ярославское шоссе, д. 26. Инженер-расчетчик АО НИЦ СтаДиО; E-mail: rabitfew@gmail.com

International Journal for Computational Civil and Structural Engineering, 22(1) 169–178 (2026)

DOI:10.22337/2587-9618-2026-22-1-169-178

CONSTRUCTION PROPERTIES OF SUBSIDIBLE SOILS IN MONGOLIA UNDER CLIMATE CHANGE: PROBLEM AND SOLUTION

Nyamdorj Setev, Uranchimeg Davaasuren, Sukh-Erdene Khureltsooj, Erdenetsetseg Enkhbaatar

Technician and Technological University, Ulaanbaatar, MONGOLIA

Abstract: The main regional features of subsidence clay soils common in Mongolia are high porosity, low humidity and underfilling within the seasonal deep freezing due to their heaving and sublimation loosening. Using such soils as foundations for buildings and structures under conditions of increasing humidity is difficult at the design and construction stages, as well as during operation. This paper examines the results of analytical calculations to identify the dependence of a decrease in the physical and mechanical properties of subsidence soils on an increase in humidity and constructs the corresponding dependence graphs. Numerical modeling of the quantitative and qualitative assessment of the subsidence properties of sandy loam and loamy soils using the method of indirect signs and the probability of the formation of a subsidence process during soaking is also carried out.

Keywords: global warming, sublimation loosening, underfilling, atmospheric precipitation, sandy loam and loamy soils, deterioration of physical and mechanical properties

КОНСТРУКТИВНЫЕ СВОЙСТВА НЕУСТОЙЧИВЫХ ГРУНТОВ МОНГОЛИИ В УСЛОВИЯХ ИЗМЕНЕНИЯ КЛИМАТА: ПРОБЛЕММЫ И РЕШЕНИЯ

Сэтэв Ньямдорж, Даваасурэн Уранчимэг, Хурэлцооож Сух-Эрдэнэ, Энхбаатар Эрдэнэцэцэг

Технический и технологический университет, г. Улан-Батор, МОНГОЛИЯ

Аннотация. Основными региональными особенностями просадочных глинистых грунтов, широко распространённых на территории Монголии, являются высокая пористость, низкая влажность и недоуплотнённость в условиях сезонного глубокого промерзания, обусловленные процессами морозного пучения и сублимационного разрыхления. Использование таких грунтов в качестве оснований зданий и сооружений при увеличении влажности представляет значительные трудности как на стадиях проектирования и строительства, так и в процессе эксплуатации. В настоящей работе рассмотрены результаты аналитических расчётов, направленных на выявление зависимости снижения физико-механических свойств просадочных грунтов от увеличения влажности, а также построены соответствующие графики зависимостей. Выполнено численное моделирование количественной и качественной оценки просадочных свойств супесчаных и суглинистых грунтов с применением метода косвенных признаков, а также оценена вероятность формирования просадочного процесса при замачивании.

Ключевые слова: глобальное потепление, сублимационное разрыхление, недоуплотнение, атмосферные осадки, супесчаные и суглинистые грунты, ухудшение физико-механических свойств.

INTRODUCTION

In recent years, the amount of precipitation has increased sharply due to changes in climatic conditions due to global warming almost all over the world, including Mongolia. As a result, the moisture content of the foundation soil increases to the point of water saturation, weakening and disintegration of the crystallization and cementation structural bonds of clay soils, and, as a rule, deterioration of their construction properties.

The problems of changing climatic conditions due to global warming are the subject of many researchers' works [1; 2; 3; 4; 5; 6; 7 and 8].

The territory of Mongolia is located at the altitude of the Central Asian plateau, the thickness of the vegetation layer and snow cover in winter is relatively small, the average annual temperature of the territory is about 0 ℃, and the average number of days with negative temperature is more than 200. According to the norm of BNBD (SNiP) "Climatology of the territory of Mongolia", the depth of seasonal freezing of soils is 3.5 ... 5.0 m and sometimes in real conditions the depth of seasonal freezing of water-saturated coarse-grained soils with sandy loam and loamy filler reaches 6.0 meters, in rare cases permafrost is found under it [9; 10].

As a rule, wet clay soils to the depth of seasonal freezing are from weak to strong degree of heaving, in the thawed state have high porosity, relatively low humidity, undercompact.

Currently, in Mongolia there is an increase in the number of deformed buildings and engineering structures for the above-mentioned reasons. In this regard, the task of identifying the cause and developing a rational design solution are relevant for the construction industry of Mongolia.

Based on this, in order to clarify the pattern and dependence of the decrease in the construction properties of subsidence clay soils on the increase in humidity, regional features of this type of soil were identified.

METHODS AND MATERIALS

A.Regional feature. Based on the results of the studies, it was established that the main reason for the increase in porosity, loosening and decrease in the construction properties of soils is the sublimation process occurring in seasonally frozen clay soils [11]. The regularity of the flow and the nature of the origin of the sublimation process in frozen soils are reflected in the works of many scientists [12; 13; 14; 15; 16; 17; 18; 19; 20].

As a result of the sublimation process of ice in seasonally frozen soils, the structure becomes loose, as a result of which the porosity n = (50...65)%, the porosity coefficient e = (0.70...0.84), the density of dry soil ρ_d = (1.35...1.60) tons/m^3 or undercompacted, the moisture content of sandy loam W = (0.04...0.06) and loam W = (0.05...0.08), and also as a result of repeated freezing and thawing, cracking and crushing of the solid part of the soil occurs, based on this, the content of dusty parts is 50…60%.

In such loose and highly porous soils, with an increase in humidity due to an increase in atmospheric precipitation, the process of changing mechanical properties actively occurs.

B. Method for determining the pattern of changes in mechanical properties from an increase in humidity. According to the method of Professor A.A. Mustafayev [21] carried out a calculation to determine the patterns of change in the mechanical properties of subsidence soils during moistening of loess-like sandy soil of the Darkhan-Selenga and Erdenet-Orkhon regions in the form of a dependence graph (Fig. 1...4).

A.A. Mustafayev defined wet loess-like sedimentary soil as a quasi-homogeneous and quasi-inhomogeneous continuous structure, and the equation of state of such a body has the form:

$$\sigma = \sigma^{\text{П}} + \sigma^{\text{В}} = \sigma^{\text{У}};\ e = e^{\text{У}} + e^{\text{П}};\quad e^{\text{П}} = e^{\text{В}};\ (1)$$

where: U, V, P - index of the stress-strain state taken into account in the viscous state.
After certain transformations and substitutions in the above equation, the following equation is obtained, expressing the stress state of the soil massif.

$$\sigma = C - \rho_d(1+e)y + W(y,z) + \lambda\left(e_y + \frac{2}{3}\mu\right)(2-f)\frac{\partial e_y}{\partial t}; \quad (2)$$

In the state $W_{кр} \le W \le W_{sat}$, the pattern of change in strength and deformation can be expressed by the mathematical law of the second-order curve. For example: the mechanical parameters of wet soil change according to the following law:

$$C_W = C_H - C_H J_L(2W_{sat} + W_i); \quad (3)$$
$$\varphi_W = \varphi_H - \varphi_H J_L(W_{sat} + \frac{W}{2}); \quad (4)$$
$$E_W = E_H - E_H J_L(W_{sat} + 0.5W); \quad (5)$$

where: C_H - the adhesion force of soil with natural moisture content; φ_H - the angle of internal friction of soil with natural moisture content; E - the modulus of deformation of soil with natural moisture content; J_L, W_L, W_p, J_p are the values adopted from the results of engineering and geological studies; W_{sat} - the moisture content of water-saturated loess soil;

$$W_{sat} = \frac{e\,\rho\,W}{\rho_s}, \quad (6)$$

where: e is the porosity coefficient of loess soil;

$$e = \frac{\rho_s - \rho_d}{\rho_d}, \quad (7)$$

CALCULATION RESULTS

The results of calculations using method Mustafaev [21] are given in tables 1 and 2. Approximate indicators for calculating the loess-like sandy soil of the Darkhan-Selenge region:

ρ_s=1.62tonns/m3	$W_L = 0.18$	$e = 0.62$	$\varphi' = 24^\circ$
ρ_s=2.38tonns/m3	$W_p = 0.14$	$W_{sat} = 0.21$	$\varphi'' = 18^\circ$
ρ_s=1.47tonns/m3	$J_p = 0.11$	$C' = 27\ kPa$	$E' = 13\ MPa$
W=0.06	$J_L = \pm 0.00$	$C'' = 21\ kPa$	$E'' = 4.1\ MPa$

Table 1. Dependence of mechanical parameters (C, φ, E) on humidity (W_L) sandy loam soils of the Darkhan-Selengi region

№	W_i	J_L	C_w, kPa, according to the formula (3)	φ_w, grad, according to the formula (4)	E_w, MPa, according to the formula (5)
1	0.04	-0,523	14.18	24.27	11.89
2	0.06	-0,256	12.23	24.13	11.76
3	0.08	0,000	7.95	23.35	11.27
4	0.10	0,328	7.06	21.31	10.85
5	0.12	0,615	6.83	18.90	5.18
6	0.14	1,000	6.24	17.81	3.91
7	0.16	1,217	5.95	17.05	3.15
8	0.18	1,485	5.64	16.68	2.68

ρ=1.64tonns/m^3	W_L=0.27	e=0.53	φ'=21°
ρ_s=2.51tonns/m^3	Wp=0.18	C'=27кПа	φ''=16°
ρ_d=1.48tonns/m^3	Wsat=0.31	C''=19кПа	E'=14.2 MPa
W=0.11	Jp=0.13		E''=4.6 MPa

Approximate indicators for calculating the loamy soil of the Erdenet-Orkhon region:

Table 2. Dependences of mechanical indicators (C,φ,E) on moisture content (W_i) of loamy soils of the Erdenet-Orkhon region

№	Wi	J_L	C_w, kPa according to the formula (3)	φ_w grad, according to the formula (4)	E_w, MPa, according to the formula (5)
1	0.06	-	47.21	22.31	12.92
2	0.08	-0,623	46.83	22.10	12.34
3	0.10	-0,381	43.55	21.60	11.98
4	0.12	0,000	27.91	20.32	9.12
5	0.14	0,431	17.83	18.61	4.87
6	0.16	0,762	14.67	17.72	4.05
7	0.18	1.243	13.05	17.30	3.29
8	0.20	1,520	11.81	16.82	2.76
9	0.22	1,836	10.71	16.47	2.68

Based on the calculation results given in Tables 1 and 2, a graph of the dependence for determining the value of mechanical indicators was constructed (Figures 1; 2; 3 and 4).

a. Graph of the dependence for determining the value of the flow index J_L

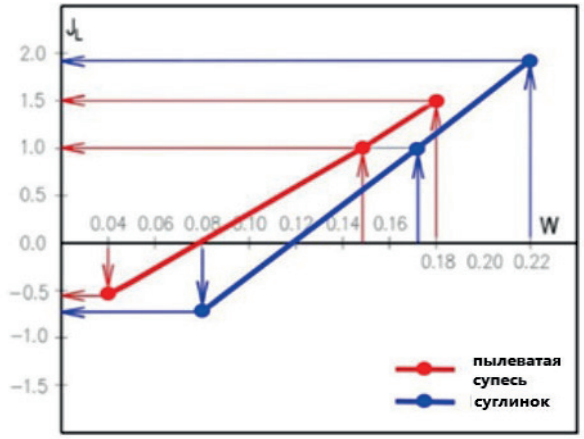


Figure 1. Graphics for determining the value of the fluidity index depending on the increase in soil moisture $J_l=f(Wi)$(Nyamdorj. 2021)

Based on the analysis of the $J_L = f(W_i)$ dependence graph, the following was established:

- for sandy loam: with an increase in soil moisture W = 0.04...0.08, the fluidity index changes J_L = – 60…0.00, with a further increase in moisture W = 0.08…0.18, the index J_L = – 0.00…1.50, i.e. it increases linearly proportionally;
- for loam: with an increase in soil moisture W = 0.08…0.12, the fluidity index changes J_L = – 0.75…0.00, with a further increase in moisture W = 0.12…0.22, the fluidity index J_L = 0.00…1.80, i.e. it increases linearly proportionally.

b. Dependency graph for determining the value of the adhesion force C_w

Based on the analysis of the graph of the dependence $C_w = f(W_i)$, the following was established:

- for sandy loam: with an increase in soil moisture W = 0.04 ... 0.08, the adhesion force changes C_w = 14.18 ... 7.95, with a further increase in moisture W = 0.08 ... 0.18, the indicator C_w = 7.95 ... 5.64 decreases according to a non-linear dependence;
- for loam: with an increase in soil moisture W = 0.06 ... 0.14, the adhesion force decreases in the range C_w = 47.21 ... 17.38, with a further increase in moisture W = 0.14 ... 0.22, adhesion C_w = 17.38 ... 10.71 decreases according to a non-linear dependence.

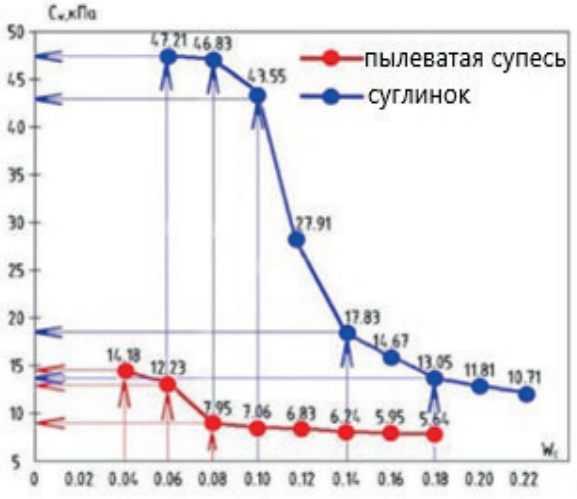


Figure 2. Graphics for determining the value of the angle of internal friction $C_w=f(Wi)$ depending on the increase in moisture content of clay soils (Nyamdorj. 2021)

c. Graph of the dependence for determining the value of the angle of internal friction φ_w

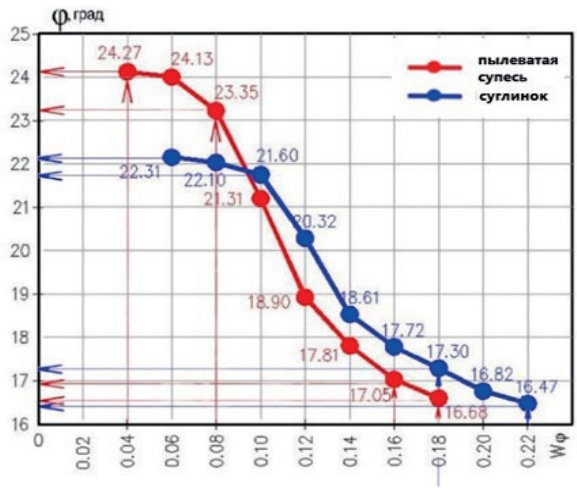


Figure 3. Graph for determining the value of the angle of internal friction $\varphi_w = f(W_i)$ depending on the increase in moisture content of clay soils (Nyamdorj. 2021)

Based on the analysis of the graph of the dependence $\varphi_w = f(W_i)$, the following was established:
- for sandy loam: with an increase in soil moisture W = 0.04…0.18, the angle of internal friction φ_w = 24.27…16.68 decreases according to a nonlinear dependence;
- for loam: with an increase in soil moisture W = W = 0.06…0.22, the angle of internal friction φ_w = 22.31…16.47 decreases according to a nonlinear dependence.

g. Graph of the dependence for determining the value of the deformation modulus E_w

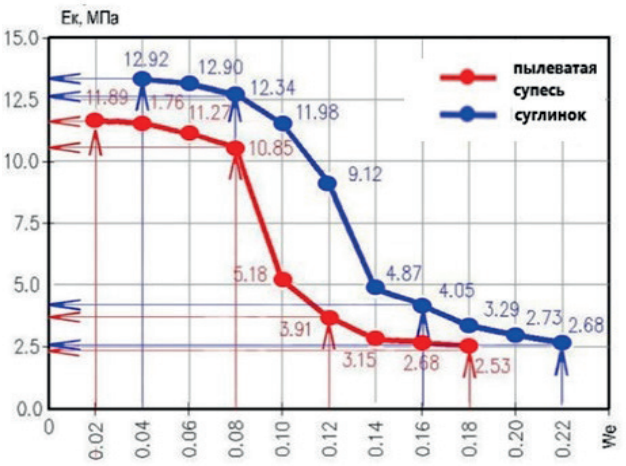


Figure 4. Graphics for determining the value of the deformation modulus $E_w = f(W_i)$ *depending on the increase in moisture content of clay soils (Nyamdorj. 2021)*

Based on the analysis of the graph of the dependence $E_w = f(W_i)$, the following was established:
- for sandy loam: with an increase in soil moisture W = 0.02…0.18, the value of the deformation modulus E_w = 11.89…2.53 MPa decreases according to a nonlinear dependence;
- for loam: with an increase in soil moisture W = 0.04…0.10, the value of the deformation modulus E_w = 12.92…2.68 MPa decreases according to a nonlinear dependence.

Based on the results of the analysis of the numerical values on the graphs $J_L = f(W_i)$, $C_w = f(W_i)$, $\varphi_w = f(W_i)$, $E_w = f(W_i)$ depending on the properties of the subsidence soil and the moisture state of the given site, the possibility of application is established taking into account the probability of change within ±5.0% and the compatibility of the numerical values determined by the graph's with the classification characteristics established by the standard, have an error of 3.0-9.0%.

B. Evaluation of subsidence properties by the method of indirect signs. Loess-like clay soils, common in some areas of Mongolia, do not belong to the category of subsidence soils according to the standards of soil classification in other countries, including Russia, but at different pressure values and an increase in humidity, a significant subsidence is observed, therefore, there is a need for classification by indirect signs. The problems of the need to classify subsidence soils by indirect signs are devoted to the works of many researchers [22; 23; 24; 25; 26; 27; 28].

Based on the results of 231 laboratory tests to determine the mechanical properties of loess-like subsidence soils common in Mongolia, a comparison was carried out in order to identify the pattern of subsidence formation and calculate the amount of subsidence under the effects of various pressures and soaking, and the results obtained are presented in Table 2.5 [11].

Based on the analysis of the research results, it is established that with the porosity coefficient value within the range of (0.300 - 0.409) ... 0.910, under the action of pressure of 0.1; 0.2; 0.3 MPa, the probability of occurrence of subsidence deformation increases. Based on the results of the numerical analysis performed using the R-Plus calculation program, the following regression equations and a diagram were compiled to assess the probability of subsidence formation (Figure 5).

$$lg\delta_1 = -1.744S_r + 0.886e_0 - 2.153;\ n=69;$$
$$S^2_{oct}(lg\delta_2) = 0.2116;$$
$$lg\delta_2 = -1.806S_r + 0.855e_0 - 2.093;\ n=121;$$
$$S^2_{oct}(lg\delta_2) = 0.2115;$$

$$lg\delta 3 = -1.641 S_r + 0.922 e_0 - 1.9972;\ n=147;$$
$$S^3_{oct}(lg\delta_3) = 0, \qquad (8)$$

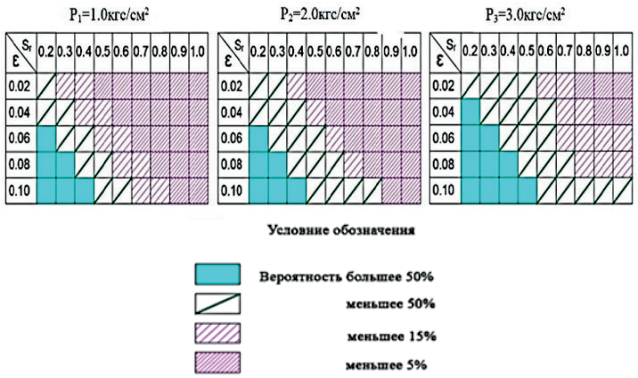


Figure 5. Diagram for assessing the probability of subsidence

RESULTS AND DISCUSSION

Currently, climate conditions are changing dramatically around the world due to global warming, as a result of which the construction properties of clayey, especially subsidence soils are deteriorating sharply, and there is a high probability of further activation of these processes. We observe that the number of deformed buildings and infrastructure structures for various reasons under the influence of increased humidity of clayey soils of foundations is noticeably increasing from year to year.

In such situations, how reliable is the calculation of a subsidence foundation and, perhaps, foundations made of other types of clayey soils for I and II limit states according to the provisions of current standards and regulatory literature? Maybe something needs to be changed and supplemented? If necessary, in what direction? Or is there nothing special, all these situations are taken into account in the calculation models, only reasonable use is necessary? The solution and discussion of this problem are important not only for Mongolia, but also in other countries where there are subsidence and non-subsidence clayey soils of different origins.

CONCLUSION

1. Analysis of numerical values on the graphs of the dependence $I_L = f(W_i)$, $C_w = f(W_i)$, $\varphi_w = f(W_i)$, $E_w = f(W_i)$ shows the possibility of application taking into account the probability of change within ±7.0% and the compatibility of numerical values determined by the graphs with the classification characteristics established by the standard with an error with a convergence of 3.0...9.0%.
2. Based on the results of solving the regression equations, the probability of occurrence of subsidence of loess-like soil is determined by indirect signs for the purpose of preliminary assessment. At the same time, it is possible to determine the probability of occurrence of subsidence with sufficient accuracy by nomogram (Figure 5).
3. Taking into account the established regional characteristics and the regularity of changes in mechanical indicators, a theoretical and methodological justification has been developed for the innovative use of scientific methods, such as pile foundations, foundations in a rammed pit, and artificial improvement of subsidence soil foundations, including compaction with heavy ramming, a soil cushion with geosynthetic reinforcement, chemical fixation by cementation and silicification methods, taking into account the soaking of the subsidence base of buildings and structures.

REFERENCES

1. **Varallyay, G.,** 1990. Potential impact of climate change on soil moisture regime and soil degradation processes. Proceedings of the International Seminar on Future Research Trends in MAB, August 20-29, 1990, Tokyo, Japan, pp: 256-267.
2. **Paul, E.A. and J. Kimble,** 2000. Global climate change: Interactions with soil properties. DOI510.1.1.526.2831&rep/rep1&type/pdf.

3. **Harnos, Z.S. and L. Csete**, 2008. Climate Change: Environment-Risk-Society. Research Results. Szaktudas Kiado Haz, Budapest, Pages: 380.
4. **Revyakin V.S., Kharlamova N.F**. 2005. Regional changes in climate and natural environment of Central Asia // World ocean, land water bodies and climate: Proceedings of the XII Congress of the Russian Geographical Society. – St. Petersburg, 2005. DOI:10.1007/1-4020-4493-3_2
5. **Rajib Karmakar.** 2016. Potential Effects of Climate Change on Soil Properties: A Review. Science International Year: 2016.Volume: 4, Issue: Page.: 51-73. DOI: 10.17311/sciintl.2016.51.73.
6. **Sherstyukov B.G.** Spatial and seasonal features of climate change during intensive global warming: author's abstract. diss. … doctor of geogr. sciences. – Kazan, 2008.
7. **Rahmstorf, S., A.** et al. 2007. Recent climate observations compared to projections. Science, May 4; 316-709. DOI:10.1126/science.1136843.Epub2007Feb1.
8. **Semenov V.A.** 2024. Climate change: causes, consequences, urgent tasks. Scientific session of the general meeting of members of the Russian Academy of Sciences. Vol. 94, No. 3 (2024). P. 246-254. DOI: https://doi.org/10.31857/S0869587324030076
9. **Dashjamts D.** et al. Geotechnical conditions of Mongolia. Engineer's Handbook. Ulaanbaatar. 2009. Page 406.
10. **Antonov, V.M.** 2002. Design of buildings under special conditions of construction and operation. – Tambov: Publishing house of Tambov state tech. univ, 2002. – 240 p.
11. **Nyamdorj S**. 2023. Scientific substantiation of development of optimal solutions of foundations, foundations of buildings and structures erected on subsidence soils of Mongolia. Abstract: diss… doctor of scence /Sc.D/. Ulaanbaatar. 2023.
12. **Ershov E.D., Komarov I.A., Kuchukov E.Z.** 1975. Sublimation of ice in dispersed rocks. Publishing house of Moscow State University, 1975, 224 p.
13. **N. Ershov E.D.,. Gurov V.V, Komarov I.A.,. Akimov Yu.P**. 1976. Regularities of heat and mass transfer during ice sublimation in dispersed rocks. Collection "Problems of Earth Cryology", from. USSR Academy of Sciences.
14. **Komarov I.A.** Study of heat and mass transfer processes during dehydration of dispersed systems in the region of negative temperatures. Abstract: diss... Cand. Tech. Sci. (Eng.). Moscow:
15. **Jane Law, Deanna Van Dijk**. 1994. Sublimation as a geomorphic process: A review. October/December 1994. https://doi.org/10.1002/ppp.3430050404.
16. **Chistotinov L.V.** Moisture migration in freezing unsaturated soils. Moscow: Nauka. 1973.
17. **Norbert Schorghofer.** 2007. Theory of ground ice stability in sublimation environments Phys. Rev. E 75, 041201. april, 2007. DOI:10.1103/PhysRevE.75.041.
18. **Starostin E.G.** 2009. Phase equilibrium of water in rocks at negative temperatures. Abstract of diss… Doctor of Technical scence /Sc.D/.Yakutsk. 2009.
19. **Benjamin Southard, Robert O. Williams III, Zhengrong Cui.** 2025. Heat transfer characteristics of sublimation from frozen thin films. https://doi.org/10.1016/j.ijpharm.2025.125346.
20. **Weisheng Zhao** ,et al. 2025. Hygroscopic effect of high clay-content shale under temperature and humidity conditions and its impact on mechanical properties. Published: March 7, 2025 https://doi.org/10.1371/journal.pone.0319672.
21. **Mustafayev, A.A.** 1979. Calculation of foundations and bases on subsidence soils [Text]: textbook for universities. - M.: Higher. school, 1979. 368 p.
22. **Krieger, N.I.** 1971. Indirect methods for assessing the subsidence properties of loess rocks. / Proceedings of PNIIS. - M.: Stroyizdat, - T. 12. - P. 191-260.
23. **Reynolds, W.D., C.F. Drury, C.S. Tan, C.A. Fox and X.M. Yang**, 2009. Use of

indicators and pore volume-function characteristics to quantify soil physical quality. Geoderma, 152: 252-263. https://doi.org/10.1016/j.geoderma.2009.06.009

24. **Salih N.B.,** "Geotechnical characteristics correlations for fine-grained soils", In IOP Conference Series: Materials Science and Engineering, vol. 737(1), (2020), 012099). https://doi.org/10.1088/1757-899X/737/1/012099.
25. **Yarkin, V.V.** 2017. Determination of subsidence deformations according to regulatory documents of Russia and Ukraine. / Modern industrial and civil engineering, 2017. - Vol. 13. - Issue. 2. - P. 111-119. ISSN: 1819-432X (print), 1993-3495 (online)
26. **Galay, B.F., Serbin V.V., Plakhtyukova V.S.** 2016. Critical comments on the provisions of regulatory documents on assessing the subsidence of loess soils based on their physical characteristics. Engineering surveys - 2016. No. 14. P. 18-23.
27. **Trofimov V.T**. 1999. Genesis of subsidence of loessial rocks. Moscow: Moscow State University Publishing House, 271 pp.: ISBN 5-211-04069-4
28. **Moebius, B.N., H.M. van Es, R.R. Schindelbeck, O.J. Idowu, D.J. Clune and J.E. Thies,** 2007. Evaluation of laboratory-measured soil properties as indicators of soil physical quality. Soil Sci., 172: 895-912. DOI:10.1097/ss.0b013e318154b520

СПИСОК ЛИТЕРАТУРЫ

1. **Varallyay, G.,** 1990. Potential impact of climate change on soil moisture regime and soil degradation processes. Proceedings of the International Seminar on Future Research Trends in MAB, August 20-29, 1990, Tokyo, Japan, pp: 256-267.
2. **Paul, E.A. and J. Kimble,** 2000. Global climate change: Interactions with soil properties. DOI510.1.1.526.2831&rep/rep1&type/pdf.
3. **Harnos, Z.S. and L. Csete**, 2008. Climate Change: Environment-Risk-Society. Research Results. Szaktudas Kiado Haz, Budapest, Pages: 380.
4. **Revyakin V.S., Kharlamova N.F**. 2005. Regional changes in climate and natural environment of Central Asia // World ocean, land water bodies and climate: Proceedings of the XII Congress of the Russian Geographical Society. – St. Petersburg, 2005. DOI:10.1007/1-4020-4493-3_2
5. **Rajib Karmakar.** 2016. Potential Effects of Climate Change on Soil Properties: A Review. Science International Year: 2016.Volume: 4, Issue: Page.: 51-73. DOI: 10.17311/sciintl.2016.51.73.
6. **Sherstyukov B.G.** Spatial and seasonal features of climate change during intensive global warming: author's abstract. diss. … doctor of geogr. sciences. – Kazan, 2008.
7. **Rahmstorf, S., A.** et al. 2007. Recent climate observations compared to projections. Science, May 4; 316-709. DOI:10.1126/science.1136843.Epub2007Feb1.
8. **Semenov V.A.** 2024. Climate change: causes, consequences, urgent tasks. Scientific session of the general meeting of members of the Russian Academy of Sciences. Vol. 94, No. 3 (2024). P. 246-254. DOI: https://doi.org/10.31857/S0869587324030076
9. **Dashjamts D.** et al. Geotechnical conditions of Mongolia. Engineer's Handbook. Ulaanbaatar. 2009. Page 406.
10. **Antonov, V.M.** 2002. Design of buildings under special conditions of construction and operation. – Tambov: Publishing house of Tambov state tech. univ, 2002. – 240 p.
11. **Nyamdorj S**. 2023. Scientific substantiation of development of optimal solutions of foundations, foundations of buildings and structures erected on subsidence soils of Mongolia. Abstract: diss… doctor of scence /Sc.D/. Ulaanbaatar. 2023.
12. **Ershov E.D., Komarov I.A., Kuchukov E.Z.** 1975. Sublimation of ice in dispersed rocks. Publishing house of Moscow State University, 1975, 224 p.

13. **N. Ershov E.D.,. Gurov V.V, Komarov I.A.,. Akimov Yu.P**. 1976. Regularities of heat and mass transfer during ice sublimation in dispersed rocks. Collection "Problems of Earth Cryology", from. USSR Academy of Sciences.
14. **Komarov I.A.** Study of heat and mass transfer processes during dehydration of dispersed systems in the region of negative temperatures. Abstract: diss... Cand. Tech. Sci. (Eng.). Moscow:
15. **Jane Law, Deanna Van Dijk**. 1994. Sublimation as a geomorphic process: A review. October/December 1994. https://doi.org/10.1002/ppp.3430050404.
16. **Chistotinov L.V.** Moisture migration in freezing unsaturated soils. Moscow: Nauka. 1973.
17. **Norbert Schorghofer.** 2007. Theory of ground ice stability in sublimation environments Phys. Rev. E 75, 041201. april, 2007. DOI:10.1103/PhysRevE.75.041.
18. **Starostin E.G.** 2009. Phase equilibrium of water in rocks at negative temperatures. Abstract of diss… Doctor of Technical scence /Sc.D/.Yakutsk. 2009.
19. **Benjamin Southard, Robert O. Williams III, Zhengrong Cui.** 2025. Heat transfer characteristics of sublimation from frozen thin films. https://doi.org/10.1016/j.ijpharm.2025.125346.
20. **Weisheng Zhao** ,et al. 2025. Hygroscopic effect of high clay-content shale under temperature and humidity conditions and its impact on mechanical properties. Published: March 7, 2025 https://doi.org/10.1371/journal.pone.0319672.
21. **Mustafayev, A.A.** 1979. Calculation of foundations and bases on subsidence soils [Text]: textbook for universities. - M.: Higher. school, 1979. 368 p.
22. **Krieger, N.I.** 1971. Indirect methods for assessing the subsidence properties of loess rocks. / Proceedings of PNIIS. - M.: Stroyizdat, - T. 12. - P. 191-260.
23. **Reynolds, W.D., C.F. Drury, C.S. Tan, C.A. Fox and X.M. Yang**, 2009. Use of indicators and pore volume-function characteristics to quantify soil physical quality. Geoderma, 152: 252-263. https://doi.org/10.1016/j.geoderma.2009.06.009
24. **Salih N.B.,** "Geotechnical characteristics correlations for fine-grained soils", In IOP Conference Series: Materials Science and Engineering, vol. 737(1), (2020), 012099). https://doi.org/10.1088/1757-899X/737/1/012099.
25. **Yarkin, V.V.** 2017. Determination of subsidence deformations according to regulatory documents of Russia and Ukraine. / Modern industrial and civil engineering, 2017. - Vol. 13. - Issue. 2. - P. 111-119. ISSN: 1819-432X (print), 1993-3495 (online)
26. **Galay, B.F., Serbin V.V., Plakhtyukova V.S.** 2016. Critical comments on the provisions of regulatory documents on assessing the subsidence of loess soils based on their physical characteristics. Engineering surveys - 2016. No. 14. P. 18-23.
27. **Trofimov V.T**. 1999. Genesis of subsidence of loessial rocks. Moscow: Moscow State University Publishing House, 271 pp.: ISBN 5-211-04069-4
28. **Moebius, B.N., H.M. van Es, R.R. Schindelbeck, O.J. Idowu, D.J. Clune and J.E. Thies,** 2007. Evaluation of laboratory-measured soil properties as indicators of soil physical quality. Soil Sci., 172: 895-912. DOI:10.1097/ss.0b013e318154b520

Nyamdorj Setev — Foreign Member of RAACS, Academician, Doctor of Science (Sc.D), Professor, Technician and Technological University, Ulaanbaatar, Mongolia. ORCID: 0000-0002-0457-6176. Address: Enkhtaivan Avenue, Ulaanbaatar 13381, Mongolia, e-mail: nyamdorj_999@yahoo.com

Сэтэв Ньямдорж — иностранный член РААСН, академик, доктор технических наук (Sc.D), профессор Технического и технологического университета, г. Улан-Батор, Монголия. Адрес: пр-т Энхтайваны, г. Улан-Батор, 13381, Монголия, e-mail: nyamdorj_999@yahoo.com

Uranchimeg Davaasuren — Ph.D, Associate Professor, Technician and Technological University, Ulaanbaatar, Mongolia. Address: Enkhtaivan Avenue, Ulaanbaatar 13381, Mongolia, e-mail: nyamdorj_999@yahoo.com

Sukh-Erdene Khureltsooj — Master's Degree, Senior Lecturer, Technician and Technological University, Ulaanbaatar, Mongolia. Address: Enkhtaivan Avenue, Ulaanbaatar 13381, Mongolia, e-mail: nyamdorj_999@yahoo.com

Erdenetsetseg Enkhbaatar — Master's Degree, Senior Lecturer, Ulaanbaatar University of Technology, Ulaanbaatar, Mongolia. Address: Enkhtaivan Avenue, Ulaanbaatar 13381, Mongolia, e-mail: nyamdorj_999@yahoo.com

Даваасурэн Уранчимэг — кандидат технических наук (Ph.D), доцент Технического и технологического университета, г. Улан-Батор, Монголия. Адрес: пр-т Энхтайваны, г. Улан-Батор, 13381, Монголия, e-mail: nyamdorj_999@yahoo.com

Хурэлцооож Сух-Эрдэнэ — магистр, старший преподаватель Технического и технологического университета, г. Улан-Батор, Монголия. Адрес: пр-т Энхтайваны, г. Улан-Батор, 13381, Монголия, e-mail: nyamdorj_999@yahoo.com

Энхбаатар Эрдэнэцэцэг — магистр, старший преподаватель Технологического университета Улан-Батора, г. Улан-Батор, Монголия. Адрес: пр-т Энхтайваны, г. Улан-Батор, 13381, Монголия, e-mail: nyamdorj_999@yahoo.com

DOI:10.22337/2587-9618-2026-22-1-179-189

ASSESSMENT OF THE INFLUENCE OF ADJACENT EXCAVATION STEP LENGTH ON SHIELD TUNNEL DEFLECTION

Nguyen Van Hung [1], ***Nguyen Trong Tam*** [2]
[1] University of Engineering and Technology (VNU-UET), Hanoi, VIETNAM
[2] Ho Chi Minh City University of Transport, Ho Chi Minh City, VIETNAM

Abstract: Protecting existing underground structures in urban areas from adverse impacts caused by surface construction activities is a significant challenge, especially when applying the open-cut sequential excavation method. This paper proposes a simple analytical method to determine the deflection of the tunnel axis induced by the sequential excavation of the overlying excavation pit segments. The method is based on identifying the changes in soil stress at the tunnel cross-section during each construction stage, followed by using analytical techniques to determine the corresponding tunnel deflection. The tunnel-soil interaction is modeled by an Euler-Bernoulli beam on an elastic foundation represented by the Winkler model. Furthermore, the paper investigates the influence of segmental excavation length on the tunnel deflection. The results show that with excavation step lengths of 3.6 m, 7.2 m, and 14.4 m, the maximum tunnel deflection increases by 135% and 193%, respectively. These results provide a basis for optimizing construction methods, minimizing risks, and effectively protecting underground structures.

Keywords: Existing shield tunnel, shield tunnel deflection, excavation step length, line 1 HCM metro, Winkler model, Euler-Bernoulli beam, Analytical approach, MIDAS GTS

ОЦЕНКА ВЛИЯНИЯ ДЛИНЫ ШАГА СМЕЖНОЙ ВЫЕМКИ НА ПРОГИБ ЩИТОВОГО ТОННЕЛЯ

Нгуен Ван Хунг [1], ***Нгуен Чонг Там*** [2]
[1] Инженерно-технологический университет (VNU-UET), Ханой, ВЬЕТНАМ
[2] Хошиминский университет транспорта, г. Хошимин, ВЬЕТНАМ

Аннотация: Защита существующих подземных сооружений в городских районах от неблагоприятных воздействий, вызванных поверхностными строительными работами, является серьезной проблемой, особенно при применении метода последовательной выемки грунта открытым способом. В данной статье предлагается простой аналитический метод определения прогиба оси тоннеля, вызванного последовательной выемкой вышележащих сегментов котлована. Метод основан на выявлении изменений напряжения грунта в поперечном сечении тоннеля на каждом этапе строительства с последующим использованием аналитических методов для определения соответствующего прогиба тоннеля. Взаимодействие тоннеля с грунтом моделируется балкой Эйлера-Бернулли на упругом основании, представленном моделью Винклера. Кроме того, в статье исследуется влияние длины шагов выемки на прогиб тоннеля. Результаты показывают, что при длине шагов выемки 3,6 м, 7,2 м и 14,4 м максимальный прогиб тоннеля увеличивается на 135% и 193% соответственно. Эти результаты создают основу для оптимизации методов строительства, минимизации рисков и эффективной защиты подземных сооружений.

Ключевые слова: Существующий тоннель, Прогиб щитового тоннеля, длина шага выемки, Линия 1 метрополитена Хошимина, Модель Винклера, : Балка Эйлера-Бернулли, Аналитический подход, MIDAS GTS

1. INTRODUCTION

In recent years, rapid urban development in major Vietnamese cities has coincided with the construction of underground metro systems. This has resulted in cases where foundation excavations of adjacent structures (such as high-rise buildings and utility infrastructure) are carried out near shield tunnels (TBM tunnels). Such adjacent excavation activities can impose significant adverse impacts on shield tunnels by altering their initial stress state, thereby posing serious risks to operational safety. Documented damages include cracking of reinforced concrete tunnel segments, displacement and detachment of the concrete invert slab from the tunnel lining [1]. Excessive deformations of this nature may reduce load-bearing capacity, induce water leakage, and even threaten the overall stability of the tunnel system, potentially leading to cracking, leakage, reduced train speeds, or in extreme cases, collapse.

To predict the behavior of shield tunnels under the influence of adjacent foundation excavation, numerous studies have been conducted, which can generally be classified into three main approaches: finite element methods, physical modeling, and analytical methods.

Three-dimensional centrifuge model tests have been employed to investigate the effects of deep excavations or twin tunnels on existing tunnels and pile groups [2-3]. This technique provides valuable insights into complex soil–structure interaction mechanisms under simulated gravity conditions. Physical modeling offers important experimental data; however, simplifications in stratigraphic conditions and construction sequences may introduce uncertainties when extrapolating results to real projects, while also being costly and time-consuming.

The finite element method is a widely used approach that enables the modeling of complex soil-structure interactions, including the elasto-plastic behavior of soil and construction sequencing [2, 4-10]. Software such as FLAC3D, PLAXIS3D, and Midas GTS NX are commonly employed to analyze the impacts of excavations on existing tunnels. The finite element method provides in-depth analysis of deformations and internal forces, with the capability to simulate intricate processes in detail. However, this method requires significant computational resources, specialized software, and a considerable number of assumed parameters, making the modeling process complex.

The analytical method provides theoretical formulas that allow rapid estimation of tunnel deformations. In this approach, tunnels in soil are commonly idealized as beam-on-elastic-foundation problems, employing the Euler–Bernoulli or Timoshenko beam models in conjunction with Winkler, Pasternak, or Vlazov foundation models [9], [11-17]. Due to its simplicity, cost-effectiveness, and the ability to produce quick forecasts, the analytical method is considered a valuable tool in the early stages of tunnel design and construction.

However, current analytical studies still have limitations, as they have not fully considered the load changes over a large range such as the entire length of the excavation, nor have they evaluated the effects of different excavation steps on tunnel deformation. Meanwhile, optimizing construction parameters such as depth and length of excavation steps plays a key role in ensuring the safety and efficiency of underground works.

In this paper, the authors propose an analytical framework in which the shield tunnel is idealized as an Euler–Bernoulli beam, while the surrounding ground is simulated using a Winkler elastic foundation model. For validation, the analytical outcomes are benchmarked against a three-dimensional finite element model, calibrated with monitoring and design data from Metro Line No. 1 of the Ho Chi Minh City Urban Railway.

2. ANALYTICAL APPROACH

To approach the problem analytically, it is necessary to accept the following assumptions. The surrounding ground of the tunnel is considered as an elastic foundation characterized by a Winkler model coefficient. The TBM tunnel excavated in

the soil environment is considered as a beam on elastic foundation problem. The consideration of internal forces in the cross-section is ignored. And the beam is considered to have infinite length. In addition, the deflection of the tunnel is within the elastic limit of the structure.

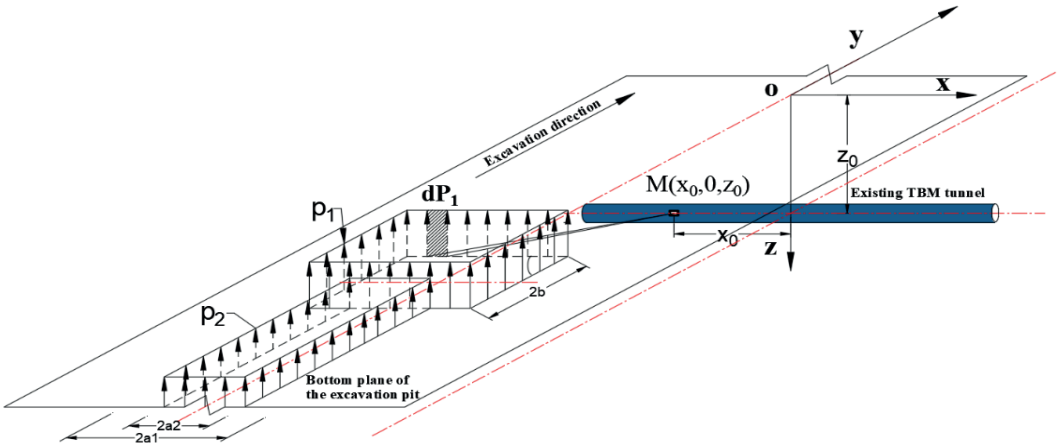


Figure 1. Force Distribution in a homogeneous elastic half-space

In this problem, the influence of the tunnel on the stress generation, as well as the longitudinal and shear stresses in the tunnel, is ignored.

2.1 Load acting on the tunnel lining

The process of excavating the upper excavation segment, changes the load above the tunnel from the complete unloading (state 1) of an excavation segment of size $2a_1 * 2b$, with the value of $p_1(x)$, to the completed state (state 2) which will be the value of $p_2(x) = p_1(x) - \Delta p(x)$, $\Delta p(x)$- the load difference between the unloaded soil weight and the completed stage load. The change in load on the tunnel structure during excavation is shown in Figure 1. The value of the bottom plane load of an excavation element is shown by the following formula (1):

$$p(x) = \begin{cases} p_1, & |x| \le a_1, |y - y_0| \le b \\ p_2, & |x| \le a_2, y - y_0 < -b \end{cases} \quad (1)$$

in which, y_0- coordinates of the center of the excavation pit along the y-axis; $2a_1$- width of the excavation pit; $2a_2$- width of the permanent structure placed in the excavation pit; $2b$- length of the excavation step.

The problem of concentrated loads in half-space was solved by Sneddon using the Fourier transform in 1951 [18], the formula for the vertical stress change at depth z under the action of a concentrated load P, is determined by the following formula:

$$\sigma_{zz} = \frac{3P}{2\pi}\frac{z^3}{R^5}, R = \sqrt{x^2 + y^2 + z^2} \quad (2)$$

The generalization for vertical stress acting on the tunnel axis due to uniformly distributed load with varying intensity is determined as follows:

$$\sigma_{zz} = \int_{-a_1}^{a_1}\int_{y_0-b}^{y_0+b} \frac{3p_1}{2\pi}\frac{z^3}{R^5}dxdy + \int_{-a_2}^{a_2}\int_{-\infty}^{y_0-b} \frac{3p_2}{2\pi}\frac{z^3}{R^5}dxdy \quad (3)$$

With the initial assumptions when approaching the analytical method, the vertical stress at depth H, due to the distributed load placed at the bottom of the excavation hole in the upward direction as shown in Figure 1, is determined by the following formula:

$$\sigma_{zz} = \int_{-a_1}^{a_1}\int_{y_0-b}^{y_0+b} \frac{3}{2}\frac{\gamma_0 H_0}{\pi}\frac{(H-H_0)^3}{\left[(x-x_0)^2 + y^2 + (H-H_0)^2\right]^{5/2}}dxdy + \int_{-a_2}^{a_2}\int_{-\infty}^{y_0-b} \frac{3p_2}{2\pi}\frac{(H-H_0)^3}{\left[(x-x_0)^2 + y^2 + (H-H_0)^2\right]^{5/2}}dxdy \quad (4)$$

where: γ_0 - the unit weight of the soil layer within the excavation pit; H_0 - the distance from the bottom of the excavation pit to the ground surface; H - the distance from the existing tunnel axis to the ground surface.

2.2 Tunnel deflection equation

The existing tunnel is considered as an Euler-Bernoulli beam resting on a Winkler foundation model. The Winkler foundation model is regarded as a one-dimensional spring, with individual springs acting independently of each other. The differential equation for the beam on the elastic foundation [14] is expressed as:

$$EI_{eq}\frac{d^4w(x)}{dx^4}+KDw(x)=D\sigma_{zz}(x) \tag{5}$$

where: D - the outer diameter of the existing tunnel; EI_{eq} - the equivalent bending stiffness of the existing tunnel accounting for the influence of longitudinal connections in the tunnel; K - the subgrade coefficient of the surrounding soil environment; $w(x)$ - the displacement of the tunnel axis, $\sigma_{zz}(x)$ - the vertical stress acting on the tunnel.

The total solution of equation (5) is determined based on the solution of the homogeneous equation and the boundary conditions. With the initial assumption, we consider this as an infinite beam problem on an elastic foundation, from which the deflection of the tunnel is determined by the following equation:

$$w(x)=\frac{PD}{8EI\beta^3}e^{-\beta|x|}\left(\cos\beta|x|+\sin\beta|x|\right),\ where:\ \beta=\sqrt[4]{\frac{KD}{4EI_{eq}}} \tag{6}$$

To analyze the effects of excavation above the tunnel below, first consider the tunnel with a concentrated load placed on the Winkler foundation. The total vertical stress P is simplified to act at the neutral axis of the tunnel and can then be transmitted directly to the foundation as a concentrated load, from which the deflection of the tunnel under the force can be determined. Once the deflection of the tunnel under the concentrated load has been determined, this result can be used to deduce the deflection of the existing tunnel under the uniformly distributed load. Based on the transformations, the deflection of the tunnel due to the change of load in the range $(-\infty;+\infty)$ can be determined by formula:

$$w(x)=\int_{-\infty}^{+\infty}\frac{\sigma_{zz}(\xi)D}{8EI_{eq}\beta^3}e^{-\beta|x-\xi|}\left(\cos\beta|x-\xi|+\sin\beta|x-\xi|\right)d\xi \tag{7}$$

The convolution integral in equation (7) used to determine the displacement will be performed in MATLAB with a sufficiently large integration interval.

2.3 Define the parameters

The tunnel axis deflection below depends on the interaction between geology and the bearing capacity of the existing structure. Therefore, special attention should be paid to parameters such as equivalent bending stiffness EI_{eq} and the subgrade modulus coefficient K, as they determine the resistance to deflection and settlement of the foundation.

2.4 Equivalent bending stiffness of TBM tunnel

Due to the segmental joints, the longitudinal bending stiffness of the TBM tunnel is significantly smaller than that of the continuous concrete tunnel. According to Liao [15], the equivalent longitudinal bending stiffness of the shield tunnel is only about 1/5 to 1/7 of that of the continuous tunnel, which has been experimentally verified.

$$EI_{eq}=\frac{E_c}{5\sim 7}\frac{\pi\left(D^4-d^4\right)}{64} \tag{8}$$

where E_c is the Young's modulus of the TBM tunnel sections; D is the outer diameter of the TBM tunnel; and d is the inner diameter of the TBM tunnel.

2.5 Subgrade modulus coefficient

The foundation modulus factor in Winkler models for analyzing pipe–soil interactions was originally proposed by Attewell et al. [19] based on the expression of Vesic [20], usually with a double value for buried pipes. To improve this method, Yu et al. [13] developed a modified

Winkler foundation modulus factor expression, applicable to arbitrarily buried pipes subjected to free ground displacements of any curve shape, while considering the buried depth ratio (H/D) of the pipe. The modified subgrade modulus coefficient according to Yu et al., which is employed in this study, is expressed as follows:

$$K = \frac{1,3E_s}{\eta D\left(1-\mu^2\right)}\sqrt[12]{\frac{E_s D^4}{EI}}, \quad (9)$$

$$where: \eta = \begin{cases} 2,18 & H/D \le 0,5 \\ 1+\dfrac{1}{1,7H/D} & H/D > 0,5 \end{cases}$$

where: E_s - the elastic modulus of the soil, μ - Poisson's, D - the outer diameter of the existing tunnel, H - the distance from the existing tunnel axis to the ground surface, and EI is equal to EI_{eq}

3. EXAMPLE VALIDATION

To provide a visual insight from the obtained analysis results, the authors considered an example from a real project in Ho Chi Minh City and compared it with the results from the 3D finite element model.

3.1 Case study

Ho Chi Minh City Urban Railway Line 1, with a total length of 19.7 km, includes 2.6 km underground and 17.1 km elevated. The underground section includes two shield tunnels: the East Tunnel (EB) and the West Tunnel (WB), constructed by a pressure balance tunnel boring machine (TBM). According to the geological survey results of the Ben Thanh - Suoi Tien Urban Railway Line 1 project, the hydrogeological data used in the model were taken from experiments at borehole U-175 (km 1+553), located about 2 meters from the center of the TBM tunnel [4]. Through analysis, the soil layers were classified into three main groups: Fill soil, alluvial soil and alluvial soil. More specifically, the soil layers at the intersection area include five main layers: Fill soil, AC2, AS1, AS2 and DC.

The geological and hydrogeological data were obtained from the geological reports of the urban railway, summarized in table 1. The intersection point between the underground drainage system project and the TBM tunnel of Line 1 is located at km 1+555 (according to the centerline of the urban railway). The parameters related to the tunnel lining structure are presented in table 2.

Table 1. Properties of soils

Parameter	Layer				
	Fill	AC2	AS1	AS2	DC
E (kPa)	10000	3000	12500	37500	136000
ν	0,3	0,3	0,3	0,3	0,3
γ (kN/m^3)	19	16,5	20,5	20,5	21
K_0	0,577	0,8	0,5	0,455	0,5
γ_{sat} (kN/m^3)	19	16,5	20,5	20,5	21
k (m/s)	1x10^{-6}	1x10^{-9}	2x10^{-5}	2x10^{-5}	1x10^{-8}
c (kPa)	10	0	0	0	170
φ (^{o})	25	24	30	33	35

Table 2. Parameters for tunnelling

Parameter	Tunnel lining
Tunnel Inner Diameter, D_{int} (m)	6,05
Tunnel lining thickness (m)	0,3
Tunnel center line position, H (m)	11
Equivalent Elastic Modulus, E^* (kPa)	7,2x10^6
Poisson's Ratio, ν	0,2
Bulk Density, γ (kN/m^3)	24

The E^* values in the table are equivalent values, indicating the reduction in the bending stiffness of the shield tunnel in the model. The excavation pit has the following dimensions: width $2a_1 = 5m$; excavation pit depth: $H_0 = 1.6m$;the excavation pit is located in the topsoil layer, $\gamma_0 = 19kN/m^3$. The value of the uniformly distributed load due to the process of unloading the soil mass in the excavation pit is: $p_1 = \gamma_0 * H_0 = 30.4(kPa)$. The load value after the soil is placed $p_2 = 0.5 * p_1$; the width of the culvert considered is $2a_2 = 3.5m$.

3.2 Analysis results and discussion

The finite element model and tunnel deflection for comparison, are taken from the paper Nguyen, et al. [4]. The finite element software used is MIDAS GTS, with the properties of the soil layers determined by the Mohr-Coulomb model, the tunnel lining is a plate element, the tunnel material is considered as isotropic elastic. Interface elements are used to model the interaction between the soil and the tunnel lining, with the strength reduction factor Rinter=0.67. The tunnel axis deflection is determined by the average value of the displacement at the crown and bottom of the tunnel.

After performing calculations using MATLAB software with the input data considered in section A, the tunnel axis deflection determined by the two methods is shown in Figure 2, with the maximum displacement value of the tunnel according to the analytical method being 4.7 mm, while according to the finite element method it is 4.41 mm.

The displacement value of the tunnel is about 6.2% larger according to the analytical method than that of the finite element method (FEM), and the deflection area according to the analytical method is also larger. The area affected by the displacement of the tunnel extends about 40 meters (about 10 times the width of the excavation) on both sides. Beyond this 40m range, the displacement value becomes negligible.

From the analysis results, this analysis method provides a higher margin of safety in terms of displacement. This can be explained by the following reasons: (1) The soil model does not consider the sliding interaction between layers (two-factor soil model), (2) The influence of different soil layers is not considered in the model, affecting the determination of the foundation coefficient.

4. PARAMETRIC SURVEY

To examine the influence of the excavation step length on the displacement of the tunnel, the authors conducted a survey with different excavation lengths, respectively 2b=3.6m; 7.2m & 14.4m. The displacement of the tunnel when moving with different segments is shown in Figure 3. When the excavation step changes from 3.6m to 7.2m, the maximum deflection of the shield tunnel changes from 1.92 mm to 2.59 mm; the maximum displacement value increases to 3.71mm when the excavation step increases to 14.4m. The choice of excavation length greatly affects the maximum displacement value of the tunnel. When the excavation step is doubled, the maximum deflection of the tunnel axis increases by 135% & 193% respectively compared to the maximum displacement value when the initial excavation step length is selected. The graph also shows that when the excavation/filling takes place within a range of 15m or more from the tunnel centerline, the deflection of the tunnel axis does not change significantly. This range can be the basis for determining the scope of the model size survey when modeling with finite elements. The residual deflection of the shield tunnel centerline when the excavation and filling process is completed is recorded according to the model as ~1.6mm.

The change in the maximum deflection of the tunnel when changing the width of the excavation pit is shown in Figure 4. The change of the maximum deflection of the tunnel when the width of the excavation pit changes is shown in Figure 4. The maximum deflection value changes rapidly when the width of the excavation pit changes from 4-15m. Then the maximum deflection value increases gradually. When the width of the excavation pit is from 25m or more, the maximum displacement of the tunnel has a stable value, even though the width of the excavation pit still increases. The maximum deflection of the tunnel axis currently is 4.7mm.

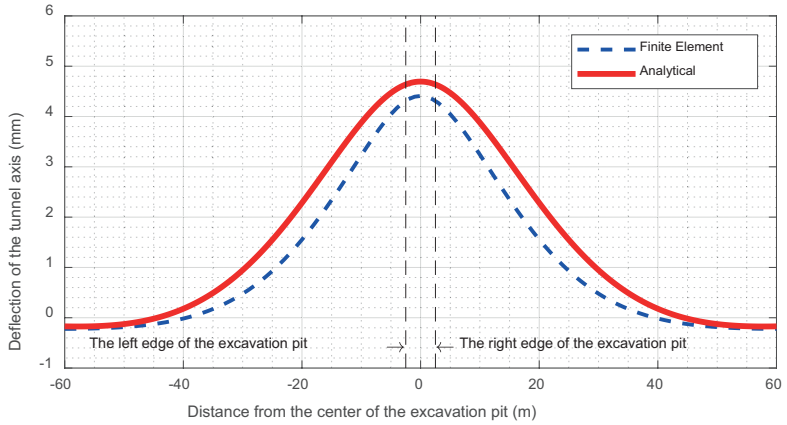


Figure 2. Deflection of the tunnel axis due to full-length excavation

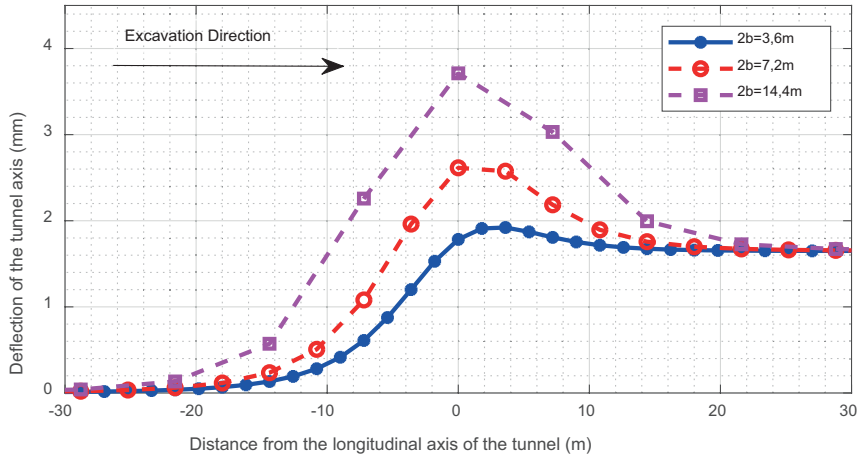


Figure 3. Maximum deflection of the tunnel axis with changing excavation position along the excavation direction and varying excavation step lengths

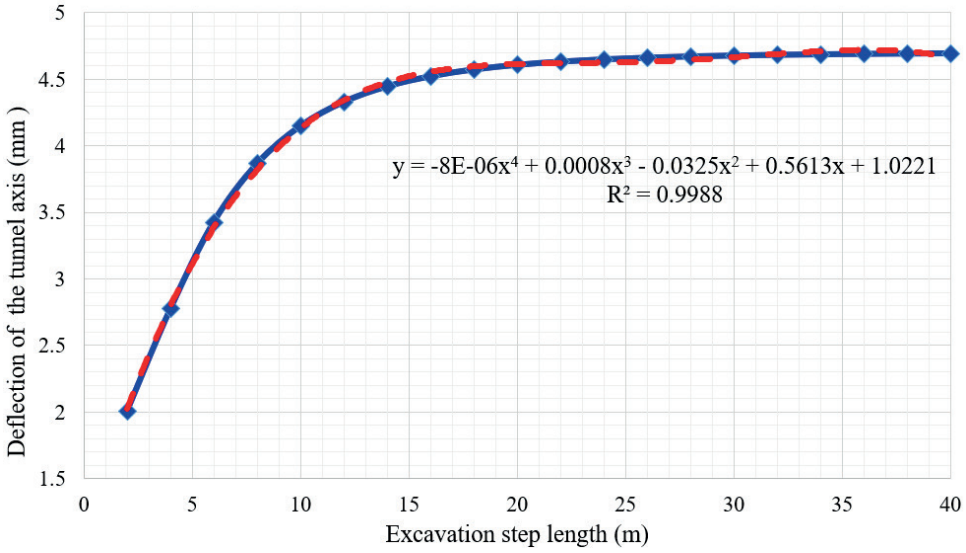


Figure 4. Maximum deflection of the tunnel axis with varying excavation step length

From the survey results, the relationship between the width of the excavation and the maximum deflection value of the tunnel centerline is established, the results are shown through the fourth-order function in Figure 4.

With the variance percentage R^2=0.9988, showing a good fit of the regression function, it can be used to predict values in the middle of the surveyed points.

5. CONCLUSIONS

The analytical approach for determining tunnel axis displacement during staged excavation of a foundation pit provides an important preliminary assessment tool, supporting the selection of suitable excavation step lengths. The results indicate that when excavation step lengths of 3.6 m, 7.2 m, and 14.4 m, the maximum tunnel deflection increases by approximately 135% and 193%, respectively, highlighting the significant influence of excavation step size. Based on these findings, an appropriate excavation step length can be selected to optimize construction performance.

This analytical method offers a simplified and efficient means of estimating tunnel displacement without the need for complex numerical tools such as the finite element method (FEM). However, the results obtained tend to be more conservative compared to FEM, as the analytical method neglects several influencing factors, including foundation stiffness and advanced soil constitutive models. Further research is therefore required, particularly with the incorporation of soil–structure interaction models such as the Pasternak two-parameter foundation model, as well as advanced structural models like the Timoshenko beam theory.

Upon completion of the excavation process, the maximum residual deflection observed at the tunnel crown is approximately 1.6 mm, regardless of excavation step length. Thus, when assessing safety with respect to deflection limits, both cumulative construction-induced deflections and long-term residual deflections during operation must be taken into consideration.

ACKNOWLEDGEMENTS

This research has been done under the research project QG.25.21 « Study on the behavior of shield tunnels during the construction of foundation pits of adjacent structures » of Vietnam National University, Hanoi.

REFERENCES

1. **Chang C.T., Sun C.W., Duann S.W., Hwang R.N.** (2001). Response of a Taipei rapid transit system (TRTS) tunnel to adjacent excavation. *Tunnelling and Underground Space Technology*, 16, pp. 151-158. DOI: 10.1016/S0886-7798(01)00049-9
2. **Huang H., Huang X., Zhang D.** (2014). Centrifuge modelling of deep excavation over existing tunnels. *Proc. ICE-Geotech. Eng.*, 167, pp. 113-127. DOI: 10.1680/geng.11.00045
3. **Ng C.W.W.N., Sheng J., Hong Y.** (2013). Three-dimensional centrifuge modelling of basement excavation effects on an existing tunnel in dry sand. *Can. Geotech. J.*, 50, pp. 874-888. DOI: 10.1139/cgj-2012-0423
4. **Nguyen H.V., Nguyen D.D., Nguyen T.T., Le D.T.** (2024). A 3D finite element analysis and field monitoring of the residual displacement of the existing TBM tunnel after underground culvert construction: a case study in Ho Chi Minh City. *Proceedings of the 5th International Conference on Geotechnics for Sustainable Infrastructure Development (GEOTEC 2023)*, 395. https://doi.org/10.1007/978-981-99-9722-0_41.
5. **Hung N.V., Tam N.T.** (2024). Evaluate the influence of the excavation geometry of full-length construction on the longitudinal deformation of the existing tunnel when

constructing the excavation using an analytical approach. *Journal of Transportation Science and Technology*, 13, pp. 11-23. https://www.doi.org/10.55228/JTST.13(3).24-32

6. **Lou P., Li Y., Lu S., Xiao H., Zhang Z.** (2022). Deformation and mechanical characteristics of existing foundation pit and tunnel itself caused by shield tunnel undercrossing. *Symmetry*, 14, 0263. https://doi.org/10.3390/sym14020263
7. **Tam N.T., Hung N.V., Bac N.V., Tuan N.A.** (2023). Deformation analysis of existing tunnel using finite element method during construction of a full-length excavation pit. *Journal of Transportation Science and Technology*, 12, pp. 1-9. DOI: 10.55228/JTST.12(1).1-9
8. **Zhao X., Li Z., Dai G., Wang H., Yin Z., Cao S.** (2022). Numerical study on the effect of large deep foundation excavation on underlying complex intersecting tunnels. *Appl. Sci.*, 12, 4530. https://doi.org/10.3390/app12094530
9. **Tao X., Luan P., Ma J., Song W.** (2022). Influence of sublevel unloading excavation with deep consideration of the superposition effect on deformation of an existing tunnel under an intelligent geotechnical concept. *Wireless Communications and Mobile Computing*, 1400114. DOI: 10.1155/2022/1400114
10. **Yang Z., Wang X.** (2020). Influence of metro tunnel excavation on deformation of existing pedestrian underpass in Changzhou railway station platform. *IEEE Access*, 8, 2981343. DOI: 10.1109/ACCESS.2020.2984836
11. **Liu J., Shi C., Lei M., Cao C., Lin Y.** (2020). Improved analytical method for evaluating the responses of shield tunnel to adjacent excavations and its application. *Tunnelling and Underground Space Technology*, 98, 103339. https://doi.org/10.1016/j.tust.2020.103339
12. **Yu J., Zhang C.R., Huang M.S.** (2005). Soil–pile interaction due to tunnelling: comparison between Winkler and elastic continuum solutions. *Geotechnique*, 55, pp. 461-466. DOI: 10.1680/geot.2005.55.10.713
13. **Yu J., Zahng C., Hang M.** (2013). Soil–pipe interaction due to tunnelling: assessment of Winkler modulus for underground pipelines. *Computers and Geotechnics*, 55, pp. 17-28. https://doi.org/10.1016/j.compgeo.2012.12.005
14. **Nguyen T.T., Nguyen V.H.** (2024). Analytical approach to determine longitudinal deformation of the existing precast tunnel during construction of a full-length excavation pit. *International Journal for Computational Civil and Structural Engineering*, 20, pp. 46-56. https://doi.org/10.22337/2587-9618-2024-20-1-46-56
15. **Liao S.M., Peng F.L., Shen S.L.** (2008). Analysis of shearing effect on tunnel induced by load transfer along longitudinal direction. *Tunnelling and Underground Space Technology*, 23, pp. 421-430. DOI: 10.1016/j.tust.2007.07.001
16. **Zhuang X., Ou X., Fu J.** (2017). Deformation response of an existing tunnel to upper excavation of foundation pit and associated dewatering. *Int. J. Geomech.*, 17, 04016112. DOI: 10.1061/(ASCE)GM.1943-5622.0000814
17. **Zhang Z., Huang M., Wang W.** (2013). Evaluation of deformation response for adjacent tunnels due to soil unloading in excavation engineering. *Tunnelling and Underground Space Technology*, 38, pp. 244-253. https://doi.org/10.1016/j.tust.2013.07.002
18. **Verruijt A.** (2009). An introduction to soil dynamics. *Delft University of Technology*.
19. **Attewell P.B., Yeates J., Selby A.R.** (1987). Soil movements induced by tunnelling and their effects on pipelines and structures. *Chapman & Hall*.
20. **Vesic A.B.** (1961). Bending of beams resting on isotropic elastic solids. *Journal of*

Engineering Mechanics Division, ASCE, 87, pp. 35-53.

СПИСОК ЛИТЕРАТУРЫ

1. **Chang C.T., Sun C.W., Duann S.W., Hwang R.N.** (2001). Response of a Taipei rapid transit system (TRTS) tunnel to adjacent excavation. *Tunnelling and Underground Space Technology*, 16, pp. 151-158. DOI: 10.1016/S0886-7798(01)00049-9
2. **Huang H., Huang X., Zhang D.** (2014). Centrifuge modelling of deep excavation over existing tunnels. *Proc. ICE-Geotech. Eng.*, 167, pp. 113-127. DOI: 10.1680/geng.11.00045
3. **Ng C.W.W.N., Sheng J., Hong Y.** (2013). Three-dimensional centrifuge modelling of basement excavation effects on an existing tunnel in dry sand. *Can. Geotech. J.*, 50, pp. 874-888. DOI: 10.1139/cgj-2012-0423
4. **Nguyen H.V., Nguyen D.D., Nguyen T.T., Le D.T.** (2024). A 3D finite element analysis and field monitoring of the residual displacement of the existing TBM tunnel after underground culvert construction: a case study in Ho Chi Minh City. *Proceedings of the 5th International Conference on Geotechnics for Sustainable Infrastructure Development (GEOTEC 2023)*, 395. https://doi.org/10.1007/978-981-99-9722-0_41.
5. **Hung N.V., Tam N.T.** (2024). Evaluate the influence of the excavation geometry of full-length construction on the longitudinal deformation of the existing tunnel when constructing the excavation using an analytical approach. *Journal of Transportation Science and Technology*, 13, pp. 11-23. https://www.doi.org/10.55228/JTST.13(3).24-32
6. **Lou P., Li Y., Lu S., Xiao H., Zhang Z.** (2022). Deformation and mechanical characteristics of existing foundation pit and tunnel itself caused by shield tunnel undercrossing. *Symmetry*, 14, 0263. https://doi.org/10.3390/sym14020263
7. **Tam N.T., Hung N.V., Bac N.V., Tuan N.A.** (2023). Deformation analysis of existing tunnel using finite element method during construction of a full-length excavation pit. *Journal of Transportation Science and Technology*, 12, pp. 1-9. DOI: 10.55228/JTST.12(1).1-9
8. **Zhao X., Li Z., Dai G., Wang H., Yin Z., Cao S.** (2022). Numerical study on the effect of large deep foundation excavation on underlying complex intersecting tunnels. *Appl. Sci.*, 12, 4530. https://doi.org/10.3390/app12094530
9. **Tao X., Luan P., Ma J., Song W.** (2022). Influence of sublevel unloading excavation with deep consideration of the superposition effect on deformation of an existing tunnel under an intelligent geotechnical concept. *Wireless Communications and Mobile Computing*, 1400114. DOI: 10.1155/2022/1400114
10. **Yang Z., Wang X.** (2020). Influence of metro tunnel excavation on deformation of existing pedestrian underpass in Changzhou railway station platform. *IEEE Access*, 8, 2981343. DOI: 10.1109/ACCESS.2020.2984836
11. **Liu J., Shi C., Lei M., Cao C., Lin Y.** (2020). Improved analytical method for evaluating the responses of shield tunnel to adjacent excavations and its application. *Tunnelling and Underground Space Technology*, 98, 103339. https://doi.org/10.1016/j.tust.2020.103339
12. **Yu J., Zhang C.R., Huang M.S.** (2005). Soil–pile interaction due to tunnelling: comparison between Winkler and elastic continuum solutions. *Geotechnique*, 55, pp. 461-466. DOI: 10.1680/geot.2005.55.10.713
13. **Yu J., Zhang C., Hang M.** (2013). Soil–pipe interaction due to tunnelling: assessment of Winkler modulus for underground pipelines. *Computers and Geotechnics*, 55, pp. 17-28. https://doi.org/10.1016/j.compgeo.2012.12.005

14. **Nguyen T.T., Nguyen V.H.** (2024). Analytical approach to determine longitudinal deformation of the existing precast tunnel during construction of a full-length excavation pit. *International Journal for Computational Civil and Structural Engineering*, 20, pp. 46-56. https://doi.org/10.22337/2587-9618-2024-20-1-46-56
15. **Liao S.M., Peng F.L., Shen S.L.** (2008). Analysis of shearing effect on tunnel induced by load transfer along longitudinal direction. *Tunnelling and Underground Space Technology*, 23, pp. 421-430. DOI: 10.1016/j.tust.2007.07.001
16. **Zhuang X., Ou X., Fu J.** (2017). Deformation response of an existing tunnel to upper excavation of foundation pit and associated dewatering. *Int. J. Geomech.*, 17, 04016112. DOI: 10.1061/(ASCE)GM.1943-5622.0000814
17. **Zhang Z., Huang M., Wang W.** (2013). Evaluation of deformation response for adjacent tunnels due to soil unloading in excavation engineering. *Tunnelling and Underground Space Technology*, 38, pp. 244-253. https://doi.org/10.1016/j.tust.2013.07.002
18. **Verruijt A.** (2009). An introduction to soil dynamics. *Delft University of Technology*.
19. **Attewell P.B., Yeates J., Selby A.R.** (1987). Soil movements induced by tunnelling and their effects on pipelines and structures. *Chapman & Hall*.
20. **Vesic A.B.** (1961). Bending of beams resting on isotropic elastic solids. *Journal of Engineering Mechanics Division, ASCE*, 87, pp. 35-53.

Nguyen Van Hung, Ph.D. in Engineering, lecturer, Faculty civil engineering, university of engineering and tecnology, 123105 Vietnam, Hanoi, Xuan Thuy, 144, email: vanhung.nguyen@vnu.edu.vn

Нгуен Ван Хунг – кандидат технических наук, предподователь кафедра «Строительные - Транспортные технологии», университет технологий (VNU-UET); 123105 Вьетнам, Ханой, Суан Тхуй, стр. 144, email: vanhung.nguyen@vnu.edu.vn

Nguyen Trong Tam, Ph.D. in Engineering, Head of the Department of Railways and Metro, Ho Chi Minh City University of Transport; 717066 Vietnam, Ho Chi Minh City, Vo Oanh, 2, tel. +842838991373, email: trongtam.nguyen@ut.edu.vn

Нгуен Чонг Там, кандидат технических наук, заведующий департамент «Железная дорога и метрополитен», Хошиминский университет транспорта; 717066 Вьетнам, г. Хошимин, Во Оань, стр. 2, тел. +842838991373, e-mail: trongtam.nguyen@ut.edu.vn